APPLIED COMPUTATIONAL ELECTROMAGNETICS SOCIETY JOURNAL

March 2016
Vol. 31 No. 3
ISSN 1054-4887

The ACES Journal is abstracted in INSPEC, in Engineering Index, DTIC, Science Citation Index Expanded, the Research Alert, and to Current Contents/Engineering, Computing & Technology.

The illustrations on the front cover have been obtained from the research groups at the Department of Electrical Engineering, The University of Mississippi.

EMERITUS EDITORIAL ASSISTANTS

MARCH 2016 REVIEWERS

THE APPLIED COMPUTATIONAL ELECTROMAGNETICS SOCIETY

JOURNAL

Vol. 31 No. 3 March 2016

TABLE OF CONTENTS

Discretized Aperture Integration, Surface Integration Analysis of Airborne Radomes

Jared Williams Jordan [1] and Benjamin L. Cannon [2]

[1] Raytheon Missile Systems
Tucson, AZ 85756, USA
jaredwilliamsjordan@gmail.com

[2] Nuvotronics LLC
Durham, NC 27703, USA
bcannon@nuvotronics.com

***Abstract* —** Full-wave electromagnetic methods are becoming increasingly more viable for the design and analysis of airborne radomes; however, there still exist many applications that require the speed associated with high frequency approximation methods. Presented here are accuracy improvements to the aperture integration surface integration (AiSi) method by incorporating both aperture and radome discretization into smaller groups in advance of the propagation routines, herein referred to as discretized radome discretized aperture integration surface integration (DrDaiSi). Dyadic Green's functions are utilized to determine exact field vectors from source current vectors. The capabilities of DrDaiSi are well-tested for typical airborne radomes, and a case study is presented which includes a 2:1 fineness ratio tangent ogive radome with dielectric constant of 7 and a metallic tip. The benefits of the DrDaiSi algorithm over a non-discretized AiSi method for predicting radome loss, boresight error, and radiation pattern degradation are demonstrated. Results are compared to a full-wave solution of the antenna and radome problem that was solved in CST to represent "truth." Transmission loss agreement is achieved to within 0.4 dB or better, and boresight error agreement is achieved to within 0.2 deg. or better in both elevation and azimuth scan planes for a severely detuned radome.

***Index Terms* —** Airborne radomes, aperture antennas, aperture integration surface integration (AiSi), boresight error (BSE), dyadic Green's functions, monopulse radar.

I. INTRODUCTION

Modern computing resources are capable of performing full-wave electromagnetic simulations of electrically large antenna and radome problems with ever increasing speed and accuracy. As computing technology and commercially-available solvers continue to improve their capabilities, a full-wave approach at airborne radome design and analysis will continue to become progressively more viable, providing improved accuracy over conventional high-frequency approximation solvers. However, at present-day there still exist many applications where full-wave solvers cannot be used due to prohibitively long run times, or the lack of available computing resources for an accurate solution. Global optimization schemes (*e.g.*, particle swarm, genetic algorithm, etc.) that are often used for antenna and radome design can require hundreds to thousands of iterations depending upon the number of design variables involved. Additionally, simulating radome performance over an entire field-of-regard for various environmental conditions can require a multitude of simulations. Furthermore, multi-layered radome wall configurations often require significant mesh densities to resolve thin layers or fine features along the radome wall, which can result in large RAM usage and excessive computational runtime. For all of the aforementioned reasons, there still exist many benefits of continuing the development of approximation solvers and not to model the entire problem space with full-wave methods.

Over the years, several advances have been made to increase the fidelity of codes utilizing high-frequency approximation methods, and the topic continues to be of interest today. Physical optics (PO) methods and aperture integration surface integration (AiSi) methods [2]-[8] were developed to treat monolithic and layered radomes as scattering objects. In both the PO and AiSi approximations, equivalent electric and magnetic "currents" induced on the radome surfaces are integrated to determine radome effects. For each of these methods, though, the specific propagation functions that are used and the formulation of the scattering currents are what set apart each of the various algorithms that have been developed over the last half-century.

Meng et al. [4] indicate that Paris was the first to integrate the fields incident upon the inner surface of a

Submitted On: August 19, 2014
Accepted On: July 28, 2015

radome from an antenna, propagate the energy to the radome outer surface with transmission coefficients, and determine the resulting far-field characteristics by integrating these transmitted fields [9]. Paris spends much of the paper presenting the aperture-integration, surface-integration (AiSi) algorithm formulation, discussing how much of the radome must be included in the final integration to the far-field and how finely sample points should be spaced in the analysis. The author compares far-field pattern measurements to predictions for a horn antenna looking through the nose of a large, asymmetric, well-tuned A-sandwich radome.

Wu and Ruddick replace the aperture integration engine with a plane wave spectrum (PWS) representation of the antenna to determine the fields on the inner radome surface, referring to their algorithm as PWS-SI [10]. The motivation for moving from AI to PWS was to avoid "excessive computation time required for the large number of antenna near-field calculations." Additionally, the authors state that the individual plane waves in the PWS can be propagated through the radome by applying individual transmission coefficients and then summing the resulting fields on the outer radome surface. Furthermore, the benefit of using a true near-field engine inside the radome, as opposed to ray-tracing, is discussed. Predicted versus measured boresight error results are provided in one principle plane for two well-tuned radomes with corresponding fineness ratios of 1:1 and 2:1.

Shifflett demonstrates the capabilities of a radome analysis code, CADDRAD [11], which can utilize either ray-tracing to model the antenna or an aperture representation much like Paris [9]. The aperture integration version is capable of including a single internal radome bounce, and applies normal incidence transmission coefficients to the one-bounce energy that propagates through the radome. Transmission from the aperture through the radome can be performed at an individual current element-by-element level—which is similar to what will be shown herein—or at the full aperture level. Finally, radome surface currents are integrated to determine far-field radiation patterns. Comparisons between measured and predicted beam peak loss for three beam positions are provided. Additionally, agreement between measured boresight error (BSE) with simulated predictions is presented for a single scan plane.

The current paper outlines and demonstrates an aperture integration surface integration algorithm which utilizes dyadic Green's functions as the current-to-field propagator. Furthermore, both the aperture and radome are discretized into groups before the resulting propagated fields are transmitted through the radome. The authors refer to the algorithm as discretized radome, discretized aperture integration, surface integration (DrDaiSi). Additionally, DrDaiSi has the ability to model as many internal radome reflections as necessary for electromagnetic predictions of interest to reach satisfactory convergence. Far-field radiation patterns are predicted at three radome scan directions of interest and antenna boresight radome transmission and boresight errors in both the azimuth and elevation plane are compared to full-wave simulations. The prediction capabilities of DrDaiSi are well-tested for typical airborne radomes, as the presented radome case study possesses a large metallic tip, is significantly detuned, possesses a fineness ratio of 2:1, and the edge of the enclosed antenna are located within fractions of a wavelength to the radome wall.

II. FORMULATION OF DRDAISI

As was stated previously, DrDaiSi is an aperture integration surface integration (AiSi) code which includes discretization of the aperture surface—as well as the inner radome surface—into groups prior to the propagation, transmission, and integration algorithm procedures. This method involves the linear superposition of transmitted fields through the radome from these discretized groups. This simple modification will be shown to result in significant improvements over non-discretized AiSi for modeling the effects of a radome on an enclosed antenna when the antenna is in close proximity to the radome. Additionally, well-chosen aperture and radome group sizes can speed up computation time without significantly impacting accuracy.

DrDaiSi will first be briefly outlined, then details of the algorithm will provided:

1) *The inner surface of the radome is meshed using triangular facets. The dimensions of each facet are chosen such that they are small in comparison to the operating frequency wavelength and will ultimately produce converged results for the model predictions of interest; e.g., far-field radiation patterns, boresight errors, boresight radome loss.*
2) *Electric and magnetic currents that comprise the aperture are discretized into aperture groups in preparation for propagation to the radome inner surface.*
3) *For each individual aperture group, the induced electric and magnetic fields at the inner surface of the radome are calculated.*
4) *For each individual aperture group, the resultant reflected and transmitted fields on the radome surface are calculated using planar transmission and reflection coefficients.*
5) *The total transmitted fields from all aperture groups are translated to the outer surface of the radome, converted to equivalent currents and propagated to the far-field.*
6) *The total reflected fields are converted to equivalent currents. These equivalent currents are discretized into radome groups, each of which is individually radiated to the entire radome inner surface.*

7) *For each radome group, the resultant transmitted and reflected fields on the radome surface are calculated using planar transmission and reflection coefficients.*
8) *The total transmitted fields from all radome groups are moved to the outer surface of the radome, converted to equivalent currents and propagated to the far-field.*
9) *Steps 6-8 represent the propagation bounce energy within the radome and are repeated for as many bounces as are required to achieve satisfactory convergence for the model prediction parameters of interest.*

The equations for the full dyadic Green's functions (DGFs) in a homogenous and isotropic region are derived in Diaz and Milligan [12] and are summarized below. The DGFs are convenient as current-to-field propagators. The DGFs transform current sources, with arbitrary coordinates and vector components in a Cartesian coordinate system into corresponding field vectors defined at any observation point in a homogenous and isotropic medium. This enables one to keep track of the polarization of the radiated fields with respect to the source currents. The first type of DGF is used in the calculation of an electric field **E** due to an electric current **J**, denoted as $\underline{\underline{G}}_{EJ}$ and a magnetic field **H** due to a magnetic current **M**, denoted as $\underline{\underline{G}}_{HM}$, as shown in (1). The difference between the two being the replacement of ε with μ, in $\underline{\underline{G}}_{HM}$ to produce $\underline{\underline{G}}_{EJ}$; as the duality theorem dictates [13]:

$$\underline{\underline{G}}_{EJ}(\mathbf{R}) = \frac{\mu}{\varepsilon}\underline{\underline{G}}_{HM}(\mathbf{R}) = j\omega\mu\frac{e^{-jkR}}{4\pi R}\underline{\underline{X}}, \tag{1}$$

where, $\underline{\underline{X}}$ is defined as:

$$\underline{\underline{X}} = \left[\left(\underline{\underline{1}} - \hat{\mathbf{R}}\hat{\mathbf{R}}^{T}\right)\left(1 - \frac{1}{k^2R^2} - j\frac{1}{kR}\right) + \hat{\mathbf{R}}\hat{\mathbf{R}}^{T}\left(\frac{2}{k^2R^2} + j\frac{2}{kR}\right)\right]. \tag{2}$$

The second type of DGF is used for the calculation of a magnetic field due to an electric current, denoted as $\underline{\underline{G}}_{HJ}$ and an electric field due to a magnetic current, denoted as $\underline{\underline{G}}_{EM}$, as is provided in (3). The difference between the two being the replacement of +1 factor with a -1 factor, in $\underline{\underline{G}}_{HJ}$ to produce $\underline{\underline{G}}_{EM}$; as also dictated by the duality theorem:

$$\underline{\underline{G}}_{EM}(\mathbf{R}) = -\underline{\underline{G}}_{HJ}(\mathbf{R}) = -\frac{e^{-jkR}}{4\pi R}\left(\frac{1}{R} + jk\right)\hat{\mathbf{R}}\times\underline{\underline{1}}, \tag{3}$$

where, $\hat{\mathbf{R}}\times\underline{\underline{1}} = (\hat{\mathbf{R}}\times\hat{\mathbf{x}})\hat{\mathbf{x}}^{\mathbf{T}} + (\hat{\mathbf{R}}\times\hat{\mathbf{y}})\hat{\mathbf{y}}^{\mathbf{T}} + (\hat{\mathbf{R}}\times\hat{\mathbf{z}})\hat{\mathbf{z}}^{\mathbf{T}}$ and $\hat{\mathbf{x}}, \hat{\mathbf{y}}$, and $\hat{\mathbf{z}}$ are Cartesian unit column vectors. More details on dyadic Green's functions can be found in [12]-[15].

The above DGFs utilize the transport distance column vector, **R**, and its unit normal, $\hat{\mathbf{R}}$, (4), where primed coordinates refer to source current locations and unprimed coordinates refer to field observation positions:

$$\hat{\mathbf{R}} = \frac{\mathbf{R}}{R} = \frac{\mathbf{r}-\mathbf{r}'}{|\mathbf{r}-\mathbf{r}'|} = \frac{1}{\sqrt{(x-x')^2 + (y-y')^2 + (z-z')^2}}\begin{bmatrix} x-x' \\ y-y' \\ z-z' \end{bmatrix}. \tag{4}$$

The resulting four DGFs, $\left(\underline{\underline{G}}_{EJ}, \underline{\underline{G}}_{HM}, \underline{\underline{G}}_{EM}, \underline{\underline{G}}_{HJ}\right)$, then provide the electric and magnetic fields at an observation location ***r*** due to a source described by an electric current element and a magnetic current element. The resulting fields from the individual currents are summed, via superposition [13], to produce the overall source current distribution's electric and magnetic field responses, (5) and (6) respectively:

$$\mathbf{E}(r,\mathbf{J},\mathbf{M}) = -\iint_{S'}\underline{\underline{G}}_{EJ}(\mathbf{R})\cdot\mathbf{J}(\mathbf{r}')dS' - \iint_{S'}\underline{\underline{G}}_{EM}(\mathbf{R})\cdot\mathbf{M}(\mathbf{r}')dS', \tag{5}$$

$$\mathbf{H}(r,\mathbf{J},\mathbf{M}) = -\iint_{S'}\underline{\underline{G}}_{HJ}(\mathbf{R})\cdot\mathbf{J}(\mathbf{r}')dS' - \iint_{S'}\underline{\underline{G}}_{HM}(\mathbf{R})\cdot\mathbf{M}(\mathbf{r}')dS'. \tag{6}$$

DrDaiSi differs from non-discretized AiSi in how it propagates energy from the aperture through the radome. Rather than radiating the entire aperture to the radome inner surface and applying transmission/reflection coefficients to these total fields, the aperture is instead discretized into smaller, user-specified aperture groups whose energy is propagated through the radome individually. Without aperture discretization, a radome observation point often exists in the near-field of the enclosed aperture. Consequently, any near-field component existing along the primary direction of propagation is lost during the conversion to perpendicular and parallel components before the application of the transmission/reflection coefficients. By discretizing the aperture into smaller groups, the radiative far-field distance for the aperture groups become much shorter, and the radome thus exists in the far-field of the smaller aperture groups. Under this condition, negligible energy is lost during the conversion to perpendicular and parallel components, yielding more accurate results.

To appreciate the discretized aperture concept, the authors find it beneficial to draw comparisons to the plane wave spectrum (PWS) method for calculating electromagnetic fields. PWS is a transformation of the aperture fields into a set of propagating and non-propagating plane wave modes which emanate from the aperture plane in all directions. In practice, though, this expansion is typically truncated to a finite number of modes. At an observation point on the radome surface, the superposition of these plane waves can then recreate the near and far fields above the aperture plane. The radiation from a discretized aperture via DGFs is the

summation of electric and magnetic dipoles defined within individual aperture groups, whose phase centers correspond to the physical locations of the aperture groups. In this case, a point on the radome's inner surface "observes" a set of spherical waves radiating from each of the aperture group's phase center, which is a similar observation to what is witnessed during the PWS method when aperture groups are sufficiently small. Said another way, a point on the radome surface observes a finite set of spherical waves, instead of a finite set of plane waves, propagating from several different directions.

To ensure the radome is sufficiently in the far-field of each of the aperture groups, the following condition should be met [16], where *D* is the largest extent of the aperture group:

$$\text{FraunhoferRegion (Far-Field):} \quad R > \frac{2D^2}{\lambda}. \tag{7}$$

It should be noted that by meeting the above far-field condition (7), the user may decide to remove the $1/R^2$ and $1/R^3$ terms in the DGFs to reduce the calculation time of the algorithm. The authors decided against this since the improvement in calculation time was not appreciable enough to warrant this additional approximation to the method. Furthermore, by discretizing the aperture into well-chosen aperture group sizes, minimal energy is lost in the direction of propagation, and excessive calculations of transmission/reflection coefficients are avoided, since it is not necessary to perform this operation for every individual current element.

Before transmission and reflection coefficients can be determined for energy incident upon an inner radome surface triangular facet, the unit Poynting vector is calculated from [9]:

$$\hat{\mathbf{s}} = \frac{\mathrm{Re}\left(\mathbf{E_i} \times \mathbf{H_i^*}\right)}{\left|\mathrm{Re}\left(\mathbf{E_i} \times \mathbf{H_i^*}\right)\right|}. \tag{8}$$

The energy propagation direction is then used to determine the angle of incidence with respect to the facet's normal, which points into the radome.

The incident field energy is modified by transmission and reflection coefficients to determine the amount of energy that will leave the radome, to propagate to the far-field, and how much energy will be reflected and re-propagated inside the radome as bounce energy. These coefficients describe the behavior of a plane wave incident upon a flat wall of infinite extent. It is this approximation that removes the necessity of meshing the multiple layers that may compose the radome wall. A significant advantage of modeling an antenna/radome system with an aperture integration, surface integration method is the freedom in defining the transmission and reflection coefficients; they can be analytic expressions, numerically determined, experimentally measured or a combination of all. The presented antenna/radome problem made use of Fresnel coefficients [15].

Calculation of the transmitted fields through the radome is as follows. The incident fields are decomposed into perpendicular and parallel components, the corresponding orthogonal transmission coefficients are applied, and the modified field components are recombined. This process is summarized in (9) and (10), where the perpendicular and parallel transmission coefficients, $T_\perp$ and $T_{//}$, are defined with respect to the electric field vector. Magnetic fields are orthogonal to electric fields and as such the parallel transmission coefficient is used to modify the perpendicular component of the magnetic field and vice versa:

$$\mathbf{E_T} = \left(\mathbf{E_i} \cdot \hat{\mathbf{u}}_\perp\right) T_\perp \hat{\mathbf{u}}_\perp + \left(\mathbf{E_i} \cdot \hat{\mathbf{u}}_{//}\right) T_{//} \hat{\mathbf{u}}_{//}, \tag{9}$$

$$\mathbf{H_T} = \left(\mathbf{H_i} \cdot \hat{\mathbf{u}}_\perp\right) T_{//} \hat{\mathbf{u}}_\perp + \left(\mathbf{H_i} \cdot \hat{\mathbf{u}}_{//}\right) T_\perp \hat{\mathbf{u}}_{//}. \tag{10}$$

Similarly, the reflected fields (11) and (12) are calculated [6]:

$$\mathbf{E_R} = \left(\mathbf{E_i} \cdot \hat{\mathbf{u}}_\perp\right) R_\perp \hat{\mathbf{u}}_\perp + \left(\mathbf{E_i} \cdot \hat{\mathbf{u}}_{//}\right) R_{//} \hat{\mathbf{u}}_{//}, \tag{11}$$

$$\mathbf{H_R} = \left(\mathbf{H_i} \cdot \hat{\mathbf{u}}_\perp\right) R_{//} \hat{\mathbf{u}}_\perp + \left(\mathbf{H_i} \cdot \hat{\mathbf{u}}_{//}\right) R_\perp \hat{\mathbf{u}}_{//}. \tag{12}$$

As a first order approximation, the radome tip is modeled as a perfect electric conductor (PEC) and is treated as a simple blockage. All energy incident on a radome facet defined as PEC is reflected back into the radome. To account for the reflection from a perfect electric conductor using Fresnel coefficients, the following approximation is used [17]:

$$\text{PEC Approx:} \quad \varepsilon_r = 1 - j100{,}000; \quad \mu_r = 1 - j0. \tag{13}$$

Every inner radome surface facet has a corresponding outer radome surface facet. Each triangular facet is defined by three nodes. The facets surrounding each node are determined and the following is performed to determine the location of the outer facet node locations:

$$\mathbf{Node}_{Outer} = \mathbf{Node}_{Inner} + \frac{\sum_{n=1}^{N} FT_n \mathbf{FN}_n}{N}, \tag{14}$$

where *N* is the number of facets surrounding the node, *FT* is the facet thickness and **FN** is the facet unit normal.

Fields that are transported to the outer radome surface, from direct aperture illumination and consecutive bounce energy, are converted to current sources:

$$\mathbf{J_S} = \hat{\mathbf{n}} \times \mathbf{H}, \qquad \mathbf{M_S} = -\hat{\mathbf{n}} \times \mathbf{E}, \tag{15}$$

where $\hat{\mathbf{n}}$ is the outer surface normal. Electric and magnetic fields that are not transmitted through the radome from direct aperture illumination or consecutive radome bounce energy are also converted to tangential magnetic and electric currents (15), and serve as the consecutive bounce source currents. The radome was discretized into 4 longitudinal quadrants, defined by the intersection of the XZ and YZ planes when the radome is gimbaled to 0 deg. in azimuth and elevation. The radome quadrants are herein referred to as radome groups. Discretizing the radome into more groups did not produce better results. The authors believe that since the

radome is sourcing itself during bounce-energy propagation—often at grazing incidence—the determination of radome group size is not as well-defined as aperture group size. This is a topic of ongoing investigation.

The resulting bounce source currents are used to rattle energy within the radome, where transmitted fields at the outer radome surface from each radome group are summed via superposition in preparation for computation of far-field quantities of interest. After all, bounce energy has left the radome and outer surface currents have converged, the resultant outer radome surface currents are an approximation to the equivalence principle [13]. The antenna and radome are removed and a sheet of tangential electric and magnetic currents radiates in their place. It is only an approximation to equivalence principle since the sheet of current does not fully enclose the antenna and radome system, and any fields propagated to the aperture plane are neglected. It is believed that inclusion of these currents, in the computation of boresight radome loss and errors, possesses a relatively low impact for practical airborne radomes.

Converged tangential currents on the outer radome surface are then propagated to the far-field to calculate radiation patterns, boresight radome loss (16) and boresight errors (17), (18), where S_{EL} and S_{AZ} represent the monopulse slope values of the aperture in the elevation and azimuth planes, respectively [18]. The sum and delta patterns are formed from radiating the quadrants individually and applying superposition to the far-fields. Symmetry was utilized in the principle plane scans, and as a result only two of the four quadrants were needed per radome look direction in both the azimuth and elevation planes:

$$\text{RadomeLoss}_{dB} = 20\log_{10}\left(\frac{Efar_{SUM}(\text{Radome})}{Efar_{SUM}(\text{AirRadome})}\right), \quad (16)$$

$$BSE_{EL} = \frac{1}{S_{EL}}\,imag\left(\frac{Efar_{\Delta EL}}{Efar_{SUM}}\right), \quad (17)$$

$$BSE_{AZ} = \frac{1}{S_{AZ}}\,imag\left(\frac{Efar_{\Delta AZ}}{Efar_{SUM}}\right). \quad (18)$$

III. RADOME/ANTENNA PROBLEM UNDER INVESTIGATION

The radome and antenna system under evaluation was also used as a case study in the authors' previous paper [19] and will be shown again here in Fig. 1 and its dimensions will be restated for completeness of this paper. The antenna diameter is 10 in. and consists of 4 quadrants, each containing 17 half-wavelength resonant slots [20] designed for operation at 7 GHz. Each slot is individually fed by a WR-137 waveguide located behind the ground plane. The radome is a tangent ogive with an approximate fineness ratio of 2:1, inside base radius of 11 in., and an inner length of 22 in. The radome gimbal center is positioned 4 in. into the radome from its base. The plane that the slots reside in is located 1 in. from the gimbal center. The edge of the antenna is less than 0.25 in. (15% of a freespace wavelength at 7 GHz) from the inside of the radome. The top 1 in. of the radome is a metal tip, modeled as a perfect electric conductor (PEC). The radome shell is 0.3 in. thick and is constructed from a lossless dielectric with a relative permittivity of 7. The thickness of the radome wall was intentionally chosen to provide a detuned response at the operating frequency of 7 GHz to demonstrate the presented modeling methodology in a circumstance where significant bounce energy exists.

The normal of the antenna faceplate is directed along the positive z-axis and the radiating slots are y-polarized. The elevation plane is defined as the YZ plane, and the azimuth plane is defined as the XZ plane. The radome is gimbaled about the gimbal center, while the antenna is fixed and results will be presented as such.

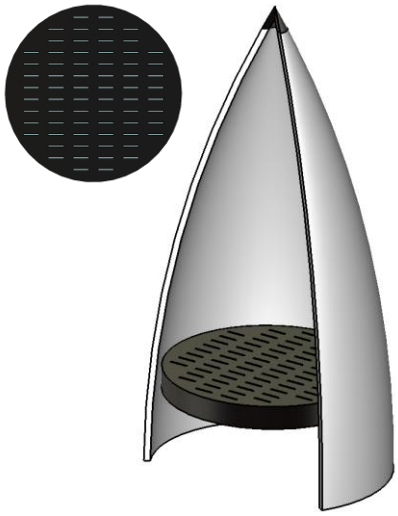

Fig. 1. Radome and antenna geometry under evaluation. The antenna is an array of 68 half-wavelength resonant radiating slots and is in close proximity to the radome.

IV. RADOME MODELING RESULTS AND DISCUSSION

In a previous publication by the authors [19], the same antenna and radome problem is analyzed, where the antenna and radome simulated together in a full-wave solver is presented as "truth" and is used as the baseline for comparison to quantify the accuracy of the proposed modeling method. Similarly, this paper will use the same baseline results to quantify the performance of DrDaiSi. However, the results corresponding to the equivalent aperture, used in conjunction with CST's full-wave solver, will not be revisited here since it is not the focus of this paper. Instead, the reader is encouraged to compare the results of the two antenna/radome methods and determine which of the two better serves their needs.

Furthermore, both modeling methods utilize the same equivalent aperture representation of the radiating slot antenna quads and the reader is referred to the author's previous publication to understand how they are formed [19].

The normalized magnitude of the electric field transmitted to the outer radome surface from direct quadrant 1 aperture illumination and the three consecutive bounces is illustrated in Fig. 2. Transmitted electric fields from direct aperture illumination are presented in Figs. 2 (a) and (b), where the radome is oriented in the XY and the XZ planes, respectively. As it can be seen, most of the energy is focused on the part of the radome existing in the first quadrant, indicating that the aperture is well-collimated. The magnitude of the transmitted field for the first bounce, Fig. 2 (c), is a clear indicator that the radome is detuned and bounce energy should be considered in the analysis. The magnitudes of the transmitted fields for the second radome bounce are significantly lower, Fig. 2 (d), but are still present. It is not until the third radome bounce, Fig. 2 (e), that the transmitted fields are significantly lower (less than the 30 dB colormap range) than the transmitted fields from direct aperture illumination. For this case study, including bounce energy past three iterations had a negligible impact on far-field radiation patterns, boresight radome loss and boresight error.

The transmitted fields on the outer radome surface in Fig. 2 incorporated discretization of the aperture and the radome. In an effort to demonstrate the impact of aperture and radome discretization on far-field results, DrDaiSi is also compared to the scenario where the aperture radiates as a whole to the radome and the entire inner radome surface serves as a source to itself as one group for consecutive bounce iterations; herein this scenario will be referred to as AiSi.

Far-field patterns for the antenna looking out the nose of the radome are presented in Figs. 3 (a) and (b), where normalized gain values are calculated in the elevation and azimuth planes. Normalization is with respect to the peak antenna/aperture only results. Full-wave results are obtained using CST's finite integration technique solver and are labeled accordingly. In reference to the elevation plane, AiSi incorrectly predicts the magnitude of the main beam, and is quantified in Fig. 6. In addition to over predicting the boresight antenna/aperture gain by almost 1.5 dB, the structure of the main beam is not captured. In contrast, the DrDaiSi results are much better; the boresight antenna/aperture gain is approximately 0.4 dB too large and the main beam structure is better captured. Furthermore, AiSi predicted first null and first sidelobe are poorly predicted and their locations are off by 3 deg. in the elevation plane, whereas DrDaiSi captures this behavior well within 1 deg. With respect to both the azimuth and elevation far-field patterns, the peak sidelobe levels are predicted by AiSi within 5-6 dB and within 2-3 dB by DrDaiSi. However, both methods begin to deviate from the full-wave CST results past 60 deg., where alignment of sidelobe peaks and nulls falls apart and magnitudes of sidelobe peaks can be greater than 5 dB from "truth." This is largely in part due to the fact that the antenna is represented by an equivalent aperture.

The elevation plane farfield patterns, for radome gimbal direction of 0 deg. azimuth and 20 deg. elevation is presented in Fig. 4. This radome look direction is of particular interest since it demonstrates significant deflection of the main beam, as is shown in Fig. 7 (a) to be approximately 1 deg. DrDaiSi accurately predicts the far-field response but starts to deviate from CST past -60 deg. AiSi does not perform as well; the transmission prediction is too high, the first sidelobe levels are approximately 2 dB too large, and the rippled sidelobe behavior that occurs near 60 deg. is not well-captured. This ripple in the sidelobes is a product of the constructive and destructive interference of scattered energy transmitted through the radome, and is non-existent for antenna-only radiation.

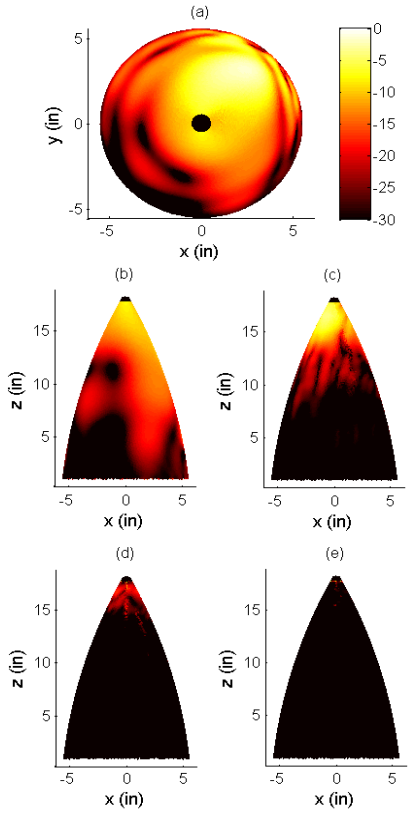

Fig. 2. Normalized magnitude of the transmitted electric fields from direct Quadrant 1 aperture illumination and bounce energy when the radome is gimbaled 0 degrees in azimuth and 0 degrees in elevation. Transmitted fields are a result of: (a) direct aperture illumination, (b) direct aperture illumination (c) first radome bounce, (d) second radome bounce, and (e) third radome bounce.

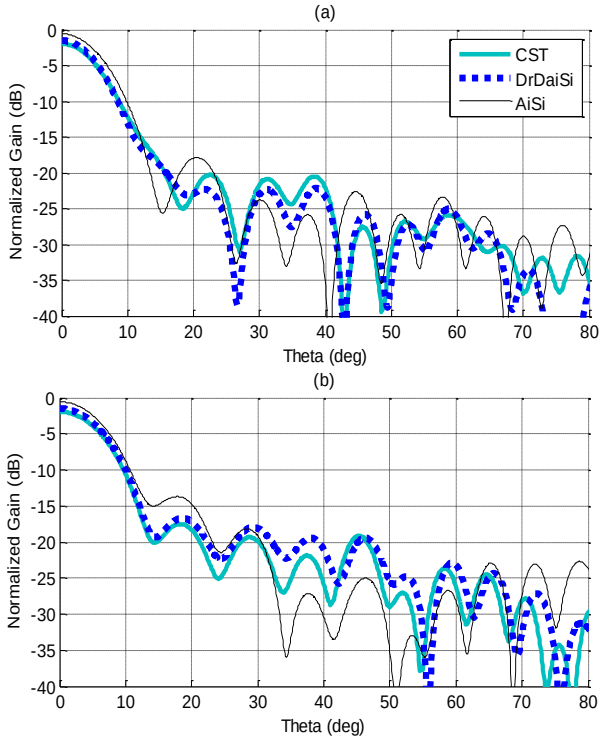

Fig. 3. Effect of radome on antenna/aperture far-field patterns where the radome is gimbaled 0 degrees in azimuth and 0 degrees in elevation. (a) Far-field patterns in EL-plane, and (b) far-field patterns in AZ-plane. Patterns are normalized to peak antenna/aperture far-field value.

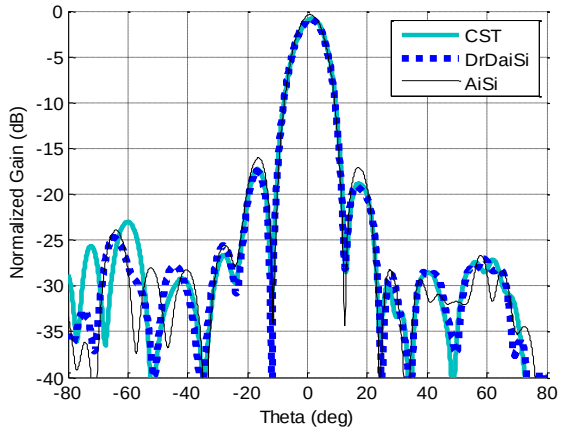

Fig. 4. Effect of radome on antenna/aperture EL-plane far-field patterns where the radome is gimbaled 0 degrees in azimuth and 20 degrees in elevation. Patterns are normalized to peak antenna/aperture far-field value.

The last presented radome look direction of interest, with respect to far-field patterns, is radome gimbal direction of 14 deg. azimuth and 0 deg. in elevation, provided in Fig. 5. Here, an interesting phenomenon referred to as a "bounce lobe" or "flash lobe" appears centered around 55 deg. Bounce lobes are typically dominant in an H-plane scan where radome transmission is dominated by perpendicular polarized energy. The dominant energy constructing a bounce lobe is the energy from the first bounce reflecting from the radome back wall, transmitting through the front wall. Often this reflection occurs on the back wall close to the radome tip, as is with the case of the current radome under investigation. The nose of the radome is where small radii of curvature exist and where the current modeling method starts to break-down. To increase the accuracy of the proposed method a full-wave solver such as method of moments could be incorporated with the presented modeling method to capture a more representative scattering effect from the radome tip [1]. With that being said, both DrDaiSi and AiSi capture the presence of a flash lobe with the correct number of peaks and valleys with corresponding magnitude values within 3-4 dB from CST. DrDaiSi does outperform AiSi with respect to peak main beam normalized gain by deviating from "truth" by only 0.1 dB as opposed to almost 1 dB, see Fig. 6 (b).

The presented farfield radiation patterns indicate the presence of boresight transmission loss and boresight errors, but it is difficult to quantify their values from the radiation pattern plots with much accuracy; therefore, the data will be presented in a more digestible form. Boresight radome loss and errors are calculated using (16) through (18) for both the elevation and azimuth planes and are plotted versus radome look direction in Fig. 6 and Fig. 7. Boresight radome loss will be presented with the scale of zero attenuation to half-power loss. In the case of this radome, the energy is not lost to a dielectric loss tangent, but rather to re-radiation of energy into different directions, resulting in the distortion of the main-beam and an increase in side lobe levels.

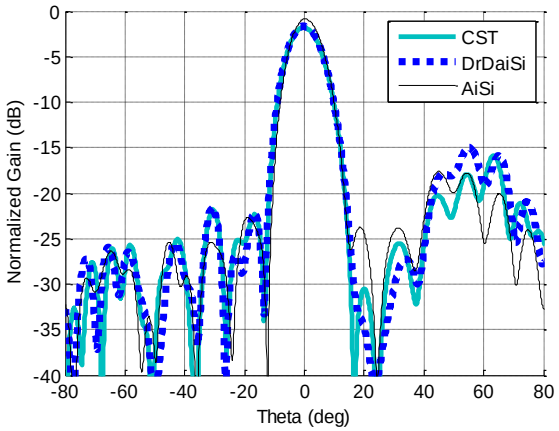

Fig. 5. Effect of radome on antenna/aperture AZ-plane far-field patterns where the radome is gimbaled 14 degrees in azimuth and 0 degrees in elevation. Patterns are normalized to peak antenna/aperture far-field value.

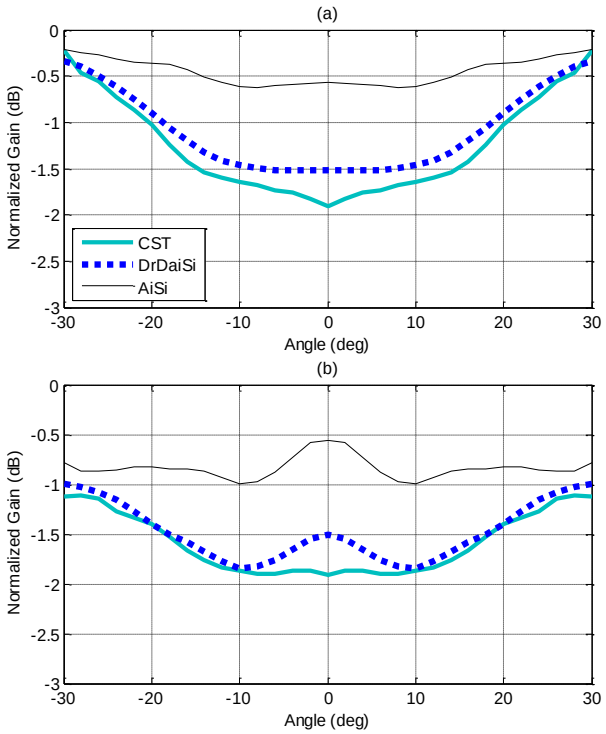

Fig. 6. Effect of radome on antenna/aperture bore-sight transmission as radome is gimbaled in the: (a) elevation and (b) azimuth planes. Transmission values are normalized to antenna/aperture bore-sight transmission.

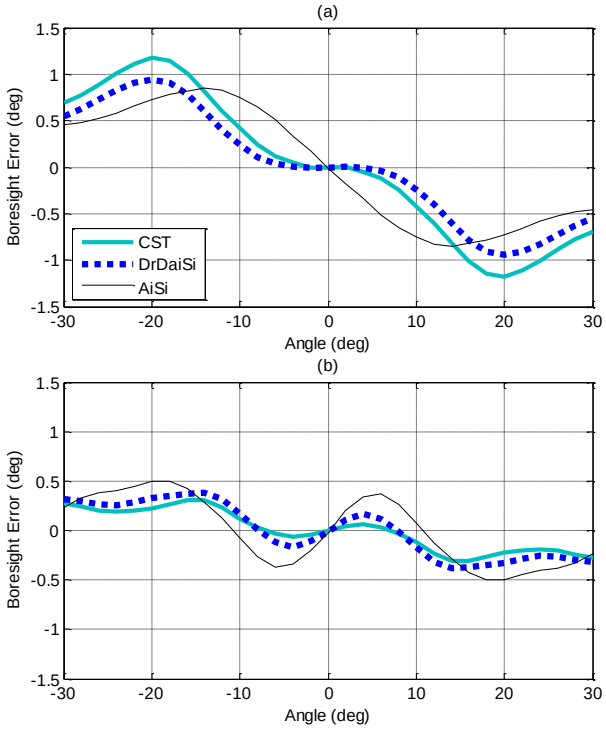

Fig. 7. Antenna/Aperture bore-sight error as radome is gimbaled in the: (a) elevation and (b) azimuth planes.

In reference to Fig. 6, a couple of important observations can be quickly deduced. Firstly and most importantly, the AiSi results deviate from CST significantly more than DrDaiSi. The worst agreement for both modeling methods corresponds to the antenna/aperture looking out the radome nose, where AiSi over predicts the gain by 1.3 dB and the DrDaiSi predicted gain value is almost 1 dB closer to "truth". The effect of incorporating the discretized aperture and radome into the aperture integration, surface integration algorithm has a significant impact on improving the accuracy of predicted gain values.

Furthermore, the limitations of the proposed method are also illustrated in Fig. 6. By comparing the DrDaiSi and CST results starting from the antenna/aperture looking out the radome nose to looking out the side of the radome, an increase in correlation is witnessed. Additionally, the DrDaiSi results are consistently higher than CST along both cuts, with the peak gain discrepancy corresponding to looking out the radome nose. These results indicate that too much energy is being propagated from the radome outer surface to the far field. The radome nose is where the smallest radi of curvature exist and where inner surface facets grow to correspondingly larger outer surface facets, as dictated by (14). Planar transmission coefficients assume the incident surface is equal in area to the transmission surface. In an attempt to more accurately represent the fields toward the radome tip, the fields could be tapered down as a result of the outer surface growth. The proposed method could possibly benefit from some sort of divergence factor and could be a topic for further investigation.

In reference to Fig. 7, the benefit of the discretized aperture and radome can be clearly seen in the boresight error results. The location of CST's peak BSE is 20 deg. in the elevation plane and 14 deg. in the azimuth plane, both accurately predicted by DrDaiSi. AiSi incorrectly predicts the maximum BSE locations to be 14 deg. in the elevation plane and 19 deg. in the azimuth plane, which is a 5-6 deg. deviation from "truth". The boresight error slope is also better captured by DrDaiSi, especially through the radome nose in the elevation plane. However, DrDaiSi's predicted peak BSE magnitude is off from CST by approximately 0.2 deg. in the elevation plane. Keeping in mind all of the modeling difficulties associated with this specific antenna/radome case study, i.e., high fineness ratio, detuned wall design, large metal tip, antenna/aperture in close proximity to the radome, some prediction inaccuracies associated with utilizing a high frequency approximation technique are expected.

Boresight error can be a very sensitive radome characteristic. The presence of a metal tip can affect the boresight error out to large radome gimbal angles even when the tip is outside the main beam of energy propagating from the antenna/aperture. If more accuracy is desired in predicting boresight error, and the user has the access to more computational hardware/software and

can accept longer simulation times, the modeling technique outlined in the authors' previous publication is recommended [19].

V. CONCLUSIONS

The benefits, of including discretization into the aperture integration, surface integration radome modeling technique have been demonstrated. Good agreement between far-field radiation patterns, boresight radome loss and boresight error predictions from CST and DrDaiSi has been shown. The notion of discretizing the aperture and radome extends the AiSi method's applicability to the analysis and design of airborne radomes which exist in the near-field of an enclosed antenna. Such near-field radome modeling would otherwise need to be performed with a full-wave method such as FIT, FDTD, MoM, or some other full-wave technique. In addition, the use of dyadic Green's functions as the field propagators was provided as a straightforward, matrix-math implementation.

Future research could include the hybridization of a full-wave solver to model the tip region; however, modeling the metal tip as a simple PEC blockage produced very good results for a fast and easily implementable high frequency approximation method. Additionally, the inclusion of a divergence factor to account for the growing outer radome surface facet area, as opposed to directly transporting fields from the inner to the outer radome surface via infinite flat planar transmission coefficients could provide improved transmission results. Fundamentally, all of these types of potential upgrades are still an approximation to the true electromagnetic interactions that occur. It is ultimately at the discretion of the radome engineer to decide when these approximations are valid, or when a full-wave technique must be used.

REFERENCES

[1] M. A. Abdel Moneum, Z. Shen, J. L. Volakis, and O. Graham, "Hybrid PO-MoM analysis of large axi-symmetric radomes," *Antennas and Propagation, IEEE Transactions on*, vol. 49, no. 12, pp. 1657-1666, 2001.

[2] A. Renuka and V. G. Borkar, "Computer-aided analysis for tangent Ogive airborne radome using physical optics method," *In Microwave Conference Proceedings, 2005, APMC 2005, Asia-Pacific Conference Proceedings*, vol. 5, pp. 4-pp., IEEE, 2005.

[3] C. D. Finlay, S. Gregson, R. W. Lyon, and J. McCormick, "SPIKE a physical optics based code for the analysis of antenna radome interactions," *In Radar Systems, 2007 IET International Conference on*, pp. 1-5, IET, 2007.

[4] H. F. Meng, W. Dou, and K. Yin, "Analysis of antenna-radome system at millimeter wave band," *In Millimeter Waves, 2008, GSMM 2008, Global Symposium on*, pp. 380-383, IEEE, 2008.

[5] H. Meng and W. Dou, *Analysis and Design of Radome in Millimeter Wave Band*, Microwave and Millimeter Wave Technologies from Photonic Bandgap Devices to Antenna and Applications, Igor Minin (ed.), ISBN: 978-953-7619-66-4, InTech, DOI: 10.5772/9054, 2010.

[6] H. F. Meng and W. Dou, "Rapid analysis of electrically large radome," *In Microwave and Millimeter Wave Technology (ICMMT), 2010 International Conference on*, pp. 99-101, IEEE, 2010.

[7] H. F. Meng and W-B. Dou, "Fast analysis of electrically large radome in millimeter wave band with fast multipole acceleration," *Progress In Electromagnetics Research 120*, pp. 371-385, 2011.

[8] T. Schuster and M. Sabielny, "REACH/PREACH—a physical optics based tool for simulation of radome effects on antenna patterns," *In Antennas and Propagation (EUCAP), 2012 6th European Conference on*, pp. 3225-3229, IEEE, 2012.

[9] D. Paris, "Computer-aided radome analysis," *Antennas and Propagation, IEEE Transactions on*, vol. 18, no. 1, pp. 7-15, 1970.

[10] D. C. Wu and R. Rudduck, "Plane wave spectrum-surface integration technique for radome analysis," *Antennas and Propagation, IEEE Transactions on*, vol. 22, no. 3, pp. 497-500, 1974.

[11] J. A. Shifflett, "CADDRAD: a physical optics radar/radome analysis code for arbitrary 3D geometries," *Antennas and Propagation Magazine, IEEE*, vol. 39, no. 6, pp. 73-79, 1997.

[12] L. Diaz and T. A. Milligan, *Antenna Engineering Using Physical Optics: Practical CAD Techniques and Software*, Artech House, Inc., 1996.

[13] R. F. Harrington, *Time Harmonic Electromagnetic Fields*, McGraw-Hill Book Co., New York, 1961.

[14] L. B. Felsen and N. Marcuvitz, *Radiation and Scattering of Waves*, Englewood Cliffs, NJ: Prentice-Hall, 1973.

[15] C.A.Balanis, *Advanced Engineering Electromagnetics*, New York, NY: John Wiley & Sons, 1989.

[16] C. A. Balanis, *Antenna Theory: Analysis and Design*, (3rd edition), New York, NY: John Wiley & Sons, 2005.

[17] B. M. Kolundzija, "Electromagnetic modeling of composite metallic and dielectric structures," *Microwave Theory and Techniques, IEEE Transactions on*, vol. 47, no. 7, pp. 1021-1032, 1999.

[18] D.J.Kozakoff, *Analysis of Radome-Enclosed Antennas*, Artech House Publishers, 2009.

[19] B. L. Cannon and J. W. Jordan, "Integration of an equivalent aperture method into full-wave electromagnetic simulation of airborne radomes."

[20] R. S. Elliott, *Antenna Theory and Design*, John

Wiley & Sons, 2003.

Jared Williams Jordan was born in Farmington, Maine on February 6, 1983. He received the B.S. degree in Electrical and Computer Engineering from University of Maine, Orono, ME, in 2005 and the M.S. degree in Electrical and Computer Engineering from University of Arizona, Tucson, AZ, in 2008. He has worked at Newpage Corporation as a Reliability Engineer (2005-2006) and at the University of Arizona as a Senior Research Engineer (2008-2010). He previously worked as a Senior Electrical Engineer at Raytheon Missile Systems, Tucson, AZ (2010-2014), and is currently an Associate Technical Staff at MIT Lincoln Laboratory, Lexington, MA in the Advanced Technology Division: RF Technology (group 86). His current research interests include antenna and radome analysis and design, computational electromagnetics and material characterization.

Benjamin L. Cannon was born in McKeesport, PA in 1986. He received the B.S. degree in Electrical and Computer Engineering from Carnegie Mellon University, Pittsburgh, PA, in 2008 and the S.M. degree in Electrical Engineering from the Massachusetts Institute of Technology, Cambridge, MA in 2010. He previously worked as a Senior Electrical Engineer at Raytheon Missile Systems, Tucson, AZ (2010-2013), and is currently a Member of the Technical Staff at Nuvotronics, LLC, Durham, NC. He is interested in electromagnetic field and wave interactions with materials.

Indoor Wave Propagation Prediction for Corridors Segments with Partially Reflecting Walls by Using 3D Waveguide Modal Analysis

Hany M. El-Maghrabi [1], Ahmed M. Attiya [2], and Essam A. Hashish [3]

[1] Department of Electromechnical
Housing and National Research Center, Cairo, Egypt
helmaghrabi@hbrc.edu.eg

[2] Department of Microwave Engineering
Electronic Research Institute, Cairo, Egypt
attiya@eri.sci.eg

[3] Department of Electronics and Electrical Communication
Cairo University, Cairo, Egypt
essamhh@ieee.org

Abstract ─ In this paper, a model is presented to simulate wave propagation in indoor corridors with partially reflecting walls. The model is based on combination of modal analysis, dyadic Green's function, mode matching method and generalized scattering matrix. A new approach to simulate the effect of partial reflectivity of the walls of the waveguide model is proposed. This approach is based on approximating the fields inside the space of the actual waveguide section by equivalent waveguide sections of larger dimensions with PEC (Perfect Electric Conductor) walls. A simple scenario is considered in order to check the accuracy of this model. This scenario is verified by comparing experimental and numerical simulation results. The obtained results show that the proposed model is suitable for predicting accurate electric field strength due to an electromagnetic source in an indoor environment with partially reflecting boundaries.

Index Terms ─ Dyadic Green's function, indoor propagation, mode matching method, partially reflecting walls, waveguide model.

I. INTRODUCTION

Modeling indoor wave propagation for wireless communication is challenging problem because of the large dimensions compared with the operating wavelength and complex geometry of buildings [1-3]. However, understanding how electromagnetic waves propagate in indoor environments becomes increasingly important as wireless devices become more involved in lifestyle. Laptops, smart phones, tablet computers and others are overwhelming the market now more than ever and wireless networks have to work in all environments to satisfy the increasing demand. Predicting wave propagation in indoor environment is especially complicated problem due to the operating wavelength is usually much smaller than the size of different objects in the normal building in addition to the complicated shapes and structures inside indoor environment. Variations of room size, building materials and furniture placements as well as moving persons affect wave propagation in indoor environment in different ways. To predict how indoor environment affects the wave propagation, different models have been developed. These models are divided into empirical and theoretical models.

Empirical models represent traditional approaches for estimating signal power received from a source employing a stochastic approximation that combines all the surrounding environmental effects in a given location into a simple attenuation-distance relation [4]. Path-loss model requires very little computational resources as it does not incorporate any rigorous calculations of Maxwell's equations or wave equation. In this method loss parameters are extrapolated through the averaging of many physical measurement samples over a large area in an attempt to model an overall trend that estimates the decay of signal strength away from the transmitter. However, the time and resources saved by applying the simple decay equations are often offset by the effort required to gather enough on-site measurements for a more accurate estimation. Also, this method cannot accurately predict the power levels at every point in the environment considered. Different empirical models have been used for predicting the path loss along corridors in office environments [5-6]. On the other

Submitted On: October 4, 2015
Accepted On: February 20, 2016

hand, deterministic models are based on solving Maxwell's equations, which can be done in different ways by making certain assumptions about the wave propagation and the geometry of the environment. Ray tracing [7-8] and waveguide model [9-13] are the most common theoretical models used to predict indoor propagation. Ray-tracing is based on the fact that at high frequencies the electromagnetic waves may be thought of as behaving like rays that travel in straight lines provided that the permittivity of the medium is homogeneous [14]. Geometrical optics (GO) [15] approximates the field strength at any point as the sum of the field associated with the direct ray from the transmitter to the receiver, plus the reflected and refracted rays from the surrounding walls. Reflection and refraction due to penetrable walls can be modeled generally by multiple rays. However, for simplicity single ray approximation is usually used. Discontinuities at the edges of the walls, doors and windows introduce additional diffracted rays. Geometrical Theory of Diffraction (GTD) and its uniform extension, Uniform GTD (UTD) are used to model diffracted rays from the edges [16]. The practical limitation of applying GTD to indoor propagation is that each diffraction point on an edge behaves as a secondary source giving rise to a new family of rays. Accounting for many such secondary sources becomes very time consuming and in many cases impractical.

It has been shown in simulations [13] and measurements [9-12] that corridors have a waveguiding effect. Basic theory of waveguide is already used to model corridors and tunnels. The advantage offered by the waveguide modeling approach over existing methods is that an overall picture of power levels in a large area can be obtained with very small computational and database requirements. The model requires very little detailed information about the environment, and provides accurate predictions of the major phenomena.

So far 2D analytical models treat corridors as perfect electric conducting boundaries [9]. Recently, dielectric waveguides with uniform cross-section have been developed to improve this 2-D waveguide model [11]. In the case of dielectric waveguide model the walls are modeled as infinitely thick [10]. This model is modified to be more realistic by using finite dielectric layer thickness to represent the surrounding walls [11].

In hybrid models theoretical models are combined with numerical models as FDTD (Finite Difference Time Domain) [11], [17]. For example, one can utilize ray tracing or waveguide model in simpler regions where these models are valid and can be applied efficiently. A more versatile and detailed numerical model is then used to solve for the field distribution in regions where the previously mentioned models cannot be used for accurate results. This saves computational time as the detailed numerical model are only required to be implemented in certain small regions.

As it is mentioned, previous work based on waveguide model was only based on 2D analysis for the corridors segments [9-12]. The proposed model in the present paper is based on 3D waveguide model. This 3D waveguide model is suggested to be combined with mode matching method and generalized scattering matrix method to include the discontinuities inside the indoor environment. The antenna of the wireless system is presented as a small point source to excite the waveguide sections which represent the indoor environment. The guided waves in the corridors are presented in terms of the corresponding modes of a rectangular perfect electric conducting waveguide of the same dimensions of the corridors. Large number of modes are propagating in the corridor due to the short wavelength used in wireless communication and the large cross-section of the corridor. At intersections of waveguides with different cross sections, each mode is backscattered and transmitted in a different way. To determine the backscattered and transmitted fields for a large number of propagating modes, an effective mode matching method [20] is developed for dealing with three dimensional (3D) waveguide structures [21]. Mode matching method is used for analyzing transitions between waveguides with different cross section. Electromagnetic fields are then expanded in waveguide modes in each region. At the waveguide intersection the electromagnetic boundary conditions are applied to the field expansions for the different regions, then a generalized scattering matrix is determined. This scattering matrix relates the coefficients of incident, backscattered and transmitted modes.

In order to consider the effect of partial reflectivity of the walls a new approach is introduced as an extension of a paper by the authors [22]. The proposed method is based on using PEC waveguide model but the PEC waveguide sections in this case have larger dimensions such that the fields inside the equivalent waveguide would be nearly the same as the corresponding ones inside area of the original partially reflecting waveguide sections.

Full wave numerical analysis of the same problem based on HFSS (High Frequency Structural Simulator) simulation [19] is used to verify the obtained results based on modal analysis. Experimental results are also conducted with a simple dipole antenna in a specific office corridor. The measurements are presented at Wi-Fi frequency band 2.40-2.48 GHz.

II. MODAL ANALYSIS OF INDOOR PROPAGATION BASED ON PEC BOUNDARY CONDITIONS

Simple indoor environment can be represented as a combination of multi-mode rectangular waveguide sections as shown in Fig. 1. The excitation source is

assumed to be an infinitesimal dipole located at one of these waveguide sections. The electric field at any point inside the waveguide containing the excitation source can be formulated as dyadic Green's function inside the waveguide section. The reflected and transmitted fields from one section to the directly connected sections can be obtained by using mode matching method. The interactions between all these waveguide sections are represented in the form of generalized scattering matrices. The following analysis is based on assuming that the boundaries of the waveguide section are PEC. Then the problem of 3-D waveguide model with partially reflecting walls is discussed.

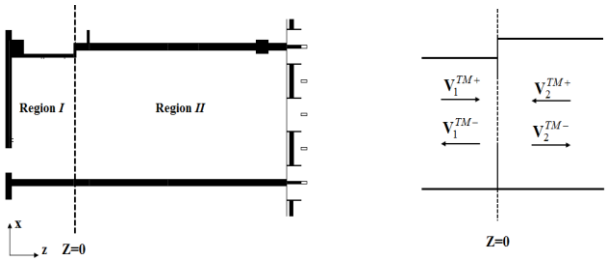

(a) (b)

Fig. 1. (a) Schematic drawing of an example for an indoor environment. (b) Equivalent waveguide representation for an intersection between two corridors.

Following the same analysis in [18], electromagnetic fields inside rectangular waveguide section due to an infinitesimal point source can be represented in terms of a complete set of orthonormal eigenfunctions as follows:

$$\mathbf{E}_t(x,y,z)=\sum_m\sum_n V_{mn}^{TM}(z)\mathbf{e}_{mn}^{TM}(x,y)+\sum_m\sum_n V_{mn}^{TE}(z)\mathbf{e}_{mn}^{TE}(x,y), \quad (1\text{-a})$$

$$\mathbf{H}_t(x,y,z)=\sum_m\sum_n I_{mn}^{TM}(z)\mathbf{h}_{mn}^{TM}(x,y)+\sum_m\sum_n I_{mn}^{TE}(z)\mathbf{h}_{mn}^{TE}(x,y), \quad (1\text{-b})$$

$$j\omega\varepsilon E_z(x,y,z)=-J_z(x,y,z)+\sum_m\sum_n V_{mn}^{TM}(z)\nabla\cdot\mathbf{e}_{mn}^{TM}(x,y), \quad (1\text{-c})$$

$$j\omega\mu H_z(x,y,z)=\sum_m\sum_n V_{mn}^{TE}(z)\nabla\cdot\mathbf{h}_{mn}^{TE}(x,y), \quad (1\text{-d})$$

where $\mathbf{e}_{mn}^{TE/TM}$ and $\mathbf{h}_{mn}^{TE/TM}$ correspond to the mn^{th} electric and magnetic eigen TE/TM (Transverse Electric/ Transverse Magnetic) modes. Details of these eigen modes are discussed in [18]. For the case of an excited waveguide section, the amplitudes of these modes V^{TM}, V^{TE}, I^{TM}, I^{TE} are functions of the amplitudes and locations excitation sources inside the waveguide section, More details about the analysis method including mode matching technique and generalized scattering matrix are presented in [22].

A. Approximation of partially reflecting walls in modal analysis

A new approach is proposed in order to simulate the effect of partial reflectivity of the walls forming indoor environment by using the PEC waveguide model. The basic idea of the proposed method is that the field distribution inside a waveguide section with partially reflecting boundaries can be approximated by the field distribution of a PEC waveguide of the same cross section configuration and larger size as shown in Fig. 2. Figure 3 shows schematically how the field distribution of larger PEC waveguide can be used as an approximation for the field distribution inside a smaller waveguide section with partially reflecting boundaries. It should be noted that, this approximation is valid only inside the cross section area of the partially reflecting waveguide section.

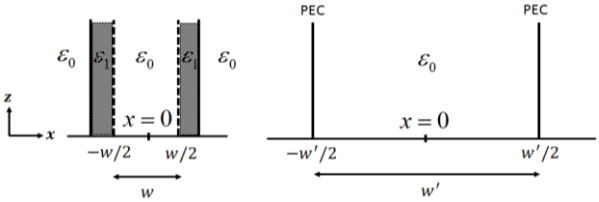

(a) (b)

Fig. 2. Geometry of the problem of 2D waveguide section: (a) actual waveguide section with partially reflecting boundaries, and (b) equivalent waveguide section with PEC boundaries.

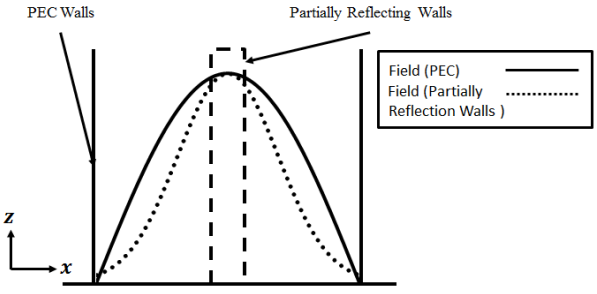

Fig. 3. Sample electric field distribution for PEC walls and partially reflecting walls.

To verify this technique numerically, a simple example based on single mode is studied. The transverse electric field mode TM_1 for a parallel plate with PEC boundaries as shown in Fig. 2 (b) is given by:

$$\mathbf{E}_t(x)=\cos\frac{\pi x}{w'},|x|\le w'/2\,. \quad (2)$$

On the other hand, the corresponding transverse electric field mode for partially reflecting boundary as shown in Fig. 2 (a) is given by [23]:

$$\mathbf{E}_t(x)=\begin{cases}cos(k_{x1}x), & |x|\le w/2\\ e^{k_{x2}(w-|x|)}, & |x|\ge w/2\end{cases}, \quad (3)$$

where k_{x1} is given by:

$$k_{x1} = \frac{\pi}{w}[1 + 2j\,\bar{Z}_s/k_0 w], \quad (4)$$

and $\bar{Z}_s = 1/\sqrt{\varepsilon_r - 1 - i\sigma/\omega\varepsilon_0}$ is the wall impedance normalized to the free space wave impedance η_0 with wall's permittivity ε_r and conductivity σ [23].

Equation (3) represents the actual field distribution inside and outside the partially reflecting waveguide structure. The field inside this waveguide in the region $|x| < w/2$ can be approximated by using (2) with larger value of w'. In this case the optimum value of w' can be obtained by minimizing the error function given by:

$$\varepsilon(w') = \int_{-w/2}^{w/2} \left|\cos k_{x1}x - \cos\frac{\pi x}{w'}\right|^2 dx. \quad (5)$$

Figure 4 shows an example for this approximation technique where $\bar{Z}_s = 0.4 + j0.25$, $w = 0.5\,m$ and the operating frequency is $f = 0.9$ GHz. In this case, it is found that the optimum value of the equivalent waveguide section is $w' = 1.2\,w$ for dominate mode as shown in Fig. 4.

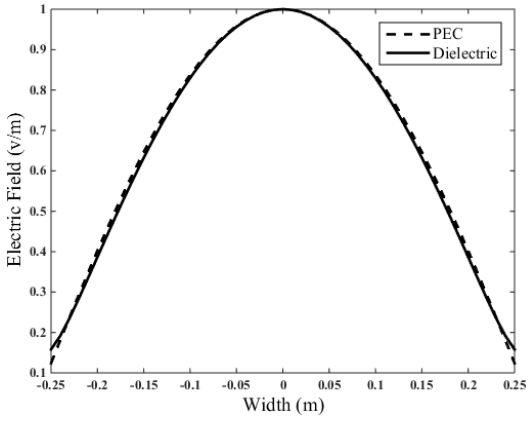

Fig. 4. Actual and approximate field distributions inside a parallel plate waveguide with partially reflecting boundaries.

This technique can be generalized to simulate wave propagation inside indoor environment with partial reflecting boundaries as shown in Fig. 5. In this case, Fig. 5 (a) shows the cross section of the original corridor with partially reflecting walls and Fig. 5 (b) shows the equivalent PEC model which introduces nearly the same field distribution inside the area of the original corridor.

Full wave numerical analysis based on finite element analysis by using HFSS simulator is used to verify this technique for 2-D waveguide section. Figure 6 (a) shows the normalized electric field distribution for a waveguide section with partially reflecting walls. In this case wave port excitation of dominant mode only is used as the excitation. The dielectric constant of the wall of this waveguide is $\varepsilon_r = 3$ and the conductivity is $\sigma = 0.01\,s/m$. The inner dimensions of this waveguide are $w = 1m$ and $h = 0.5m$. The thickness of the walls of this waveguide is 0.1 m and the operating frequency is 0.9 GHz. On the other hand, Fig. 6 (b) shows the corresponding normalized electric field distribution for the equivalent PEC rectangular waveguide section. In this case the optimum equivalent waveguide with PEC boundaries is found to be $w' = 1.23$ m. It should be noted that the width of the waveguide h in this case does not change because the field distribution is independent on this direction in this case.

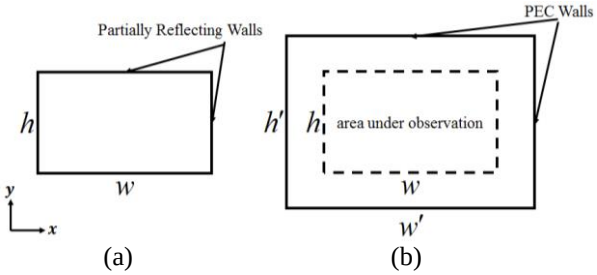

Fig. 5. Equivalent waveguide representation for partially reflecting walls: (a) corridor section with partially reflecting walls, and (b) equivalent PEC representation.

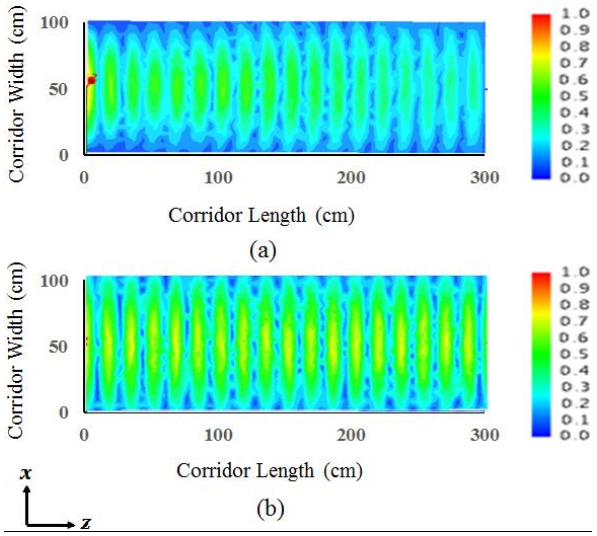

Fig. 6. Magnitude of normalized electric field, x-z plan, for corridor segment at frequency band 0.90 GHz: (a) HFSS model for partially reflecting walls, and (b) PEC model.

III. SIMULATION RESULTS

In this section sample results are presented to verify the accuracy of the proposed model by comparing the obtained results with both simulations and experimental results. Numerical simulations of indoor structures are obtained by using ray tracing technique based on FEKO software [24]. Different configurations of the excitation sources are presented to show the effect of the polarization on the indoor wave propagation.

A. Vertically polarized dipole

The first example here is based on a vertical dipole parallel to the y axis as shown in Fig. 7. The field is calculated at a plane parallel to the ground. Figure 8 (a) shows the electric field distribution for a waveguide section with partially reflecting walls. The operating frequency is assumed to be 0.90 GHz corresponding to lower GSM band. The length, width and height of the corridor are assumed to be 15 m, 3 m and 3 m respectively. The permittivity of the walls is 3 and conductivity is σ = 0.01 s/m [11]. The thickness of the wall is 10 cm. The dipole is located at the point (1.5 m, 1.5 m, 0.5 m). Figure 8 (a) shows the magnitude of the normalized electric field in the plane parallel to the ground at a height 2.25m. On the other hand, Fig. 8 (b) shows the corresponding normalized electric field distribution for the equivalent PEC rectangular waveguide section. In this case the optimum equivalent waveguide with PEC boundaries is found to be w'=1.02 w and h'=1.33 h. It should be noted that the bottom and upper walls have more effect on the field distribution in this case than the side walls. This explains the small ratio of w' compared with the corresponding ratio h'.

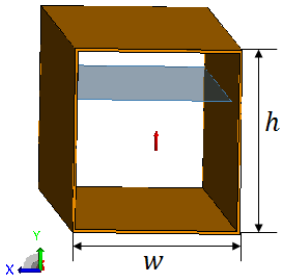

Fig. 7. Vertical polarization simulation model.

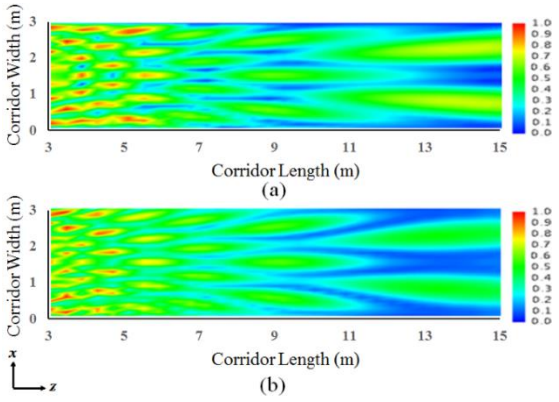

Fig. 8. Magnitude of normalized electric field, x-z plan y = 2.25 m for a corridor segment at frequency 900 MHz: (a) FEKO model for partially reflecting walls, and (b) equivalent PEC model.

This analysis is repeated for other two frequencies in the wireless communication band from 0.9 GHz to 2.5 GHz to cover most common applications for indoor propagations like WiFi and the upper GSM band. Figures 9 shows the same problem at frequencies 1.5 GHz, where Fig. 9 (a) shows the normalized electric field distribution for a waveguide section with partially reflecting walls in the plane parallel to the ground at a height 2.25 m. On the other hand, Fig. 9 (b) shows the corresponding normalized electric field distribution for the equivalent PEC rectangular waveguide section. In this case the optimum equivalent waveguide with PEC boundaries is found to be $w' = 1.02\ w$ and $h' = 1.15\ h$.

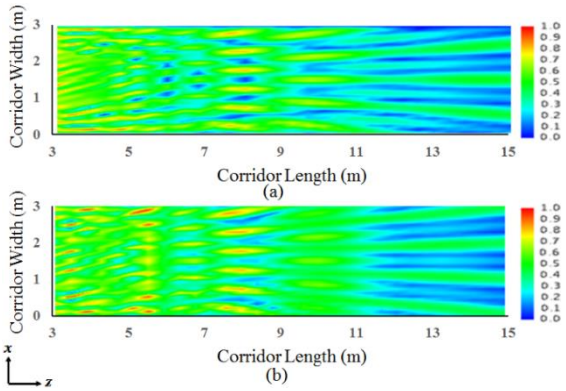

Fig. 9. Magnitude of normalized electric field, x-z plan, for corridor segment at frequency band 1.5 GHz: (a) FEKO model for partially reflecting walls, and (b) equivalent PEC model.

Figures 10 shows the same problem at frequencies 2.5 GHz where in this case the optimum equivalent waveguide with PEC boundaries is found to be $w' = 1.02\ w$ and $h' = 1.05h$. It should be noted that the bottom and upper walls have more effect on the field distribution in this case than the side walls. This explains the small ratio of w' compared with the corresponding ratio h'.

The error is calculated using Mathematica 10.3 by comparing the percentage difference between figures of the simulation and model results and it is found that the error is ranging from 13.3% to 14.9% for the proposed results. It can be noted the good accuracy of the modal analysis of equivalent PEC waveguide section compared with the FEKO simulation results of the partially reflecting wall waveguides. The relation between the dimensions of the equivalent PEC waveguide and the corresponding dimensions of original partially reflecting wall waveguide as functions of frequency is shown in Fig. 11. It is shown that the ratio of h'/h decreases by increasing the operating frequency to be nearly unity at the higher frequency limit. This can be explained due to the localization of the propagated waves inside the section of the waveguide at higher frequencies. Thus, the effect of the boundary walls would be decreased in this case. On the other hand, the ratio of w'/w is nearly unity

in all cases for vertically polarized dipole. Thus this result is omitted here.

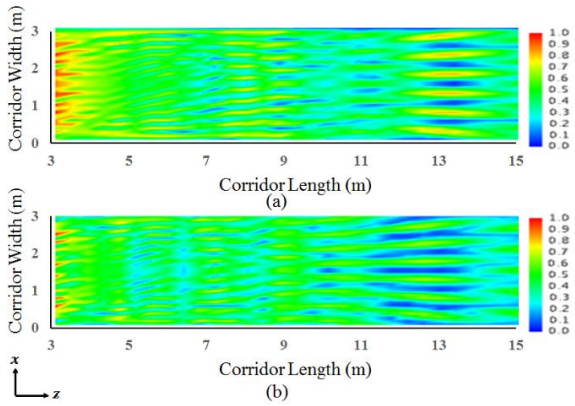

Fig. 10 Magnitude of normalized electric field, x-z plan, for corridor segment at frequency band 2.5 GHz: (a) FEKO model for partially reflecting walls, and (b) equivalent PEC model.

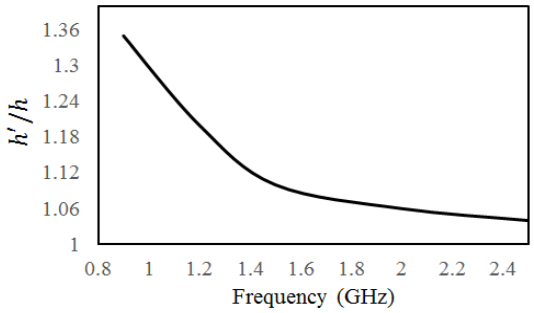

Fig. 11. Relation between corridor segment with partially reflecting walls and the corresponding PEC model.

B. Horizontally polarized excitation

The second example here is based on a horizontal dipole parallel to the *x*. The field is calculated at a plane parallel to the ground. Figure 12 (a) shows the normalized electric field distribution for a waveguide section with partially reflecting walls. The operating frequency is assumed to be 0.90 GHz corresponding to lower GSM band. The length, width and height of the corridor are assumed to be 15 m, 5 m and 5 m respectively. The permittivity of the walls is 3 and conductivity is $\sigma = 0.01\ s/m$ [11]. The thickness of the wall 10 cm. The dipole is located at the point (1.5 m, 1.5 m, 0.5 m). Figure 12 (a) shows the magnitude of the total electric field in the plane parallel to the ground at a height 2.25 m. On the other hand, Fig. 12 (b) shows the corresponding normalized electric field distribution for the equivalent PEC rectangular waveguide section. In this case the optimum equivalent waveguide with PEC boundaries is found to be $h' = 1.03\,h$ and $w' = 1.35\,w$. The calculated error between the model and simulation figures is about 15.6%. It should be noted that the bottom and upper walls have more effect on the field distribution in this case than the side walls. This explains the small ratio of h' compared with the corresponding ratio w'. This analysis is repeated for other two frequencies in the wireless communication band from 0.9 GHz to 2.5 GHz to cover most common applications for indoor propagations like WiFi and GSM bands.

It can be noted the good accuracy of the modal analysis of equivalent PEC waveguide section compared with the FEKO simulation results of the partially reflecting wall waveguides. The relation between the dimensions of the equivalent PEC waveguide and the corresponding dimensions of original partially reflecting wall waveguide as functions of frequency is shown in Fig. 13. It is shown that the ratio of w'/w decreases by increasing the operating frequency to be nearly unity at the higher frequency limit. This can be explained due to the localization of the propagated waves inside the section of the waveguide at higher frequencies. Thus, the effect of the boundary walls would be decreased in this case. On the other hand, the ratio of h'/h is nearly unity in all cases for vertically polarized dipole. Thus this result is omitted here.

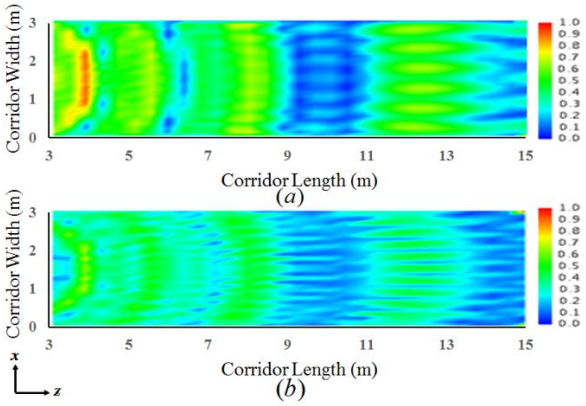

Fig. 12. Magnitude of normalized electric field, x-z plan, for corridor segment at frequency band 0.90 GHz: (a) FEKO model for partially reflecting walls, and (b) PEC model.

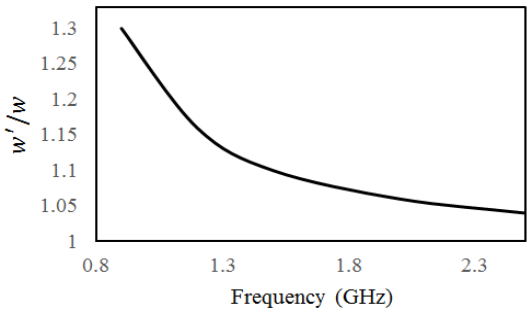

Fig. 13. Relation between corridor segment with partially reflecting walls and the corresponding PEC model.

C. Cascaded sections simulation

Real indoor environment, as shown in Fig. 14, can be presented as cascaded regions with different geometrical properties. In this case generalized scattering matrices are calculated independently for the intersection between each two connected regions. Then these generalized scattering matrices would be cascaded with appropriate phase delay matrix to compute the overall generalized scattering matrix for the entire indoor environment [20]. The above analysis is extended to simulate the intersection of two corridor segments with different widths by using mode matching. The width of the first segment is assumed to be 3 m while the width of the second segment is assumed to be 5 m. The height of both segments is assumed to be 3 m. The lengths of the two segments are 10 m and 10 m respectively. The operating frequency is assumed to be 900 MHz. The transmitting antenna is assumed to be vertically polarized and located at the mid of the first segment at a height 1.5 m. Figure 15 (a) shows the calculated electric field distribution at the plane parallel to the ground plane at a height of 2.25 m from the floor. Figure 15 (b) shows the corresponding PEC model with $h' = 1.3h$ for both sections. It can be noted the good accuracy of the modal analysis compared with the FEKO simulation results.

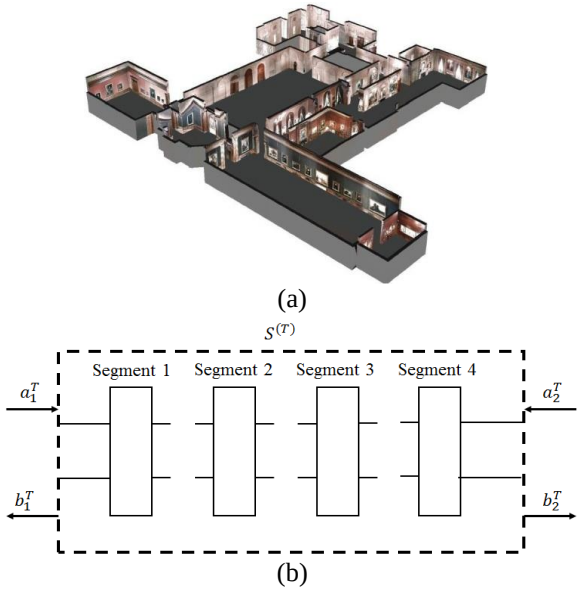

Fig. 14. (a) Schematic drawing of a real indoor environment, and (b) equivalent cascaded generalized scattering matrix for complicated multi-section indoor environment.

The model is implemented in Matlab which runs on a laptop with an Intel 2.4 GHz processor, 4 GB of RAM and Windows 7 64-bit, the total program runtime for the above example is only 9 minutes. The calculation of S-matrices is done for each corridor segment and every frequency sample while the cascade coupling is done once for every frequency. The mesh generation for the electric field is done for every corridor segment and frequency sample. The latter includes summing up the electric field for every mode at every x- and z-position in the corridor segment. The E-field mesh generation is the bottleneck in the numerical calculations and the largest influence on program speed is the mesh resolution and the number of modes included. On the other hand, the same example is simulated using FEKO version 7.0 with the same computer resources. It is found that the simulation takes about 41 minutes using FEKO Physical Optics (PO) solver. IT can be noted that the proposed model is faster than the simulation package and the differences will be increased by increasing the dimensions or operating frequency.

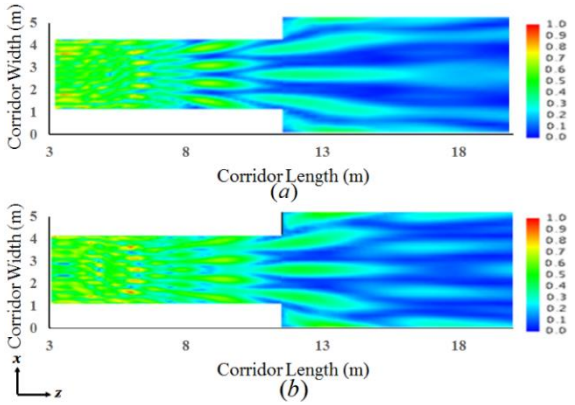

Fig. 15. Magnitude of normalized electric field, x-z plan, for two corridor segments at frequency band 0.90 GHz: (a) FEKO model for partially reflecting walls, and (b) PEC model.

IV. MEASUREMENTS

In this section sample results are presented to verify the accuracy of the present model by comparing the obtained results with experimental results. The proposed model is used to simulate simple cascaded sections of indoor propagation with partially reflecting walls and the equivalent PEC model.

This simple scenario of a straight corridor section is verified experimentally at Wi-Fi frequency 2.4 GHz for two different locations with different corridors dimensions in to verify the presented model in different buildings structures. The first scenario has been done in corridor of commercial building with brick walls. The experimental setup consists of two wooden carts. One cart is used to hold the transmitting antenna and the transmitter and the other one is used to hold the receiving antenna, the receiver and data collecting computer as shown in Fig. 16. Cisco Aironet 1242 access point with dipole antenna with gain of 2.2 dBi is used as transmitter. The transmitting and receiving antennas are kept

vertically polarized. Most of the measurements were taken with the transmitter is located at a fixed location and the receiver is moved along the corridor. Figure 16 shows the locations of the transmitter and the receiver for the relevant measurements. The transmitter was fixed at certain position and the receive antenna was moved along a straight line away from the transmitter in steps of 30 cm. The length of the corridor is about 15 m. The height of both transmitting and receiving antennas is kept 60 cm above the ground. Figure 17 shows a comparison between the measures received power in dBm and calculated power by using modal analysis for partially reflecting walls. In this case, the optimum equivalent waveguide with PEC boundaries is found to be equivalent PEC width is 1.02 of the walls width while the equivalent PEC height is about 1.06 of the walls height. Good agreement between the measured and calculated power is obtained. The slight differences can be explained due to errors in the manual positioning of the receiving antenna and differences due to the boundary conditions of the actual corridor. The calculated error between the model and measured results is about 7.3%.

(a) (b)

Fig. 16. Measurement setup: (a) transmitter and (b) receiver.

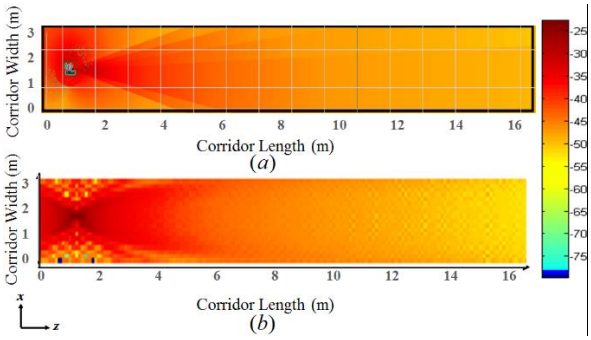

Fig. 17. Received power distribution (dBm) across the corridor. (a) Measured signal strength and (b) calculated signal strength.

On the other hand, the same setup is used to test the model for corridor segment with another commercial building of gypsum walls as show in Fig. 18 (a). The area under test is highlighted in Fig. 18 (b) in the structure layout.

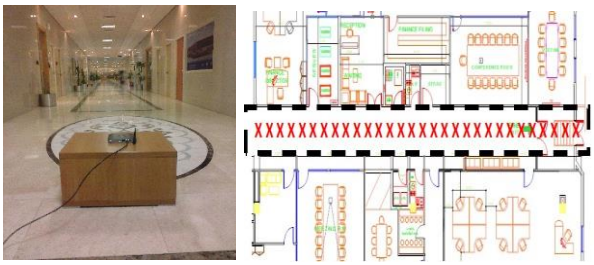

(a) (b)

Fig. 18. Corridor section of indoor commercial building: (a) transmitter and (b) structure layout.

Figure 19 shows a comparison between the measured received power in dBm and calculated power by using modal analysis for partially reflecting walls, the difference error between the two results is about 7.8%. It can be noted that the total field distribution is not confined within the hallway boundaries, resulting in significant illumination of the adjacent rooms. It should also be noted that there is considerable interference penetrating through the walls. This through-wall interference is distributed along the entire length of the side hallway.

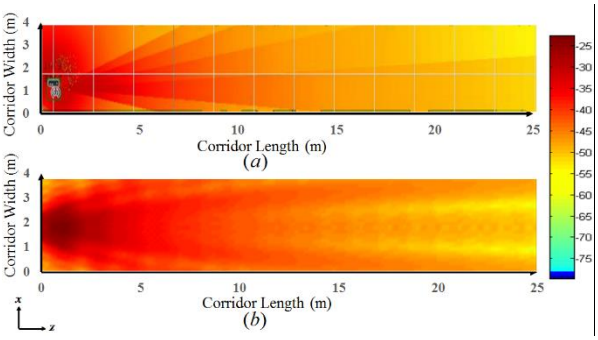

Fig. 19. Received power distribution (dBm) across the corridor. (a) Measured signal strength and (b) calculated signal strength.

V. CONCLUSION

In this paper, a new approach is proposed to simulate electromagnetic wave propagation in indoor environment with taking into consideration the effect of partial reflectivity of the walls forming indoor environment by using equivalent PEC waveguide model. The basic idea of the proposed method is that the field distribution inside a waveguide section with partially reflecting boundaries can be approximated by a field distribution of a PEC waveguide of the same cross section shape with expanded lateral dimensions. Vertical

and horizontal polarizations are studied and it found that the bottom and upper walls have more effect on the field distribution in the case of vertically polarized excitation than the side walls while the reverse is true for the horizontally polarized excitation. The results of the presented model are verified by comparison with numerical results and experimental results. Good agreements are obtained from these comparisons. The present model represents a good tool for planning appropriate wireless links in indoor environment.

REFERENCES

[1] J. Michael, M. Leung, and J. Cater, "Inter-building propagation modelling for indoor wireless communications system deployment," *Conference on Antennas and Propagation (EuCAP)*, pp. 791-793, Apr. 2014.

[2] M. Rana, M. Shohan, M. Hossen, M. Islam, S. Ullah, K. Hoque, and M. Rahman, "Indoor propagation modelling for UWB communications," *Conference on Informatics, Electronics & Vision (ICIEV)*, pp. 1-5, May 2014.

[3] W. Yunchun, H. Xingzhe, S. Hongliang, K. Zheng, W. Qiandong, Y. Jun, and C. Xiaoming, "Measurement and analysis of environment impact on indoor wireless channel characteristics," *Conference on Wireless, Mobile and Multimedia Networks (ICWMMN 2013), 5th IET International*, pp. 24-28, Nov. 2013.

[4] J. Andersen, T. Rappaport, and S. Yoshida, "Propagation measurements and models for wireless communications channels," *IEEE Communications Mag*., vol. 33, no. 1, pp. 42-49, Jan. 1995.

[5] J. Medbo and J. E. Berg, "Simple and accurate path loss modeling at 5 GHz in complex indoor environments with Corridors," *Proc. of COST Conference 273*, Espoo, Finland, pp. 30-36, May 2002.

[6] A. M. Najafi, "Indoor propagation path loss measurements and empirical models for 2.4 GHz," M.Sc. Dissertation, Royal Institute of Technology and Ericsson Research, Stockholm Sweden, Nov. 2011.

[7] S. Sidhu, A. Khosla, and A. Sharma," Implementation of 3-D ray tracing propagation model for indoor wireless communication," *International Journal of Electronics Engineering*, vol. 4, pp. 43-47, Apr. 2012.

[8] J. Zhong, L. Bin-Hong, W. Hao-Xing, C. Hsing-Yi, and K. Sarkar, "Efficient ray-tracing methods for propagation prediction for indoor wireless communications," *IEEE Antenna and Propagations Mag*., vol. 43, no. 2, pp. 41-49, Apr. 2003.

[9] P. Kyritsi, "Multiple element antenna systems in an indoor environment, Ph.D. Dissertation, Stanford University, 2001.

[10] D. Porrat and D. Cox, "UHF propagation in indoor hallways," *IEEE Transactions on Wireless Communications*, pp. 1188-1198, July 2002.

[11] J. Leung, "Hybrid waveguide theory-based modeling of indoor wireless propagation," Thesis for the degree of Master of Applied Science, Graduate Department of Electrical and Computer Engineering, University of Toronto, 2009.

[12] D. Soderman, "A 2D indoor propagation model based on waveguiding, mode matching and cascade coupling, M.Sc. Dissertation, KTH and Ericsson Research in Kista, 2012.

[13] A. Alighanbari and C. Sarris, "Rigorous and efficient time-domain modeling of electromagnetic wave propagation and fading statistics in indoor wireless channels," *IEEE Transactions on Antennas and Propagation*, vol. 55, pp. 2373-2381, Aug. 2007.

[14] W. Tam and V. Tran, "Propagation modeling for indoor wireless communication," *Electronics & Communication Engineering Journal*, pp. 221-228, Oct. 1995.

[15] K. Morris, *Electromagnetic Theory and Geometrical Optics*, Courant Institute of Mathematical Sciences, New York University, 1962.

[16] C. A. Balanis, *Advanced Engineering Electromagnetics*, 2nd ed., Wiley, 2012.

[17] M. Thiel and K. Sarabandi, "3D-wave propagation analysis of indoor wireless channels utilizing hybrid methods," *IEEE Transactions on Antennas and Propagation*, vol. 57, no. 5, pp. 1539-1546, May 2009.

[18] L. Felsen, M. Mongiardo, and P. Russer, *Electromagnetic Field Computation by Network Methods*, Berlin, Germany: Springer-Verlag, 2009.

[19] Ansoft High Frequency Structure Simulation (HFSS), ver. 15, Ansoft Corporation, Pittsburgh, PA, 2013.

[20] A. Ruiz-Cruz, R. Montejo-Garai, and M. Rebollar, "Computer aided design of waveguide devices by mode-matching methods," *Passive Microwave Components and Antennas*, Vitaliy Zhurbenko (Ed.), InTech, 2010.

[21] G. Conciauro, M. Gugliemi, and R. Sorrentino, *Advanced Modal Analysis*, CAD Techniques for Waveguide Components and Techniques, John Wiley & Sons, Ltd., Chichester, 1999.

[22] H. El-Maghrabi, A. Attiya, and E. Hashish, "Indoor wave propagation prediction by using 3D waveguide model," 32nd *National Radio Science Conference (NRSC), 2015*, pp. 91-99, Mar. 2015.

[23] S. F. Mahmoud, *Wireless Transmission in Tunnels, Mobile and Wireless Communications Physical Layer Development and Implementation*, 2010, Salma Ait Fares and Fumiyuki Adachi (Ed.), ISBN: 978-953-307-043-8, InTech.

[24] FEKO Suite 7.0, Altair Engineering, 2014.

Hany M. El-Maghrabi received the B.S. degree, with Honor Degree, and M.S. degree in Electrical Engineering from the Cairo University (Egypt). El-Maghrabi has received a position of Research Assistant in Housing and Building National Research Center (HBNRC), Institute of Electromechanical, Department of Communication (Egypt) at 2005. He became Assistant Researcher at HBNRC at 2011. He has co-authored technical journal article and conference papers. El-Maghrabi has experience in electromagnetics, antennas, microstrip structures, numerical methods, wave propgation and their applications in microwave. El-Maghrabi awarded the best paper in NRSC 2015.

Ahmed M. Attiya M.Sc. and Ph.D. Electronics and Electrical Communications, Faculty of Engineering, Cairo University at 1996 and 2001 respectively. He joined Electronics Research Institute as a Researcher Assistant in 1991. In the period from 2002 to 2004 he was a Postdoc in Bradley Department of Electrical and Computer Engineering at Virginia Tech. In the period from 2004 to 2005 he was a Visiting Scholar in Electrical Engineering Dept. in University of Mississippi. In the period from 2008 to 2012 he was a Visiting Teaching Member in King Saud University. He is currently Full Professor and the Head of Microwave Engineering Dept. in Electronics Research Institute. He is also the Director of Nanotechnology Lab. in Electronics Research Institute. His research interests include Electromagnetic waves, antennas and wave propagations, microwave passive circuits and systems, microstrip and planar circuits and antennas, antenna measurement techniques, microwave measurement techniques, UWB and short pulse signals, numerical techniques in electromagnetics, analytical techniques in electromagnetics, periodic structures, artificial electromagnetic materials, nanotechnology, carbon nanotubes, graphene, plasmonics and non-linear optics. Attiya published more than 60 journal and conference papers and two book chapters. Attiya is Editor-in-Chief of "Open Journal of Antennas and Propagation". In 2008, Attiya was awarded the Encouragement Award in Engineering Science from Egyptian Scientific and Research Academy. Activities and positions held and similar information for other professional societies.

Essam A.Hashish (M'96) received the B.Sc., M.Sc., and Ph.D. degrees from the Electronics and Communications Department, Faculty of Engineering, Cairo University, Giza, Egypt, in 1973, 1977, and 1985, respectively. He is currently a Professor with the Electromagnetics Group at the same department. His main interest is electromagnetic remote sensing, wave propagation, and microwave antennas.

Analysis and Simulation of Energy Leakage for the Surface-Wave Waveguide Based on Tunable Impedance Cells

YongHong Zhou [1,2], Xing Chen [1], and ZhangJie Luo [3]

[1] College of Electronics and Information Engineering
Sichuan University, Chengdu, 610064, China
scnczyh@163.com, xingcsc@yahoo.com.cn

[2] College of Electronics and Information Engineering
China West Normal University, Nanchong, 637002, China
scnczyh@163.com

[3] Institute of Electronic Engineering
China Academy of Engineering Physics, Mianyang, 621900, China
zhangjie_luo_cn@126.com

Abstract ─ Controlling energy leakage is of great importance for users of surface-wave waveguides (SWGs) because it determines the propagating efficiency of surface waves. In this paper, a novel theoretical analysis of the energy leakage for these two types of SWGs is proposed, and the effects of some key parameters to the leakage such as the path width of the SWG and effective impedance of cell and incident angle are discussed more deeply. To verify the theoretical method, a model of the SWG consisting of 30 × 30 impedance-tunable cells driven by TM surface waves, whose impedance ranges from j370 Ω to j780 Ω according to our previous measurements, is simulated in HFSS. The simulation results are in good agreement with the theoretical ones, demonstrating that the leakage is inversely proportional to the width of the SWG and an increase of effective impedance of the guided path; furthermore, by using the impedance-tunable cells, the multi-functionality of the SWG is illustrated. The analyzing methods can be a guide for designing other SWGs without energy leakage, and as an inspiration for more complex SWG applications.

Index Terms ─ Broken-line SWG, energy leakage, metamaterials, Straight SWG, Surface-Wave Waveguide (SWG), tunable impedance cell.

I. INTRODUCTION

A surface wave is a type of electromagnetic wave that exists on the interface between metal and free space [1]. While propagating along the interface, they are restrained on the surface with their electric fields decaying exponentially along normal direction of the interface. According to the polarization of their electromagnetic fields, surface waves can be classified as transverse-magnetic (TM) or transverse-electric (TE), respectively.

Smooth metal surfaces support surface waves over a broad range of frequencies, spanning from DC up to visible light [1]. By applying a periodic texture, one can eliminate some surface waves over a finite frequency band. By purposely designing metal-dielectric periodic textures, one can change the effective impedance of the surface structure, and thus control the properties of the surface waves [2]. These surface structures with periodic textures are usually called impedance surfaces, and the unit-cell of the impedance surface is called an impedance cell, all of them are also called metamaterials.

Surface-wave waveguide (SWG) is a two-dimensional (2D) structure that guides the surface wave (SW) to propagate along a confined path [3]. Many articles have reported various SWGs. For instance, SWGs were designed based on pure metallic structures [4-5], plasmon structures [6], negative refraction or anisotropic chiral metamaterials [8-10], and impedance surfaces [3, 11-14]. The SWG based on impedance surfaces has become more and more popular because of its portability, economy and ease of processing.

The SWG can be used for various applications. For example, it can be utilized to transmit microwave energy [4-6], feed leaky-wave holographic antennas [7], and guide SW along a preferred path where they will not produce unwanted effects, such as scattering off objects into the surrounding space [3].

The remainder of this paper is organized as follows. The present research status of the SWG based on

Submitted On: January 20, 2016
Accepted On: March 10, 2016

impedance cells is given in Section II. Section III first briefly describes the unit-cell with tunable impedance properties, because it is the basis of the SWG that we proposed and several key data points must be obtained from it, and then it discusses in detailed theoretical models and analyzes ways of evaluating and suppressing energy leakage for the straight and broken-line SWG models. Numerical simulations and a discussion of the results have been done to verify our theory in Section IV. Finally, conclusions are drawn in Section V.

II. THE STATE OF ART

Gregoire and Kabakian reported that many SWGs, based on various-textured impedance cells in 2011, used textures that included a square with a slice through it, a rectangle, a diamond, and an anisotropic Jerusalem cross. Guided paths formed by these cells vary, such as straight, curved, and even hooked-shaped guide paths [3]. Quarfoth and Sievenpiper introduced the ray optics method to analyze the straight SWG model in 2011 [11], reported the simulation method of SWGs based on tensor impedance cells in 2013 [12], and then demonstrated two practical SWGs based on tensor impedance cells with a straight and arched guided paths, respectively, in 2015. Besides all these, Quarfoth analyzed the losses for a smooth bent SWG merely by the ray-optics method, in which the analysis process included a set of complicated equations [13].

All of above the mentioned research works are excellent, but the need still exist for their contents to be improved. For example, at least one common guided path has not be mentioned—the broken-line path. The broken-line SWG consists of several straight SWGs with heads-tails connecting in different directions on the same plane and it can replace the curved SWG. It is potentially advantageous over the curved SWG because its design and analysis are less complicated. Moreover, for SWGs, controlling energy leakage is very important since it determines the efficiency of surface wave propagation; however, as far as the authors' knowledge, no research on the analysis of the energy leakage has been reported. How to evaluate and suppress the energy leakage is not discussed either. Although the proposed ray-optics method has proved to be valid for the SWG made of impedance surface in some literatures. For instance, Quarfoth analyzed the losses for a smooth bent SWG by the ray-optics method in [13]. However, if we merely use this method to analyze the energy leakage of the straight and broken-line SWGs, the process will be very complicated.

In this work, by making use of the parallel plate waveguide theory together with the ray-optics method, several simple and effective equations will be acquired to forecast and control the energy leakage for the straight and broken-line SWGs. Moreover, by using surface-impedance-tunable cells introduced in our previous work [2], reconfigurable SWGs can be built with advantages such as low cost and multi-functionality. Furthermore, to judge whether the energy is leaky, a criterion of the energy leakage for the SWG is defined in this paper. Because the finite element method (FEM) had been verified in different domains [15-19], so all of numerical experiments of this paper are done in HFSS, a very popular commercial software based on the FEM.

III. METHODOLOGY

A. A brief introduction to the tunable impedance cell

The SWG can be regarded as a higher-impedance channel surrounded by two lower-impedance areas on a plane [12]. By utilizing tunable impedance cells properly, the SWG that we have proposed could now be built. From [22-25], the impedance of cells can be tuned by electric tuning or mechanical tuning. The goal of these two tuning methods is to change the equivalent capacitance of the cell. A modified slotted mushroom-like cell loaded with varactor diodes had been designed by us previously in [2], as shown in Fig. 1. On the top are a square metal patch, a square-ring-shaped metal patch and 4 varactor diodes across the slot. Five vertical vias are located on the patches, through the substrate, and isolated from the metal ground layer with clearances. Optimized dimensions of the structure are shown.

Spurred by TM surface waves, the measurement data indicated that its effective impedance ranges from j370 Ω to j780 Ω at 1.65 GHz when the bias voltage of varactor diodes decreases from 14 V to 2.3 V [2]. Using a simple voltage-switch, one can choose the impedance values of j370 Ω or j780 Ω. The circuit is also shown in Fig. 1.The impedance data and frequency of the unit-cell was adopted to perform the simulations in this paper.

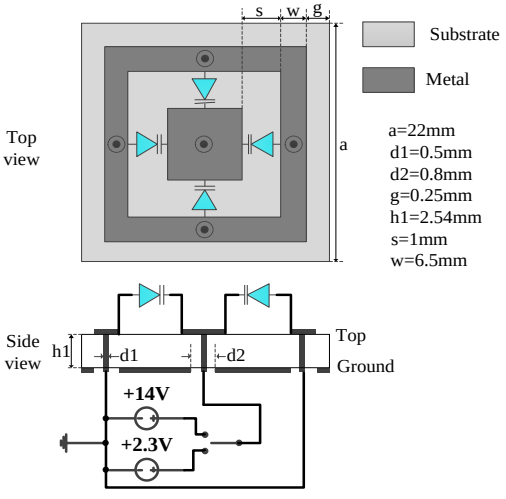

Fig. 1. The modified slotted mushroom-like unit-cell, not to scale. The central via is connected to a voltage of +2.3V or +14V for high or low impedance, respectively.

B. The topological structure of the SWG

An SWG based on impedance surface consisting of 30×30 tunable impedance units is modeled by HFSS, to illustrate multi-functionality, three different guiding paths on the same surface are exhibited in the figure, as shown in Fig. 2.

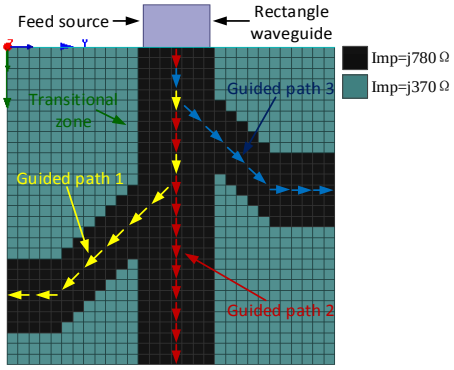

Fig. 2. Three different guided paths on the same impedance surface.

Obviously, from this figure we should notice that the curved path (path 1 or path 3) is just like a broken-line. Since the purpose of the SWG is to propagate surface waves with as little leakage as possible, it is reasonable to define a criterion for it. As for an antenna, S11 of its input port should be less than -10 dB. We believe the criterion of the energy leakage here should be stricter than return loss of antenna. Reference to return loss of antenna, if the ratio of the maximum electric field from outside to the inside of the SWG is converted to dB, the value (R) should be greater than -20 dB, or, $R = 20\lg(|E|_{\max\_outside} / |E|_{\max\_inside}) > -20dB$. It shows that the electromagnetic energy leaked from the black region to the blue region in Fig. 2 is larger than 1/100. In this case, the SW energy is considered to be leaky.

C. Theoretical models and analysis

A typical guided path (path 1 in Fig. 2) is chosen for theoretical analysis. To simplify the analysis, the stair-stepping boundary of the bent zone of the SWG is set to a straight line. The model in detail is shown in Fig. 3.

The whole guided path is a broken-line, but the front part is a straight line. According to the ray optics method, the propagation way of the TM surface wave in straight SWG is similar to that of the TM plane wave in parallel plate waveguide; both of them propagate by bouncing ways [11-13, 21]. Furthermore, it is clear that the parallel lines in Fig. 3 (for instance, y = 0 and y = d) are just like the profile of the parallel plate waveguide, therefore, the parallel plate waveguide theory is adopted to explain transmission properties of the TM surface-wave in straight SWG.

The width of the SWG is assumed to be d; the impedance of the inner zone is Z_1; the impedance of the outer zone is Z_2; and the angle between the wave vector of TM surface-waves (k) and z axial is θ. According to parallel plate waveguide theory [21],

$$k\sin\theta = \pi / d, \tag{2}$$

$$k = \omega\sqrt{\varepsilon\mu}, \tag{3}$$

where ω is the angular frequency of surface-wave, ε and μ are the effective dielectric constant and the effective magnetic conductivity of media, respectively. The light speed in media C_{media} is:

$$C_{media} = 1/\sqrt{\varepsilon\mu}. \tag{4}$$

From [2], the relation of surface impedance Z and the effective index of media n can be found,

$$Z = Z_0\sqrt{1-n^2}, \tag{5}$$

where Z_0 is the impedance of free space. Besides,

$$C_{media} = C_0 / n, \tag{6}$$

where C_0 is the light speed in free space.

By combining Equations (2) to (6), considering that $Z=Z_1$, we can figure out:

$$\theta = \sin^{-1}\left(\frac{\pi C_0}{d\cdot\omega\sqrt{1-\frac{Z_1^2}{Z_0^2}}}\right). \tag{7}$$

From Equation (7), different incident angles ϕ (complementary angle of θ) corresponding to different widths can be calculated as followed:

$$\phi = 90^\circ - \theta. \tag{8}$$

Based on the ray optics method [11-13], the critical angle $\alpha_{critical}$ can be solved when total inner refraction occurs.

$$\alpha_{critical} = \sin^{-1}\left(\frac{n_2}{n_1}\right) = \sin^{-1}\left(\frac{\sqrt{1-\frac{Z_2^2}{Z_0^2}}}{\sqrt{1-\frac{Z_1^2}{Z_0^2}}}\right). \tag{9}$$

According to the ray optics method, if $\phi \geq \alpha_{critical}$, then the leaky waves (energy leakage) in the straight zone would not appear.

When the waves arrive in the bent zone, leaky waves, if any occur, only appear on the outer-side boundary [13]. Just as Fig. 3 shows, we assume the bent angle is γ. According to geometry, we have:

$$\alpha + \theta + \gamma = 90^\circ. \tag{10}$$

Similarly, if $\alpha \geq \alpha_{critical}$, leaky waves in the bent zone would not appear either.

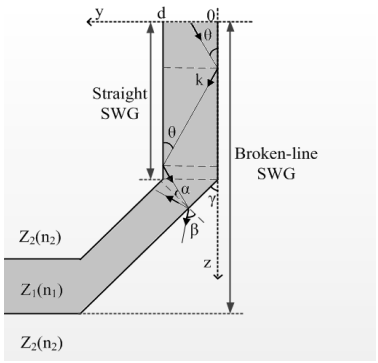

Fig. 3. Analyzing model of the SWG.

IV. RESULT ANALYSIS AND DISCUSSION

A. Computational results and analysis

According to Section II, let $Z_1 = j780\ \Omega$, $Z_2 = j370\ \Omega$ and $Z_0 = 377\ \Omega$ in Equation (9), $\alpha_{critical} = 37.6^\circ$ can be obtained. Incident angles corresponding to widths from 1×22 mm to 10×22 mm are calculated for straight and broken-line SWGs by the above equations, and the calculation results and the predictions of energy leakage are shown in Table 1 and Table 2, respectively.

Table 1: Incident angles corresponding to different width for the straight SWG

d (mm)	θ (degree)	ϕ (degree)	$\alpha_{critical}$ (degree)	Leak or Not
1×22	90-68.3j°	68.3j°	37.6°	Meaningless
2×22	64.1°	25.9°		Leaky
3×22	36.8°	53.2°		Not
4×22	26.7°	63.3°		Not
5×22	21.1°	68.9°		Not
6×22	17.4°	72.6°		Not
7×22	14.9°	75.1°		Not
8×22	13.0°	77.0°		Not
9×22	11.5°	78.5°		Not
10×22	10.4°	79.6°		Not

Table 2: Incident angles corresponding to different width for the broken-line SWG

d (mm)	θ (degree)	γ (degree)	α (degree)	$\alpha_{critical}$ (degree)	Leak or Not
1×22	90-68.3j°	45°	-45+68.3°	37.6°	Meaningless
2×22	64.1°		-19.1°		Leaky
3×22	36.8°		8.2°		Leaky
4×22	26.7°		18.3°		Leaky
5×22	21.1°		23.9°		Leaky
6×22	17.4°		27.6°		Leaky
7×22	14.9°		30.1°		Leaky
8×22	13.0°		32.0°		Leaky
9×22	11.5°		33.5°		Leaky
10×22	10.4°		34.6°		Leaky

From above tables, when the width of the straight SWG is less than 3×22 mm, the straight SWG begin to be leaky, however, the bent SWG is always leaky for all dimensions. Though θ is pure imaginary number in our calculation when d = 1×22 mm, we can't draw a conclusion directly from this result. Fortunately, because the leaky waves are obvious when d = 1×22 mm, we can infer that the leaky waves will appear heavily when d = 1×22 mm on the basis of Equation (6) and (7).

B. Simulation model and setup

In order to verify the theory, simulation experiments are performed. Based on [20], model of a straight SWG in HFSS is shown in Fig. 4. All the surfaces of the vacuum box are set to be radiation boundary except for the bottom surface. According to [2, 20], the rectangular waveguide WR-430 is used as feed source. All boundary conditions and feed source are the same for both straight and bent SWGs.

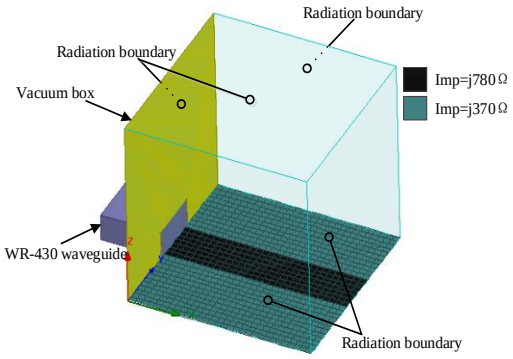

Fig. 4. Simulation model of a straight SWG in HFSS driven mode solver, not to scale.

C. Simulation results and analysis

For the straight SWG, path widths of 10×22, 6×22, 2×22, and 1×22 mm are chosen. The results have been demonstrated in Figs. 5 (a), (b), (c), and (d), respectively.

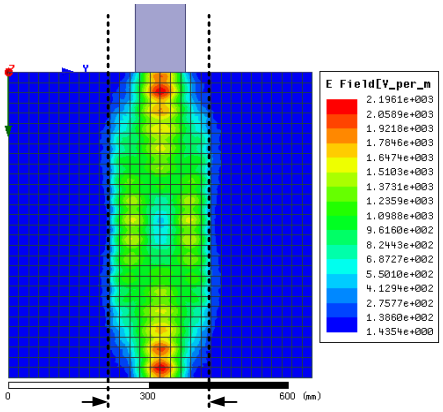

10×22(mm)

(a)

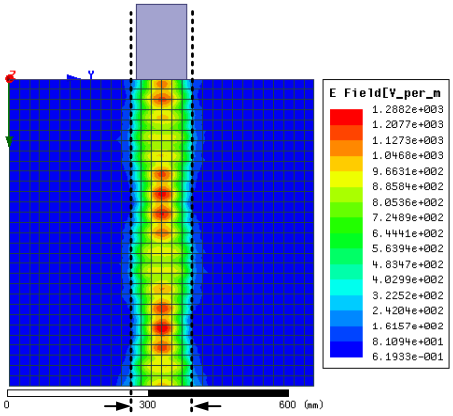

(b)

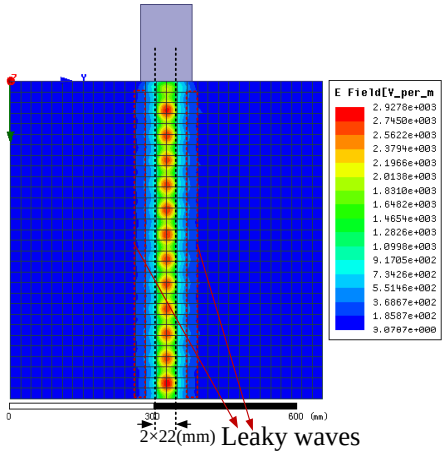

(c)

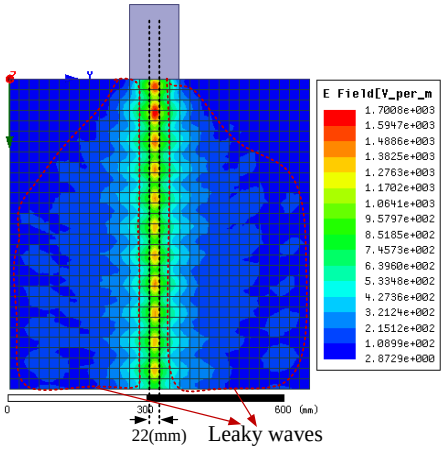

(d)

Fig. 5. Simulation results while d = 10×22 mm (a), 6×22 mm (b), 2×22 mm (c), and 1×22 mm (d).

From electric field data obtained by the simulation, we can calculate the ratio of the maximum electric field from outside o the inside of the SWG, respectively:

$$R_{10\times22} = 20\lg(150/2473) = -24.2dB < -20dB,$$

$$R_{6\times22} = 20\lg(93/1288) = -22.8dB < -20dB,$$

$$R_{2\times22} = 20\lg(368/2927) = -18dB > -20dB,$$

$$R_{1\times22} = 20\lg(533/1700) = -10dB > -20dB.$$

According to Equation (1), the latter two situations lead to energy leakage, which is completely in accordance with the theory. Moreover, it can be observed that the leakage increases as the width decreases.

For the broken-line SWG, according our theoretical forecast, the surface wave energy will always be leaky at the bent zone. The result is shown in Fig. 6.

According to Fig. 6, we can obtain that:

$$R_{6\times22\_b} = 20\lg(550/1863) = -10.6dB > -20dB.$$

The result demonstrates that the theory is correct.

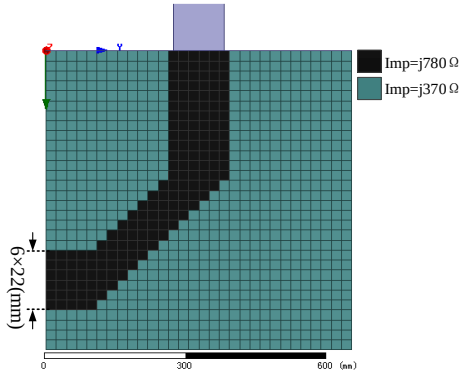

(a)

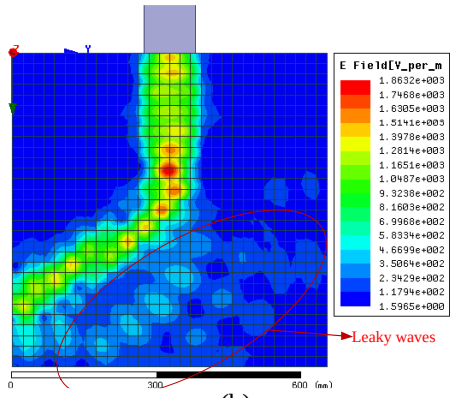

(b)

Fig. 6. Simulation model and result for the broken-line SWG with $Z_1 = j780\ \Omega$, (a) is model in HFSS, and (b) is simulation result.

What's more, the energy leakage can be suppressed further by increasing the impedance value of Z_1, while the other parameters remain the same. Specifically, in this case, the impedance range of Z_1 can be solved by combining Equations (6), (7), (8), and (9),

$$90^\circ - \gamma - \sin^{-1}\left(\frac{\pi \cdot C_0}{d \cdot \omega \sqrt{1+\frac{Z_1^2}{Z_0^2}}}\right) > \sin^{-1}\left(\frac{\sqrt{1-\frac{Z_2^2}{Z_0^2}}}{\sqrt{1-\frac{Z_1^2}{Z_0^2}}}\right). \quad (11)$$

Taking $\gamma = 45^\circ$, $d = 0.132$ m, $Z_0 = 377\ \Omega$, $Z_2 = 370\ \Omega$, and $f = 1.65$ GHz into Eq. 11. Through the numerical method, it can be obtained that Z_1 should be larger than $j970\ \Omega$. To guarantee a better suppression effect, we performed a simulation with $Z_1 = j1000\ \Omega$ in HFSS, and the simulation model and result are shown in Fig. 7.

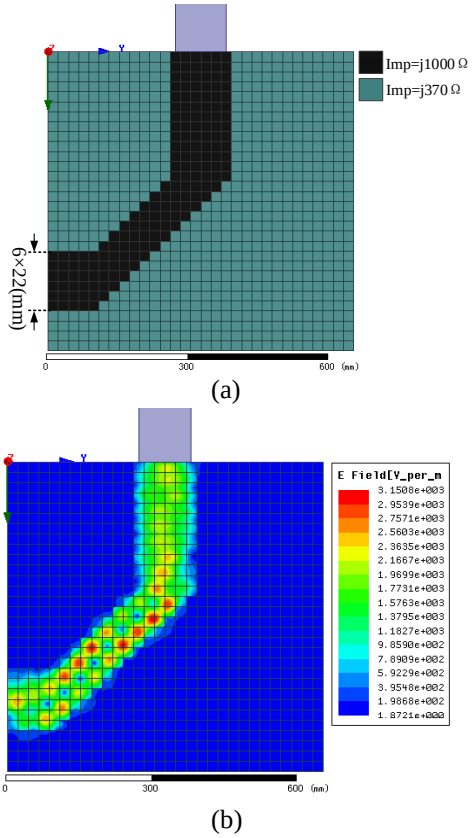

Fig. 7. Simulation result for the broken-line SWG with $Z_1 = j1000\ \Omega$; meanwhile the other parameters are unchanged, (a) is model in HFSS, and (b) is simulation result.

From Fig. 7, we can see that the leaky waves disappear. According to Equation (1), the ratio:

$$R = 20\lg(147/3150) = -26.6dB < -20dB,$$

which serves as a good example for the absence of leakage. Besides, we can draw another conclusion that the leakage decreases as the impedance of the guided path increases, and the leakage can be completely suppressed by increasing effective impedance of the guided path while the other parameters remain the same.

V. CONCLUSION

SWGs have been proposed for years, but their guiding efficiency, which is affected largely by surface wave leakage, has not been discussed thoroughly. To evaluate and suppress energy leakage for both straight and broken-line SWGs, simple and effective equations are derived. Differing from Quarfoth's analysis of the losses for a bent SWG, the analysis of the energy leakage for the proposed SWG is based on parallel plate waveguide theory and ray optics method in this paper, and the theory has been demonstrated to be evidently simpler and more effective. The multi-functionality of the SWG consisting of tunable impedance cells has been illustrated at the same time.

Structural parameters of the proposed SWG, such as the path width, incident angle, and effective impedance of guided path are analyzed in detail. The results are further verified by simulations, showing the satisfied accuracy of the theory. Besides that, a useful conclusion was arrived at, in that the leakage is inversely proportional to the width of the SWG and an increase of the effective impedance of the guided path. Furthermore, if the adjustment of other parameters for the proposed SWG is not convenient, one can control the energy leakage by increasing the impedance of the guided path. Although the results of HFSS are already very believable, measurement data always have more persuasive power, so our next work will be fabrication and testing to verify the contents of this paper.

ACKNOWLEDGMENT

The authors are thankful for financial support provided in part by the Youth Fund of the Education Department of Sichuan Province [Grant Number 11ZB031] and in part by a grant from China West Normal University [Grant Number CXTD2014-12].

REFERENCES

[1] D. F. Sievenpiper, "High-impedance electromagnetic surfaces," *Ph.D. Dissertation*, Dept. Electrical Engineering, Univ. California, Los Angeles, CA, USA, pp. 9-35, 1999.

[2] Z. Luo, X. Chen, J. Long, et al., "Nonlinear power-dependent impedance surface," *IEEE Transactions on Antennas and Propagation*, vol. 63, no. 4, pp. 736-1745, Apr. 2015.

[3] D. J. Gregoire and A. V. Kabakian, "Surface-wave waveguides," *IEEE Antennas and Wireless Propagation Letters*, vol. 10, pp. 1512-1515, 2011.

[4] W. Rotman, "A study of single-surface corrugated guides," *Proceedings of the IRE*, vol. 39, no. 8, pp. 952-959, Aug. 1951.

[5] R. Hougardy and R. Hansen, "Scanning surface wave antennas-oblique surface waves over a corrugated conductor," *IRE Transactions on*

Antennas and Propagation, vol. 6, no. 4, pp. 370-376, Oct. 1958.

[6] D. H. Lee and M.-H. Lee, "Gapped surface plasmon polariton waveguides for plasmonic signal modulation applications," *Journal of Nanoscience and Nanotechnology*, vol. 15, no. 10, pp. 7679-7684, Oct. 2015.

[7] B. Fong, J. Colburn, J. Ottusch, J. Visher, and D. Sievenpiper, "Scalar and tensor holographic artificial impedance surfaces," *IEEE Transactions on Antennas and Propagation*, vol. 58, no. 10, pp. 3212-3221, Oct. 2010.

[8] A. I. Ass'ad and H. S. Ashour, "TE magnetostatic surface waves in symmetric dielectric negative permittivity material waveguide," *Advances In Condensed Matter Physics*, Article Number: 867638, 2009.

[9] J. F. Dong, "Surface wave modes in chiral negative refraction grounded slab waveguides," *Progress In Electromagnetics Research, PIER 95*, pp. 153-166, 2009.

[10] J. R. Canto, C. R. Paiva, and A. M Barbosa, "Dispersion and losses in surface waveguides containing double negative or chiral metamaterials," *Progress In Electromagnetics Research, PIER 116*, pp. 409-423, 2011.

[11] R. Quarfoth and D. F. Sievenpiper, "Artificial tensor impedance surface waveguides," *IEEE Transactions on Antennas and Propagation*, vol. 61, no. 7, pp. 3597-3606, Jul. 2013.

[12] R. Quarfoth and D. Sievenpiper, "Impedance surface waveguide theory and simulation," *Proceedings of the 2011 IEEE Antennas and Propagation Society International Symposium and USNC/URSI National Radio Science Meeting*, pp. 1159-1162, Jul. 2011.

[13] R. G. Quarfoth and D. F. Sievenpiper, "Nonscattering waveguides based on tensor impedance surface," *IEEE Transactions on Antennas and Propagation*, vol. 63, no. 4, pp. 1746-1755, Apr. 2015.

[14] R. Quarfoth and D. F. Sievenpiper, "Simulation of anisotropic artificial impedance surface with rectangular and diamond lattices," *Proceedings of the 2011 IEEE Antennas and Propagation Society International Symposium and USNC/URSI National Radio Science Meeting*, pp. 1498-1501, Jul. 2011.

[15] A. Saldana-Robles, E. Aguilera-Gomez, H. Plascencia-Mora, et al., "Three-dimensional modeling of surface roughness for burnishing process," *DYNA*, vol. 90, no. 4, pp. 423-432, Jul.-Aug. 2015.

[16] D. A. Mantaras and P. Luque, "Assessing motorcyclist protection systems using finite element simulations," *International Journal of Simulation Modelling*, vol. 14, no. 1, pp. 110-120, Mar. 2015.

[17] B. Cirkovic, I. Camagic, and N. Vasic, "Analysis of the supporting structure of composite material tool machine using the finite element method," *Tehnicki Vjesnik*, vol. 22, no. 1, pp. 95-98, Feb. 2015.

[18] S. Shabazpanahi, A. A. A. Ali, F. N. Aznieta, et al., "Finite element modeling of crack propagation in RC beam by using energy approach," *Journal of Engineering Science and Technology Review*, vol. 7, no. 1, pp. 65-70, 2014.

[19] K. Lubikowski, S. Radkowski, K. Szczurowski, et al., "Seebeck phenomenon, calculation method comparison," *Journal of Power Technologies*, vol. 95, no. 2015, pp. 63-67, 2015.

[20] Z. Luo, X. Chen, J. Long, et al., "Self-focusing of electromagnetic surface waves on a nonlinear impedance surface," *Applied Physics Letters*, vol. 106, no. 21, pp. 2111021-5, May 2015.

[21] D. M. Pozar, *Microwave Engineering*, Third Edition, John Wiley & Sons, pp. 85-88, 2005.

[22] D. Sievenpiper and J. Schaffner, "Beam steering microwave reflector based on electrically tunable impedance surface," *Electronics Letters*, vol. 38, no. 21, pp. 1237-1238, Oct. 2002.

[23] R. S. Schofield, J. C. Soric, D. Rainwater, et al., "Scattering suppression and wideband tunability of a flexible mantle cloak for finite-length conducting rods," *New Journal of Physics*, vol. 16, Article Number: 063063, Jun. 2014.

[24] D. Sievenpiper, J. Schaffner, J. J. Lee, et al., "A steerable leaky-wave antenna using a tunable impedance ground plane," *IEEE Antennas and Wireless Propagation Letters*, vol. 1, pp. 179-182, 2002.

[25] H. Liu, S. Gao, and T. H. Loh, "Low-cost beam-switching circularly-polarised antenna using tunable high impedance surface," *Proceedings of the 2012 Loughborough Antennas & Propagation Conference (LAPC)*, Nov. 2012.

Yonghong Zhou received his M.S. degree in Computer Applications Technology from Southwest Petroleum University, Chengdu, China, in 2005. He is currently pursuing Ph.D. in Radio Physics at Sichuan University. He joined the teaching staff in 2005 and is currently an Associate-Professor with the College of Electronics and Information Engineering, China West Normal University. His research area includes surface

wave metamaterials and numerical methods applied in electromagnetics.

Xing Chen received the M.S. degree in Radio Physics and the Ph.D. degree in Biomedical Engineering from Sichuan University, Sichuan, China, in 1999 and 2004, respectively. He joined the teaching staff in 1991 and is currently a Professor with the College of Electronics and Information Engineering, Sichuan University. His main research interests are in the fields of antenna, microwave imaging, global optimization, numerical methods applied in electromagnetics, and parallel computation. Chen is a Senior Member of the Chinese Institute of Electronics.

Zhangjie Luo received his B.S. degree in Electronic and Information Engineering and the Ph.D. degree in Radio Physics from Sichuan University, Chengdu, China, in 2008 and 2015, respectively. He is currently a Research Staff with the Institute of Electronic Engineering, China Academy of Engineering Physics. From 2012 to 2014, he worked in the Applied Electromagnetics Group at the University of California, San Diego, USA, as a visiting Ph.D. student. His research area includes surface wave metamaterials, circular waveguides, and microstrip antennas.

Short Pulse Propagation along Microstrip Meander Delay Lines with Design Constraints: Comparative Analysis of the Quasi-static and Electromagnetic Approaches

Pavel Orlov, Talgat Gazizov, and Aleksander Zabolotsky

Department of Television and Control
Tomsk State University of Control Systems and Radioelectronics, Tomsk, 634050, Russia
praetorian281@gmail.com, talgat@tu.tusur.ru, zabolotsky_am@mail.ru

Abstract ─ Short pulse propagation along microstrip meander delay lines is considered. Electromagnetic analysis is used in the CST MWS software. A quasi-static analysis in TALGAT software is used as another approach, for which the complete computational models for capacitive matrix calculation are presented. The results of simulations are given. It is shown that if a number of turns is increased and their length is reduced proportionally, distortions of a pulse signal in the line are reduced. At the same time, though the electrical width of the structure increases, an agreement between the results of quasi-static and electromagnetic analyses is improved. Memory costs of electromagnetic analysis and quasi-static analysis are comparable, while the latter is significantly less time-consuming. Thus, it is demonstrated that a quasi-static analysis can be quite relevant during the design of the microstrip meander delay lines with minimal distortions.

Index Terms ─ Electromagnetic analysis, meander delay line, quasi-static approach.

I. INTRODUCTION

Trends of modern electronics devices development (decrease in dimensions, increase in the upper frequency of signal spectrum, etc.) lead to increase in package density and to the need for signals asynchrony minimization. In this regard, delay lines, particularly in the form of a meander, as the simplest structure, are widely used. However, crosstalk arises, and it can distort waveform and reduce delay time of a pulse propagating in the line [1]. There are different approaches to crosstalk level reduction, for example, use of guard traces [2], but it increases the area of meander lines. Meanwhile, it is often required to minimize the area of meander lines.

These factors lead to the need for numerical analysis of meander lines. Two approaches to the analysis are used: quasi-static and electromagnetic. The first approach is usually less consumptive but it is an approximation, as it is based on the telegraph equations, which are valid only for small electrical width of a structure. The second approach takes into account higher order modes but is more consumptive and requires more user's competencies [3] than the work with the quasi-static approach.

Electromagnetic analysis for a one set of parameters of the microstrip meander delay line is presented in [4]. A similar analysis, but in the range of parameters, is made in [5]. Comparison between the electromagnetic and quasi-static analysis results and the experimental results obtained for the strip line is given in [6]. Comparison of the results obtained by three different numerical methods for one set of microstrip line parameters is presented in [7]. These studies did not investigate applicability of the quasi-static analysis for the case of electrically wide structures, in particular, when delay time and area of the meander microstrip line are defined and it is necessary to minimize distortions of the pulse signal. Meanwhile, such a research is very important for design process because it will help to optimize both parameters and analysis process of the meander delay lines. The aim of this paper is to compare the results of electromagnetic and quasi-static simulations of a short pulse propagation along microstrip meander delay lines with design constraints.

II. SIMULATION APPROACHES

In this paper simulation of the meander lines was executed in the CST MWS and TALGAT software without accounting the losses in conductors and dielectrics.

In CST MWS a combination of the perfect boundary approximation with the Finite Integration Technique is used [8]. The transient solver allows to make full-wave 3D analysis of structures of various complexities. In general, the system is widely known to give it a more detailed description. In order to demonstrate that quasi-static approach can be useful for simulation of meander lines, TALGAT software is used. Let us give a more detailed description of the features of quasi-static

Submitted On: August 19, 2015
Accepted On: February 26, 2016

approach implemented in TALGAT software.

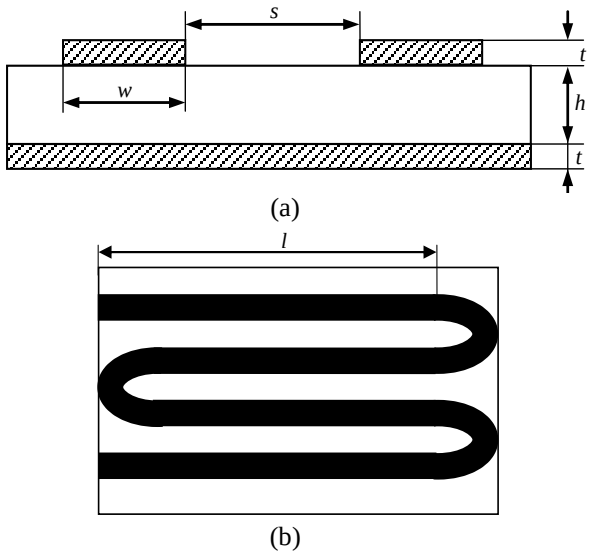

Fig. 1. Cross section of a turn model (a) and top view of two turns (b).

The TALGAT software is based on the method of moments and allows to make 2D quasi-static analysis. The algorithm implemented in the system allows to calculate all elements of a moment matrix by fully analytical formulae only, avoiding the time-consuming and approximate numerical integration. It can be useful for effective calculation of a capacitive matrix of two-dimensional systems of various complexities [9]. In this paper the simulation of the short pulse propagation in meander lines is carried out. A multiconductor transmission line is a base of the considered structures. It is assumed in the analysis that a transmission line is uniform along its length with an arbitrary cross section. The cross section, in general case, with N signal conductors and a reference, is represented by the following $N\times N$ matrices of line per unit length parameters: inductance (**L**), coefficients of electrostatic induction (**C**), resistance (**R**), conductance (**G**). In paper [10], an approach based on a modified nodal admittance matrix has been presented for formulation of network equations including the coupled transmission line, terminal, and interconnecting networks. The approach is used and voltages in the time domain are obtained by applying the inverse fast Fourier transform. Matrixes **L** and **C** are calculated by a method of moments and the mathematical model for considered case of linear and orthogonal boundaries of conductors and dielectrics [11] implemented in TALGAT system is described below.

First we are segmenting the conductor-dielectric boundaries (subdividing them into intervals further called subintervals) and assign numbers from 1 to Nc to these subintervals. Then we digitize the dielectric-dielectric boundaries and assign them numbers from Nc + 1 to N. (The infinite ground plane is not digitized. If there is a second infinite plane, it is bounded at a point far removed from the conductors, digitized as a conventional conductor, and considered to be at zero potential. If there are other conductors that are always at zero potential, they all are conventionally digitized.) In so doing, we first digitize and number the conductor-dielectric subintervals orthogonal to the Y axis (the serial number of the last subinterval is Nc_Y), digitize and number the conductor-dielectric subintervals orthogonal to the X axis (the serial number of the last subinterval is Nc), digitize and number the dielectric-dielectric subintervals orthogonal to the Y axis (the serial number of the last subinterval is Nd_Y), and finally digitize and number the dielectric-dielectric subintervals orthogonal to the X axis (the serial number of the last subinterval is N).

Each subinterval has the following parameters: the coordinate of the X-center of the nth subinterval is x_n, the coordinate of the Y-center of the nth subinterval is y_n, the length of the nth subinterval is d_n; the permittivity of the nth conductor-dielectric subinterval is ε_n, and the permittivities on the positive (to which the vector $\boldsymbol{n}_n$ is pointed) and negative sides (from which the vector $\boldsymbol{n}_n$ is emanated) of the nth dielectric-dielectric subinterval are ε_n^+ and ε_n^-, respectively. Here $\boldsymbol{n}_n$ is a unit normal vector drawn from the center of the nth subinterval. These parameters are used to calculate the entries of matrix of linear system to be solved.

For the matrix rows with numbers $m = 1, \ldots, Nc$ we have:

$$S_{mn} = \frac{1}{2\pi\varepsilon_0}\left(\hat{I}_{mn} - I_{mn}\right), \quad \begin{cases} m=1, ..., Nc \\ n=1, ..., N \end{cases}.$$

Here for $n = 1, \ldots, Nc_Y, (Nc + 1), \ldots, Nd_Y$ we have:

$$I_{mn} = a_1 \cdot \ln\left(a_1^2 + c_1^2\right) - 2a_1 + 2c_1 \cdot \operatorname{arctg}\left(\frac{a_1}{c_1}\right) - a_2 \cdot \ln\left(a_2^2 + c_1^2\right) + 2a_2 - 2c_1 \cdot \operatorname{arctg}\left(\frac{a_2}{c_1}\right), \quad (1)$$

where

$$a_1 = \frac{d_n}{2} - (x_m - x_n);\ a_2 = \frac{-d_n}{2} - (x_m - x_n);\ c_1 = y_m - y_n. \quad (2)$$

$\hat{I}_{mn}$ is calculated from Eq. (1) in which c_1 is substituted by c_2. Then we obtain:

$$a_1 = \frac{d_n}{2} - (x_m - x_n);\ a_2 = \frac{-d_n}{2} - (x_m - x_n);\ c_1 = y_m - y_n. \quad (3)$$

For $n = (Nc_Y + 1), \ldots, Nc, (Nd_Y + 1), \ldots, N$, I_{mn} is calculated from Eq. (1) and,

$$a_1 = \frac{d_n}{2} - (y_m - y_n);\ a_2 = \frac{-d_n}{2} - (y_m - y_n);\ c_1 = x_m - x_n. \quad (4)$$

$\hat{I}_{mn}$ is calculated from Eq. (1) in which c_1 is replaced by c_2:

$$a_1 = \frac{d_n}{2} + (y_m + y_n);\ a_2 = \frac{-d_n}{2} + (y_m + y_n);\ c_2 = x_m - x_n. \quad (5)$$

For the matrix rows with numbers $m = (Nc + 1), \ldots, N$, we have:

$$S_{mn} = \frac{1}{2\pi\varepsilon_0}\left(I_{mn} - \hat{I}_{mn}\right),\ \begin{cases} m=(Nc+1),\ \ldots,\ N \\ n=1,\ \ldots,\ N \end{cases},\ m \neq n;$$

$$S_{mm} = \frac{1}{2\pi\varepsilon_0}\left(I_{mm} - \hat{I}_{mm}\right) + \frac{1}{2\varepsilon_0}\frac{\varepsilon_m^+ + \varepsilon_m^-}{\varepsilon_m^+ - \varepsilon_m^-},\ m=(Nc+1),\ \ldots N,$$

where for the rows with numbers $m = (Nc + 1), \ldots, Nd_Y$ for $n = 1, \ldots, Nc_Y, (Nc + 1), \ldots, Nd_Y$,

$$I_{mn} = \operatorname{arctg}\left(\frac{a_1}{c_1}\right) - \operatorname{arctg}\left(\frac{a_2}{c_1}\right), \quad (6)$$

and the variables coincide with those defined by Eq. (2); $\hat{I}_{mn}$ is calculated from Eq. (6) after replacement of c_1 by c_2 and substitution of Eq. (3), and for $n = (Nc_Y + 1), \ldots, Nc, (Nd_Y + 1), \ldots, N$, we have:

$$I_{mn} = \frac{1}{2}\ln\left(\frac{a_2^2 + c_1^2}{a_1^2 + c_1^2}\right), \quad (7)$$

where the variables coincide with those defined by Eq. (4), and $\hat{I}_{mn}$ is calculated from Eq. (7) taken with opposite sign after replacement of c_1 by c_2 and substitution of Eq. (5). For the matrix rows with numbers $m = (Nd_Y + 1), \ldots, N$ for $n = 1, \ldots, Nc_Y, (Nc + 1), \ldots, Nd_Y$, I_{mn} is calculated from Eq. (7) with variables defined by Eq. (2), and $\hat{I}_{mn}$ is calculated from Eq. (7) after replacement of c_1 by c_2 and substitution of Eq. (3). For $n = (Nc_Y + 1), \ldots, Nc, (Nd_Y + 1), \ldots, N$, I_{mn} is calculated from Eq. (6) with the variables coinciding with those defined by Eq. (4), and $\hat{I}_{mn}$ is calculated from Eq. (6) after replacement of c_1 by c_2 and substitution of Eq. (5).

Now the linear system to be solved assumes the form:

$$\sum_{n=1}^{N} S_{mn}\sigma_n = \begin{cases} V_i,\ m=1,\ \ldots, Nc, \\ 0,\ m=(Nc+1),\ \ldots, N \end{cases}.$$

The subscript i here means that each digitized element belonging to the ith conductor is at the potential required for the determination of the capacitance matrix. The components S_{mn} gathered together yield the quadratic matrix **S** relating the charge densities of segmented elements on the conductors and the dielectric boundaries, forming the vector **σ**, with the potentials of these elements forming the vector **V**, and the problem itself is expressed in the compact linear system form $\mathbf{S}\sigma = \mathbf{V}$, which is solved Ncond times (where $Ncond$ is the number of conductors in the system disregarding the reference conductor), and in the ith solution, the conductor potential V_i, $i = 1, \ldots, Ncond$, is set equal to 1 V, and the potentials of all remaining conductors are set equal to 0 V. Finally, from the definition of the entry of the capacitance matrix we obtain:

$$C_{ij} = \sum_{n=NF_i}^{NL_i} \frac{\varepsilon_n}{\varepsilon_0}\sigma_n^{(j)} d_n,\ i, j = 1, \ldots, Ncond.$$

Here, NF_i and NL_i are the numbers of the first and last subintervals of the ith conductor, the subscript i denotes the conductor for which charges $\sigma_n^{(j)}$ are summed, and the superscript j indicates the serial number of σ_n calculated when the potential of the jth conductor is set equal to 1 V and the potentials of the remaining conductors are set equal to 0 V.

III. SIMULATION RESULTS

In the TALGAT system the meander line structure was represented like N-conductor transmission line, with ends of the conductors connected respectively (see Fig. 2). Structures with N = 2; 4; 8; 16; 32, with the length (l) of 20; 10; 5; 2.5; 1.25 mm were selected respectively. It allows to get electrically narrow and wide structures with a constant total length of conductors. The cross section of the analyzed structure is shown in Fig. 1 (a). Its parameters are: conductors thickness (t) – 35 μm, conductors width (w) – 50 μm, distance between conductors (s) – 50 μm, dielectric material (ε_r = 3.8; thickness (h) – 2 mm). These parameters were chosen in such a way that a high level of electromagnetic coupling is generated between the half-turns, which maximizes the pulse distortions. The value of the resistance at the ends of the line was chosen under pseudomatching conditions as 205 Ω. A trapezoidal signal with EMF 1 V and duration of rise and fall – 0.1 ns, flat top – 1 ns was chosen as the excitation source. Memory costs and computational costs are given in Table 1. Waveforms at the output of the meander line are shown in Fig. 3. Signal propagation delays at "0.5" level are given in Table 2.

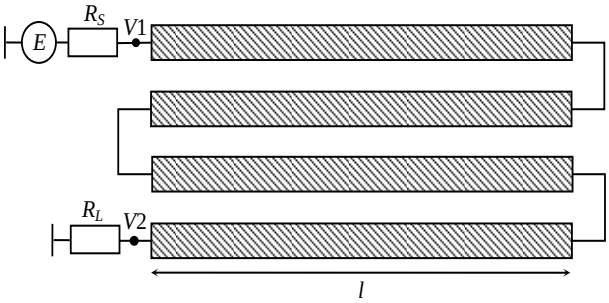

Fig. 2. Circuit diagram of a meander line model for quasi-static simulation with N = 4.

Table 1: The consumption of computer memory and CPU time for CST MWS and TALGAT

	CST MWS		TALGAT	
N	Time, sec	Peak Memory Usage, Mb	Time, sec	Peak Memory Usage, Mb
2	1002	345	3	85
4	822	306	6.2	107
8	730	288	17.3	185
16	635	263	60	586
32	796	303	62	501

Table 2: Comparison of delay times at level «0.5» from Fig. 3

N	*l*, mm	T_{CST}, ps	T_{TALGAT}, ps	ΔT, ps	$\frac{\lvert T_{CST} - T_{TALGAT} \rvert}{T_{CST} + T_{TALGAT}} \cdot 100\%$
2	20	87	206	119	40
4	10	105	129	24	10
8	5	93	109	16	8
16	2.5	90	100	10	5
32	1.25	89	104	15	8

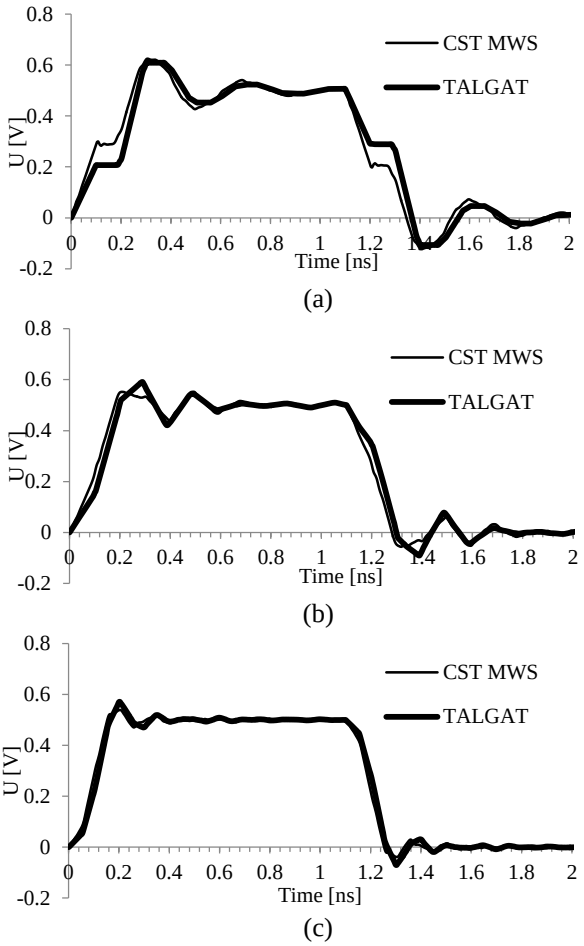

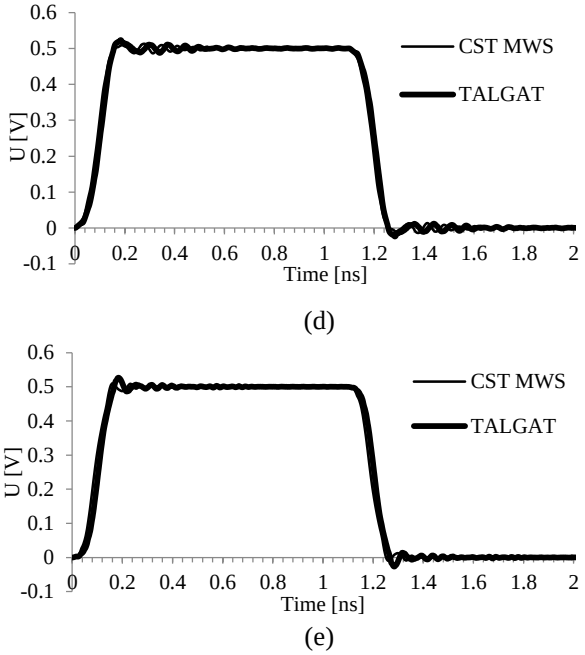

Fig. 3. Output waveforms of the examined structures with N = 2 (a); 4 (b); 8 (c); 16 (d); and 32 (e).

From these results it is clear that the waveform of the signal is subjected to distortions caused by electromagnetic coupling between the half-turns. However, the results of quasi-static and electromagnetic analysis showed good agreement: delays difference does not exceed 10%, and only in case of N = 2 it equals to 40% due to the difference of the near end crosstalk levels, that may be caused by neglect of edge effects at the ends of the halfturns in quasi-static analysis. Reduction of pulse distortion, obtained through the increase of N and corresponding reduction of half-turn length, can be explained by the reduction of propagation delay in a single turn and, consequently, reduction of delay between the signal and the near end crosstalk. It leads to the reduction of distortions at the rise and fall of a pulse, which are significant for N = 2 only. As far as the difference between the results of electromagnetic and quasi-static analyses is most obviously observed in difference of their amplitudes of the near end crosstalk (which is clearly seen in Fig. 3 (a)), the increase of N and the corresponding decrease of the turn length provide more coincident results.

For the upper frequency of signal spectrum (10 GHz) the wavelength in vacuum equals to 3 cm and with the dielectric it is somewhat smaller. When N = 32, structure width (3.25 mm) is more than 0.1λ, which can lead to incorrect results of quasi-static analysis. However, we observe the overall coincidence of quasi-

static and electromagnetic analysis results that allows us to conclude the correctness of the quasi-static analysis for structures of this type. For the considered cases, memory costs of CST MWS and TALGAT are comparable, while TALGAT is 12–334 times less time-consuming.

IV. CONCLUSION

The complete computational models for capacitive matrix calculation of quasi-static approach are presented. In spite of the considered simplicity and limitations of the quasi-static approach, it can give accurate, on a par with electromagnetic approaches, and fast results even for structures with complex electromagnetic coupling. It is worth noting, though the electrical width of a structure increases, the agreement between the results of quasi-static and electromagnetic analyses is improved. Thus, it is demonstrated that a quasi-static analysis can be quite relevant during the design of microstrip meander delay lines with minimal distortions. This is especially important at the stage of optimization that requires repetitive calculations.

Results of simulation allow to conclude that the larger number of turns gives smaller waveform distortions for structures with the same total length of lines.

ACKNOWLEDGMENT

Authors thank reviewers for valuable comments. Development of necessary software was supported by the state contract 8.1802.2014/K of the Russian Ministry of Education and Science, modeling of coupled lines was supported by RFBR grant 14-29-09254, simulation of waveforms was carried out at the expense of RSF grant 14-19-01232 in TUSUR University.

REFERENCES

[1] R. B. Wu and F. L. Chao, "Laddering wave in serpentine delay line," *IEEE Trans. Compon., Packag., Manuf. Technol*., vol. 18, no. 4, pt. B, pp. 644-650, Nov. 1995.

[2] S. Guang-Hwa, C. Chia-Ying, and R. B. Wu, "Guard trace design for improvement on transient waveforms and eye diagrams of serpentine delay lines," *IEEE Transactions on Advanced Packaging*, vol. 33, no. 4, p. 1051-1060, 2010.

[3] A. Bruce, "Importance and process of validation for all levels of modeling problems," *Proc. of the 2009 IEEE Int. Symp. on EMC*, 2009.

[4] E. Topsakal and J. Volakis, "Finite element method for the accurate analysis of delay line propagation characteristics," *IEEE International Symposium on EMC*, vol. 2, pp. 1074-1076, 2003.

[5] A. Kabiri, Q. He, M. H. Kermani, and O. M. Ramahi, "Design of a controllable delay line," *IEEE Transactions on Advanced Packaging*, vol. 33, no. 4, pp. 1080-1087, 2010.

[6] B. J. Rubin and B. Singh, "Study of meander line delay in circuit boards," *IEEE Transactions on Microwave Theory and Techniques*, vol. 48, no. 9, pp. 1452-1460, 2000.

[7] A. U Bhobe, C. L. Holloway, and M. Piket-May, "Meander delay line challenge problem: a comparison using FDTD, FEM and MoM," *IEEE International Symposium on EMC*, vol. 2, pp. 805-810, 2001.

[8] *The Finite Integration Technique*, [Online]. Available: https://www.cst.com/Products/CSTmws/FIT

[9] T. R. Gazizov, "Analytic expressions for Mom calculation of capacitance matrix of two dimensional system of conductors and dielectrics having arbitrary oriented boundaries," *Proc. of the 2001 IEEE EMC Symposium, Montreal, Canada*, vol. 1. pp. 151-155, Aug. 13-17, 2001.

[10] J. R. Griffith and M. S. Nakhla, "Time-domain analysis of lossy coupled transmission lines," *IEEE Transactions on Microwave Theory and Techniques*, vol. 38, pp. 1480-1487, 1990.

[11] T. R. Gazizov, "Calculation of a capacitance matrix for a two-dimensional configuration of conductors and dielectrics with orthogonal boundaries," *Russian Physics Journal*, vol. 47, pp. 326-328, 2004.

Orlov Pavel Evgenievich was born in 1986. He received the Ph.D. degree from Tomsk State University of Control Systems and Radioelectronics, Tomsk Region, Russia in 2013. His research interest is electromagnetic compatibility. Evgenievich is the author of 47 scientific papers.

Gazizov Talgat Rashitovich was born in 1963. He got his higher professional education on Radioengineering in 1985 in the Tomsk Institute of Automatic Control Systems and Radioelectronics, Ph.D degree in 1999, and Doctor of Sciences degree in 2010. His research interest is electromagnetic compatibility. He is author of 242 scientific publications.

Zabolotsky Alexander Mikhailovich was born in 1982. He got his higher professional education on Radioengineering in 2004 in the Tomsk State University of Control Systems and Radioelectronics, Ph.D. degree in 2010. His research interest is electromagnetic compatibility. He is author of 160 scientific publications.

Broad-Band and Wide Scan Phased Array Element Design Using Data Mining

Golamreza Dadashzadeh, Mohammad Kargar, Yalda Torabi, and Bahman Rahmati

Department of Electrical and Electronic Engineering
Shahed University, Tehran, 0098, IRAN
gdadashzadeh@shahed.ac.ir, m.kargar@shahed.ac.ir, y.torabi@shahed.ac.ir, brahmati@shahed.ac.ir

Abstract ─ Novel synthesis procedure, exploiting data mining technique for antenna design is presented. By utilizing data mining, investigating various combinations of a typical antenna configuration, all together, is feasible and this fact allows the selection of the specific design which possesses the desired properties. In this paper, a broad-band and wide scanning angle probe-fed microstrip patch array element with shorting posts is designed based on this procedure. For achieving acceptable bandwidth, scan angle and polarization, the coordination positions and the number of the incorporated shorting posts were considered as the design parameters. For a substrate with a thickness of $0.05\lambda_0$, the simulation results show a 15% frequency bandwidth with a scanning range of 70° in the main E, H and D-planes.

Index Terms ─ Broad-band antennas, data mining, phased array, shorting posts.

I. INTRODUCTION

Until now, much work has been done on designing vast scanning range or wide bandwidth phased array elements [1]. Also, wide bandwidth phased array elements have been thoroughly studied [2]. However, the phased array structures with simultaneous wideband and wide scan angle, have been less investigated in the literature such as [3] in which a tapered slot array has been investigated. Another example is the work done on aperture coupled microstrip array antenna [4]. Most of these structures have a bulky configuration. Having a low profile phased array elements with wideband and wide scanning range properties, is desirable. A microstrip patch antenna is a suitable low profile antenna as a phased array element, which has small size and light weight as well as relatively inexpensive production; however, its scanning range and bandwidth is limited [5]. A general and simple method for increasing the bandwidth of a microstrip patch antenna is increasing the substrate thickness. Although this approach promotes the chance of inducing surface waves. Surface wave propagation severely limits the scan angle in large microstrip arrays and moves the scan-blindness angle further to the broadsight ($\theta=0^{\circ}$) [6]. Limited scanning angle of patch phased array antennas is dominantly due to the presence of surface wave which has been alleviated to a great extent, by exploiting shorting posts [7]. However, the bandwidth of these types of antennas hasn't been addressed and the usual bandwidths presented are about 1-2 percent [8].

In this paper, we investigate the probe-fed microstrip patch antenna with different configurations of single, dual and triple-shorting post positions as the unit cell of phased array antenna for achieving vast scanning angles and large bandwidth. To this end, the positions of shorting posts are optimized by a data mining technique [9]. This technique is based on providing a data-base of different simulation results relating to single, dual and triple shorting post positions and then classifying the results. The advantage of this method is coming up with all possible cases without the need of simulating all of them. Thus the optimum cases would also be discovered. It should be mentioned that this method is not restricted to a typical group of antennas and could be extended to different antenna structures.

II. DATA MINING SYNTHESIS PROCEDURE

A. Data mining definition

Data mining is a branch of science emerged from the combination of different sciences such as statistics, artificial intelligence, machine learning, pattern recognition, and database technology. It is used for extracting the relationship existing between a large set of data. The main steps in applying data mining to a collection of data are:

1. Data preparation.
2. Relation discovery.
3. Evaluation and interpretation.

The aim of data preparation is creating a comprehensive look-up table of data, representing different aspects of the under-studying phenomenon. The look-up table is made up of columns of dataset related to different attributes and rows of different

Submitted On: October 18, 2015
Accepted On: February 26, 2016

samples regarded as records. In the second step by considering the data types and using various algorithms (such as classification or clustering), the correlation among the data is extracted. Afterwards, the achieved knowledge from the second stage is evaluated and its validity is determined in third step [10]. Two general methods for data mining are classification and clustering. In the former one, the data are divided into two sets called train dataset and test dataset. The train dataset is used for rendering a model and the test dataset is applied to the model for validating the accuracy of the model. One of the various attributes is always considered as a critique attribute for classification which is named label. In the clustering method, similarity critiques are chosen which upon them, records having the most similarity together are grouped into one cluster. This technique attempts to put most analogous records in common groups and separate the less similar ones.

B. Antenna design, utilizing data mining procedure

As mentioned in the introduction, by increasing the microstrip substrate and placing shorting posts at appropriate locations one can achieve high bandwidth and wide scan angle. In this section, conventional probe-fed patch antenna with single shorting post, dual shorting posts and triple shorting posts as the unit cells of an array antenna, are investigated by a data mining procedure to achieve broadband frequency and wide scanning range performance. To this end, a basic framework for exerting data mining techniques to antenna design is presented. Due to the fact that data mining is based on manipulating data, the first step in utilizing this technique for antenna design, is to convert design parameters and the result aspects into a dataset. Accomplishing this task, requires establishing a data base in which each column is dedicated to each specific design parameter or outcome aspect and for each variation of the design parameters a separate row is added to the data base accommodating the corresponding results. The procedure of applying data mining for antenna design is graphically shown in the diagram of Fig. 1.

The first step in applying data mining to antenna design is gathering a table of assets, indicating one or several of the antenna specifications for all different cases of the antenna design parameters. It should be emphasized that antenna specifications are chosen according to the antenna design goals and also the algorithm considered for data mining. It is feasible to use a minimum set of antenna specifications which results in less computational effort. As an example, for designing a wideband antenna, considering characteristics related to the bandwidth such as the reflection coefficient, is sufficient. Moreover, in the proposed procedure those assets which upon them data are clustered, should be chosen. Virtually, data which are irrelevant to the design goals, degrade the accuracy of the clustering process. For the antenna design case studied in this paper, the parameters consisting of return loss, polarization and shorting posts' positions are considered as the appropriate assets.

In the second step and before applying clustering based on analysis methods, outlying samples of records or simulation results which significantly differ from the rest of the records, are separated so that these outlying records couldn't degrade the accuracy of the clustering process. However, the mentioned records are all together considered as a single-member cluster because there might be a case where the optimum results would be found in these far apart records.

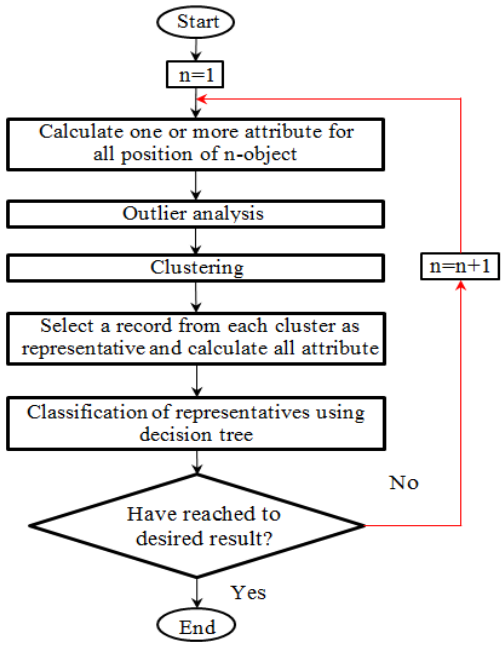

Fig. 1. Flowchart of antenna design using data mining.

In the third step, based on a clustering method such as K-medoids [11], different configurations of the antenna base structure are categorized. At the end of this stage, all design configurations with similar simulation results would be gathered into a unique group. The next step is choosing a member from each group as a representative of the cluster and then calculating all necessary aspects of the chosen members. Because every member in a specific group has similar antenna characteristics, the aspects calculated for the representing member of the group could be extended to assign to all the constitutive group members. Then by using a decision tree model and considering the design goal as the label, the data set is classified. This classification helps to arrive at a comprehensive overview of different aspects and attributes and facilitates decision making for choosing the most appropriate

configuration. This is especially helpful when a large number of clusters are available and prevents from encountering probable errors. This process can be extended through adding more objects to the base structure for achieving the specific structure resulting to the desired properties. Although at each addition phase, the combination of the representatives of the former phase and the newly added object is considered rather than considering all permutations of former objects and the newly added one. In fact, this is the prominent advantage of the proposed procedure because it provides the prospective view into all various configurations of an antenna design with their corresponding results without the need of spending excessive time. In such a case, all cases or the optimum case could be achieved. Another advantage of the proposed procedure is that with only calculating a few numbers of aspects, the whole number of aspects can be calculated.

III. SHORTING POST PATCH ANTENNA, CASE STUDY

In this section, first, an array antenna with a conventional probe-fed microstrip patch unit cell as a basic configuration is designed. The unit cell has a length of $L = 0.29\lambda_0$, width of $W = 0.28\lambda_0$ and a height of $h = 0.06\lambda_0$ with a patch metal of $0.29\lambda_0 \times 0.28\lambda_0$ where λ_0 is the wavelength parameter at 5 GHz and the substrate has a dielectric constant of $\epsilon_r = 2.55$. The active reflection coefficient in the three principal planes for this array is depicted in Figs. 2-4. The simulations have been carried out by HFSS [12] and CST [13] softwares in which a floquet port has been applied to the unit cell structure for $\theta = 0$ and $\phi = 0$. These conditions create an infinite array based on the specified unit cell. As it can be inferred from Figs. 2-4, the array has a scanning range of 70 in the H- and D-planes, whereas in the E-plane, scanning angles up to 60 has been achieved. However, in the three planes the fractional bandwidth remains as low as 4 percent. Now, in order to improve bandwidth and scanning range, simultaneously, the proposed approach is utilizing shorting posts in different positions on the unit cell patch and using data mining method to find the best shorting post configuration. To this end, the patch surface is meshed with the size of shorting post diameter ($0.009\lambda_0$) where each grid indicates a position to reside a shorting post. Obviously, the shorting post position could be set at any point on the metallic patch. In this section, single-, dual- and triple-shorting post configurations are investigated. Figure 5 shows geometrical details of a typical triple-shorting post configuration. The coordinates of the shorting posts are designated as X_i and Y_i (i=1,2 and 3). X_f, Y_f and r_f indicate the position of the probe-feed and its radius, respectively. Also Dx and Dy are the overall dimensions of unit cell. Figure 6 indicates a typical illustration of the meshed surface patch plate, where the filled spots indicate cluster representatives in the single shorting post step.

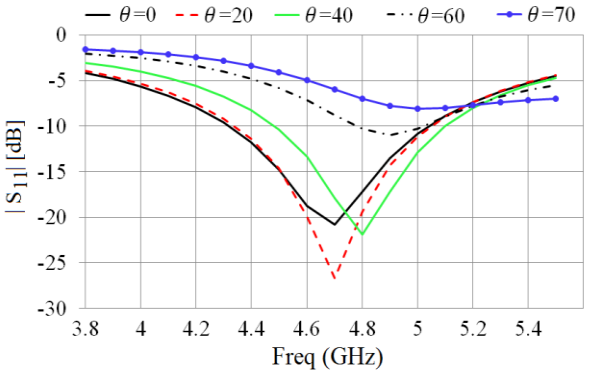

Fig. 2. Reflection coefficients of a conventional probe-fed microstrip patch array for E-plane scan ($\epsilon_r = 2.55$, $h = 0.06\lambda_0$, $W = 0.28\lambda_0$, $L = 0.29\lambda_0$, $X_f = 0.081\lambda_0$, $Y_f = 0$, $r_f = 0.009\lambda_0$, $D_x = D_y = 0.5\lambda_0$).

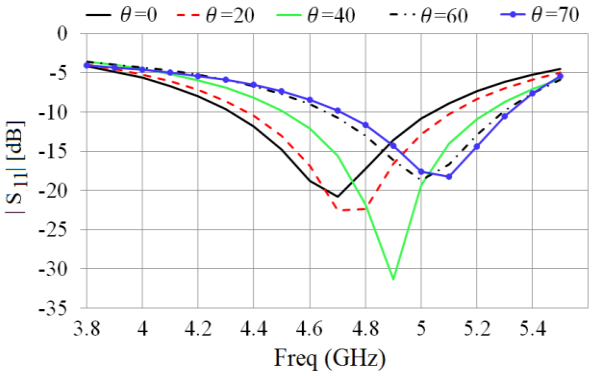

Fig. 3. Reflection coefficients of a conventional probe-fed microstrip patch array for H-plane scan (parameters, as in Fig. 2).

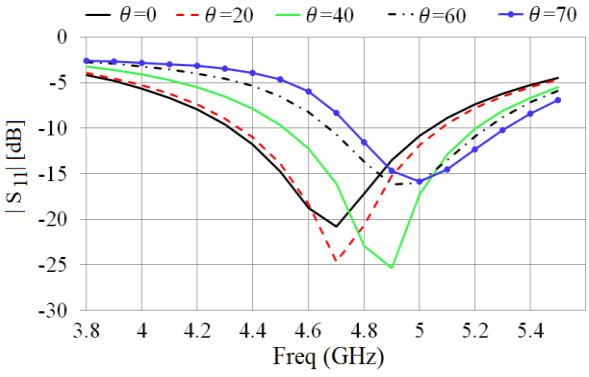

Fig. 4. Reflection coefficients of a conventional probe-fed microstrip patch array for D-plane scan (parameters, as in Fig. 2).

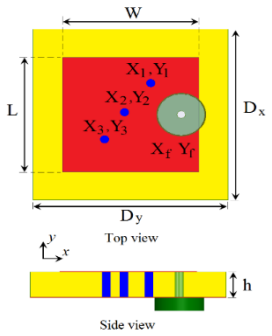

Fig. 5. Top view and side view of triple shorting post.

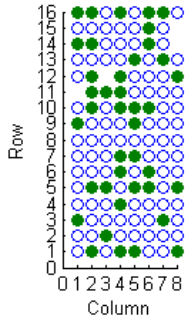

Fig. 6. Meshed surface of a patch element metal plate which the filled spots indicate cluster representative in the single shorting post step.

A. Applying data mining procedure to design patch antenna with shorting posts

Applying the data-mining procedure to a probe-fed microstrip patch antenna with shorting posts, starts with gathering a table of reflection coefficient values for all possible single shorting post configuration cases. Next, based on the X-means clustering method [14], single shorting post configurations which have a similar reflection coefficient curve are categorized in various groups which are named clusters. To achieve a more precise clustering, simulation results which are too different from others are left out from the clustering procedure by using outlier analysis introduced in [15]. Each of these out-left simulations are considered as a single member cluster because their combination with other clusters in proceeding steps may have good characteristics. The number of these clusters is determined by cluster evaluation algorithms which in this work the SSE method has been used and its result is shown in Fig. 7. All members of a single cluster would have similar antenna characteristics including bandwidth and scanning range in the E, H and D-planes (ϕ=45°). A specific member is chosen from each cluster which would represent its cluster. In the third step, the dual shorting post configuration should be determined, that is a composition of two single shorting post configurations. Therefore, instead of considering all two possible combinations of single shorting post configurations, the possible mixture of the cluster which represents the single post configuration, is considered. The reason for this proposition is that the results from the representative combinations will be similar to that of the corresponding cluster group members' combination. The outcome of the representative combination would be clustered again and for each one of them too, a representative would be chosen. In a similar manner, for achieving various cases of triple shorting post configuration, combinations of dual and single shorting post structures representatives are combined together. This procedure could be continued for any multiple shorting post configurations. After the stage of clustering an N-shorting posted configuration, the representative members of that configuration are simulated and their characteristics are extracted and exported into a data set table.

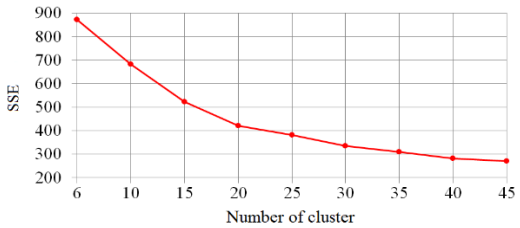

Fig. 7. Find number of cluster in two post using SSE.

As mentioned in the previous section, different single shorting post positions individually are simulated. In our simulations, we have considered that the probe feed is placed at the center line of the patch. Also, the shorting post is only placed on one half side of the patch surface which is determined by the patch center line. The obtained parameters from simulations are exported in a data set table. An inappropriate selection of parameters for exportation would result in a wrong clustering result. The parameters which are selected as the data set attributes must have a reasonable relation with the design goal. In this work, the parameters considered as attribute in the data set table are the coordinates of the shorting post and the reflection coefficient over the sufficient frequency band. The data set is clustered and the representatives of each cluster are shown as filled circles in Fig. 6. The representative cases are further simulated in E-, H- and D-plane with different scan angles. Once again the simulation results for the representative cases are exported as another table and by using the decision tree method and considering bandwidth as a label this table are classified. The classified results are shown in Fig. 8. For the problem addressed in this paper, 25 base structures were categorized in one post configuration and 37 base structures were categorized in two post configuration. It should be pointed out that it is possible that some post could be repeated in several branches of the decision tree.

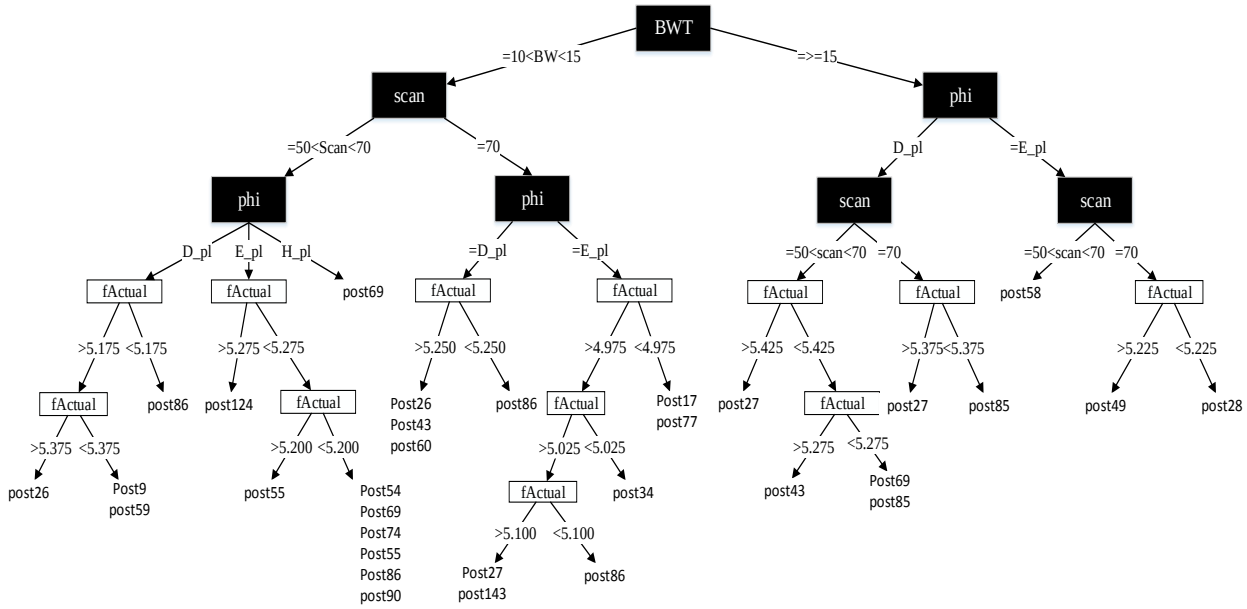

Fig. 8. Decision tree for one post.

B. Wide band and wide scanning element

As we can see in Figs. 9-11, by placing a shorting post on the specific and optimized point, the scanning angle is increased of about 60 degrees in the E and H-plane while the bandwidth is kept about 20 percent. Then with the increasing of posts to two posts, the scanning angle of 70 degrees and a bandwidth of 15% in the E and H-plane is achieved. It is observable in Figs. 12-14 as expected, a bit of bandwidth has been lost. However, the scanning angle has been increased about 10 degrees relative to the previous stage. At the final step, after a large number of simulations using data mining, the number of posts is increased to three posts and the results are depicted in Figs. 15-17. It can be seen that the bandwidth and scanning angle have improved slightly compared to the results of two posts. This process can be continued to N posts but three posts has been considered sufficient in this work, since the results of three posts were not significantly better than two posts.

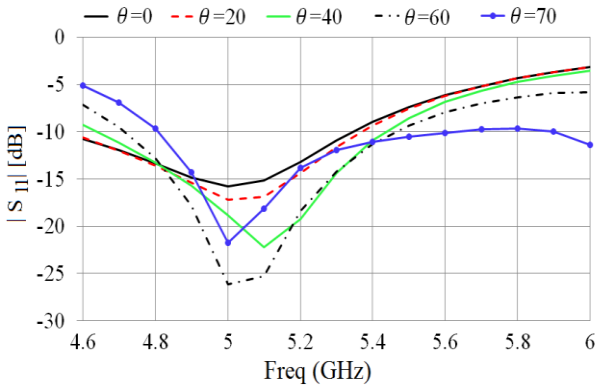

Fig. 9. Active reflection coefficient for single shorting post patch configuration in the E-plane ($\epsilon_r = 2.55$, $h = 0.06\lambda_0$, $W = 0.28\lambda_0$, $L=0.29\lambda_0$, $X_f = 0.081\lambda_0$, $Y_f = 0$, $X_1 = -0.06\lambda_0$, $Y_1 = 0.43\lambda_0$, $r_f=r_1=0.009\lambda_0$, $D_x=D_y=0.5\lambda_0$).

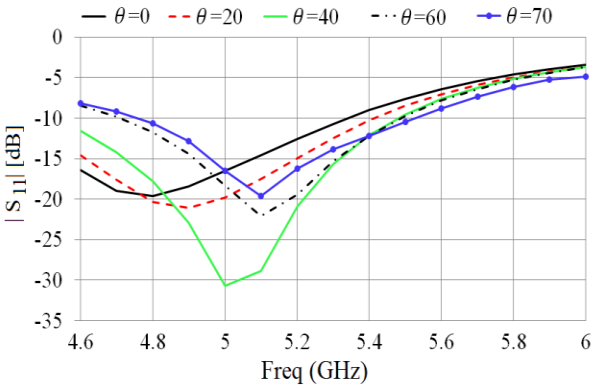

Fig. 10. Active reflection coefficient for single shorting post patch configuration in the H-plane ($X_1 = -0.095\lambda_0$, $Y_1 = 0.007\lambda_0$, the rest of the parameters are as in Fig. 9).

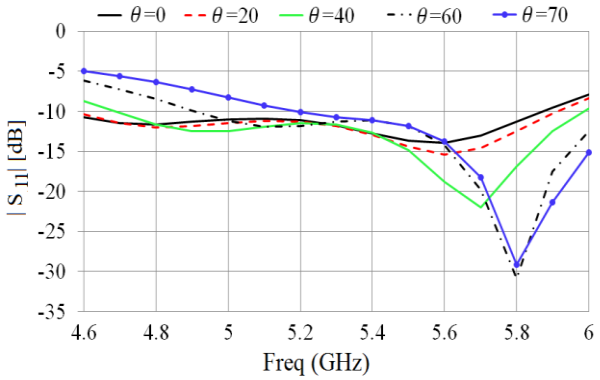

Fig. 11. Active reflection coefficient for single shorting post patch configuration in the D-plane ($X_1 = -0.113\lambda_0$, $Y_1 = 0.43\lambda_0$, the rest of the parameters are as in Fig. 9).

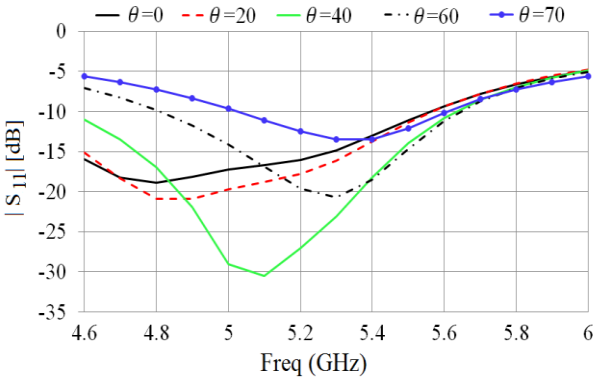

Fig. 14. Active reflection coefficient for double shorting posts patch configuration in the D-plane (parameters, as in Fig. 13).

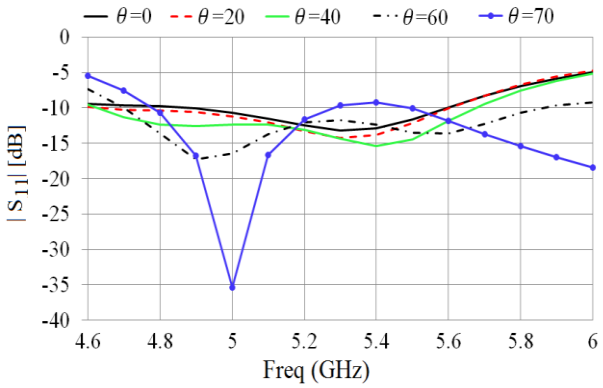

Fig. 12. Active reflection coefficient for double shorting post patch configuration in the E-plane ($\epsilon_r = 2.55$, $h = 0.06\lambda_0$, $W = 0.28\lambda_0$, $L = 0.29\lambda_0$, $X_f = 0.081\lambda_0$, $Y_f = 0$, $X_1 = -0.077\lambda_0$, $Y_1 = 0.06\lambda_0$, $X_2 = -0.023\lambda_0$, $Y_2 = 0.08\lambda_0$, $r_f = r_1 = r_2 = 0.009\lambda_0$, $D_x = D_y = 0.5\lambda_0$).

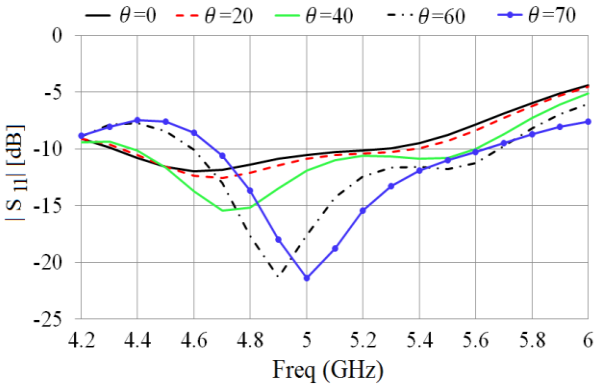

Fig. 15. Active reflection coefficient for triple shorting posts patch configuration in the E-plane ($\epsilon_r = 2.55$, $h = 0.06\lambda_0$, $W = 0.28\lambda_0$, $L = 0.29\lambda_0$, $X_f = 0.081\lambda_0$, $Y_f = 0$, $X_1 = -0.077\lambda_0$, $Y_1 = 0.043\lambda_0$, $X_2 = 0.041\lambda_0$, $Y_2 = -0.046\lambda_0$, $X_3 = -0.005\lambda_0$, $Y_3 = -0.01$, $r_f = r_1 = r_3 = 0.009\lambda_0$, $D_x = D_y = 0.5\lambda_0$).

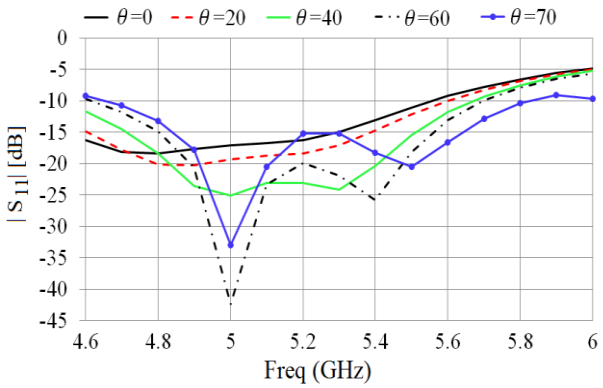

Fig. 13. Active reflection coefficient for double shorting post patch configuration in the H-plane ($X_1 = -0.113\lambda_0$, $Y_1 = 0.025\lambda_0$, $X_2 = -0.023\lambda_0$, $Y_2 = 0.08\lambda_0$, the rest of the parameters are as in Fig. 12).

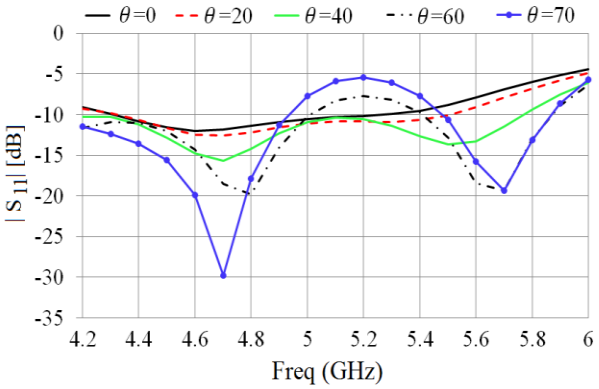

Fig. 16. Active reflection coefficient for triple shorting posts patch configuration in the H-plane (parameters, as in Fig. 15).

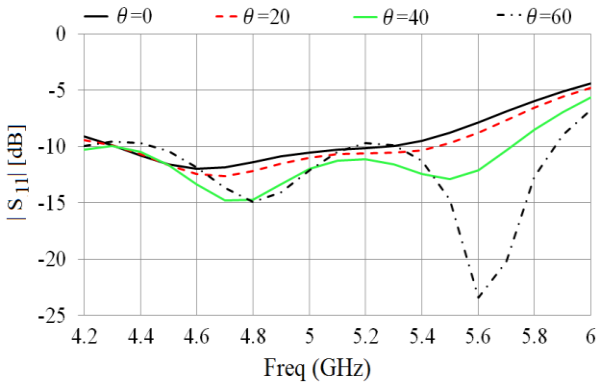

Fig. 17. Active reflection coefficient for triple shorting posts patch configuration in the D-plane (parameters, as in Fig. 15).

Figures 18 to 20 respectively show the reflection coefficients resulted from simulating single-post, dual-post and triple-post configurations in H-plane and E-plane conducted by HFSS and CST simulation softwares. The good agreement between these two simulation software results is an indication of the validity of the design procedure.

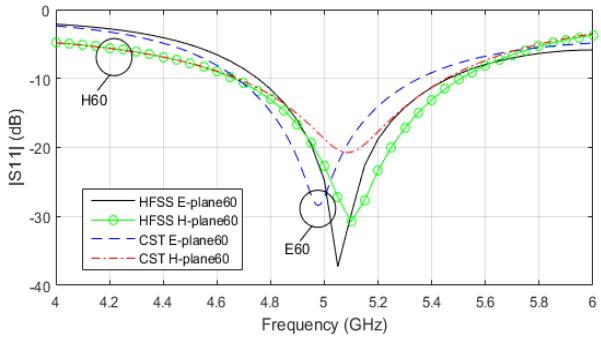

Fig. 18. Active reflection coefficient for single shorting post configuration in 60º E- and H-plane scan. CST Microwave Studio compared with HFSS.

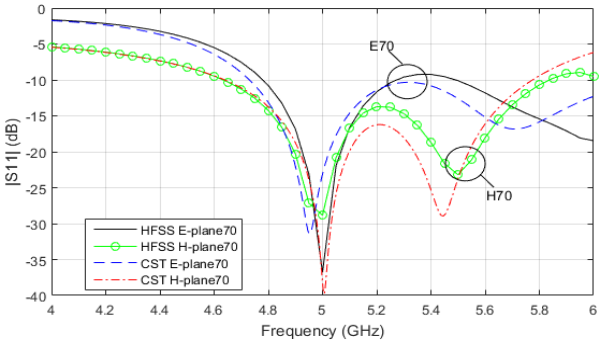

Fig. 19. Active reflection coefficient for double shorting post configuration in 70º E- and H-plane scan. CST Microwave Studio compared with HFSS.

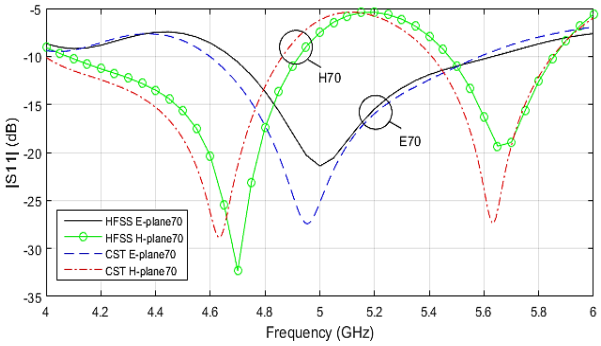

Fig. 20. Active reflection coefficient for triple shorting post configuration in 70º E- and H-plane scan. CST Microwave Studio compared with HFSS.

IV. CONCLUSION

Simulation of two posts and three posts, indicates that with increasing the number of posts positioned at specific points on the substrate, the scanning angle is improved while the bandwidth is slightly decreased. As the matter of fact that the scanning angle and bandwidth are inversely related together, increasing one of them leads to the decrement in the other one. Therefore with applying data-mining techniques on the locations of shorting posts, one can achieve the certain cases that the scanning angle increment has negligible effect on the bandwidth. The proposed method is very convenient and time saving for complex structures which are stemmed from a unique basic structure, and improves the optimization accuracy.

REFERENCES

[1] A. Ellgardt and H. Steyskal, "Antenna elements for wide-angle phased arrays," *Division of Electromagnetic Theory, Royal Institute of Technology*, Tech. Rep., 2005.

[2] B. Thors, H. Steyskal, and H. Holter, "Broad-band fragmented aperture phased array element design using genetic algorithms," *Antennas and Propagation, IEEE Transactions on*, vol. 53, no. 10, pp. 3280-3287, Oct. 2005.

[3] A. Ellgardt and A. Wikström, "A single polarized triangular grid tapered-slot array antenna," *IEEE Transaction on Antennas and Propagation*, vol. 57, no. 9, Sept. 2009.

[4] L.-G. Huss, R. Gunnarsson, P. Andersson, and R. Erickson, "Wideband, wide angle scan, microstrip array antenna element," *European Microwave Conf.*, Paris, Oct. 2005.

[5] C.-C. Liu, A. Hessel, and J. Shmoys, "Performance of probe-fed microstrip-patch element phased arrays," *Antennas and Propagation, IEEE Transactions on*, vol. 36, no. 8, pp. 1501-1509, Aug. 1988.

[6] R. B. Waterhouse, "The use of shorting posts to

improve the scanning range of probe fed microstrip patch phased arrays," *IEEE Trans. Antennas Propagat*., vol. 44, pp. 302-309, Mar. 1996.

[7] R. B. Waterhouse and N. V. Shuley, "Scan performance of infinite arrays of microstrip elements loaded with varactor diodes," *IEEE Trans. Antennas Propagat*., vol. 41, pp. 1273-1280, Sept. 1993.

[8] S. Chattopadhyay, "Rectangular microstrip patch on a composite dielectric substrate for high-gain wide-beam radiation patterns, antennas and propagation," *IEEE Trans. Antennas Propagat*., vol. 57, no. 10, pp. 3325-3328, Oct. 2009.

[9] J. Han and M. Kamber, *Data Mining: Concepts and Techniques*, Second Edition, Elsevier Inc., 2006.

[10] D. Zhang and L. Zhou, "Discovering golden nuggets: data mining in financial application," *IEEE Trans. on Systems, Man, and Cybernetics*, vol. 34, no. 4, Nov. 2004.

[11] D. Lian, X. Lida, G. Feng, L. Jun, and Y. Baopin, "A local-density based spatial clustering algorithm with noise," *Inf. Syst*., vol. 32, pp. 978-986, Nov. 2007.

[12] Ansoft High Frequency Structure Simulation (HFSS), ver. 11.1, Ansoft Corporation, 2008.

[13] CST Microwave Studio, ver. 2015, Computer Simulation Technology, 2015.

[14] D. Pelleg and A. Moore, "X-means: extended K-means with efficient fstimation of the number of clusters," *Proc. of the 17th International Conference on Machine Leaning*, pp. 727-734, 2000.

[15] S. Ramaswamy, R. Rastogi, and S. Kyuseok, "Efficient algorithms for mining outliers from large data sets," *Proc. ACM SIGMOD Int., Conf. on Management of Data*, 2000.

Gholamreza Dadashzadeh was born in Urmia, IRAN, in 1964. He received the B.Sc. degree in Communication Engineering from Shiraz University, Shiraz, Iran in 1992 and M.Sc. and Ph.D. degree in Communication Engineering from Tarbiat Modarres University (TMU), Tehran, Iran, in 1996 and 2002, respectively. He is currently an Associate Professor in the Department of Electrical Engineering at Shahed University, Tehran, Iran.

Mohammad Kargar was born in Tehran, Iran, in 1988. He received B.Sc. and M.Sc. degrees in Electrical Engineering from Shahed University, Tehran, Iran, in 2012 and 2014 respectively. He has cooperated with the Antenna Laboratory of Shahed University for two years from 2012 to 2014, as a Laboratory Supervisor. His research interests include phased array antennas, millimeter and sub-millimeter wave structures.

Seyede Yalda Torabi was born in Zanjan, Iran in 1987. She received her B.Sc. degree in Electrical Engineering from Tabriz University, Tabriz, Iran in 2009 and the M.Sc. degree from the Iran University of Science and Technology (IUST), Tehran, Iran in 2012 and is currently working towards the Ph.D. degree in Electrical Engineering at Shahed University, Tehran, Iran. She has completed several projects on electronic and communication circuits. Her research interests are in application of metamaterial for the design of antennas, filters, couplers and waveguides.

Bahman Rahmati received the B.Sc. degree in Communication Engineering from Imam Hosain University, Tehran, Iran, in 2007, and the M.Sc. degree in Communication Engineering from the University of Shahed, Tehran, Iran, in 2009, where he is currently working towards the Ph.D. degree. His main research interests are ultra-wide band antennas, periodic structures, array lens, reflect array antennas, and beam scanning.

A Compact MIMO Ultra-Wide Band Antenna with Low Mutual Coupling

Quoc Dinh Nguyen [1], Trong Trung Le [1], Dinh Thanh Le [1], Xuan Nam Tran [1], and Yoshihide Yamada [2]

[1] Faculty of Radio-Electronics
Le Quy Don Technical University, Ha Noi, Viet Nam

[2] Department of Electronic System Engineering
Malaysia-Japan International Institute of Technology, Kuala Lumpur, Malaysia
dinhnq@mta.edu.vn

Abstract ─ In this paper, a novel compact multiple-input multiple-output (MIMO) antenna with the size of 26 mm × 60 mm × 1.6 mm for ultra-wide band (UWB) applications is proposed. The proposed MIMO antenna consists of two single UWB antennas and a stub placed between the two antennas to reduce the mutual coupling. The proposed antenna achieves the voltage standing wave ratio (VSWR) less than 2 and more than 86% radiation efficiency over the whole band of interest. Performance of the antenna is examined using both simulation and experiment.

Index Terms ─ MIMO antennas, planar antenna, printed antenna, Ultra-Wide Band (UWB), Ultra-Wide Band antenna.

I. INTRODUCTION

Recently, the Ultra-Wide Band (UWB) communications were proposed to achieve high-rate data transmission over the short range. In order to enhance further the transmission rate and increase the coverage, the combination of the UWB communication systems with the Multiple-Input Multiple-Output (MIMO) transmission schemes has gained considerable attention recently. In such combined UWB-MIMO systems, multiple antennas need to be carefully designed to achieve maximum system performance.

A UWB MIMO antenna often consists of multiple radiation elements placed next to each other. Due to space constrain, the distance between radiation elements is often small, leading to considerably large mutual-coupling between them. This coupling phenomenon is considered as a bottleneck in the MIMO UWB systems and should be minimized to improve the stability and radiation efficiency of the whole system. The design of a UWB MIMO antenna is thus not only related to each element but also reduction of mutual coupling between elements. During the last decade, various UWB MIMO antennas constructed from compact UWB antennas with different structures have been proposed.

In [1], Gopikrishna *et al.* proposed a UWB slot antenna on the dielectric plate FR4 with ε_r = 4.4, tanδ = 0.02, and the small size of 30 mm × 13.5 mm × 1.6 mm. Another small UWB slot antenna introduced by Kumar and Gogoi [2] has the size of 14.6 mm × 28.1 mm × 0.8 mm. Both the antenna and the ground plane are made by copper with the thickness of 30 μm on the FR4 with dielectric permittivity ε_r = 4.4 and tangent loss tanδ = 0.02. The antenna can cover the entire spectrum of the UWB band from 2.9 GHz to 11.0 GHz. The antenna designed by Zheng *et al.* [3] has the size of 22 mm × 15 mm × 0.8 mm and ε_r = 2.55, and can work over the frequency range from 3.8 GHz to 11.0 GHz for VSWR < 2.

Recently, some UWB MIMO antennas with two elements using different structures and materials have also been proposed. These MIMO antennas are composed of either identical stepped patch or identical circular-disc monopole elements. Both the planar UWB antennas fed by 50 Ω microstrip line, i.e., stepped patch, and the circular-disc monopole were presented in [4] and [5], respectively. The selection of these antennas to design MIMO antennas can be justified by their good performance, small size and ease of integration. However, these antennas have been redesigned to adapt the changes in substrate and thereafter optimized to reduce their dimension as compared with those presented in [4] and [5].

In [6], Najam *et al.* proposed a MIMO antenna composed of two rounded antennas with radius R = 12 mm and dimension of 40 mm × 68 mm × 1.6 mm on FR4 dielectric substrate. In a different work [7], Cheng *et al.* proposed a MIMO antenna which has dimension of 62 mm × 55 mm × 1 mm on dielectrics with ε_r = 2.65 and tanδ = 0.001. In another design given in [8], Li *et al*. proposed a similar MIMO antenna on dielectrics with ε_r=2.65 but slightly different dimension of

Submitted On: October 5, 2015
Accepted On: February 25, 2016

70 mm × 62 mm × 1 mm and tanδ = 0.002. Although these antennas were shown to have good performance, their dimension is still relatively large which may prevent them from being implemented in small devices. Moreover, mutual coupling was not considered in their designs, which may result in degraded performance.

In this paper, a compact MIMO UWB antenna with thin structure, suitable for general structure of UWB equipment, is proposed. The structure of the antenna elements is fabricated on the FR4 substrate with dielectric permittivity ε_r = 4.4 and loss tangent tanδ = 0.02. As a general design rule, we first calculate and tune the parameters of the antenna elements, set suitable distance between them and select suitable size of the dielectric substrate to achieve the desired voltage standing wave ratio (VSWR ≤ 2), omni-directional pattern and antenna gain. In order to minimize the mutual coupling between antennas, a stub is placed between two elements in the MIMO antenna. The prototype was then fabricated and its characteristics were measured and compared with simulation results.

II. DESIGN OF UWB MIMO ANTENNA

A. Antenna structure

The configuration of the proposed UWB MIMO antenna is shown in Fig. 1. It is developed from the slot format UWB antenna in [9].

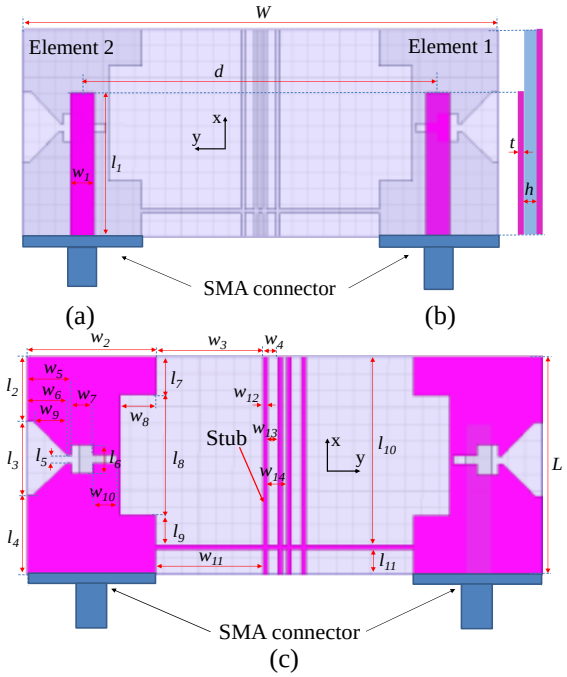

Fig. 1. Configuration of MIMO antenna: (a) top view, (b) side view, and (c) bottom view.

The original antenna has the size of 15 mm × 26 mm ×1.6 mm and consists of a feed line of size l_1 = 18 mm, w_1 = 3 mm. Its rear is a gouged ground plane in order to reduce the antenna size and create multiple resonances to expand the operating bandwidth. The UWB MIMO antenna is built by placing two single antennas at a distance of $d = 0.45\lambda_{max}$ = 45 mm with $\lambda_{max} = c/f_{min}$ and f_{min} is the minimum operating frequency. In order to reduce the small degree of interoperability between the elements of the antenna, a copper stub having an appropriate shape and size is placed in the middle of the two elements. This stub acts as a filter to prevent a certain range of mutual influence between the two elements in the MIMO antenna. The size of the elements in the MIMO antenna is adjusted slightly comapred to [9]. In the MIMO antenna structure, each single antenna still has the size of 15 mm × 26 mm × 1.6 mm but different dimensional parameters of slots. The final design of the UWB MIMO antenna has the size of L = 26 mm, W = 60 mm, and other geometrical parameters as summarized in Table 1.

Table 1: The optimal geometrical parameters (mm)

Parameter	Value	Parameter	Value	Parameter	Value
L	26	l_7	4.6	w_6	4.5
W	60	l_8	14.4	w_7	2.5
t	0.035	l_9	3.5	w_8	4.2
h	1.6	l_{10}	22.5	w_9	3.8
l_1	18	l_{11}	3	w_{10}	3.1
l_2	7.8	w_1	3	w_{11}	12.5
l_3	8.8	w_2	15	w_{12}	0.5
l_4	9.4	w_3	12.5	w_{13}	1.25
l_5	1	w_4	1.75	w_{14}	2
l_6	3.6	w_5	5	d	45

B. Performance evaluation

The Ansoft HFSS software with the finite element method was used to investigate antenna dimensions in order to find the optimal structure for the antenna. Simulations were performed under the condition that both the elements in the MIMO antenna can work concurrently.

The first investigated parameter is the VSWR of the MIMO antenna. In order to reduce the mutual coupling between the two antennas, a copper stub is placed on the plane of the MIMO antenna to separate its two elements. The simulated VSWR of the MIMO UWB antenna with and without stub is shown in Fig. 2. As can be seen from the figure, in case of using the stub the VSWR is smaller than that of the case without stub. The recorded VSWR is less than 2 in the whole frequency range for both antenna elements. In the case without stub, when one antenna is excited it will induce the other causing considerable mutual coupling between the two elements due to limited spacing. When the stub is present, the excited antenna will induce the stub before the other antenna, which reduces induction from

one to the other. As a result, the mutual coupling between the two antennas is diminished. However, the induced current on the stub will create a secondary electromagnetic field which in turn will affect both the antenna elements. This will influence not only the mutual coupling between the two antennas but also their VSWR.

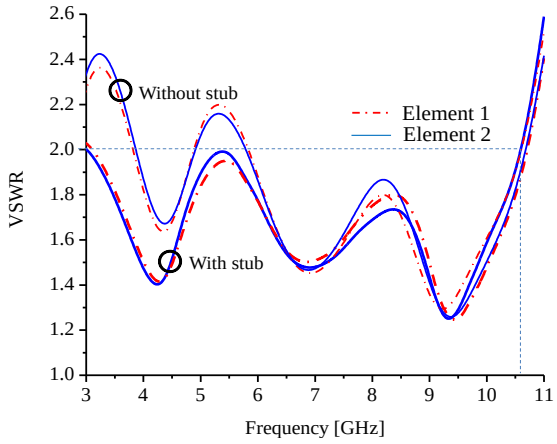

Fig. 2. Simulated VSWR of antenna elements.

The correlation coefficient between two antennas can be determined via *S*-parameters using the following equation [10]:

$$r_e = |r_{12}| = \frac{\left|S_{11}^* S_{12} + S_{21}^* S_{22}\right|^2}{\left(\sqrt{1-|S_{11}|^2-|S_{21}|^2}\right)\left(\sqrt{1-|S_{22}|^2-|S_{12}|^2}\right)}. \quad (1)$$

In order to ensure that the MIMO antenna can work properly when VSWR is less than 2 (equivalent to the return loss ratios S_{11} and S_{22} are less than 10 dB) it is required that ρ_e < 0.5 [11], which is equivalent to the fact that S_{12} and S_{21} are less than -15 dB.

Figure 3 shows the simulated parameters S_{12} and S_{21} of the MIMO antenna for the case with and without the stub. It can be seen from the figure that the two parameters decrease significantly as the frequency increases. For the case with the stub the two parameters S_{12} and S_{21} can achieve the target of less than -15 dB over the whole frequency band of interest. Whereas, if the stub is not used the two parameters can not achieve the target for the frequency less than 3.5 GHz.

Using the simulated results and using (1) we can obtain the correlation coefficient ρ_e for the case using the stub as shown in Fig. 4. It can be seen that the correlation coefficient is less than -22 dB over the whole band of interest with the minimum value of -67 dB. This attainable correlation coefficient guarantees the suitability of the antenna for mobile communications with a minimum acceptable correlation coefficient of 0.5. It is also worth noting that the low correlation coefficient will improve the antenna diversity gain.

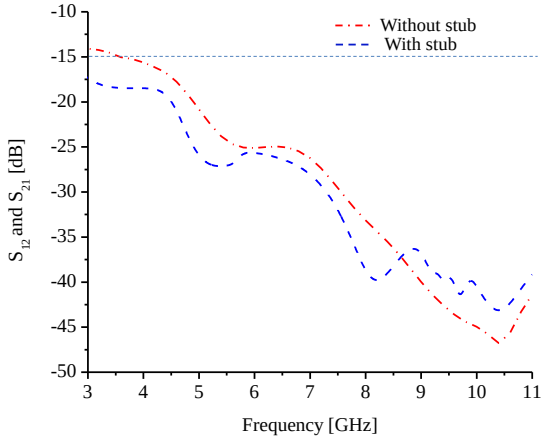

Fig. 3. Simulated parameters S_{12} and S_{21}.

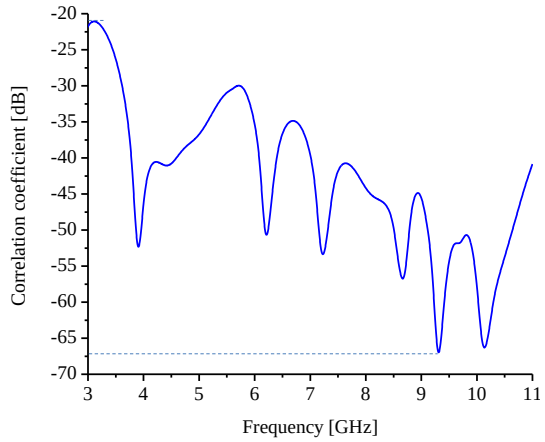

Fig. 4. Simulated antenna envelope correlation coefficient.

To better understand the mutual coupling effect between the two elements in the MIMO antenna, the surface current distribution is plotted in Fig. 5 for the case element 2 is excited while element 1 is not. When the stub is not used it is clear that the current of element 1 significantly induces element 2. However, when the stub is used the current of element 1 will induce mainly on the stub leading to reduced induced current on element 2.

From the above observations, it is clear that the use of the stub can reduce mutual coupling effect between two elements in the proposed MIMO antenna.

Next we will investigate other antenna characteristics. Figure 6 shows the radiation patterns of the proposed antenna when one element is fed while the other is matched by a 50 Ω load impedance. The radiation patterns of the antenna are simulated at the frequencies of 3.1 GHz, 5.0 GHz, 7.0 GHz, 9.0 GHz and 10.6 GHz. In the figure, the dashed-dotted lines denote the radiation patterns in the xz plane while the short dashed line in the

yz plane for the case element 1 is excited while element 2 is not (case 1). The patterns for the case element 2 is excited while antenna 1 is not identical to the case 1 but symmetric about the x axis. To simplify the presentation, these patterns are omitted in the figure. The solid lines denote the radiation patterns in the zx plane while the dashed lines in the yz plane for the case both the elements are excited (case 2). It can be seen from the figure that in the yz plane, the radiation patterns of the two elements are different but most of them are axially symmetric. Also, the radiation pattern of each element is almost omni-directional, particularly in the yz plane for the whole band of interest.

Figure 7 depicts the peak gain of the MIMO antenna within the investigated frequency range (case 2). It is apparent that although the antenna peak gain varies with frequencies, it is still higher than 3.1 dBi within the frequency band of interest. The antenna gain achieves its peak value of 5.4 dBi at the frequency of 10.0 GHz.

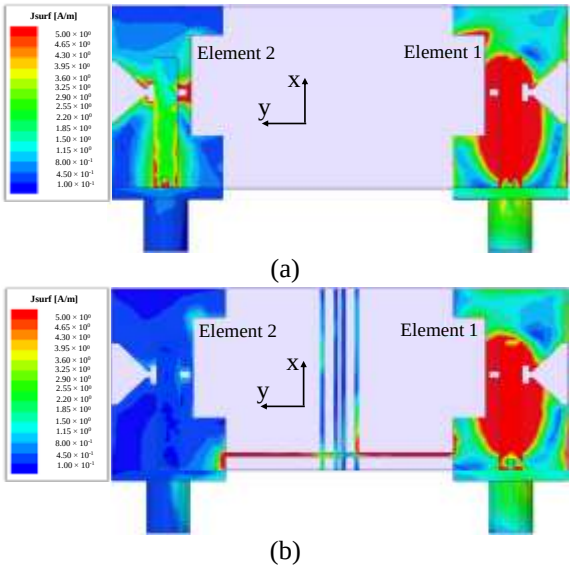

Fig. 5. Suface current distribution at 3.5 GHz: (a) without the stub and (b) with the stub.

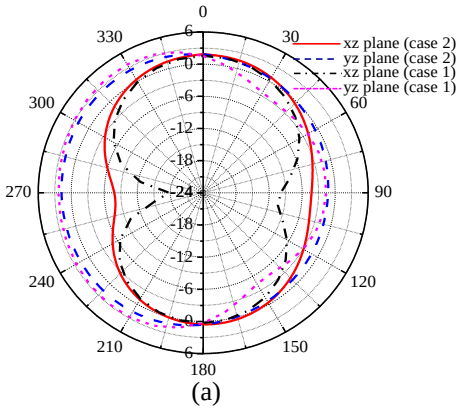

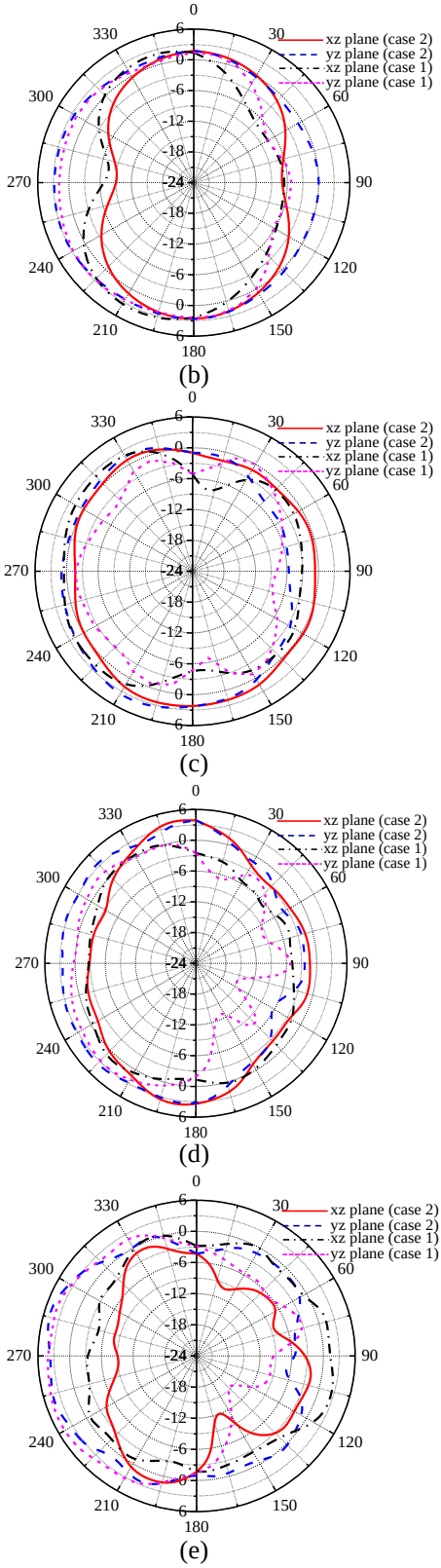

Fig. 6. Radiation patterns of the proposed antenna: (a) 3.1 GHz, (b) 5.0 GHz, (c) 7.0 GHz, (d) 9.0 GHz, and (e) 10.6 GHz.

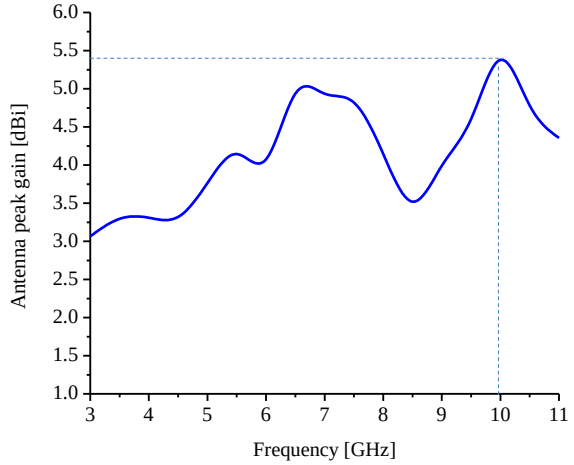

Fig. 7. Antenna peak gain versus frequency.

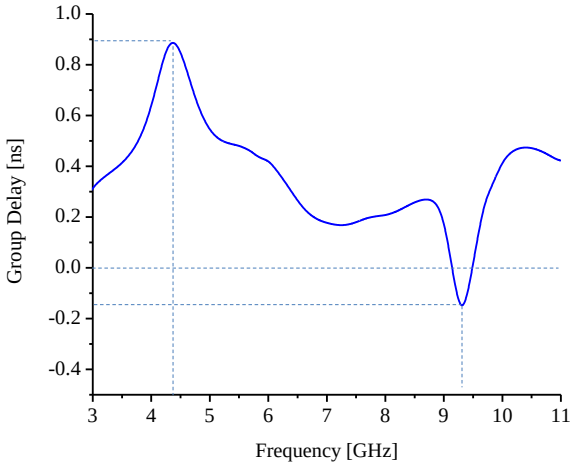

Fig. 8. Simulated group delay.

The group delay of the proposed MIMO antenna is shown in Fig. 8. It can be seen from the figure that the variation of the group delay is less than 1ns, which exhibits good phase linearity within the band of interest. This good group delay characteristic guarantees the suitability of the antenna for UWB applications.

The simulated radiation efficiency is shown in Fig. 9. It can be seen clearly from the figure that the proposed antenna achieves more than 86% efficiency over the band of interest with the maximum value of 96% at 7.25 GHz.

Next, we evaluate the Total Active Reflection Coefficient (TARC) of the proposed MIMO antenna. As TARC also takes the mutual effects into connsideration, it provides a more meaningful measure of the antenna performance than the reflection coefficient. TARC of a 2×2 MIMO antenna can be directly calculated from the scattering matrix elements as follows [12]:

$$\Gamma_a^{'} = \sqrt{\frac{\left|S_{11} + S_{12}e^{j\theta}\right|^2 + \left|S_{21} + S_{22}e^{j\theta}\right|^2}{2}}, \qquad (2)$$

where θ represents the random phase. The average TARC with 12 excitation vectors for the MIMO antenna are shown in Fig. 10. As can be seen in the figure, TARC for the case with stub exhibits lower values than for the case without stub at most frequencies.

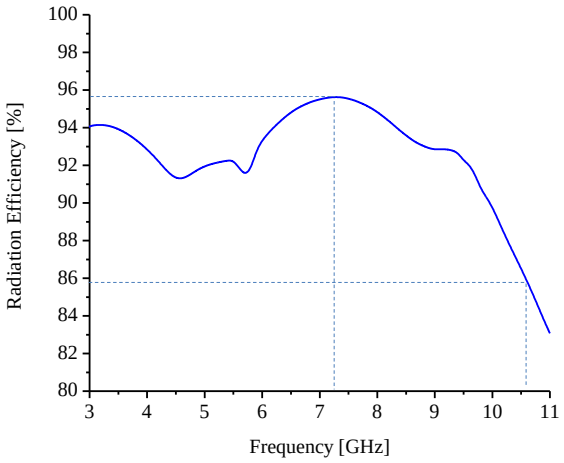

Fig. 9. Simulated radiation efficiency.

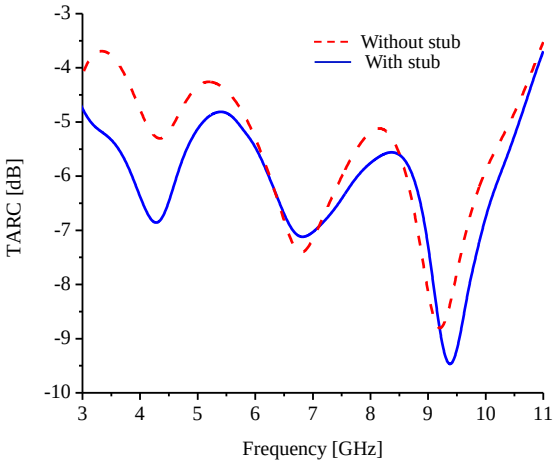

Fig. 10. Calculated TARC for the proposed MIMO antenna.

C. Measured results and discussions

Based on the simulated results, a prototype of the proposed antenna has been fabricated as shown in Fig. 11. The VSWR of the two elements were measured and compared with simulated results in Fig. 12 and Fig. 13. From these figures, it can be seen that both the measured and simulated VSWR are similar. The maximum VSWR recorded for the two antennas are both less than 2, which proves that the proposed

antenna satisfies the requirement of VSWR for a MIMO UWB antenna.

When measuring the mutual coupling effect between the two antennas, we note that since the two antenna elements can be considered as a two-port reciprocal network, the two parameters S_{12} and S_{21} are the same. Therefore, it is enough to investigate one, such as S_{12}, of the two parameters. Figure 14 compares the measured and simulated results of S_{12} (and S_{21}). It can be seen from the figure that both the measured and simulated curves have the similar shape and agree pretty well with each other. Moreover, the maximum measured value of S_{12}, and also S_{21}, is less than -20 dB which is similar to other proposed antennas in [6,13,14,16].

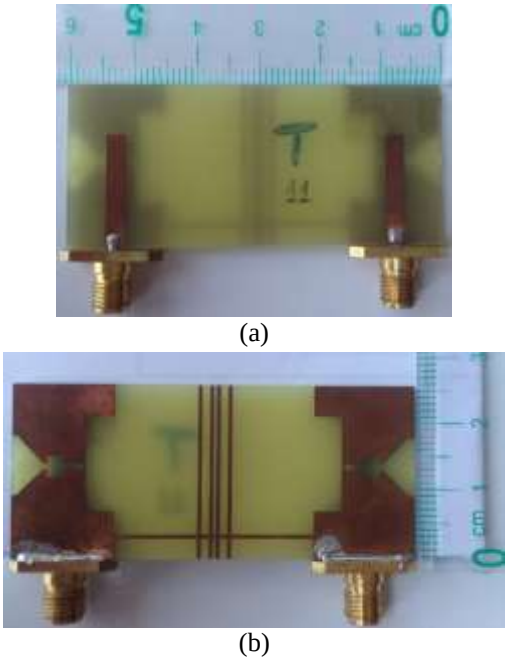

(a)

(b)

Fig. 11. Photograph of the fabricated MIMO antenna: (a) front view and (b) bottom view.

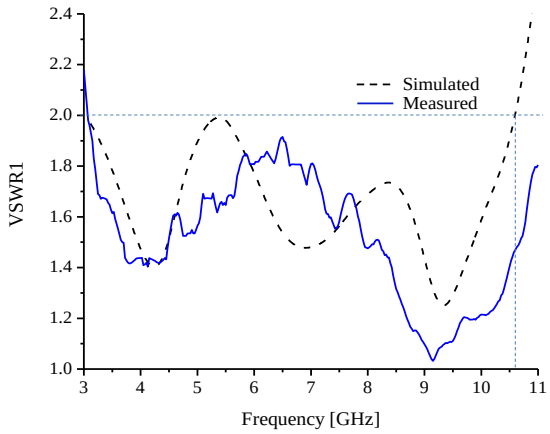

Fig. 12. Measured and simulated VSWR of antenna 1.

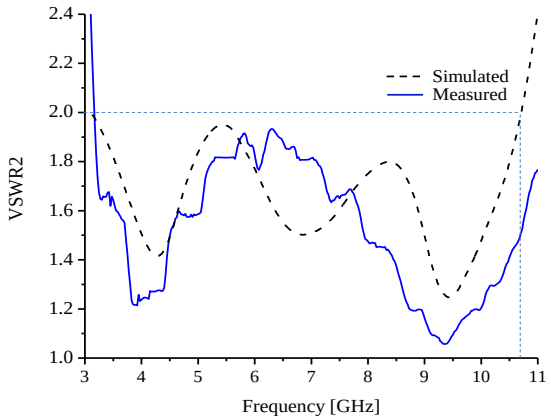

Fig. 13. Measured and simulated VSWR of antenna 2.

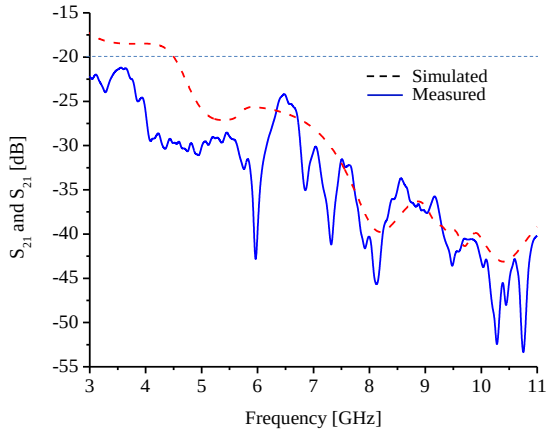

Fig.14. Measured and simulated results of S_{12}.

Table 2 compares our proposed antenna with other relevant UWB MIMO antennas in the literature in terms of antenna size, maximum gain, and parameter S_{12}. Compared with the proposed antennas in [6], [13], [14], [15], [16], our antenna has clearly smaller size while achieving higher maximum gain. In terms of the measured parameter S_{12}, our antenna achieves the same value of less than -20 dB as those in [6], [13], [14], [16] but smaller than that in [15]. This achieved value is far less than the requirement of -15 dB to make our design suitable for a compact and low mutual coupling UWB MIMO antenna.

Table 2: The proposed antenna versus other works

Works	Dimensions (mm)	G_{max} (dBi)	S_{12} (dB)
[6]	40×68×1.6	2.2 dBi	< -20 dB
[13]	43×80×0.8	3.5 dBi	< -20 dB
[14]	30×68×1.6	2.5 dBi	< -20 dB
[15]	38×91	5.3 dBi	< -17 dB
[16]	40×68	2.5 dBi	< -20 dB
Proposed MIMO antenna	26×60×1.6	5.4 dBi	< -20 dB

III. CONCLUSION

In this paper, we have proposed a compact UWB MIMO antenna with low mutual coupling. The antenna structure is simple and easy for fabrication by using printed circuit technology. The proposed antenna has VSWR less than 2 in the whole frequency band of interest from 3.0 GHz to 10.6 GHz, which corresponds to 101.4% of the center frequency. The attainable radiation patterns are almost omni-directional in the whole frequency band. The peak gain achieved by the antenna varies from 3.1 dBi to 5.4 dBi denpending on the frequency with the maximum at 10.0 GHz. The proposed antenna also achieves the maximum radiation efficiency of 96% thanks to the attainable low mutual coupling. The fabricated prototype of the antenna was measured and shown that it meets the requirements for an UWB MIMO antenna.

ACKNOWLEDGMENT

This research is funded by Vietnam National Foundation for Science and Technology Development (NAFOSTED) under grant number 102.01-2012.19.

REFERENCES

[1] M. Gopikrishna, D. D. Krishna, C. K. Aanandan, P. Mohanan, and K. Vasudevan, "Compact linear tapered slot antenna for UWB applications," *Electronics Letters*, vol. 44, no. 20, pp. 1-2, Sept. 2008.

[2] S. V. Kumar and A. K. Gogoi, "Design of T-shaped slot antenna for UWB communications systems," *Proc. 2011 International Conference on Broadband and Wireless Computing, Communication and Applications*, Barcelona, Spain, pp. 112-115, Oct. 2011.

[3] Z. A. Zheng, Q. X. Chu, and Z. H. Tu, "Compact band-rejected ultrawideband slot antennas inserting with λ/2 and λ/4 resonators," *IEEE Transactions on Antennas and Propagation*, vol. 59, no. 2, pp. 390-397, Feb. 2011.

[4] S. H. Choi, J. K. Park, S. K. Kim, and J. Y. Park, "A new ultrawideband antenna for UWB applications," *Microwave and Optical Technology Letters*, vol. 40, no. 5, pp. 399-401, Mar. 2004.

[5] J. Liang, C. C. Chiau, X. D. Chen, and C. G. Parini "Study of a printed circular disc monopole antenna for UWB systems," *IEEE Transactions on Antennas and Propagation*, vol. 53, no. 11, pp. 3500-3504, Nov. 2005.

[6] A. Najam, Y. Duroc, and S. Tedjni, "UWB-MIMO antenna with novel stub structure," *Progress In Electromagnetics Research C*, vol. 19, pp. 245-257, Feb. 2011.

[7] Y. Cheng, W. J. Lu, and C. H. Cheng, "Printed diversity antenna for ultra-wideband applications," *Proc. 2010 IEEE International Conference on Ultra-Wideband*, Nanjing, China, pp. 1-4, Sept. 2010.

[8] Y. Li, W. X. Li, C. Liu, and T. Jian, "Two UWB-MIMO antennas with high isolation using sleeve coupled stepped impedance resonators," *Proc. 2012 IEEE Asia-Pacific Conference on Antennas and Propagation*, Singapore, pp21-22, Aug. 2012.

[9] L. T. Trung and N. Q. Dinh, "A proposal of a compact ultra-wide band antenna works as a magnetic dipole," *Proc. The 2014 International Conference on Advanced Technologies for Communications*, Ha Noi, Viet Nam, pp. 577-581, Oct. 2014.

[10] I. Salonen and P. Vainikainen, "Estimation of signal correlation in antenna arrays," *Proc. 12th International Symposium on Antennas*, vol. 2, Nice, France, pp. 383-386, Nov. 2002.

[11] S. C. K. Ko and R. D. Murch, "Compact integrated diversity antenna for wireless communications," *IEEE Transaction on Antennas and Propagation*, vol. 49, no. 6, pp. 954-960, June 2001.

[12] S. H. Chae, S. K. Oh, and S. O. Park, "Analysis of mutual coupling, correlations, and TARC in WiBro MIMO array antenna," *IEEE Antennas and Wireless Propagation Letters*, vol. 6, pp. 122-125, 2007.

[13] A. I. Najam, Y. Duroc, and S. Tedjini, "Design and analysis of MIMO for UWB communications," *Proc. 4th European Conference Antennas and Propagation*, Barcelona, Spain, pp. 134-138, Apr. 2010.

[14] A. I. Najam, Y. Duroc, and S. Tedjini, "A novel collocated antennas system for UWB-MIMO applications," *Proc. IEEE Radio and Wireless Symposium*, San Diego, USA, pp. 368-371, Jan. 2009.

[15] M. Jusoh, M. F. Jamlos, M. R. Kamarudin, and F. Malek, "A MIMO antenna design challenges for UWB application," *Progress In Electromagnetics Research B*, vol. 36, pp. 357-371, 2012.

[16] A. Najam, Y. Duroc, and S. Tedjni, "UWB-MIMO antenna with novel stub structure," *Progress In Electromagnetics Research C*, vol. 19, pp. 245-257, 2011.

Nguyen Quoc Dinh received the B.E., M.E. and D.E. degrees in Department of Electrical & Electronic Engineering, National Defense Academy, Yokosuka, Japan, in 2006, 2008, and 2011, respectively. Since 2011, he has been a Research Associate at the Department of Fundamentals of Radio and Electronic Engineering, Le Quy Don Technical University, Hanoi, Vietnam.

His research interests include very small antennas, array antennas, UWB antennas, and MIMO antennas. He is a member of the Institute of Electronics, Information and Communication Engineers (IEICE), Japan. He was the recipient of the Young Scientist Award of the IEICE Antennas and Propagation Society Japan Chapter, Japan (2011).

Le Trong Trung received the B.E., the M.E. degrees in Electronic Engineering from Le Quy Don Technical University, Ha Noi-City, Viet Nam, in 2006, 2011. He is currently pursuing the Ph.D. degree in Electronic Engineering at Department of Fundamental of Radio and Electronic Engineering, Le Quy Don Technical University, Ha Noi City, Viet Nam.

His research interests include UWB antennas, MIMO antennas.

Dinh Thanh Le received Ph.D. degree from University of Electro-Communications (UEC), Tokyo, Japan in 2012. From May 2012 to Aug. 2014, he was a Researcher at Electromagnetic Compatibility Laboratory, National Institute of Information and Communications Technology (NICT), Japan. Since Sep. 2014, he is with Le Quy Don Technical University, Hanoi, Vietnam. His research expertise is in the area of applied electromagnetics, including the topics of bio-electromagnetics, SAR measurement techniques, and designs of broadband antennas. Le was the recipient Research Activities Award from the University of Electro-Communications, Tokyo in 2012. He also received Best Paper Award in 2012 TriSAI Conference, Young Scientist Excellent Paper Award in the 2012 Pan-Pacific EMC Joint Meeting (PPEMC'12) organized by EMCJ, Japan, and Student Paper Competition Honorable Mention in IEEE 2011 AP-S Symposium and USNC/URSI Meeting held in Washington, US. His paper in the EuCAP2015 conference was one of the finalists for Best Measurement Paper Award.

Xuan Nam Tran is currently an Associate Professor at Department of Communications Engineering, Le Quy Don Technical University Vietnam. He received his Master of Engineering (ME) in Tele-communications Engineering from University of Technology Sydney, Australia in 1998, and Doctor of Engineering in Electronic Engineering from The University of Electro-Communications, Japan in 2003. From November 2003 to March 2006 he was a Research Associate at the Information and Communication Systems Group, Department of Information and Communication Engineering, The University of Electro-Communications, Tokyo, Japan. Tran's research interests are in the areas of adaptive antennas, space- time processing, space-time coding, MIMO and cooperative communications. Tran is a recipient of the 2003 IEEE AP-S Japan Chapter Young Engineer Award, and a co-recipient of two best papers from The 2012 International Conference on Advanced Technologies for Communications and the 2014 National Conference on Electronics, Communications and Information Technology. He is a Member of IEEE, IEICE and the Radio-Electronics Association of Vietnam (REV).

Yoshihide Yamada received the B.E. and M.E. degrees on Electronics from Nagoya Institute of Technology, Nagoya, Japan in 1971 and 1973, respectively. And he received the D.E. degree on Electrical Engineering from Tokyo Institute of Technology, Tokyo, Japan in 1989. In 1973, he joined the Electrical Communication Laboratories of Nippon Telegraph and Telephone Corporation (NTT). Till 1984, he was engaged in research and development of reflector antennas for terrestrial and satellite communications. From 1985, he engaged in R&D of base station antennas for mobile radio systems. In 1993, he moved to NTT Mobile Communications Network Inc. (NTT DoCoMo). In 1995, he was temporarily transferred to YRP Mobile Telecommunications Key Technology Research Laboratories Co., Ltd. At the same time, he was a Guest Professor of the Cooperative Research Center of Niigata University, and a Lecturer of Science University of Tokyo, both from 1996 to 1997. In 1998, he changed his occupation to a Professor of National Defense Academy, Kanagawa, Japan. In 2014, he has started working as a Professor at Malaysia-Japan International Institute of Technology, Universiti Teknologi Malaysia, Kuala Lumpur, Malaysia. He received the Best Paper Award and the Best Tutorial Paper Award from IEICE in 2013 and 2014,

respectively. Now, he is interested in very small antennas, array antennas, aperture antennas and electromagnetic simulation of RCS. He is a Fellow Member of the IEICE and is a Senior Member of IEEE AP Society. He is also a Member of the ACES.

The Sinusoidal Ground Electrode: Theory and Case Study Results

António M. R. Martins [1,2], Sílvio J. P. S. Mariano [2,3], Maria R. A. Calado [2,3], and José A. M. Felippe de Souza [3]

[1] Department of Computer Science
Polytechnic Institute, Guarda, 6300-559, Portugal
amrmartins@ipg.pt

[2] IT–Instituto de Telecomunicações, Branch Covilhã
[3] Department of Electromechanical Engineering
University of Beira Interior, Covilhã, 6201-001, Portugal
sm@ubi.pt, rc@ubi.pt, felippe@ubi.pt

Abstract ─ This paper presents the analytical analysis of the sinusoidal ground electrode commonly used in Portugal by the Portuguese Electric Company. This electrode is easy to install, particularly for two layer soils with rocky bottom layer, and costs much less than it does a strip conductor. Both the theoretical results as well as measurements in the field have shown that the empirical model used by the company leads to large errors. Here the authors propose a new procedure to calculate the grounding resistance for this type of electrode using the average resistance between the wire and strip electrodes, which the calculation is well-established. To avoid heavy computation, the authors also propose the use of simple formulas in order to easily compute the strip resistance. The theoretical results and field measurements are compared and show the validity of the procedure being proposed here.

Index Terms ─ Electrical power distribution, ground electrodes, layered soil, matrix method.

I. INTRODUCTION

The calculation of a ground electrode resistance using a two layer soil model is widely found in the literature. Several methods had been used. Salama et al. have developed formulas for grid in two layers soil using the synthetic-asymptote approach [1]. Berberovic et al. explored the Method of Moments in the calculation of ground resistance by using higher order polynomials approximation in the unknown current distribution [2] and with a variation on that, Sharma and De Four used the Galerkin's Moment Method [3]. The Boundary Element Method is another theoretical tool commonly used by authors such as Columinas et al. [4-6] and Adriano et al [7]. These authors transformed the differential equation that governs the physical phenomenon into an equivalent boundary integral equation. On the other hand, Coa used the Matrix/ Integration Method for calculating the mutual resistance between segments in a homogeneous soil one and in a two layer soil [8], and Ma and Dawalibi used an optimized method of images for multilayer soils [9]. The two layer ground model has been used even in the study of the phenomena of ionization [10]. Mombello et al. developed a method for obtaining the optimized two layer soil parameters using the Least Square Method in order to obtain a two layer resistivity soil curve that fits the actual one [11]. Recently Khan presented the effect of low resistance materials filling in an optimized pit surrounding a rod working in a two layer soil [12]. In general these works have used the theory of images, which implies infinite series for the expanded Green function [2]. However, some of these studies do not compare their work neither with experimental data, nor with data from other references. In this paper, the authors analyse the sinusoidal grounding conductor used in Portugal.

The calculations for the diffusion resistance of the sinusoidal electrode were done using the Matrix Method in homogeneous and two layer soil. The field measurements have also been carried out.

The paper is structured as follows. Section II presents the sinusoidal electrode. Section III briefly introduces the theoretical and empirical models for electrodes in homogeneous and two layer soil. Section IV presents the illustrative results. Section V discusses the obtained results and proposes a new procedure for calculating the sinusoidal electrode resistance comparing the results with field measurements. Finally, Section VI concludes the paper.

II. ELECTRODE PRESENTATION

The sinusoidal grounding electrode is commonly used in Portugal by the Portuguese electric company, in

Submitted On: June 29, 2015
Accepted On: January 9, 2016

soils where the bottom layer is rocky and hence, the voltage reflection coefficient is positive. This type of electrode has its relevance for these kind of soils since the second layer is rocky, making difficult, or even impossible, the rod burying which is the solution adopted in alluvial soils. Its implementation is accomplished manually by the profile of a cupper conductor with section of 35 mm^2 and sinusoidal shape. Its placement is done in trenches of 3, 6 or 10 m long, 0.6 m wide and a maximum depth of 0.8 m. The wire length varies from 10 to 38 m with a section of 35 mm^2, for ground resistances up to 20 Ω. Figure 1 shows a picture of the installation of a sinusoidal electrode.

Fig. 1. Sinusoidal grounding electrode [13].

In the present work, this type of electrode is modeled as a sinusoid, whose amplitude is 0.25 m, almost half the width of the ditch with three maxima per meter, which is nearly 10 m long for an electrode corresponding to a trench of 3 m long. The wire axis was divided into source points whose abscissas are spaced 0.01 m apart. For each generated point source, there is a point at the conductor's surface which shares the same abscissae and ordinates, but whose quota is greater than the point source quota. The difference between the two quotas is the radius of the conductor. A schematic drawing is presented in Fig. 2. The point sources are in parallel position since the conductor is in the horizontal plane.

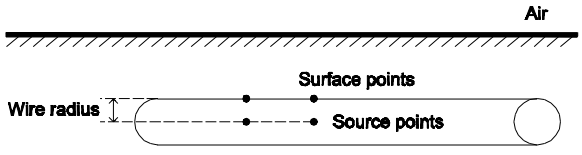

Fig. 2. Source and surface points, for the sinusoidal grounding electrode.

III. THEORETICAL MODEL

A. Homogeneous soil

Fault currents in alternate current power systems, that are harmful to persons and equipment, do not need to be modeled as a time varying phenomenon. Instead, a direct current analysis is sufficient for most applications since the dimensions of a grounding system are much smaller than the penetration depth at industrial frequency as well as for the resistivity of soils commonly encountered [14]. This approach results in a conductive electrostatic model represented by a Laplace equation on the electric potential *v*,

$$\nabla^2 v(x,y,z) = 0. \quad (1)$$

A current source point at P_f injecting an electric current I_f into a homogeneous soil with resistivity ρ Ωm was considered in (1). Its solution is the potential at any point [14] and is given by:

$$v = \frac{\rho I_f}{4\pi}\left(\frac{1}{r} + \frac{1}{r'}\right), \quad (2)$$

where r and r' are the Cartesian distance between the source point and the point where potential is being calculated and the Cartesian distance between point of interest and source point image, respectively. The expression for the potential presented in (2) is the Laplacian solution, considering Dirichlet open boundaries which can be expressed as:

$$v = q_{i,j} I_f, \quad (3)$$

where q_{ij} is a position factor, depending of point *i*, with the potential being calculated from source point *j* and soil resistivity. With *n* source points, the electrode potential surface in each discretized surface point is, by the superposition principle [14]:

$$\begin{bmatrix} V_1 \\ V_2 \\ \vdots \\ V_n \end{bmatrix} = \begin{bmatrix} q_{11} q_{12} \cdots q_{1n} \\ q_{21} q_{22} \cdots q_{2n} \\ \vdots \quad \vdots \quad \dots \quad \vdots \\ q_{n1} q_{n2} \cdots q_{nn} \end{bmatrix} \begin{bmatrix} I_1 \\ I_2 \\ \vdots \\ I_n \end{bmatrix}. \quad (4)$$

As the potential at the electrode surface is constant, a value to it can be arbitrated:

$$V_1 = V_2 = \cdots = V_n = V_{const}. \quad (5)$$

Equations (4) and (5) become a system of *n* equations with the *n* currents points. The total current is the sum of all the source point currents and therefore the resistance of the electrode is found by Ohm's law:

$$R = \frac{V_{const}}{\sum_{k=1}^{n} I_k}. \quad (6)$$

B. Two layer soil

The formulation for a sinusoidal electrode in the upper layer of a two layer soil is almost the same as in the case of homogeneous soil. The sinusoidal electrode axis was discretized again, into source points whose abscissae are spaced 0.01 m apart.

In this case, the expression for the potential is also the Laplacian solution, considering Dirichlet open boundaries. Potential at surface point is given by Equation (3) again, but with a different position factor

which is now expressed in the following manner [16]:

$$q_{ij} = \frac{\rho_2}{4\pi}\{G(x_i - x_j, y_i - y_j, z_i - z_j) - k_{12}\sum_{m=0}^{\infty} K^m G[x_i - x_j, y_i - y_j, z_i + z_j - 2(m-1)D] + \sum_{m=1}^{\infty} K^m G(x_i - x_j, y_i - y_j, z_i - z_j - 2mD) - k_{32}\sum_{m=0}^{\infty} K^m G(x_i - x_j, y_i - y_j, z_i + z_j + 2mD) + \sum_{m=1}^{\infty} K^m G(x_i - x_j, y_i - y_j, z_i - z_j + 2mD)\}. \quad (7)$$

The reflection coefficient of voltage is given by:

$$K = k_{12}k_{32}, \quad (8)$$

where $k_{12} = \frac{\sigma_1 - \sigma_2}{\sigma_1 + \sigma_2}$, $k_{32} = \frac{\sigma_3 - \sigma_2}{\sigma_3 + \sigma_2}$, and σ_1 is the bottom layer conductivity, σ_2 the top layer conductivity, σ_3 the air conductivity, ρ_2 the top layer resistivity, G the Green function, k_{12} the voltage reflection between layers 1 and 2, k_{32} the voltage reflection between layers 2 and air (which is -1), and D the top layer thickness. As in the case of homogeneous soil, for each source point was considered a surface point which quota is a radius higher than the source point quota. With *n* source points, the electrode potential surface, in the each discretized surface point is also given by (4), with the new position factor (7).

C. Empirical model

An empirical model to compute the sinusoidal electrode resistance which has been proposed and adopted by the Portuguese electric company consists of the next simplified scheme [13]:

$$R = \begin{Bmatrix} 0.2\rho \ for\ a\ 3\ m\ trench \\ 0.15\rho \ for\ a\ 6\ m\ trench \\ 0.08\rho \ for\ a\ 10\ m\ trench \end{Bmatrix}. \quad (9)$$

The resistivity used in (9) can be obtained by checking on tables of soil materials, or by an average of a few measurements of the apparent resistivity, using Wenner method.

IV. ILLUSTRATIVE RESULTS

This section presents a comparison between electrode resistances for sinusoidal electrode, strip and wire. Moreover, the average of the theoretical resistance of these two last electrodes is also presented. This comparison is made both for homogeneous and two layer soil considering the top layer with higher or lower resistivity than the bottom layer. In every case a comparison between the obtained solutions with the empirical model is also done. Potentials at surface are also compared in all cases. A comparison for the resistance values obtained with the matrix method and the empirical model will be presented in the next section.

A. Electrode in homogeneous soil

In this case, it was considered a soil with resistivity of 100 Ωm, a sinusoidal electrode buried in a trench with 0.5 m deep and 0.6 m wide. The trench length has been varied from 1 to 10 m. The cable and the sinusoidal electrode have a radius of 3.3 mm. Figure 3 shows the comparing results for a horizontal conductor, a sinusoidal electrode with three maxima per meter, ensuring that the sinusoidal electrode length is accordingly to the trench length as defined by the Portuguese power company, a strip horizontal conductor and for the average resistance between wire and strip. The values of resistance for the horizontal wire and strip were obtained by using Dwight's formulas [15]. Note that, the resistance of the sinusoidal electrode is very close to the average resistance of the wire with horizontal strip and a mean error of 4.7%. In the worst case, the referred average is 11.2% higher than the value of the sinusoidal electrode. Furthermore, the resistance of the sinusoidal electrode gets closer to the strip resistance value when the trench length increases.

For illustrative purposes, the surface potential due to the sinusoidal electrode in a 6 m trench, considering an injected current of 100 A, is presented in Fig. 4.

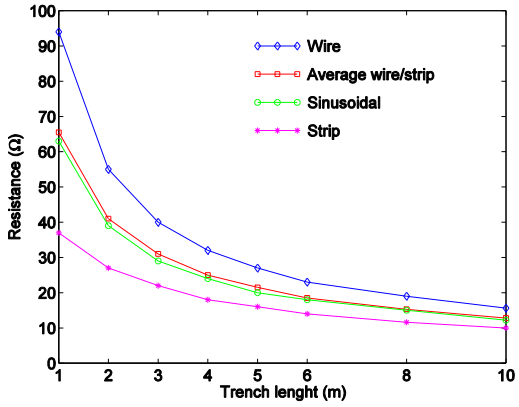

Fig. 3. Comparison between electrodes in homogeneous soil ($K = 0$).

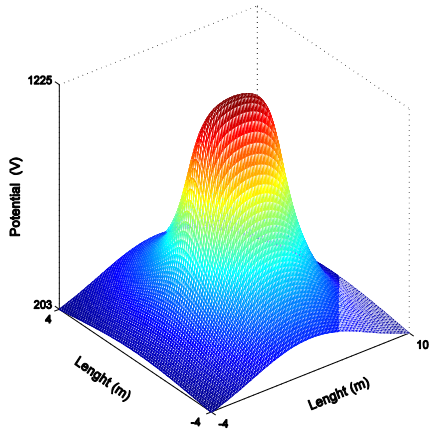

Fig. 4. Surface potential for sinusoidal electrode.

On the other hand, surface potential due to the three types of electrodes, for the same injected current, along axis trench and in a direction perpendicular to the middle

of the trench, is presented in Fig. 5. It can easily be seen that the sinusoidal electrode generates a smaller surface potential than the other electrodes.

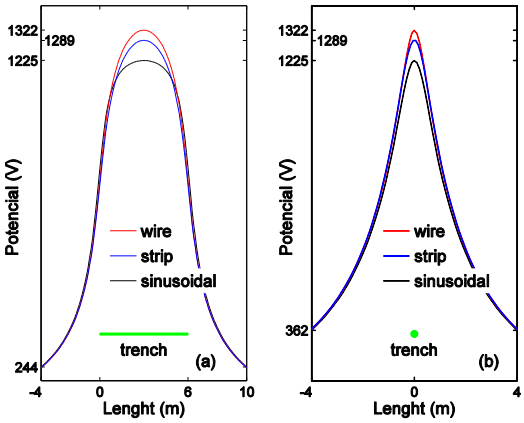

Fig. 5. Surface potential: (a) along axis trench and (b) perpendicular to the middle of the trench.

B. Electrodes in a two layer soil for positive voltage reflection

In this case, it was considered a two layer soil with a positive voltage reflection coefficient. The value of the resistivity of the upper layer, with 1 m thickness, was 100 Ωm and the value of the resistivity of the lower layer was 500 Ωm ($K = 2/3$). For comparison purposes, the buried deep was maintained at 0.5 m.

The resistance of the horizontal wire was calculated by using Tagg's formula [16] and the resistance of the horizontal strip has been calculated by using the moment methods, as shown in the Appendix. The theoretical results for the horizontal conductor, the sinusoidal electrode with three maxima per meter, the strip and for the average resistance between wire and strip are shown in Fig. 6. It can be noticed that the average resistance between strip and wire is very close to the sinusoidal electrode resistance with a 3.4% mean error. In the worst case, the error is 6.5%. Furthermore, as length increases, the resistance of the sinusoidal electrode becomes closer to the strip resistance value.

For illustrative purposes, the surface potential due to the sinusoidal electrode in a 6 m trench, considering an injected current of 100 A, is presented in Fig. 7. Also, surface potential due to the three types of electrodes, for the same injected current, along axis trench as well as in a direction perpendicular to the middle of the trench is shown in Fig. 8. Outside the trench the potentials are almost coincident. The surface voltage perpendicular to the middle of the trench due to the strip electrode is larger, due to a surface leaking current, as expected. The peak voltage produced by the sinusoidal electrode is smaller than those produced by the other electrodes, approximately 5% smaller than the peak produced by the strip electrode.

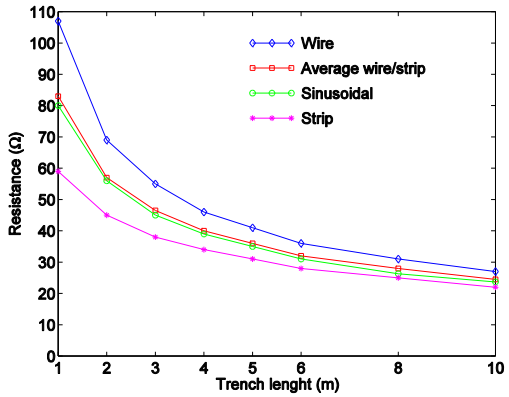

Fig. 6. Comparison between electrodes in a two layer soil ($K = 2/3$).

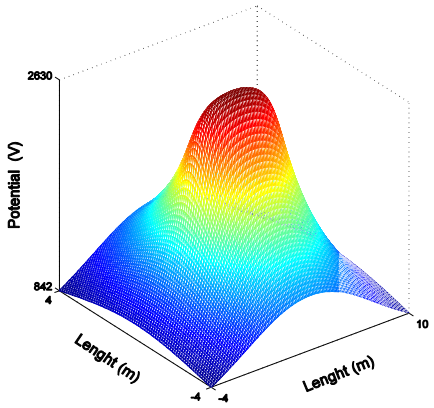

Fig. 7. Surface potential due to sinusoidal electrode.

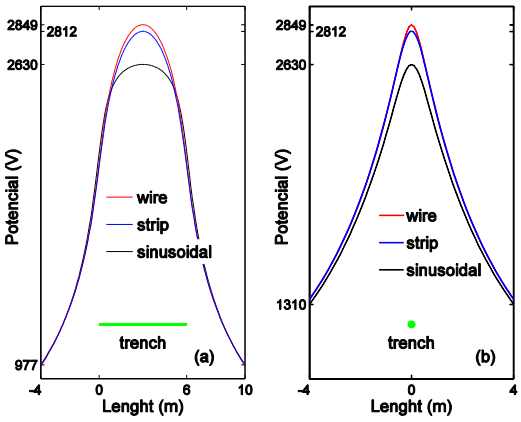

Fig. 8. Surface potential: (a) along axis trench and (b) perpendicular to the middle of the trench.

C. Electrodes in a two layer soil for negative voltage reflection

Switching the values of the layers resistivity

considered in the above subsection, the reflection coefficient of voltage becomes negative ($K = -2/3$). Once more, for comparison purposes, the buried deep is maintained at 0.5 m. Also, in this case, the resistance was computed with the methods brought up in previous subsection for all the electrodes considered.

The theoretical results for the horizontal wire, for the sinusoidal electrode with three maxima per meter, for the strip and for the average resistance between wire and strip are all shown in Fig. 9. Again, the average resistance between strip and wire turn out to be close to the sinusoidal electrode resistance and, as trench length increases, the resistance of the sinusoidal electrode becomes closer to the strip resistance. For small trenches, the average resistance between strip and wire can reach 20% above the resistance of the sinusoidal electrode. The mean error of the average is 18%.

A mention deserves to be done here: the electrode under study is not used in this type of soil since it is extremely easy to bury rods which are the most common electrodes for these soils.

Surface potential due to the sinusoidal electrode in a 6 m trench, considering an injected current of 100 A, is shown in Fig. 10.

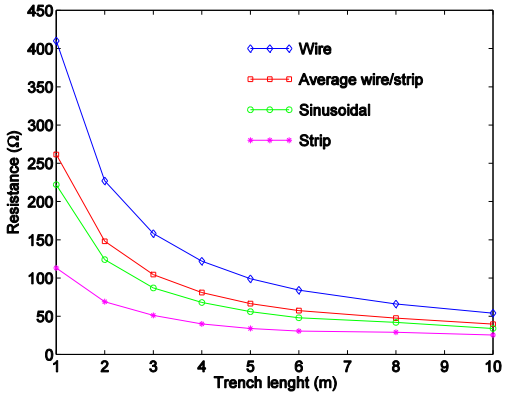

Fig. 9. Comparison between electrodes in a two layer soil ($K = -2/3$).

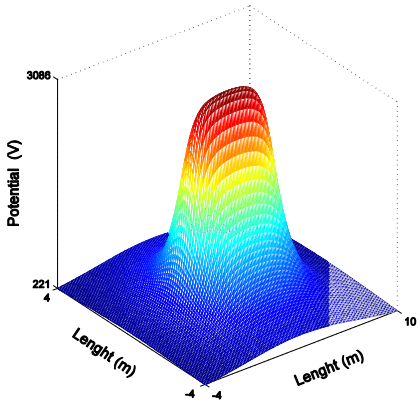

Fig. 10. Surface potential due to sinusoidal electrode.

For the same injected current, surface potential due to the three types of electrodes along axis trench, as well as in a direction perpendicular to the middle of the trench, are both shown in Fig. 11. The potential due to the sinusoidal electrode has the smallest maximum surface voltage, being 5.2% less than for the strip electrode.

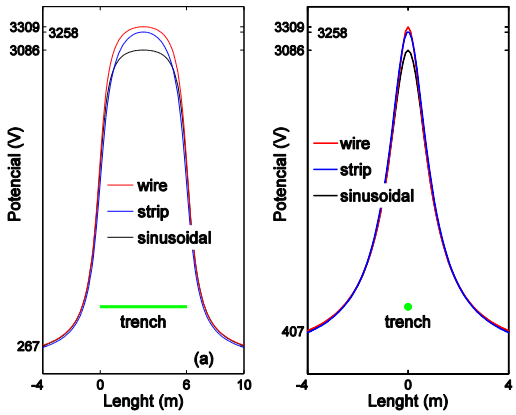

Fig. 11. Surface potential: (a) along axis trench and (b) perpendicular to the middle of the trench.

V. DISCUSSION, PROPOSED APPROACH AND FIELD MEASUREMENTS

A comparison between the resistance values for the sinusoidal electrode obtained by the matrix method and by the empirical model is shown in Fig. 12. In homogeneous soil ($K = 0$) as well as in two layer soil with positive voltage reflection coefficient ($K > 0$), where the bottom layer has higher resistivity, the empirical model produces errors which are significant and values which are smaller than those obtained with the matrix method (not conservative). The sinusoidal electrode is widely used in this type of soil. Only in soils where the bottom layer is less resistive ($K < 0$) than the top layer, due to the water table for instance, the empirical formulas are conservative, but still presenting errors, particularly for 6 and 10 m trench lengths. Note that, relative errors of the empirical model do not necessarily decrease with growing trench length. With respect to the surface potential, the sinusoidal electrode produces a smaller maximum voltage than the remaining electrodes.

Concerning the cost of the sinusoidal electrode, it is about 15% of the cost of the steel sheet commonly used in Portugal. The horizontal cable costs around 3 times less than sinusoidal electrode due to the greater length of the latter. The cost of cable is 6.70 euros per meter, whereas sinusoidal length with 3 maxima per meter stands at 21.90 € per meter of trench. The strip with dimensions of 1x0.5x0.003 m costs roughly 146 €. Considering the comparison between the resistance values of the three types of electrodes and their costs, one

reaches the conclusion that the sinusoidal electrode is an excellent choice.

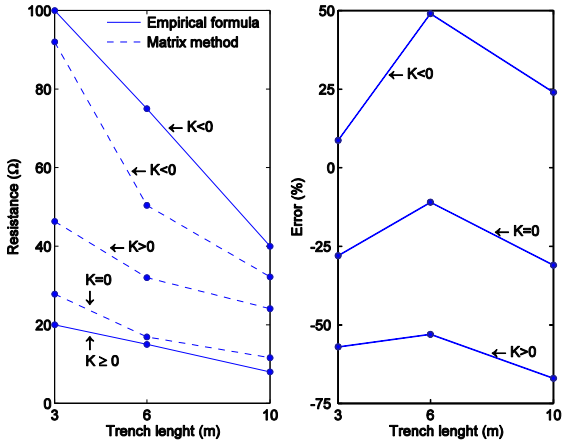

Fig. 12. Calculated values of the sinusoidal electrode grounding resistance with empirical formulas and matrix method and their corresponding errors.

Once the empirical model is not the best choice for computing the sinusoidal electrode resistance, the authors propose a new procedure for that calculation, based on the average resistance between wire and strip, which leads to better results as it has been previously shown. This choice is a good option since the mean error is less than 5% for homogeneous and two layer soil with more resistive bottom. When the bottom layer is the water table, the mean error reaches 18%. These errors are always conservative with respect to the resistance value given by the matrix method, as it can be seen in Fig. 3, Fig. 6 and Fig. 9.

The proposed calculations have been performed accurately and based in widely known numerical methods that demand a computer program with specific software requirements. With the purpose to provide the field engineer with a tool for calculating the strip resistance in a two layer soil, it is proposed the adoption of the simple formula [1]. This formula is used here for computing the strip resistance at small burring depth:

$$R = \rho_2 \left[\frac{1}{\sqrt{2\pi A}} - \frac{\ln\left(\frac{2\rho_2}{\rho_2+\rho_1}\right)}{2\pi(D+h_0)} \right], \qquad (10)$$

where A is the area of the strip and,

$$h_0 = \sqrt{\frac{A}{2\pi}}\ \ln\left(\frac{2\rho_2}{\rho_2+\rho_1}\right)\ \left(\frac{\rho_2}{\rho_2-\rho_1}\right).$$

The proposed procedure to estimate the sinusoidal electrode resistance is: (i) determine the strip resistance by using formula (10); (ii) determine the wire resistance by using the Tagg formula; and (iii) compute the estimated sinusoidal electrode resistance as being equal to the average of the values obtained in previous steps.

Now considering the most important case, in which the bottom layer is more resistive (such as for example a rocky layer), the average between the strip resistance, calculated by using (10), and horizontal wire resistance is presented in Fig. 13. The results then obtained are a conservative approach to the sinusoidal electrode with a maximum relative error of 27%, 22% and 19%, respectively for a 10 m, 6 m and 3 m trenches.

This simple formula and the proposed procedure to use the average value between strip and wire is a much better approach than expressions which are given by the empirical model, whose errors, in spite of not being conservative, are also of -67%, -53% and -57%, respectively for a 10 m, 6 m and 3 m trenches, as can be seen in Fig. 12.

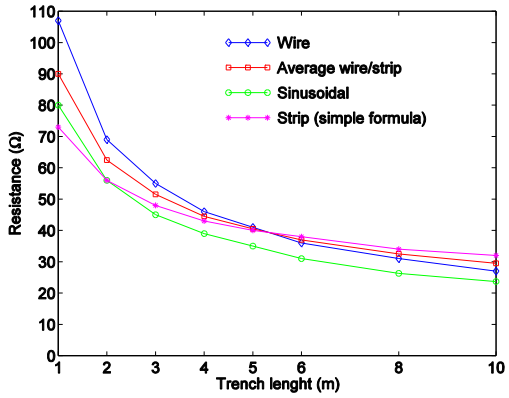

Fig. 13. Comparison between the grounding resistance in a two layer soil ($K = 2/3$) when applying the simple formula for the strip.

For soils with a less resistive bottom layer (K<0), were this type of electrode is not generally used, the calculation of the strip resistance by using (10) leads to average resistance between strip and wire with values greater than the previous case (K>0), but still conservative however.

Next, experimental data are presented and compared with the theoretical values for two layer soil, where the water table produces the bottom layer and a horizontal discontinuity plane between layers. Tests with three electrodes have been performed in a 1 m trench, with a depth of 0.3 m and sandy soil. This type of soil can be modelled as a two layer soil. The resistivity of the upper layer is 2400 Ωm with 1.5 m thickness, whereas the bottom layer has a resistivity of 443 Ωm due to the presence of water. This type of soil has been chosen in order to guarantee a discontinuity plane (or with separation between layers) and levelled with the soil's surface. Nevertheless, the type of soil considered is geologically homogeneous and the water table generates the bottom layer with less resistivity. A linear extrapolation of the empirical model coefficients, found in Equation (9), would bring a calculation for a 1 m trench of the kind $R = 0.23\rho$ and that yield the value 560 Ω for

a sinusoidal electrode with 1 m length. This represents a considerable error when compared to the measured value. The results are shown in Table 1.

The lack of a perfect contact between the strip bottom surface and the soil, with the presence of air bags, can explain the unexpected error of -44% for the theoretical value obtained with the method of moments. The value obtained by using (10) which should be bigger than the previous one, presents a small error however.

If the wire and strip resistances were computed with errors about -35%, -30%, -20%, -10% and 0%, the proposed method would give results having errors of -21%, -15%, -2%, +10% and +22%, respectively. For the experimental case reported and using input data with errors about -20%, the proposed method has given results having errors of approximately -2%. The estimation of wire and strip resistances with values close to the measured ones makes the average resistance to have a higher error, with an expected value around 20%, as mentioned in Section IV.C for this type of soil. It should be pointed out that the proposed average for the sinusoidal resistance is better than the empirical method, which has in this case an error of -68%. That error is much higher than the maximum absolute error of approximately 20% obtained with the proposed method, using estimated wire and strip resistances with errors from -35% to 0%.

The adoption of the new procedure introduced here based on the average values between the theoretical resistances of the wire and the strip turned out as an excellent choice to estimate the field resistance of the sinusoidal electrode.

Table 1: Measured and calculated values

Electrode	Ground Resistance (Ω)/Error (%)					
	Measured	Calculated/Error to Measured	Eq. (10)/Error to Measured	Empirical Model/Error to Measured	Average Wire–Strip/Error to Measured	
					Wire Calculated and Strip Calculated	Wire Calculated and Strip Eq. (10)
Wire	2660	2167/-19	–	–	–	–
Strip	1566	870/-44	1235/-21	–	–	–
Sinusoidal	1735	1364/-21	–	560/-67.7	1518/-12.5	1701/-2

VI. CONCLUSION

A new procedure to calculate the grounding resistance of the sinusoidal electrode was proposed and validated here, particularly for two layer soils with rocky bottom layer (positive voltage reflection). The errors are minor and quite acceptable when compared with those obtained through the empirical model.

The use of a simple formula to calculate the strip resistance may increase the errors. Nevertheless, they still remain smaller than those obtained with the empirical model in the case of positive voltage reflection.

The field measurements agree with theoretical results, except in strip electrode due to airbags that have increased the measured value. Even in this worst case, the proposed procedure produces errors which are much smaller (-12% comparing with -67.7% of the empirical model).

In all cases considered, the surface potential due to the sinusoidal electrode was also analyzed and have shown peak voltages smaller than the remaining electrodes tested.

The sinusoidal electrode is easy to install with a cost much lower than the strip electrode and with better grounding resistance than the wire electrode. The proposed procedure allows obtaining much better accuracy in the grounding resistance estimation for the sinusoidal electrode.

APPENDIX

Here it was considered a linear source of current in the upper layer, x-oriented, centered at $P_F(x_F, y_F, z_F)$ of length $2L$, injecting the current I_F into the soil. Assuming a constant current density leaving the electrode, its value is $I_F/2L$. The current leaving the infinitesimal length dx_L is $I_F dx_L/2L$. By using Equation (3), the infinitesimal voltage caused by this infinitesimal segment at a point of the upper layer is:

$$dV = q_{i,j}\frac{I_F}{2L}dx_L, \tag{A1}$$

where $q_{i,j}$ is given by Equation (7). By integrating from $x_F - L$ to $x_F + L$ an expression for the potential generated by a linear current source in the upper layer is then obtained:

$$V_{22}(x,y,z) = \frac{\rho_2 I_F}{8\pi L}\,[F(x-x_F, y-y_F, z-z_F, L) - K_{12}\sum_{m=0}^{\infty}K^m F(x-x_F, y-y_F, z+z_F-2(m-1)D, L) + \sum_{m=1}^{\infty}K^m F(x-x_F, y-y_F, z-z_F-2mD, L) - K_{32}\sum_{m=0}^{\infty}K^m F(x-x_F, y-y_F, z+z_F+2mD, L) + \sum_{m=1}^{\infty}K^m F(x-x_F, y-y_F, z-z_F+2mD, L)], \tag{A2}$$

where F, the indefinite integral of Green function [17], is given by:

$$F(t,u,v,L) = ln\frac{t+L+\sqrt{(t+L)^2+u^2+v^2}}{t-L+\sqrt{(t-L)^2+u^2+v^2}}. \tag{A3}$$

The strip was modeled using a set of linear conductors whose diameter is the thickness of the strip with axes separated by the diameter of their corresponding

conductors.

The average potential over the length of a passive conductor, caused by a current which leaves an active conductor, must be calculated in order to create a similar system described by (4) and (5). The term q_{ij} is the mutual resistance between the segments. Since *2L* is the length of the active segment and *2C* is the length of the passive segment also *x-oriented* and centered at (x_c, y_c, z_c), the expression for the electric potential in the passive conductor is the well-known average formula:

$$V_{xx}(x_c, y_c, z_c) = \frac{1}{2C}\int_{x_c-C}^{x_c+C} V_{22}(x_c, y_c, z_c)dx_c. \quad \text{(A4)}$$

The result of the integral itself is identical to the expression in brackets in (A2) with function *H* replacing function *F*:

$$H(t,u,v,L,C) = N\cdot ln\left|N+\sqrt{N^2+u^2+v^2}\right| - \sqrt{N^2+u^2+v^2} - O\cdot ln\left|O+\sqrt{O^2+u^2+v^2}\right| + \sqrt{O^2+u^2+v^2} - P\cdot ln\left|P+\sqrt{P^2+u^2+v^2}\right| + \sqrt{P^2+u^2+v^2} + Q\cdot ln\left|Q+\sqrt{Q^2+u^2+v^2}\right| - \sqrt{Q^2+u^2+v^2}\,, \quad \text{(A5)}$$

where *N=t+L+C*, *O=t+L-C*, *P=t-L+C* and *Q=t-L-C*.

For the self-resistance of a segment, its radius must be used in the second parameter, thus avoiding zeros in the calculation of the logarithmic function.

ACKNOWLEDGMENT

This work was supported by National Funding from the FCT - Fundação para a Ciência e a Tecnologia, through the UID/EEA/50008/2013 Project.

REFERENCES

[1] M. M. Salama, M. M. Elsherbiny, and Y. L. Chow, "Calculation and interpretation of a grounding grid in two-layer earth with the synthetic-asymptote approach," *Electrc. Pow. Syst. Res.*, vol. 35, no. 3, pp. 157-165, Dec. 1995.

[2] S. Berberovic, Z. Haznadar, and Z. Stih, "Method of moments in analysis of grounding systems," *Eng. Anal. Bound. Elem.*, vol. 27, no. 4, pp. 351-360, Apr. 2003.

[3] D. Sharma and S. De Four, "Parametric analysis of grounding systems in two-layer earth using Galerkin's moment method," *IEEE PES T&D Conference & Exposition*, Dallas, TX, pp. 541-547, May 21-24, 2006.

[4] I. Colominas, J. Gomez-Calvino, F. Navarrina, and M. Casteleiro, "A general numeric model for grounding analysis in layered soils," *Adv. Eng. Softw.*, vol. 33, no. 7, pp. 641-649360, Jul. 2002.

[5] I. Colominas, F. Navarrina, and M. Casteleiro, "A numerical formulation for grounding analysis in stratified soils," *IEEE Trans. Power Deliver.*, vol. 17, no. 2, pp. 587-595, Apr. 2002.

[6] I. Colominas, J. Aneiros, F. Navarrina, and M. Casteleiro, "A BEM formulation for computational design of grounding systems in stratified soils," *The IV World Conf. on Comp. Mechanics*, Buenos Aires, Argentina, 1998.

[7] U. Adriano, O. Bottauscio, and M. Zucca, "Boundary element approach for the analysis and design of grounding systems in presence of non-homogeneousness," *IEE Gener. Transm. Distrb. Proc.*, vol. 150, no. 3, pp. 360-366, May 2003.

[8] L. M. Coa, "Comparative study between IEEE Std. 80-2000 and finite elements method application for grounding system analysis," *IEEE PES T&D Conference & Exposition*, Caracas, Venezuela, pp. 1-5, Aug. 15-18, 2006.

[9] J. Ma, F. P. Dawalibi, and R. D. Southey, "On the equivalence of uniform and two-layer soils to multilayer soils in the analysis of grounding systems," *IEE Gener. Transm. Distrb. Proc.*, vol. 143, no. 1, pp. 49-55, Jan. 1996.

[10] Y. Liu, N. Theethayi, R. Thottappillil, R. M. Gonzalez, and M. Zitnik, "An improved model for soil ionization around grounding systems and its application to stratified soil," *J. Electrostat.*, vol. 60, no. 2-4, pp. 203-209, Mar. 2004.

[11] E. Mombello, O. Trad, J. Rivera, and A. Andreoni, "Two-layer soil model for power station grounding system calculation considering multilayer soil stratification," *Electr. Pow. Syst. Res.*, vol. 37, no. 1, pp. 67-78, Apr. 1996.

[12] Y. Than, F. R. Pazheri, N. H. Malik, A. A. Al-Arainy, and M. I. Qureshi, "Novel approach of estimating grounding rod optimum dimensions in high resistivity soils," *Electr. Pow. Syst. Res.*, vol. 92, pp. 145-154, 2012.

[13] http://www.edpdistribuicao.pt/pt/profissionais/Lists/EDPDocumentosNormativos/Attachments/353/DRE-C11-040N.pdf.

[14] R. Meliopoulos, *Power System Grounding and Transients*, Marcel Dekker, Inc., New York, 1988.

[15] *IEEE, Grounding of Industrial and Commercial Power Systems*, IEEE Std. 142-2007, 2007.

[16] G. F. Tagg, *Earth Resistances*, George Newnes Limited, London, 1964.

[17] E. B. Joy, A. P. Meliopoulos, and R. P. Webb, "Touch and step calculations for substation grounding systems," *IEEE Trans. Power Ap. Syst.*, vol. PAS-98, no. 4, pp. 1143, July/Aug. 1979.

A. M. R. Martins has a Bachelor degree and an M.Sc. degree in Electrical Engineering. He worked in Portugal Telecom and he is teaching in Guarda Polytechnic Institute. His research interests are grounding systems numerical technics.

S. J. P. S. Mariano received the Electrical and Computer Engineering degree and M.Sc. degree from the Instituto Superior Técnico (IST), Portugal, in 1990 and 1994, respectively, and the Ph.D. degree from the University of Beira Interior, Portugal, in 2002. He is currently an Associate Professor at the University of Beira Interior and a researcher at the IT-Instituto de Telecomunicações. He is the author or coauthor of more than 80 scientific papers presented at international conferences or published in reviewed journals. His research interests include hydrothermal scheduling, power industry restructuring, renewable energy and optimal control.

M. R. A. Calado received the Electrical and Computer Engineering Degree from the Instituto Superior Técnico (IST), Portugal, in 1991, and the Ph.D. degree from the Universidade da Beira Interior (UBI), Portugal, in 2002. She is currently an Assistant Professor with the Department of Electromechanical Engineering, UBI and a Researcher at the IT-Instituto de Telecomunicações. Her current research concerns linear switched reluctance actuators, powerelectronics and numerical methods applied to engineering.

J. A. M. Felippe de Souza has concluded his Ph.D. in Engineering at University of Warwick, England, UK, in 1983. He is currently an Associate Professor at the University of Beira Interior. He is the author or co-author of more than 90 scientific papers presented at international conferences or published in reviewed journals. His research interests include optimal control and state estimation, multi-criteria optimization, control of biomedical systems, intelligent control, neuro-fuzzy systems and evolutionary computing.

Effects of Coil Locations on Wireless Power Transfer via Magnetic Resonance Coupling

Xinzhi Shi [1], Chang Qi [1], Meiling Qu [1], Shuangli Ye [1], and Gaofeng Wang [2,1]

[1] School of Electronics and Information
Wuhan University, Wuhan 430072, China

[2] Microelectronics CAD Center, School of Electronics and Information
Hangzhou Dianzi University, Hangzhou 310018, China
gaofeng@hdu.edu.cn

Abstract ─ The coil locations have strong impacts on efficiency, resonant frequency and bandwidth in the wireless power transfer (WPT) system with four coil resonators, which is a popular configuration for mid-range WPT via magnetic resonance coupling. Herein, effects of coil location parameters, such as the distances between neighboring coils, are investigated by virtue of full-wave electromagnetic solution and validated by measurements. Three operational regions can be defined in terms of the distances between neighboring coils: over coupling, strong coupling and under coupling. It is shown that the distance between the receiving coil and the load coil has significant impact on the power transfer efficiency whereas the distance between the driving coil and the transmitting coil may merely affect the bandwidth and the resonant frequency in the strong coupling regime. In addition, the distance between the transmitting coil and the receiving coil can have strong impact on both the bandwidth and the resonant frequency. Design guidelines for optimal coil locations, by which the highest transfer efficiency or the longest transfer distance can be achieved, are also discussed.

Index Terms ─ Magnetic resonance coupling, power transfer distance, wireless power transfer.

I. INTRODUCTION

In recent years, wireless power transfer (WPT) has been drawing a great deal of attention. The WPT technology allows elimination of unsightly, unwieldy and costly power cords and eases anxiety of running out of battery power. The WPT systems have found applications in portable electronic products (e.g., cellular phones, tablet computers), wireless sensor networks (e.g., wireless body sensor networks), implantable medical devices, etc.

Traditionally, the WPT technology has been classified into two types: radio frequency (RF) radiation and inductive coupling in low frequency (LF) bands. RF radiation, which is widely employed for exchanging data and information, can transfer only a small amount of power (e.g., a few milliwatts) because a majority of power is lost into free space [1]. The RF radiation generated by high directional antennas is usually used for WPT [2], such as applications in space solar power station [3]. It can transfer high power over long distances, but requires uninterrupted line-of-sight, which may be harmful to human bodies. On the other hand, the LF-band inductive coupling can transfer power with high efficiency. The LF-band WPT is a mature technology (e.g., it has been widely used in electric toothbrush). Recently, an industry consortium has been formed to standardize this technology for charging mobile devices [4]. However, the LF-band WPT usually transfers power only over a very short range (e.g., a few centimeters).

The recent progress in the WPT technology based on magnetic resonance coupling in high-frequency (HF) bands has opened up a new paradigm for mid-range power transfer [5]. Since then, studies on various aspects of the WPT via magnetic resonance coupling have been conducted [6-19]. The WPT via magnetic resonance coupling has also been extended into various applications [20-25], such as machinery rat [20], underwater robots [21], electric vehicles [22], LED TV [23], medical implants [24], wireless sensor networks [25], etc.

The coil locations have strong impact on efficiency and resonant frequency of the WPT systems using magnetic resonance coupling. So far, however, they are not studied in-depth. In most previous studies, the coil locations of the WPT systems using magnetic resonance coupling are set either without any explanation or simply as equally spaced. There are only a few studies that discussed the coil location effects. In [7], a simple guideline for selecting the optimum repeater locations and numbers were provided. In the case of two repeaters, for example, only two simple rules have been stated: i) the distances of every two coils are equal; ii) the distance between the transmitter and the repeater is equal to the

Submitted On: September 27, 2015
Accepted On: February 26, 2016

distance between the repeater and the receiver. In [10], the relation between resonant frequency and distance was discussed by simply assuming that the total distance is fixed and the equal space is adopted. In [26], the effects of coil inductance and placement have been analyzed.

In this work, effects of the coil locations of the four-coil WPT system via magnetic resonance coupling are studied in-depth by virtue of full-wave electromagnetic solution and validated by measurements. In particular, the dependences of the power transfer efficiency, the resonant frequency and the bandwidth on important location parameters are carefully examined. Some important observations on effects of the coil locations are drawn based on theoretical studies, which are also verified by experiments. Design guidelines for optimal coil locations are presented for the WPT system, to which the highest transfer efficiency or the longest transfer distance can be achieved.

II. SYSTEM MODEL

Consider a four-coil WPT system via magnetic resonance coupling, which is a popular configuration for mid-range WPT via magnetic resonance coupling [5]. This WPT system is composed of four coils: driving coil, transmitting coil, receiving coil and load coil, as shown in Fig. 1. The driving coil (D) is a single loop (i.e., one turn) and connects to the voltage source. The transmitting coil (T) and receiving coil (R) are helix coils. The load coil (L) is also a single loop and connects to the load. The four-coil configuration can reduce the influence of the source and the load, and hence improve the efficiency of the WPT system.

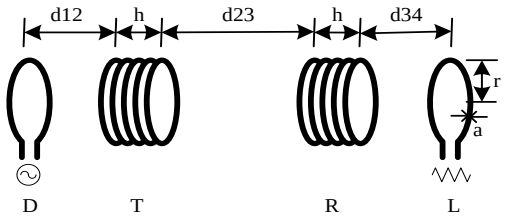

Fig. 1. Schematic of four-coil WPT system.

The four coils are resonant and contactless with each other. The distances (i.e., separations) between the driving and transmitting coils, between the transmitting and receiving coils and between the receiving and load coils are, respectively, denoted as d_{12}, d_{23} and d_{34}. The radius of the four coils, the height of the transmitting and receiving coils and the cross-sectional radius of the conductor coil wires are denoted as r, h and a respectively.

Two types of system models for the WPT system via magnetic resonance coupling are shown in Fig. 2. Panel (a) shows the widely used equivalent circuit model for circuit analysis in the previous published literature, whereas panel (b) illustrates a more accurate model by virtue of full-wave electromagnetic theory.

In panel (a), the driving, transmitting, receiving and load coils are numbered as coils 1, 2, 3 and 4 respectively, M_{ij} (i, j = 1, 2, 3, 4) denotes the mutual inductance between coil i and coil j (and $M_{ij} = M_{ji}$), V_s is ac excitation voltage source with an internal resistance denoted as R_S. The circuit elements C_i, L_i, and R_i (i = 1, 2, 3, 4) represent the parasitic capacitance, self-inductance, and resistance of coil i respectively, R_L is the load resistance connected to coil 4, and the current in coil i is denoted as I_i (i = 1, 2, 3, 4).

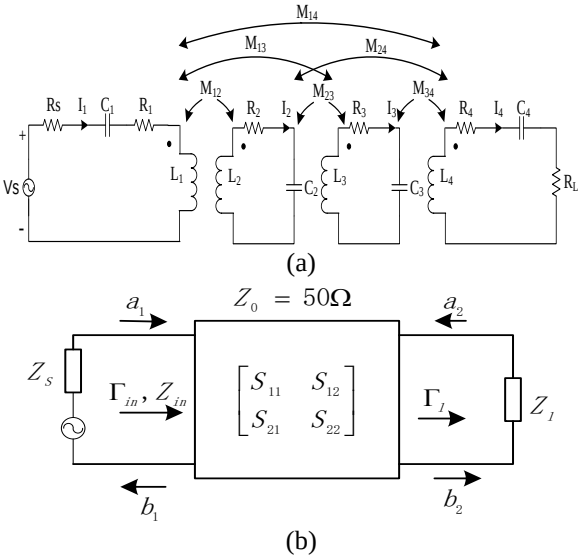

Fig. 2. System models of the WPT system. (a) Equivalent circuit model; (b) two-port S-parameter model.

In panel (b), the WPT system is treated as an integrated (or tightly coupled) unit that is fully characterized as a two-port scattering parameter matrix (i.e., S-parameters) network, in which the transmitting port is denoted as port 1 and the receiving port is denoted as port 2. The S-parameter matrix can be obtained from the full-wave electromagnetic solution. The driving coil is excited by ac excitation voltage source V_s with internal resistance R_S, while the load coil is connected to the load resistance R_L.

Instead of the equivalent circuit model, the more accurate two-port S-parameter model is adopted to study the WPT system by virtue of the full-wave electromagnetic solution. Based on the S-parameters, the power transfer efficiency of the WPT system can be evaluated as:

$$\eta = \frac{P_l}{P_{in}} = \frac{|S_{21}|^2\left(1-|\Gamma_L|^2\right)}{|1-S_{22}\Gamma_L|^2\left(1-|\Gamma_{in}|^2\right)}, \quad (1)$$

where Γ_L is the reflection coefficient at the load $Z_L = R_L$, and Γ_{in} is the reflection coefficient at port 1. They can be calculated as:

$$\Gamma_L = \frac{Z_L - Z_0}{Z_L + Z_0}, \tag{2}$$

$$\Gamma_{in} = S_{11} + \frac{S_{12}S_{21}\Gamma_L}{1 - S_{22}\Gamma_L}, \tag{3}$$

where S_{11}, S_{21}, S_{12} and S_{22} are the S-parameters, as shown in Fig. 2 (b). If mismatching at the port 1 is omitted, the maximum transfer efficiency can be achieved when the load meets the following matching condition:

$$\Gamma_l = S_{22}^*(f). \tag{4}$$

In the following section, the S-parameters are computed by using the full-wave electromagnetic solution in reference to a characteristic impedance. $Z_0 = 50\,\Omega$

III. EFFECTS OF COIL LOCATIONS

In this section, analysis on coil locations of the WPT system via magnetic resonance coupling, as shown in Fig. 1, is presented by virtue of the full-wave electromagnetic solution. The full-wave electro-magnetic solution is obtained by a commercial full-wave electromagnetic simulation tool, called FEKO. The four coils are made of Cu. The geometrical and physical parameters are listed in Table 1.

Table 1: Parameters of the WPT system

Symbol	Meaning	Value	Unit
r_1	Radius of driving coil	30	cm
r_2	Radius of transmitting coil	30	cm
r_3	Radius of receiving coil	30	cm
r_4	Radius of load coil	30	cm
a	Cross-sectional radius of coil wires	0.3	cm
h	Height of the transmitting coil and the receiving coil	20	cm
N	Number of turns of the transmitting coil and the receiving coil	5.25	turn
R_S	Internal resistance of voltage source	50	ohm
R_L	Load resistance	550	ohm

The distance parameters include d_{12}, d_{23} and d_{34}. The total transfer distance between the driving coil and the load coil is defined as:

$$d = d_{12} + d_{23} + d_{34}. \tag{5}$$

Note that the heights of the transmitting coil and the receiving coil are not included in the total transfer distance.

Electromagnetic simulations are performed by FEKO to study effects of coils locations (i.e., distances between pairs of adjacent coils) in terms of the power transfer efficiency, the resonant frequency and the bandwidth. Note that, in the WPT system via magnetic resonance coupling, the input power has little impact on the power transfer efficiency as theoretically expected since this WPT system is linear and the input power has been factored out from the power transfer efficiency as shown in its definition (1).

A. Effects of variable d_{34} with fixed d_{12} and fixed d_{23}

In this subsection, effects of d_{34} on efficiency of the WPT system via magnetic resonance coupling are studied. It is assumed that d_{34} varies from 5 cm to 60 cm with a step size of 5 cm, whereas d_{12} is fixed at 15 cm and d_{23} is fixed at 150 cm. The efficiency versus d_{34} is plotted in Fig. 3, while the efficiency versus the frequency is depicted in Fig. 4.

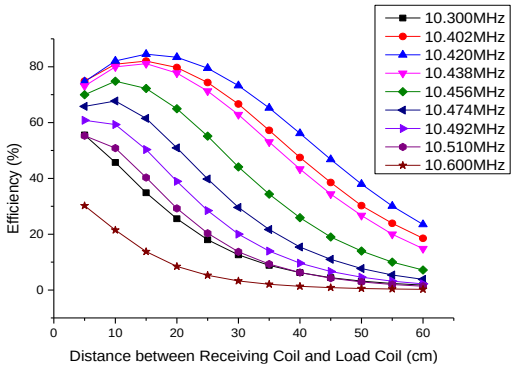

Fig. 3. Efficiency versus d_{34} (with fixed d_{12} and fixed d_{23}).

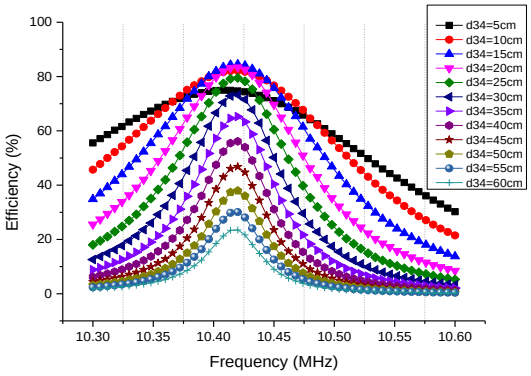

Fig. 4. Efficiency versus frequency (with fixed d_{12} and fixed d_{23}).

From Fig. 3, one can observe that when d_{34} increases from 5 cm to 60 cm, the power transfer efficiency increases at beginning, then becomes saturated, and finally decreases in a downward trend for the frequencies no larger than 10.474 MHz. When d_{34} is shorter than 10 cm, the closer the receiving and load coils are, the lower the

efficiency is. When d_{34} is between 10 cm and 20 cm, the efficiency is almost flattened within a small range from 82.07% to 84.51%. When d_{34} is beyond 20 cm, the efficiency diminishes dramatically.

The efficiency is the highest around the frequency of 10.42 MHz regardless the value of d_{34}. When the operating frequency shifts roughly 1.5% from 10.42 MHz (such as 10.300 MHz and 10.600 MHz), the efficiency decreases dramatically as shown in Fig. 3. The highest efficiency can be obtained as 85.51% when d_{34} is 15 cm and the operating frequency is 10.42 MHz.

From Fig. 4, one can observe that when d_{34} is shorter than 10 cm, the bandwidth is wide but the efficiency is not very high. For example, when d_{34} is 5 cm, the bandwidth is 0.174 MHz and the highest efficiency is only 74.97%.

When d_{34} is between 10 cm and 20 cm, the bandwidth becomes narrower, but the highest efficiency is always above 80%. For example, when d_{34} is 10 cm, 15 cm and 20 cm, the bandwidth is 0.144 MHz, 0.114 MHz and 0.090 MHz respectively, whereas the efficiency can be as high as 82.07%, 84.51% and 83.49% respectively.

When d_{34} is longer than 20 cm, the bandwidth is still narrow and the efficiency becomes lower. For example, when d_{34} is 30 cm, the bandwidth is 0.042 MHz and the highest efficiency is 73.24%. When d_{34} is 60 cm, the highest efficiency is now as low as 23.49%.

From Fig. 4, one can see that the resonant frequency is 10.408 MHz when d_{34} is 5 cm. The resonant frequency stays almost constant at 10.42 MHz for all d_{34} from 10 cm to 60 cm.

B. Effects of variable d_{23} with fixed d_{12} and fixed d_{34}

Effects of d_{23} on efficiency of the WPT system via magnetic resonance coupling are studied in this subsection. It is assumed that d_{23} varies from 20 cm to 300 cm with a step size of 20 cm, whereas d_{12} and d_{34} are fixed at 15 cm. The efficiency versus d_{23} is plotted in Fig. 5, while the efficiency versus the frequency is depicted in Fig. 6.

From Fig. 5, one can see that when d_{23} increases from 20 cm to 300 cm, the power transfer efficiency increases at beginning, then becomes saturated, and finally decreases considerably. When d_{23} is shorter than 40 cm, the closer the transmitting and receiving coils are, the lower the efficiency is. When d_{23} is between 40 cm and 120 cm, the efficiency is almost flattened within a small range from 89.69% to 92.23%. When d_{23} is beyond 120 cm, the efficiency diminishes dramatically.

The efficiency is the highest at the frequency of 10.455 MHz for most values of d_{23}. When the operating frequency shifts roughly 1.5% from 10.455 MHz (such as 10.300 MHz and 10.600 MHz), the efficiency decreases dramatically as shown in Fig. 5. The highest efficiency can be obtained as 92.23% when d_{23} is 60 cm and the operating frequency is 10.455 MHz.

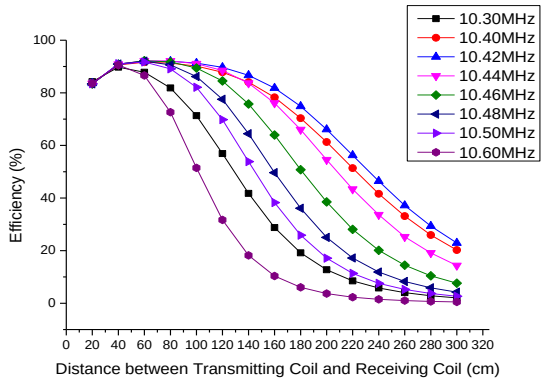

Fig. 5. Efficiency versus d_{23} (with fixed d_{12} and fixed d_{34}).

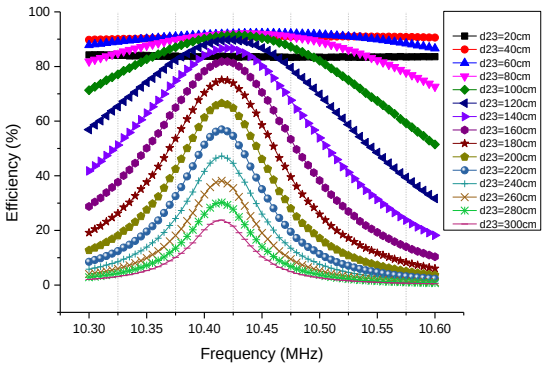

Fig. 6. Efficiency versus frequency (with fixed d_{12} and fixed d_{34}).

From Fig. 6, one can see that when d_{23} is within 40 cm, the bandwidth is very wide but the efficiency still has some room to improve. For example, when d_{23} is 20 cm, the bandwidth is wider than 0.3 MHz while the highest efficiency is 84.28%.

When d_{23} is between 40 cm and 120 cm, the bandwidth becomes narrower, but the highest efficiency is always above 85%. For example, when d_{23} is 80 cm and 120 cm, the bandwidth is 0.2 MHz and 0.065 MHz respectively, whereas the efficiency can be as high as 92.15% and 89.69% respectively.

When d_{23} is longer than 120 cm, the bandwidth is still narrow and the efficiency becomes much lower. For example, when d_{23} is 140 cm, the bandwidth is 0.025 MHz and the highest efficiency is 86.68%. When d_{23} is 300 cm, the highest efficiency is now as low as 23.82%.

From Fig. 6, one can observe that the resonant frequency is 10.31 MHz when d_{23} is 20 cm. The resonant frequency decreases when d_{23} increases from 40 cm to 120 cm. For example, the resonant frequency is 10.50 MHz, 10.43 MHz and 10.42 MHz when d_{23} is 40 cm, 80 cm and 120 cm respectively. The resonant frequency stays almost constant at 10.42 MHz for all d_{23} beyond 120 cm.

By comparing Fig. 5 to Fig. 3, one can see that the efficiency keeps high for a relatively large range of d_{23}.

That is, the distance d_{23} between the transmitting and receiving coils has a wide range of the strong coupling state. Therefore, the distance d_{23} can be used for expanding the total transmission distance.

C. Effects of variable d_{12} with fixed d_{23} and fixed d_{34}

Effects of d_{12} on efficiency of the WPT system via magnetic resonance coupling are studied in this subsection. It is assumed that d_{12} varies from 5 cm to 240 cm, whereas d_{23} is fixed at 150 cm and d_{34} is fixed at 15 cm. The efficiency versus d_{12} is plotted in Fig. 7, while the efficiency versus the frequency is depicted in Fig. 8.

From Fig. 7, one can observe that when d_{12} increases from 5 cm to 240 cm, the power transfer efficiency is stable at beginning and then rapidly decreases. When d_{12} is shorter than 60 cm, the efficiency varies slightly from 84.14% to 84.51%. When d_{12} is beyond 60 cm, the efficiency diminishes dramatically.

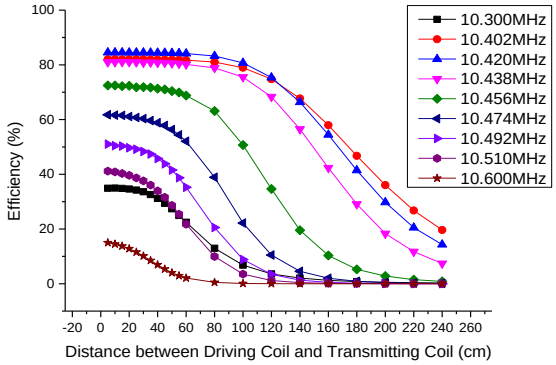

Fig. 7. Efficiency versus d_{12} (with fixed d_{23} and fixed d_{34}).

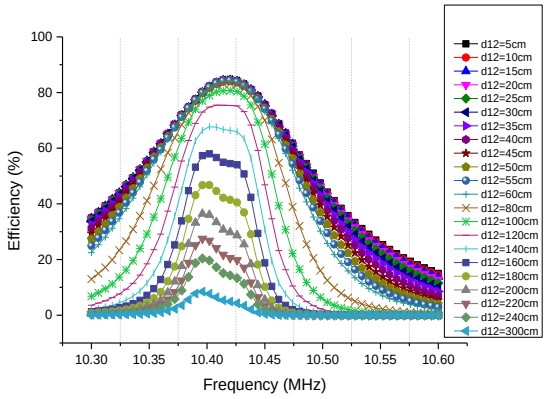

Fig. 8. Efficiency versus frequency (with fixed d_{23} and fixed d_{34}).

The efficiency is the highest at the frequency of 10.42 MHz regardless the value of d_{12}. When the operating frequency shifts roughly 1.5% from 10.42 MHz (such as 10.300 MHz and 10.600 MHz), the efficiency decreases dramatically as shown in Fig. 7. The highest efficiency can be obtained as 84.51% when d_{12} is 15 cm and the operating frequency is 10.42 MHz.

From Fig. 8, one can observe that when d_{12} is within 60 cm, the bandwidth decreases slightly along with increasing d_{12}, but the highest efficiency is nearly constant. For example, when d_{12} is 5 cm and 60 cm, the bandwidth is 0.114 MHz and 0.096 MHz while the highest efficiency is 84.51% and 84.14% respectively.

When d_{12} is longer than 60 cm, the bandwidth becomes narrower and the efficiency becomes much lower. For example, when d_{12} is 140 cm, the bandwidth is 0.042 MHz and the highest efficiency is 67.73%. When d_{12} is 240 cm, the highest efficiency is now down to 20.38%.

From Fig. 8, one can see that the resonant frequency stays almost constant at 10.42 MHz for all d_{12} from 5 cm to 100 cm. The resonant frequency slightly decreases when d_{12} gets longer beyond 100 cm. For example, when d_{12} is 120 cm and 240 cm, the resonant frequency is 10.408 MHz and 10.396 MHz respectively.

By comparing Fig. 7 to Fig. 3, it is found that the distance d_{12} between the driving and transmitting coils has a wide range of the strong coupling state, which is very beneficial for expanding the total transmission distance via increasing d_{12}.

D. Effects under fixed total transfer distance

Location effects on efficiency of the WPT system via magnetic resonance coupling are studied under a fixed total transfer distance d in this subsection. It is assumed that d is fixed at 200 cm, whereas d_{12} and d_{34} are always equal and vary from 10 cm to 70 cm with a step size of 10 cm. Correspondingly, $d_{23} = d - 2d_{12}$ varies from 180 cm to 60 cm with a step size of 20 cm. The efficiency versus d_{12} (i.e.,d_{34}) is plotted in Fig. 9, while the efficiency versus the frequency is depicted in Fig. 10.

From Fig. 9, one can observe that when d_{12} and d_{34} increase from 10 cm to 70 cm (i.e., d_{23} decreases from 180 cm to 60 cm), the power transfer efficiency increases at beginning and then decreases. From Fig. 9, one can observe that when d_{12} and d_{34} are shorter than 20 cm (i.e., d_{23} is longer than 160 cm), the closer the driving (receiving) and transmitting (load) coils are, the lower the efficiency is. Frequency splitting occurs when the distance between the driving (receiving) and transmitting (load) coils becomes too small and thus leads to lower efficiency. When d_{12} and d_{34} are longer than 20 cm, the efficiency diminishes dramatically.

The efficiency is the highest at the frequency of 10.42 MHz regardless the values of d_{12}, d_{23} and d_{34}. When the operating frequency shifts roughly 1.5% from 10.42 MHz (such as 10.300 MHz and 10.600 MHz), the efficiency decreases dramatically as shown in Fig. 9. The highest efficiency can be obtained as 81.68% when d_{12} and d_{34} are 20 cm (i.e., d_{23} is 160 cm) and the operating frequency is at the resonant frequency (i.e., 10.42 MHz).

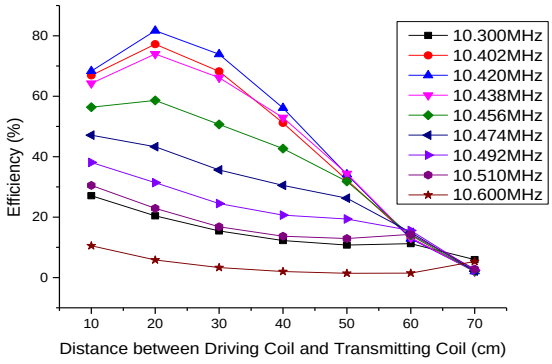

Fig. 9. Efficiency versus d_{12} (with $d_{23} = d - 2d_{12}$, $d_{34} = d_{12}$and fixed d).

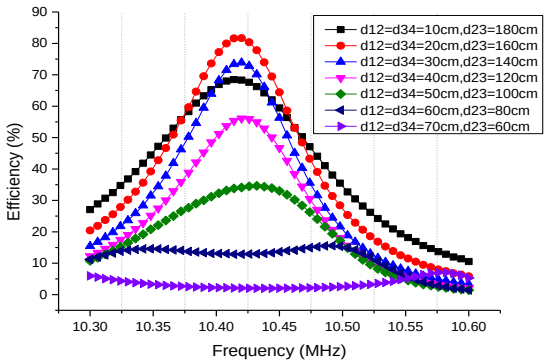

Fig. 10. Efficiency versus frequency (with $d_{23} = d - 2d_{12}$, $d_{34} = d_{12}$and fixed d).

From Fig. 10, one can observe that when d_{12} and d_{34} are within 10 cm (i.e., d_{23} is beyond 180 cm), the bandwidth is relatively wide although the efficiency is not very high. For example, when d_{12} and d_{34} are 10 cm (i.e., d_{23} is 180 cm), the bandwidth is 0.06 MHz while the highest efficiency is only 68.48%.

When d_{12} and d_{34} increase from 20 cm to 50 cm (i.e., d_{23} decreases from 160 cm to 100 cm), the bandwidth becomes narrower and the efficiency becomes lower. When d_{12} and d_{34} are longer than 60 cm (i.e., d_{23} is shorter than 80 cm), the frequency splitting occurs and the efficiency is very low.

E. Discussions

Based on the preceding subsections, it is evident that the locations of four coils have strong impact on the efficiency, the resonant frequency and the bandwidth of the WPT system via magnetic resonance coupling. Some interesting observations can be drawn as follows.

The operation of the WPT system via magnetic resonance coupling can be divided into three regions in terms of the distance between each pair of two coils: over coupling, strong coupling and under coupling. The system is in the over coupling state if two coils (e.g., driving and transmitting coils, transmitting and receiving coils, or receiving and load coils) are too close to each other. When the system is in the over coupling state, the power transfer efficiency is usually low due to frequency splitting. The closer the two coils are, the lower the efficiency is. In addition, the resonant frequency may shift to a lower frequency when the system is in over coupling.

The system is in the under coupling state if two coils are too far away. When the system is in the under coupling state, the power transfer efficiency decreases along with increasing distance due to weakened coupling.

The system is in the strong coupling state if two coils are at a suitable distance. The power transfer efficiency achieves the highest and keeps almost constant regardless the distance variation within a certain range. However, the efficiency can decrease dramatically if the operating frequency deviates too far from the resonance frequency.

By adjusting locations of four coils, the WPT system via magnetic resonance coupling can be made to operate in different states. The system operates in the strong coupling state if the following conditions are satisfied: $\frac{2}{3}r \le d_{12} \le \frac{5}{3}r$, $\frac{4}{3}r \le d_{23} \le 4r$, and $\frac{1}{3}r \le d_{34} \le \frac{2}{3}r$ (where r is the coil radius).

The distances d_{12}, d_{23} and d_{34} have different impacts on the efficiency of the WPT system via magnetic resonance coupling. The distance d_{34} between the receiving and load coils has more significant impact on the efficiency than the distance d_{12} between the driving and transmitting coils. This is because the load coil is connected to the load. The variation of d_{34} changes the load impedance and therefore affects the power transfer efficiency.

In the strong coupling state, the bandwidth is usually broadened and the resonant frequency shifts to a lower frequency. Interestingly, the distance d_{12} between the driving and transmitting coils has a wide range of the strong coupling state. Consequentially, the efficiency does not change much with the variation of d_{12} in the strong coupling state (as shown in Fig. 7), which is very beneficial for expanding the total transmission distance via increasing d_{12}.

The distance d_{23} between the transmitting and receiving coils has a wide range of the strong coupling state too. However, it has strong impact on the bandwidth and the resonant frequency of the WPT system via magnetic resonance coupling. Therefore, one may expect some small adjustment on the resonant frequency when the distance d_{23} is used for expanding the total transmission distance yet maintaining high efficiency.

There exists an optimal set of coil locations for the WPT system via magnetic resonance coupling under the assumption of a fixed total transfer distance. When the highest efficiency is the objective, the locations of four coils should be assigned according to the following

guideline: $d_{12} \approx d_{34} \approx 0.5r$ and $d_{23} \approx 2r$ (where r is the coil radius).

If the longest transfer distance is the objective under a fixed efficiency, one should hold d_{34} at the upper limit of the strong coupling region (e.g., $d_{34} \approx \frac{2}{3} r$), and then stretch d_{12} and d_{23} as much as possible over their strong coupling regions (e.g., d_{12} and d_{23} can be, respectively, as large as two and four times of the coil radius) until the efficiency hits the targeted value.

Note that, although the results obtained for the specific coil radii 30 cm, the basic concept of this work is useful and can be a good guide for other radii. For a larger system, such as a "domino" system, which has coils more than four, similar analysis can be conducted and similar design guidelines are expected. The relay coils can be inserted between the transmitting coil and the receiving coil. The effects of these coil locations on WPT systems are similar to the effect of d_{23}.

IV. PRACTICAL VERIFICATION

Experiments have been carried out to verify the theoretical studies by using a four coil WPT system via magnetic resonance coupling, as shown in Fig. 11. The geometrical and physical parameters of the system are the same as those listed in Table 1. Compensating capacitors are added to the driving, transmitting, receiving and load coils to make them resonant at the frequency of 10.42 MHz. The related parameters are listed in Table 2.

Fig. 11. Photograph of the WPT system for experiments.

Table 2: Parameters of four coils

Parameters	Value
Inductance of driving coil (μH)	1.7661
Capacitance of driving coil (pF)	132.1
Inductance of transmitting coil (μH)	51.275
Capacitance of transmitting coil (pF)	4.5499
Inductance of receiving coil (μH)	51.275
Capacitance of receiving coil (pF)	4.5499
Inductance of load coil (μH)	1.7661
Capacitance of load coil(pF)	132.1

The measurements are done by a network analyzer so that the frequency responses (both magnitude and phase) can be measured easily and accurately. The driving and load coils are connected to the ports of the network analyzer through SMA cables and connectors. The measured S-parameter is then converted into the system efficiency.

In order to check the validity of the analysis in the preceding sections, several experiments are conducted for various location combinations as shown in Table 3. The experiments for both the highest efficiency and the longest transfer distance are performed. The measured results and simulated results are compared in Fig. 12.

Table 3: Location combinations of four coils

d (cm)	d_{12} (cm)	d_{23} (cm)	d_{34} (cm)
75	10	55	10
80	10	60	10
85	15	60	10
90	15	60	15
200	60	120	20
220	60	140	20
240	60	160	20
250	70	160	20
260	80	160	20

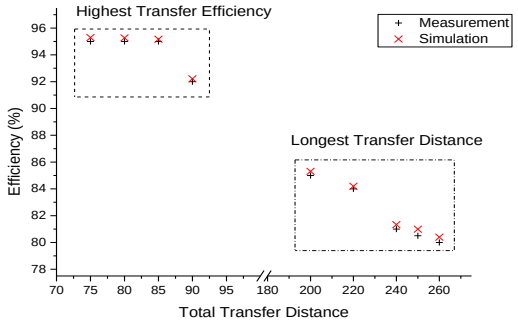

Fig. 12. Comparison of measurements and simulation results.

From Fig. 12, one can observe the highest efficiency is obtained at d_{12} = 10 cm, d_{23} = 55 cm and d_{34} = 10 cm. The highest efficiency is 95.29%. The longest transfer distance is obtained at d_{12} = 80 cm, d_{23}= 160 cm and d_{34} = 20 cm in which the efficiency is slightly higher than 80%. The longest transfer distance d is about 260 cm for a given efficiency of 80%. The measurements agree very well with the simulation results, as shown in Fig. 12.

V. CONCLUSION

Effects of coil locations of the four-coil wireless power transfer (WPT) system via magnetic resonance coupling were studied in-depth here. The location parameters of four coils, including the distance d_{12} between the driving and transmitting coils, the distance d_{23} between the transmitting and receiving coils, and the distance d_{34} between the receiving and load coils, have been used as design variables. It was found that all these three location parameters have impact on the efficiency, the resonant frequency and the bandwidth of the WPT

system via magnetic resonance coupling.

The operation of the WPT system via magnetic resonance coupling can be divided into three regions in terms of the distance between each pair of two adjacent coils: over coupling, strong coupling and under coupling. Different operating states can be achieved by adjusting locations of four coils.

The distances d_{12}, d_{23} and d_{34} have different kinds of impact on the efficiency of the WPT system via magnetic resonance coupling. The distance d_{34} has more significant impact on the efficiency than the distance d_{12}. Interestingly, the distance d_{12} has a wide range of the strong coupling state. The efficiency does not change much along with variation of d_{12} in the strong coupling state. The distance d_{23} has also a wide range of the strong coupling state. However, it has strong impact on the bandwidth and the resonant frequency of the WPT system via magnetic resonance coupling. Finally, design guidelines for optimal coil locations have been presented for the WPT system, to which the highest transfer efficiency or the longest transfer distance can be achieved.

ACKNOWLEDGMENT

This work was supported in part by the National Science Foundation of China under Grants 61331007, 61411136003, the Zhejiang Provincial Natural Science Foundation of China under grant LZ14F040001, and the CAST Foundation under Grant CAST201241 and Shenzhen Special Funds for the Development of Strategic Emerging Industries under Grant JCYJ20130401160028789.

REFERENCES

[1] A. P. Sample and J. R. Smith, "Experimental results with two wireless power transfer systems," *in Proc. IEEE RWS*, pp. 16-18, Jan. 2009.

[2] Z. Popovic, E. A. Falkenstein, D. Costinett, and R. Zane, "Low-power far-field wireless powering for wireless sensors," *Proc. IEEE*, vol. 101, no. 6, pp. 1397-1409, June 2013.

[3] B. Strassner and K. Chang, "Microwave power transmission: historical milestones and system components," *Proc. IEEE*, vol. 101, no. 6, pp. 1379-1396, June 2013.

[4] S. Y. Hui, "Planar wireless charging technology for portable electronic products and Qi," *Proc. IEEE*, vol. 101, no. 6, pp. 1290-1301, June 2013.

[5] A. Kurs, A. Karalis, R. Moffatt, J. D. Joannopoulos, P. Fisher, and M. Soljačić, "Wireless power transfer via strongly coupled magnetic resonances," *Science*, vol. 317, pp. 83-86, July 2007.

[6] J. Garnica, R. A. Chinga, and J. S. Lin, "Wireless power transmission: from far field to near field," *Proc. IEEE*, vol. 101, no. 6, pp. 1321-1331, June 2013.

[7] D. Ahn and S. Hong, "A study on magnetic field repeater in wireless power transfer," *IEEE Trans. Industrial Electronics*, vol. 60, no. 1, pp. 360-371, Jan. 2013.

[8] W. X. Zhong, C. K. Lee, and S. Y. R. Hui, "General analysis on the use of Tesla's resonators in Domino forms for wireless power transfer," *IEEE Trans. Industrial Electronics*, vol. 60, no. 1, pp. 261-270, Jan. 2013.

[9] E. M. Thomas, J. D. Heebl, C. Pfeiffer, and A. Grbic, "A power link study of wireless non-radiative power transfer systems using resonant shielded loops," *IEEE Trans. Circuits and Systems I: Regular Papers*, vol. 59, no. 9, pp. 2125-2136, Sept. 2012.

[10] C. K. Lee, W. X. Zhong, and S. Y. R. Hui, "Effects of magnetic coupling of nonadjacent resonators on wireless power Domino-resonator systems," *IEEE Trans. Power Electronics*, vol. 27, no. 4, pp. 1905-1916, Apr. 2012.

[11] A. P. Sample, D. A. Meyer, and J. R. Smith, "Analysis, experimental results, and range adaptation of magnetically coupled resonators for wireless power transfer," *IEEE Trans. Industrial Electronics*, vol. 58, no. 2, pp. 544-554, Feb. 2011.

[12] C.-J. Chen, T.-H. Chu, C.-L. Lin, and Z.-C. Jou, "A study of loosely coupled coils for wireless power transfer," *IEEE Trans. Circuits and Systems II: Express Briefs*, vol. 57, no. 7, pp. 536-540, July 2010.

[13] A. Christ, M. Douglas, J. Nadakuduti, and N. Kuster, "Assessing human exposure to electromagnetic fields from wireless power transmission systems," *Proc. IEEE*, vol. 101, no. 6, pp. 1482-1493, June 2013.

[14] W. Q. Niu, J. X. Chu, W. Gu, and A. D. Shen, "Exact analysis of frequency splitting phenomena of contactless power transfer systems," *IEEE Trans. Circuits and Systems I: Regular Papers*, vol. 60, no. 6, pp. 1670-1677, June 2013.

[15] A. P. Sample, B. H. Waters, S. T. Wisdom, and J. R. Smith, "Enabling seamless wireless power delivery in dynamic environments," *Proc. IEEE*, vol. 101, no. 6, pp. 1343-1358, June 2013.

[16] T. C. Beh, M. Kato, T. Imura, S. Oh, and Y. Hori, "Automated impedance matching system for robust wireless power transfer via magnetic resonance coupling," *IEEE Trans. Industrial Electronics*, vol. 60, no. 9, pp. 3689-3698, Sept. 2013.

[17] W. X. Zhong, C. K. Lee, and S. Y. R. Hui, "Wireless power Domino-resonator systems with non-coaxial axes and circular structures," *IEEE Trans. Power Electronics*, vol. 27, no. 11, pp. 4750-4762, Nov. 2012.

[18] D. Ahn and S. Hong, "Effect of coupling between multiple transmitters or multiple receivers on

wireless power transfer," *IEEE Trans. Power Electronics*, vol. 60, no. 7, pp. 2602-2613, July 2013.

[19] S. Cheon, Y. H. Kim, S. Y. Kang, M. L. Lee, J. M. Lee, and T. Zyung, "Circuit-model-based analysis of a wireless energy-transfer system via coupled magnetic resonances," *IEEE Trans. Industrial Electronics*, vol. 58, no. 7, pp. 2906-2914, July 2011.

[20] C. W. Chang, K. C. Hou, L. J. Shieh, S. H. Hung, and J. C. Chiou, "Wireless powering electronics and spiral coils for implant microsystem toward nanomedicine diagnosis and therapy in free-behavior animal," *Solid-State Electronics*, vol. 77, pp. 93-100, Nov. 2012.

[21] K. Abdelnour, A. Stinchcombe, M. Porfiri, J. Zhang, and S. Childress, "Wireless powering of ionic polymer metal composites toward hovering micro swimmers," *IEEE-ASME Trans. Mechatronics*, vol. 17, no. 5, pp. 924-935, Oct. 2012.

[22] S. Hasanzadeh, S. Vaez-Zadeh, and A. H. Isfahani, "Optimization of a contactless power transfer system for electric vehicles," *IEEE Trans. Vehicular Technology*, vol. 61, no. 8, pp. 3566-3573, Oct. 2012.

[23] J. Kim, H. C. Son, D. H. Kim, and Y. J. Park, "Optimal design of a wireless power transfer system with multiple self-resonators for an LED TV," *IEEE Trans. Consumer Electronics*, vol. 58, no. 3, pp. 775-780, Aug. 2012.

[24] J. S. Ho, S. Kim, and A. Poon, "Midfield wireless powering for implantable systems," *Proc. IEEE*, vol. 101, no. 6, pp. 1369-1378, June 2013.

[25] T. S. Li, Z. Han, H. Ogai, K. Sawada, and J. Wang, "A microchip-controlling wireless power transfer system for sensor network," in *2012 Proceedings Of SICE Annual Conference (SICE)*, pp. 337-341, 2012.

[26] H. Hwang, J. Moon, B. Lee, C.-H. Jeong, and S.-W. Kim, "An analysis of magnetic resonance coupling effects on wireless power transfer by coil inductance and placement," *IEEE Trans. Consumer Electronics*, vol. 60, no. 2, pp. 203-209, May 2014.

Xinzhi Shi received the Ph.D. degree in Computer Application and Technology from Wuhan University, Wuhan, China, in 2005.

She is currently an Associate Professor with the School of Electronics and Information, Wuhan University. Her research interests include optoelectronic device design, modeling, and simulation.

Chang Qi received the Ph.D. degree in Electrical Engineering from Wuhan University, Wuhan, China, in 2007.

She is currently an Associate Professor with the Institute of Microelectronics and Information Technology, Wuhan University. Her research interests include optoelectronic device design, modeling, and simulation.

Shuangli Ye received the Ph.D. degree in Physics and Material Sciences from Philipps University, Marburg, Germany, in 2005.

She is currently an Associate Professor with the Institute of Microelectronics and Information Technology, Wuhan University. Her research interests include nano-engineered magnetic thin film and spintronics MEMS for magnetologic application.

Gaofeng Wang received the Ph.D. degree in Electrical Engineering from the University of Wisconsin, Milwaukee, in 1993 and the Ph.D. degree in Scientific Computing from Stanford University, Stanford, California, in 2001.

From 1993 to 1996, he was a Scientist at Tanner Research Inc., Pasadena, CA. From 1996 to 2001, he was a Principal Research and Development Engineer at Synopsys Inc., Mountain View, CA. In the summer of 1999, he served as a Consultant at Bell Laboratories, Murray Hill, NJ. From 2001 to 2003, he was Chief Technology Officer (CTO) at Intpax, Inc., San Jose, CA. From 2004 to 2010, he was CTO at Siargo Inc., Santa Clara, CA. From 2010 to 2013, he was Chief Scientist at Lorentz Solution, Inc., Santa Clara, CA. From 2004 to 2013, he was also a Professor and the Director for the Institute of Microelectronics and Information Technology, Wuhan University, Wuhan, China. He is currently a Distinguished Professor in Electrical Engineering at Hangzhou Dianzi University, Hangzhou, China.

He has over 280 publications and is the holder of over 20 patents. His research interests include computational electromagnetics, integrated circuits, MEMS and sensor technology, wireless power transfer, and electronic design automation.

Stochastic Radiation Model for Cable Bundle with Random Wires

Jin Jia [1], Zhida Lai [1], Jianmei Lei [1], and Quandi Wang [2]

[1] Chongqing CAERI Quality Inspection and Authentication Center Co. Ltd.
China Automotive Engineering Research Institute, Chongqing, 401122, China

[2] State Key Laboratory of Power Transmission Equipment & System Security and New Technology
Chongqing University, Chongqing 400030, China

Abstract ─ Cable bundle is often the main radiation structure due to its length in automotive electrical or electronic systems. Random wire positions in a cable bundle is a challenge for the modeling in perspective of Electromagnetic Compatibility (EMC). This work addresses the uncertainty property of a cable bundle due to its random wire positions, through a stochastic-model approach. Random wire position distributions in a bundle adopt Gaussian norm. A *spline* interpolate function is used to improve the continuity of wires along the bundle. To calculate the common-mode (CM) current on the bundle, the composed non-uniform wires are modeled by cascaded uniform segments or Chebyshev Expansion Method based smooth lines. Further CM current based bundle radiation is calculated using electric-dipole model. Proposed modeling methodology is assessed by comparing CM current and radiation predictions versus measurement data and theoretical results. Predictions agree well with measurements especially in statistics.

Index Terms ─ Cable bundle, Electromagnetic Compatibility (EMC), Common-Mode (CM) current, radiation, statistics, stochastic-model.

I. INTRODUCTION

In the ALSE method according to CISPR 25 [1], the long cable bundle is often the dominant radiation structure. To predict radiated emissions from this structure at early EMC design stage, a reasonable radiation model is necessary. However, in a real automotive bundle the variability of the wire positions along the bundle lead to difference in final radiation measurements. Modeling a highly-precise cable bundle is difficult due to its random wire position. Therefore, a stochastic model is promising to simulate this uncertainty. Recent works provided a variety of methods to model stochastic characteristics of a bundle, which can be divided to two main groups, according to different approximation approaches for non-uniform transmission lines [2]. The first group method is based on MTL theory to approximate a cable bundle with cascaded uniform segments. "Monte Carlo" method [3] is introduced to divide a cable bundle into non-uniform segments of which 2-D cross sections are identical, but the positions of the wires are randomly interchanged from segment to segment. This model produces geometrical conflicts due to the uncorrelated sequence of cross sections. The "Random Mid-point Displacement" [4] and "Random Displacement Spline Interpolation" [5] are employed to improve model precision. The second group method approximates the non-uniform transmission line by specific numerical method, for example "Taylor Series Expansion Method" [6], "Chebyshev Expansion Method" [7] and "Green Function Expansion Method" [8]. The common feature of these methods is to approximate non-uniform transmission lines through smooth specific functions. However, the computation time is often long due to the applied high order approximation smooth functions. This work aims to investigate the influence to radiated emissions from random wire positions in a bundle. The wire position distribution with statistical manner is analyzed. Then, *spline* interpolation function is used to smooth position function of wires in a bundle. Cascaded approximation from the first group methodology and Chebyshev expansion approximation from the second group methodology are both applied to model a non-uniform transmission line. In essence, a stochastic cable bundle model is a set of deterministic non-uniform MTLs (Multiconductor Transmission Line) characterized with different TL (Transmission Line) parameters. Each deterministic MTL model could derive a deterministic solution of Common-Mode (CM) current distribution. Thereby, the stochastic radiation results can be calculated from a set of CM currents from non-uniform MTL models, which have different TL characteristic impedances and propagation constants.

II. APPROXIMATION METHODS FOR NON-UNIFORM TRANSMISSION LINES

In the MTLs, voltage and current on each wire are dependent on the other wires due to the coupling effects

Submitted On: January 5, 2016
Accepted On: February 25, 2016

between wires. Considering termination boundary conditions, a generalized two-port network representation for a MTL can be shown in Fig. 1.

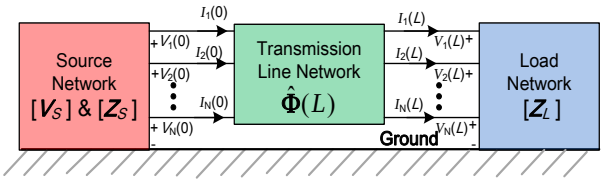

Fig. 1. Characterization of multiconductor transmission line (*N+1*-wire) as a generalized two-port.

Being analogy with two-wire transmission line, *N*×*1*-dimension vectors ***Vs*** contain the effects of the independent voltage and current sources in the source network. While the *N*×*N*-dimension ***Zs*** and ***ZL*** matrices contain the effects of the impedance in the terminal networks. Chain-parameter matrix, which can be extended to represent (*N*+1)-wire MTL, is defined by [2]:

$$\left[\hat{\boldsymbol{\Phi}}(L)\right]=\begin{bmatrix}\cosh(\sqrt{\boldsymbol{Z}'\boldsymbol{Y}'}L) & -\boldsymbol{Z}_C\sinh(\sqrt{\boldsymbol{Y}'\boldsymbol{Z}'}L)\\ -\boldsymbol{Y}_C\sinh(\sqrt{\boldsymbol{Z}'\boldsymbol{Y}'}L) & \cosh(\sqrt{\boldsymbol{Y}'\boldsymbol{Z}'}L)\end{bmatrix}. \quad (1)$$

Here ***Z′*** and ***Y′*** indicate per-unit-length impedance matrix and admittance matrix respectively; the characteristic impedance ***ZC*** and admittance matrices ***YC*** can be derived from trough diagonalizing ***Z′Y′*** and ***Y′Z′*** simultaneously [9]. In order to achieve the final stochastic model for a cable bundle, the first step is to model non-uniform transmission line. Cascaded approximation and Chebyshev expansion approximation are both used to solve telegraphic equations of MTL.

A. Cascaded approximation

Non-uniform TLs indicate that the cross-sectional dimensions or the wires positions vary along the wire axis. In this work the latter is only considered, which means the proposed stochastic model is based on the assumption the cross-sectional dimension of the bundle is identical. Considering real automotive bundles, this assumption is reasonable. Due to the variability of wire positions, the per-unit-length impedance ***Z′*** and admittance matrix ***Y′*** of MTL become functions of position *z*, denoted by ***Z′***(*z*) and ***Y′***(*z*). Therefore the MTL with non-uniform TLs can be described by non-constant coefficient differential equations:

$$\frac{\partial}{\partial z}\boldsymbol{V}(z)+\boldsymbol{Z}'(z)\boldsymbol{I}(z)=0, \quad (2)$$

$$\frac{\partial}{\partial z}\boldsymbol{I}(z)+\boldsymbol{Y}'(z)\boldsymbol{V}(z)=0, \quad (3)$$

V(*z*) and ***I***(*z*) are wire voltage and current vectors on the position *z*. Differential equations above is of great difficulty on the solution in mathematics, due to the nonlinearity property. Alternatively a set of short uniform sections could be a simple solution to represent the entire non-uniform MTL. This approach neglects the interaction between each two sections, but enough precision could be achieved through sufficient divisions of lines. Chain-parameter $\hat{\boldsymbol{\Phi}}(L)$ can associate the two port quantities of MTL as shown in Fig. 3:

$$\begin{bmatrix}\boldsymbol{V}(L)\\ \boldsymbol{I}(L)\end{bmatrix}=\left[\hat{\boldsymbol{\Phi}}(L)\right]\begin{bmatrix}\boldsymbol{V}(0)\\ \boldsymbol{I}(0)\end{bmatrix}=\begin{bmatrix}\boldsymbol{\Phi}_{11} & \boldsymbol{\Phi}_{12}\\ \boldsymbol{\Phi}_{21} & \boldsymbol{\Phi}_{22}\end{bmatrix}\begin{bmatrix}\boldsymbol{V}(0)\\ \boldsymbol{I}(0)\end{bmatrix}. \quad (4)$$

According to cascaded principle [2], the total chain-parameter $\hat{\boldsymbol{\Phi}}(L)$ for entire wires can be calculated as the product of the chain-parameter of the individual uniform segments:

$$\begin{aligned}\hat{\boldsymbol{\Phi}}(L)&=\hat{\boldsymbol{\Phi}}_1(\Delta z_1)\times\cdots\times\hat{\boldsymbol{\Phi}}_i(\Delta z_i)\times\cdots\times\hat{\boldsymbol{\Phi}}_n(\Delta z_n)\\ &=\prod_{i=1}^{n}\hat{\boldsymbol{\Phi}}_i(\Delta z_i)\end{aligned}. \quad (5)$$

Figure 2 illustrates the basic principle of breaking the non-uniform MTL into a cascade of sections, each of which can be modeled approximately as a uniform segment characterized by a chain-parameter matrix $\hat{\boldsymbol{\Phi}}_i(\Delta z_i)$. Due to each chain-parameter matrix associating voltages and currents of corresponding two ports, we can extract voltages and currents at interior points when MTL incorporated with terminal constraints at bundle ends. For example, the voltages and currents at the left port of the second subsection can be calculated from the terminal voltages and currents as:

$$\begin{bmatrix}\mathbf{V}(z_2)\\ \mathbf{I}(z_2)\end{bmatrix}=\hat{\Phi}_1(\Delta z_1)\times\hat{\Phi}_2(\Delta z_2)\begin{bmatrix}\mathbf{V}(0)\\ \mathbf{I}(0)\end{bmatrix}. \quad (6)$$

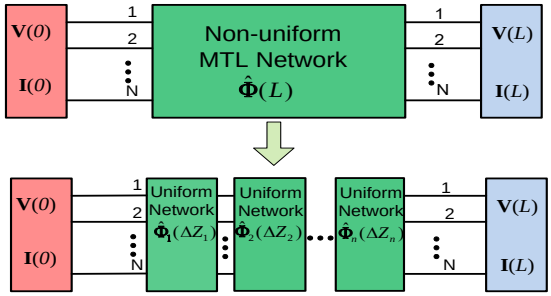

Fig. 2. Cascade approximation of entire chain-parameter.

B. Chebyshev expansion approximation

Compared with cascaded approximation method, Chebyshev expansion method [7] provides different approach to model the non-uniform MTL. This method directly solve nonlinear differential equations of MTL in (2) and (3). For example, ***V***(*z*) and ***I***(*z*) are defined by column-vectors of wire voltages and currents in a *N*-wire MTL:

$$\boldsymbol{V}(z)=\left[V_1(z),V_2(z),\cdots,V_i(z),\cdots,V_N(z)\right]^t, \quad (7)$$

$$\boldsymbol{I}(z)=\left[I_1(z),I_2(z),\cdots,I_i(z),\cdots,I_N(z)\right]^t, \quad (8)$$

$\boldsymbol{Z'}(z) = [Z_{i,j}(z)]$ and $\boldsymbol{Y'}(z) = [Y_{i,j}(z)]$ are the $N\times N$ per-unit-length impedance and admittance matrices. From these expressions, transmission line variables are functions of position z. In mathematics, any piecewise smooth and continuous function $F(z)$ can be expanded into an infinite series of Chebyshev polynomial functions [$T_k(z) = \cos(k\cos^{-1}z)$] [10]:

$$F(z)=\frac{1}{2}F^{(0)}+\sum_{k=1}^{\infty}F^{(k)}T_k(z). \quad (9)$$

Thereby transmission line variables $V_i(z)$, $I_i(z)$, $Z_{i,j}(z)$ and $Y_{i,j}(z)$ can be approximated by Chebyshev series with (M+1) elements, respectively:

$$\begin{aligned} V_i(z)&\approx\frac{1}{2}V_i^{(0)}+\sum_{k=1}^{M}V_i^{(k)}T_k(z)\\ I_i(z)&\approx\frac{1}{2}I_i^{(0)}+\sum_{k=1}^{M}I_i^{(k)}T_k(z)\\ Z_{i,j}(z)&\approx\frac{1}{2}Z_{i,j}{}^{(0)}+\sum_{k=1}^{2M}Z_{i,j}{}^{(k)}T_k(z)\\ Y_{i,j}(z)&\approx\frac{1}{2}Y_{i,j}{}^{(0)}+\sum_{k=1}^{2M}Y_{i,j}{}^{(k)}T_k(z) \end{aligned}, \quad (10)$$

where $V_i^{(k)}$, $I_i^{(k)}$, $Z_{i,j}{}^{(k)}$, $Y_{i,j}{}^{(k)}$ are Chebyshev coefficients. Using the vector notations the Chebyshev coefficients for wire voltage and current are defined by:

$$\boldsymbol{V}_i=[\frac{1}{2}V_i^{(0)},V_i^{(1)},V_i^{(2)},\cdots,V_i^{(\mathrm{M})}]^t, \quad (11)$$

$$\boldsymbol{I}_i=[\frac{1}{2}I_i^{(0)},I_i^{(1)},I_i^{(2)},\cdots,I_i^{(\mathrm{M})}]^t. \quad (12)$$

Substituting voltage and current quantities by (11)-(12), and implementing the orthogonal property and the multiplication rule of Chebyshev polynomial functions $T_k(z)$, non-constant coefficient differential Equation (2) can be transformed into [7]:

$$\begin{bmatrix}0_M & Q_M\\ 0 & 0_M^t\end{bmatrix}\boldsymbol{V}_i+\sum_{k=1}^{N}[Z_{i,k}]\boldsymbol{I}_k=0, \quad (13)$$

where $[Z_{i,k}]$, ($k = 1, 2, \ldots, N$) are (M+1)×(M+1) matrices with $(p,q)^{\text{th}}$ element defined below:

$$[Z_{i,k}]_{p,q}=\frac{1}{2}[Z_{i,k}{}^{(|p-q|)}+Z_{i,k}{}^{(|p+q-2|)}]. \quad (14)$$

And 0_M is an M×1 column vector with all zero elements and $\boldsymbol{Q}_M$ is an M×M matrix, which is defined in [7]. Assembling (13) for all $k = 1, 2, \ldots, N$, we can obtain the matrix formulation for the N-conductor system:

$$\hat{\mathbf{Q}}\hat{\mathbf{V}}+\hat{\mathbf{Z}}\hat{\mathbf{I}}=\mathbf{0}, \quad (15)$$

where

$$\begin{aligned} \hat{\mathbf{V}}&=[\boldsymbol{V}_1,\boldsymbol{V}_2,\cdots,\boldsymbol{V}_j,\cdots,\boldsymbol{V}_N]^t\\ \hat{\mathbf{I}}&=[\boldsymbol{I}_1,\boldsymbol{I}_2,\cdots,\boldsymbol{I}_j,\cdots,\boldsymbol{I}_N]^t \end{aligned}, \quad (16)$$

$\hat{\mathbf{V}}$ and $\hat{\mathbf{I}}$ are N(M+1)×1 column based on wire voltage and current (7) and (8). $\hat{\mathbf{Q}}$ consists of N-block of (M+1)×(M+1) Q-matrix:

$$\hat{\mathbf{Q}}=\begin{bmatrix}\mathbf{Q} & & & \\ & \mathbf{Q} & & \\ & & \ddots & \\ & & & \mathbf{Q}\end{bmatrix}_{[N(M+1)]\times[N(M+1]}\quad\left(\mathbf{Q}=\begin{bmatrix}0_M & Q_M\\ 0 & 0_M^t\end{bmatrix}\right). \quad (17)$$

$\hat{\mathbf{Z}}$ is constructed from the $[Z_{i,k}]$ matrix defined in (14):

$$\hat{\mathbf{Z}}=\begin{bmatrix}[Z_{1,1}] & [Z_{1,2}] & \cdots & [Z_{1,N}]\\ [Z_{2,1}] & [Z_{2,2}] & \cdots & [Z_{2,N}]\\ \vdots & \vdots & \ddots & \vdots\\ [Z_{N,1}] & [Z_{N,2}] & \cdots & [Z_{N,N}]\end{bmatrix}. \quad (18)$$

Similarly, the transmission-line Equation (3) also can be transformed into following formulation:

$$\hat{\mathbf{Q}}\hat{\mathbf{I}}+\hat{\mathbf{Y}}\hat{\mathbf{V}}=\mathbf{0}. \quad (19)$$

Therefore, the non-linear differential Equations (2) and (3) of MTL can be approximated by (15) and (19) through Chebyshev expansion. Considering the incorporated termination conditions of the transmission lines network, as shown in Fig. 1, the **V**s is the source matrix for N-conductor MTL, $\boldsymbol{Z}_S$ and $\boldsymbol{Z}_L$ are the impedance matrix of source and load terminations, we can obtain (20) through combining with (15) and (19). By solving equation system (20), Chebyshev coefficients $\hat{\mathbf{V}}$ and $\hat{\mathbf{I}}$ in (16) can be obtained, which can be further used to calculate the wire voltages and currents via (10):

$$\begin{bmatrix}\hat{\mathbf{Y}} & \hat{\mathbf{Q}}\\ \hat{\mathbf{Q}} & \hat{\mathbf{Z}}\\ \hat{\mathbf{E}}_\mathbf{n} & \mathbf{Z}_S\hat{\mathbf{E}}_\mathbf{n}\\ \left|\hat{\mathbf{E}}_\mathbf{n}\right| & -\mathbf{Z}_L\left|\hat{\mathbf{E}}_\mathbf{n}\right|\end{bmatrix}\begin{bmatrix}\hat{\mathbf{V}}\\ \hat{\mathbf{I}}\end{bmatrix}=\begin{bmatrix}\mathbf{0}\\ \mathbf{0}\\ \mathbf{V}\mathrm{s}\\ \mathbf{0}\end{bmatrix}. \quad (20)$$

Here, $\hat{\mathbf{E}}_\mathbf{n}$ is N×[N(M+1)] diagonal block matrix, of which each block is given by [7].

III. STOCHASTIC RADIATION MODEL OF CABLE BUNDLE

Stochastic model of a cable bundle, in essence, produces a set of deterministic non-uniform transmission lines randomly. The section above provides two different approximation approaches for a non-uniform transmission lines. This section discusses the wire position distribution norm via statistical manner, and proposes a determination method for the needed transmission line parameters in simulations.

A. Stochastic distribution of wire position

The wires positions in a cable bundle are usually difficult to be determined. However the wire beginning and the wire end connected to terminations are definite. Moreover, initial wire positions in a cable bundle are

distributed stochastically, but they are limited by the radius of cable bundle, as shown in Fig. 3 (a).

Here, z is the wire axial coordination; x and y are the cross-sectional coordination. In mathematics, a deterministic position distribution can be produced according "Gaussian" law instead of an absolute random position. After determining initial positions, other more positions can be interpolated through *Spline* function, which can improve the continuity of final constructed wire model [5], as shown in Fig. 3 (b). When the coordinates of variable wire positions are determined, cascaded method can further approximates the wire as a set of uniform sub-segments; or Chebyshev expansion method provides other solution to fit non-uniform transmission lines through smooth Chebyshev polynomial functions, as shown in Fig. 3 (c).

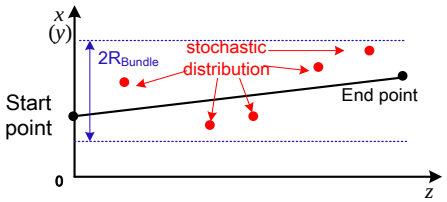

(a) Initial stochastic positions of a wire

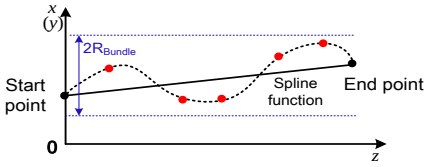

(b) Wire positions after *Spline* function

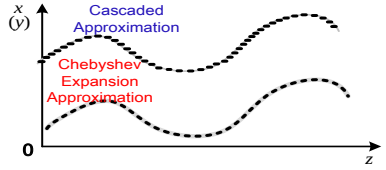

(c) Cascaded or Chebyshev expansion approximation for a wire

Fig. 3. Process illustration for modeling random wires position in a cable bundle.

B. Per-unit-length parameters

Varying wire positions in a bundle lead to non-constant of impedance and admittance matrix in telegraphic Equations (2) and (3). Numeric methods such as Finite Element Method (FEM) could acquire these parameters accurately. However, the computation time is a challenge, due to the cable bundle possibly consisting of dozens of wires for each deterministic non-uniform MTL case. Thereby, a simple approach for the TL-parameters determination is necessary. When the diameters of all the wires inside the bundle are the same and 2-D cross section of the bundle is invariant along the axial direction, the evaluation of $\boldsymbol{Z}'(z)\&\boldsymbol{Y}'(z)$ matrices only needs to be performed once. And then these determined $\boldsymbol{Z}'(z)\&\boldsymbol{Y}'(z)$ matrices can be used as basis for evaluating new impedance and admittance matrices for other segments with different wire positions. Figure 4 gives the 'wire method', which illustrates how to obtain new $\boldsymbol{Z}'(z)\&\boldsymbol{Y}'(z)$ matrices from the known impedance and admittance information [11].

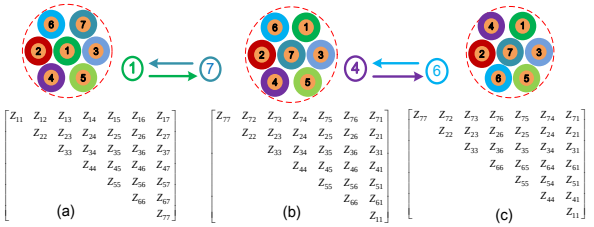

Fig. 4. Per-unit-length parameter matrix interexchange with 'wire method'.

For implementing this method, we first determine the original coordinates of wires center in a cable bundle with known $\boldsymbol{Z}'(z)\&\boldsymbol{Y}'(z)$ matrices. Then "Gaussian" law is used to produce stochastic coordinates of wire center positions. Through comparing the distance between new coordinate of wire center to original wire centers, we choose the original wire center, of which the distance is shortest to the new coordinate, as the new position of the wire.

C. Common-mode current and radiation model

After determining the parameters matrices of the cable bundle, telegraphic Equations (2) and (3) of non-uniform MTL can be solved equivalently by 'Cascaded approximation method' or directly through 'Chebyshev expansion method' for each deterministic case in stochastic analysis. Subsequently CM current at each segment, the sum of currents on the wires in this segment, can be calculated. And then each segment with known CM current can predict the radiated emission according to electric dipole model [12]. For example the y-component field is given by:

$$H_y^d = \frac{-IdL\cdot x}{4\pi r}\beta_0^2\left(j\frac{1}{\beta_0 r}+\frac{1}{\beta_0^2 r^2}\right)e^{-j\beta_0 r}, \tag{21}$$

$$E_y^d = \frac{IdL\cdot zy}{4\pi r^2}\eta_0\beta_0^2\left(j\frac{1}{\beta_0 r}+\frac{3}{\beta_0^2 r^2}-j\frac{3}{\beta_0^3 r^3}\right)e^{-j\beta_0 r}, \tag{22}$$

where r is the distance from the dipole to the observation point P; ε_0 is the dielectric constant of the vacuum; dL is dipole length; I is the current through the modeled segment; η_0 (377 Ω) is the wave impedance in the vacuum; β_0 ($2\pi/\lambda$) is the electromagnetic wave phase constant in the vacuum. Radiation from a cable bundle can be calculated by superposition, as shown in Fig. 5. Therefore, stochastic radiation model of a cable bundle should include a set of deterministic radiation models

with different CM current distribution.

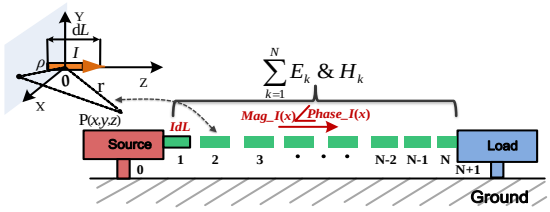

Fig. 5. Radiation from a cable bundle due to CM current.

IV. RESULTS AND EXPERIMENTS

In order to verify the proposed cascaded method and Chebyshev expansion method for modeling a non-uniform transmission line, a MTL model with analytic solution is investigated firstly, of which transmission line parameters are parabolic functions with respect to the position. Moreover, the stochastic characteristics of a real cable bundle with random wires are evaluated through simulation and measurement.

A. Parabolic multiconductor transmission line

MTL with terminations can be shown in Fig. 6 (left).

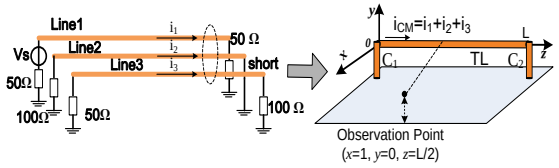

Fig. 6. Parabolic MTL with terminations (left) and its common-mode radiation model (right).

The parabolic transmission line parameters are characterized by the functions with position z:

$$\mathbf{Z}'(z, j\omega) = (1+az)^2\left[j\omega\mathbf{L} + \mathbf{R}r(\omega)\right]$$
$$\mathbf{Y}'(z, j\omega) = (1+az)^2\left[j\omega\mathbf{C} + \mathbf{G}\right] \quad , \qquad (23)$$

where

$$\mathbf{L} = \frac{1}{3600}\begin{bmatrix} 87 & 25 & 23 \\ 25 & 85 & 25 \\ 23 & 25 & 87 \end{bmatrix} \mu H/cm \qquad \mathbf{R} = diag\left[\frac{5}{12}, \frac{5}{12}, \frac{5}{12}\right] \Omega/cm$$

$$\mathbf{C} = \frac{1}{324}\begin{bmatrix} 68 & -40 & -13 \\ -40 & 95 & -40 \\ -13 & -40 & 68 \end{bmatrix} pF/cm \qquad \mathbf{G} = diag\left[\frac{3}{5.12e^6}, \frac{3}{5.12e^6}, \frac{3}{5.12e^6}\right] (\Omega \cdot cm)^{-1}. \qquad (24)$$

We analyze a general parabolic coupled transmission lines of the tapering factor a = 0.1, line length L = 2 m and $r(\omega) = r_0 + r_1\sqrt{\omega}$ for simulation of the skin-effect [13]. In cascade approximation method, the line is divided into 100 short segments. While in Chebyshev expansion method, the transmission line parameter matrices $\boldsymbol{Z}'(z, j\omega)$&$\boldsymbol{Y}'(z, j\omega)$ in (23) are expanded into 30 Chebyshev polynomial functions of position z at each frequency point according to (9). Since the high-order Chebyshev polynomial function might bring computation efficiency problem, cascaded approximation for non-uniform MTL takes more advantages when the bundle divided into enough short segments. Figure 7 depicts current at the middle position on line-3 by cascaded method, Chebyshev expansion method and analytic method from 1 MHz to 500 MHz, respectively. The analytic solution is referred to [14].

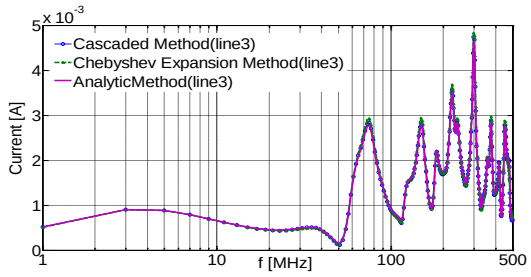

Fig. 7. Current at the middle position on line-3.

Currents on the line-3 at 200 MHz from these three methods are compared in Fig. 8. After obtaining currents on each line, CM current can be calculated by summing these line currents. Then, the radiation from the transmission lines can be evaluated with a set of short dipoles as shown in Fig. 5. Electric field in y-direction at the observation point (1 meter distant to the cable bundle) is further calculated as shown in Fig. 9. It can be seen that the results from proposed methods can match well with the analytic method.

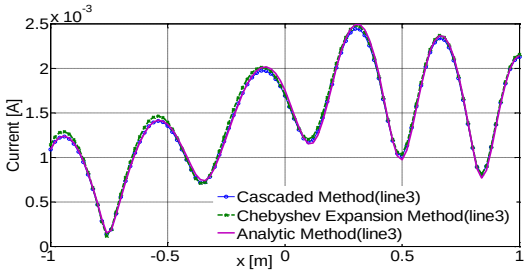

Fig. 8. Current of 200 MHz on line-3.

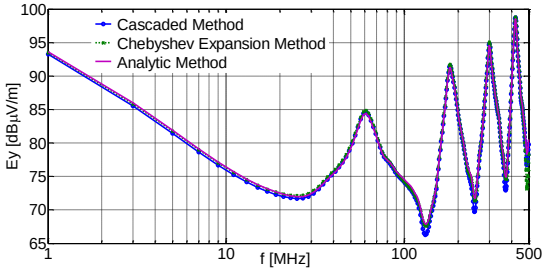

Fig. 9. Radiated emission at the observation point from parabolic transmission lines.

B. Cable bundle with random wires

In this section, CM current distribution and radiated emissions from a real cable bundle with seven random wires are investigated. Average height of the cable bundle to the ground plate is 5 cm. Diameter of each wire in the bundle is 1.2 mm, and the conductor diameter is about 0.8 mm. The detailed geometry of 2D cross section of bundle and experimental setup are shown in Fig. 10.

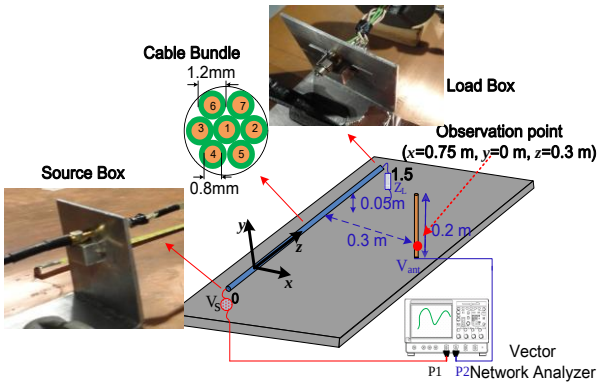

Fig. 10. Simulation and measurement configuration for a cable bundle with random wires.

The wires are terminated randomly with different resistors. In source box, one wire is driven by port 1 (P1) of a vector network analyzer (VNA); Port 2 (P2) of VNA is connected to a short rod antenna to measure electric field or a current probe to measure CM current. In the simulation and experiment, 140 different scenarios with random wire positions are implemented stochastically. Considering simulation efficiency, non-uniform transmission line in each scenario is approximated by the cascaded method. And the bundle is divided into 100 small segments. The random packed wires in cable bundles lead to non-deterministic wire position distributions in the cross sections. Stochastic non-uniform wire is difficult to be modeled via MoM and other numeric methods. Therefore with a certain stochastic function to describe random wire position, a set of deterministic non-uniform MTL can be obtained. Each non-uniform MTL produces a solution according to proposed cascaded approximation method and per-unit-length parameter deterministic method proposed above. Here stochastic-simulation sample number is 140 and total simulation time is 3.09 hours. To verify the proposed bundle stochastic-model, 140 different measurements were implemented through changing wire positions manually. CM currents at start point (beside source box), middle point and end point (beside load box) of the bundle were simulated and measured with a RF current probe. E-field at the observation point was also calculated and measured through a short rod antenna. Figure 11 shows the simulated and the measured stochastic-data distribution from 1 MHz to 1000 MHz. Maximal, mean and minimal envelop of these data are denoted. From these curves, envelop magnitudes and the main resonance frequencies from simulations and measurements agree well, which means the stochastic characteristic of a real cable bundle is close to proposed simulation model.

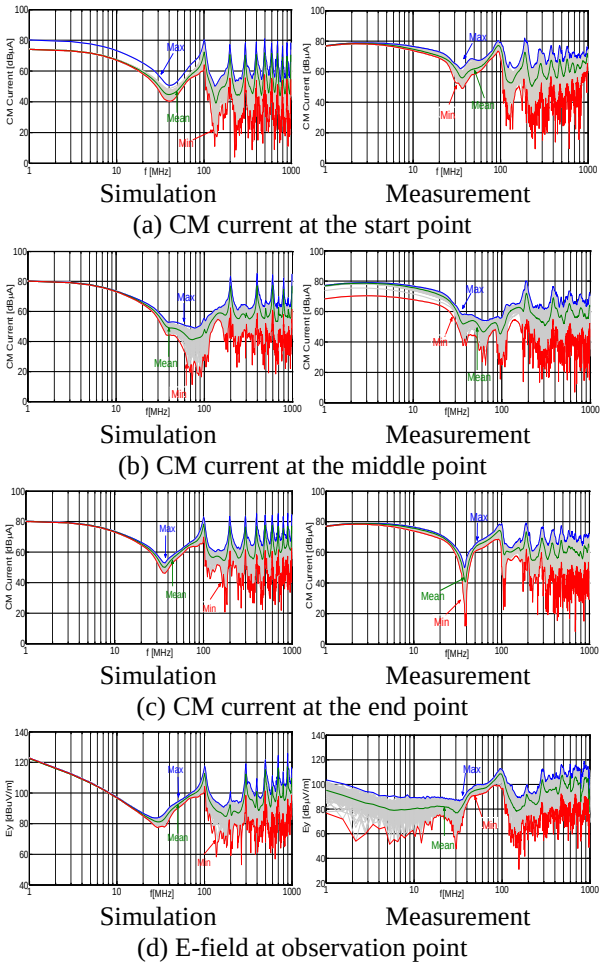

Fig. 11. Simulation *vs.* measurement of common-mode (CM) currents and E-fields from the stochastic scenario.

Further we compared the maximal, mean and minimal envelops of CM current at the bundle middle point from simulation and measurement stochastic data in Fig. 12. Basically simulated maximal and mean envelopes from 1 MHz to 1000 MHz can match well with measurements; minimal envelop except below 20 MHz can also agree well with measurements. However, the simulated peaks on the maximal and mean envelopes are higher than the measured peaks at frequencies of $N \bullet 200$ MHz (N = 1, 2, 3, 4, 5). The reason for the deviation is that MTL based simulation in this work did not consider line loss and the parasitic capacitance and inductance in source and load box.

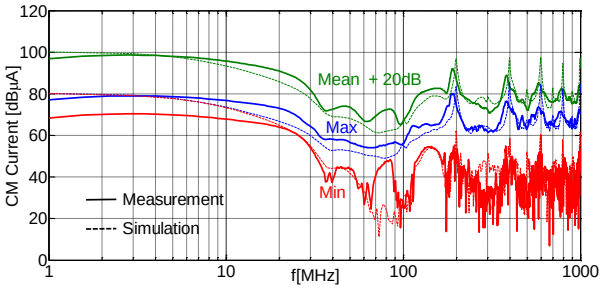

Fig. 12. Statistical analysis (Max, Mean, and Min) of CM current at the middle point on the cable bundle.

Probability density function (PDF) [15] and cumulative distribution function (CDF) [16] were also evaluated from simulated and measured CM current stochastic data. These two statistical indicators at 250 MHz were shown in Fig. 13. It can be seen that PDF from measured data express the normal distribution with mean value of 55.64 dBμA, while simulation mean value of 53.25 dBμA. CDF curves from simulated and measured data are close, which can indicate possible maximal boundary. Appearance of maximal value of common-mode current simulation data at middle point of cable bundle (250 MHz) locates at 60.35 dBμA; while appearance of maximal measured data locates at 63.22 dBμA. Similarly the maximal, mean and minimal envelopes of electric field at observation point from simulation and measurement stochastic data were compared in Fig. 14. These envelopes of electric field from 30 MHz to 1000 MHz agree well between simulated data and measured data. At low frequencies, since the used electric dipole model is sensitive to the current accuracy, the relative small error of dipole current might lead to a big difference at electric fields. Furthermore, the lower is the frequency; the bigger is the field deviation. This error can be also observed in the verification example used in [5]. Further PDF and CDF of stochastic electric field at 250 MHz from simulated and measured data are shown in Fig. 15. It can be seen that PDF from measured data expresses the normal distribution with mean value of 81.29 dBμV/m, while simulated mean value of 84.03 dBμV/m. From CDF curves from simulated and measured data, appearance of maximal value of simulation data locates at 91.03 dBμV/m; while appearance of maximal measured data locates at 94.52 dBμV/m. From simulated data, the stochastic wire position distribution (standard Gaussian rule applied in simulation) can result in CM current and field distribution obeying to lognormal rule; while from the real measured data, stochastic CM current and field due to random wire position changed manually also obey log-normal rule, but with different means and standard deviations compared with simulated data. Therefore it can be concluded that the stochastic radiation behavior of a real cable bundle due to random wire positions meets log-normal rule.

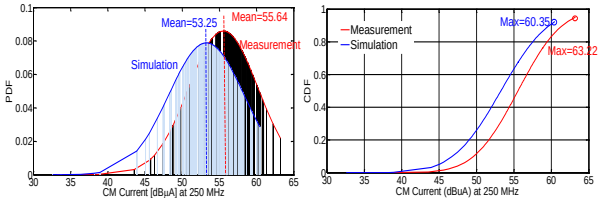

Fig. 13. Statistical analysis (PDF and CDF) of CM current at the middle point on the cable bundle (250 MHz).

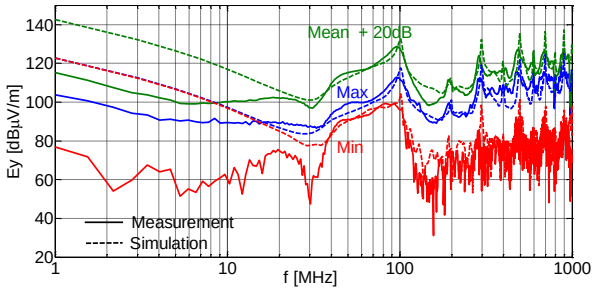

Fig. 14. Statistical analysis (Max, Mean, and Min) of E-field at the field observation point.

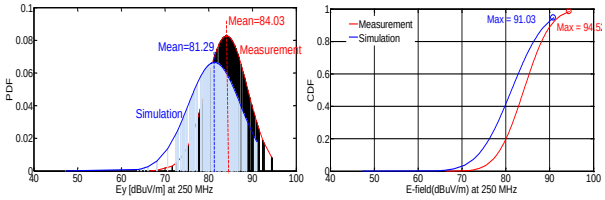

Fig. 15. Statistical analysis (PDF and CDF) of the E-field at the field observation point (250 MHz).

V. CONCLUSION

In this work, stochastic simulation models of a cable bundle were proposed based on two different approximation approaches for non-uniform transmission lines: cascaded approximation method and Chebyshev expansion method. Stochastic cable bundle model, in essence, included a set of deterministic non-uniform MTL due to random wire positions. Each non-uniform MTL can be approximated by the cascaded method through dividing them into short uniform segment; or the non-linear differential Equations (2)–(3) were directly solved by Chebyshev polynomial expansion method. This two approximation methods essentially differ from each other. One method divided the non-uniform MTL into small uniform segments physically, hence it might induce discontinuity between each two adjacent segments. The other method approximated non-linear parameters of differential equations mathematically,

thereby the high order approximation smooth polynomial functions might have computation efficiency problem. Both approximation methods were verified through a parabolic MTL with analytic solutions. Subsequently, a more general cable bundle was investigated through simulation and experiment in perspective of statistic.

ACKNOWLEDGMENT

This work was supported in part by the project of Research on Smart Internet of Vehicle and Key Components Testing Technology (Nr. cstc2015zdcy-ztzx60005).

REFERENCES

[1] *Vehicles, Boats and Internal Combustion Engines-Radio Disturbance Characteristics – Limits and Methods of Measurements for the Protection of On-board Receivers*, CISPR 25, ed. 3, 2007.

[2] C. R. Paul, *Analysis of Multiconductor Transmission Lines*, John Wiley & Sons, Inc., 2007.

[3] S. Shiran, B. Reiser, and H. Cory, "A probabilistic model for the evaluation of coupling between transmission lines," *IEEE Trans. Electromagn. Compat.*, vol. 35, no. 3, pp. 387-393, Aug. 1993.

[4] S. Salio, F. Canavero, D. Lecointe, and W. Tabbara, "Crosstalk prediction on wire bundles by kriging approach," *IEEE Int. Symp. Electrom. Compat.*, Washington, pp. 197-202, Aug. 2000.

[5] S. Sun, G. Liu, J. L. Drewniak, D. J. Pommerenke, "Hand-assembled cable bundle modeling for crosstalk and common-mode radiation prediction," *IEEE Trans. Electrom. Compat.*, vol. 49, no. 3, pp. 708-718, 2007.

[6] M. Khalaj-Amirhosseini, "Analysis of coupled nonuniform transmission lines using Taylor series expansion," *IEEE Trans. Electrom. Compat.*, vol. 48, no. 3, pp. 594-600, Aug. 2006.

[7] F. Y. Chang, "Transient simulation of frequency-dependent nonuniform coupled lossy transmission lines," *IEEE Trans. Comp. Pack. Manuf. Tech.*, vol. 17, no. 1, pp. 3-14, Feb. 1994.

[8] G. Antonini, "A dyadic Green's function based method for the transient analysis of lossy and dispersive multiconductor transmission lines," *IEEE Trans. Microwave Theory Tech.*, vol. 56, no. 4, pp. 880-895, Apr. 2008.

[9] M. T. Frederick, V. I. Michel, and K. Torbjörn, *EMC Analysis Methods and Computation Models*, John Wiley & Sons, Inc., 1997.

[10] O. A. Palusinski and A. Lee, "Analysis of transients in nonuniform and uniform multiconductor transmission lines," *IEEE Trans. Microwave Theory Tech.*, vol. 37, no. 1, pp. 127-138, Jan. 1989.

[11] M. Gonser, C. Keller, J. Hansen, and R. Weigel, "Advanced simulations of automotive EMC measurement setups using stochastic cable bundle models," *2010 Asia-Pacific Int. Symp. Electrom. Compat., Beijing*, Apr. 2010.

[12] C. R. Paul, *Introduction to Electromagnetic Compatibility*, New York: Wiley & Sons, Inc., 1992.

[13] N. S. Nahman and D. R. Holt, "Transient analysis of coaxial cables using the skin effect approximation A+B $\sqrt{s}$," *IEEE Trans. On Circuit Theory.*, vol. CT-19, pp. 443-451, Sept. 1972.

[14] F. Y. Chang, "Transient simulation of non-uniform coupled lossy transmission lines characterized with frequency-dependent parameters, Part I : Waveform relaxation analysis," *IEEE Trans. Circuits and Syst.*, vol. 39, pp. 585-603, Aug. 1992.

[15] N. G. Ushakov, *Density of a Probability Distribution*, Encyclopedia of Mathematics, Springer, 2001.

[16] D. Zwillinger and K. Stephan, *CRC Standard Probability and Statistics Table and Formula*, CRC Press, 2010.

Jin Jia received his Ph.D. degree in Electrical Engineering from the TU Dortmund University, Germany, in 2015. Now he works as EMC Engineer in China Automotive Engineering Research Institute (CAERI), Chongqing, China. His main research interests include radiation modeling of complex cable bundles and EMC modeling of automotive electrical and electronic systems.

Zhida Lai was born in Guangdong Province, China, in 1962. Currently, he is Senior Engineer and Leader of EMC Department Automotive Engineering Research Institute (CAERI), Chongqing, China. In addition, he is the Member of China National Radio Interference Standardization Committee (SAC/TC79/SC4).

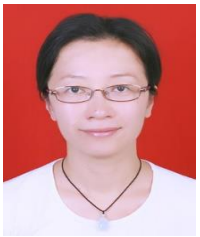

Jianmei Lei received her Ph.D. from Chongqing University in 2007. She finished her post Ph.D. Research at Chang'an Automotive Engineering Institute in 2011. Now she is the Assistant Chief Engineer of EMC Department in China Automotive Engineering Research Institute Co., Ltd.

Wang Quandi was born in Anhui Province, China, in 1954. She received her Ph.D. degree in College of Electrical Engineering from Chongqing University, Chongqing, China, in 1998. Currently, she is Professor in College of Electrical Engineering Chongqing University in China. Her main research interests are simulation and numerical computation of electromagnetic field, automotive EMC.

Compact and Planar WCDMA/WLAN/UWB Antenna with Shorted Loop and Monopole Elements

Bahadır S. Yıldırım [1], Erkul Başaran [2], and Bahattin Türetken [3]

[1] Department of Electrical and Electronics Engineering
Muğla Sıtkı Koçman University, Muğla, 48000, Turkey
bahadir.yildirim@mu.edu.tr

[2] Department of Electrical and Electronics Engineering
Piri Reis University, Tuzla, İstanbul, 34940, Turkey
ebasaran@pirireis.edu.tr

[3] Department of Electrical Engineering
University of Karabük, Karabük, Turkey
bahattinturetken@karabuk.edu.tr

Abstract ─ A compact, planar, multiband antenna with loop and monopole elements suitable for wideband code division multiple access (WCDMA), wireless LAN (WLAN), and ultra wideband (UWB) wireless communications is presented in this paper. The antenna was built on FR4-type substrate and fed by a microstrip transmission line for easy integration with RF/microwave circuitry on the same circuit board. The physical low-band of the antenna includes 1.9–2.17-GHz WCDMA and 2.45-GHz WLAN bands, whereas the high-band spans from about 3.3 to about 11-GHz including 5-GHz WLAN, 3.1–10.6-GHz UWB, and 4–8-GHz C bands. Antenna S_{11} and radiation pattern measurements are presented. It's shown that measurements and simulations are in good agreement.

Index Terms ─ Antenna measurements, electromagnetic analysis, mobile antennas, wideband antennas.

I. INTRODUCTION

A compact and multiband antenna with planar loop and monopole elements printed on FR4-type substrate has been presented in this paper for wideband code division multiple access (WCDMA), wireless LAN (WLAN), and ultra wideband (UWB) wireless communications. Various loop-type antennas have been reported in the literature. These include a loop-type antenna with an L-shaped section operating for the 3–5.1-GHz section of the UWB spectrum [1], a vertically mounted loop-type antenna on a mobile phone printed circuit board (PCB) for the 3-6-GHz band [2], a capacitively-loaded loop antenna for mobile handsets suitable for 900/1800/1900/2100 MHz mobile and 2.45/5-GHz WLAN bands [3], and a loop antenna for 2.45-GHz WLAN band [4]. Unlike the antennas described in [1-4], the presented antenna offers a significantly wider bandwidth spanning from 1.9 to 2.6-GHz and then from about 3.3 to 11-GHz. For applications requiring full UWB spectrum of the 3.1–10.6-GHz band, a loop antenna with a complex CPW/CPS type transition [5] has been reported. However, the presented antenna is multiband, provides a 2.1-GHz WCDMA band in addition to the UWB band, and does not require a complex CPW/CPS transition for feeding the antenna. A CPW-fed half loop-type antenna operating from about 3 to 20-GHz [6] has also been reported. The presented antenna offers multiband operation including 2.1-GHz WCDMA functionality, and the size of its footprint is less then half than that of the antenna described in [6]. All these antennas [1-6] have a single loop element to generate the desired band whereas the presented antenna is a multi-element antenna. Multi-element antennas including loop and monopole elements have also been reported for GSM850/900 and GSM1800/1900/UMTS functionality of laptops [7]. The presented antenna differs from [7] by its WCDMA and UWB functionality.

The motive behind the presented antenna is to achieve a compact WCDMA/UWB antenna which can be integrated with RF/microwave circuitry on the same board. The antenna employs microstrip technology and a shorted loop-type element with a tapered feed to generate the wideband response as opposed to tapered monopole structures which are commonly used as classical wideband radiators. In addition, 2.1-GHz WCDMA and 2.45-GHz WLAN functionalities have been included using an L-shaped monopole element. Basically, the antenna has two physical bands; the lower band spans from about 1.9 to 2.6-GHz, and the high

Submitted On: October 21, 2015
Accepted On: February 26, 2016

band spans from about 3.3 to 11-GHz. The low-band accommodates the 1.9–2.17-MHz WCDMA and the 2.45-GHz WLAN bands whereas the high band includes the 3.1–10.6-GHz UWB, 5-GHz WLAN, and 4–8-GHz C bands. The presented antenna has a footprint of 25×25-mm² and is compact enough to be integrated with RF circuitry on the same circuit board. Multiband UWB antennas with smaller footprints exist and one such example has been reported in [8] which uses a diamond-shaped monopole with notches. However, the design reported in [8] does not provide WCDMA functionality. Analysis of the presented antenna was carried out using extensive full-wave electromagnetic simulations with Ansoft HFSS [9] and CST Microwave Studio [10]. Antenna S_{11} and radiation pattern measurements are presented to validate the simulations.

II. ANTENNA DESIGN

A. S11 measurements and simulations

The antenna was built on 62×64×1 (mm³) FR4 substrate using microstrip technology. Antenna geometry and a photograph of the fabricated antenna are shown in Fig. 1 and Fig. 2, respectively. The substrate material FR4 whose relative dielectric constant and loss tangent are 4.4 and 0.02, respectively, has been preferred over other substrates because it is a low-cost and widely available material.

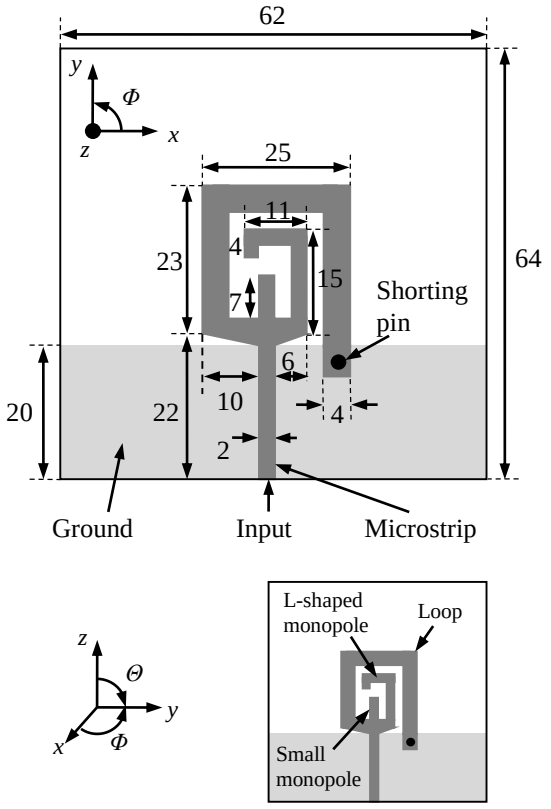

(a)

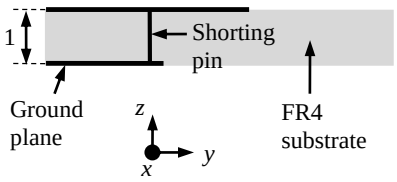

(b)

Fig. 1. Geometry of the antenna. All dimensions are in millimeters.

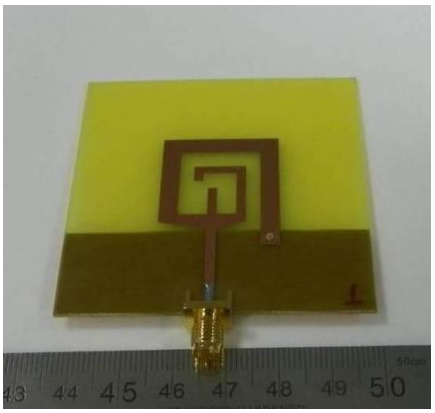

Fig. 2. Photograph of the fabricated antenna.

The antenna has three radiating elements as shown in Fig. 1 (a). Of these, the rectangular loop shaped element with tapered feed is shorted to the RF ground through a shorting pin. High-band response is primarily due to the shorted loop and the coupling between the shorted loop and monopoles. The low-band is generated primarily by the L-shaped monopole, and also due to the coupling between the L-shaped monopole and the loop. The L-shaped monopole resonates at about 0.5-λ, whereas the loop resonates at about 1-λ. First loop resonance is around 1.94-GHz. However, this resonance is weak in the sense that it does not produce a usable S_{11} bandwidth. The small monopole element improves matching from about 6 to 8-GHz. The width of the loop and monopole elements are 4-mm and 2-mm, respectively. These elements are fed by a 2-mm wide 50-Ω microstrip line. The transition from the feeding microstrip to the antenna has been tapered to improve the high-band matching. During the simulations, the shorting pin has been modeled as a 1.2-mm diameter copper tube, and top and bottom layer copper metallization has a thickness of 0.035-mm. For the fabricated antenna, a 1-mm diameter hole was drilled after the fabrication and filled with a conductive fluid which became solid after a while.

Antenna S_{11} measurements have been performed at TÜBİTAK (The Scientific and Technological Research Council of Turkey) BİLGEM (Center of Research for Advanced Technologies of Informatics and Security)

Antenna Test and Research Center using an Agilent E8362C 20-GHz PNA microwave network analyzer. Comparison of measured and simulated S_{11} responses of the antenna is shown in Fig. 3. Measurement and simulations agree well up to about 9.5-GHz. Above 9.5-GHz, measurement does not meet the industry standard -10 dB specification though it's still better than -6 dB up to 11-GHz. This problem may be due to the build quality of the SMA connector, fabrication process, substrate loss, and the shorting pin. Figure 4 shows the HFSS simulated effect of the SMA connector on the S_{11} response of the antenna from 7 to 11-GHz. It can be seen that there are slight variations in S_{11} response when the connector is present but no major variations exist. HFSS simulated effect of the short on the S_{11} response of the antenna has also been investigated by placing a 2.5-mm gap between the shorting pin and the loop to make the loop "open". Figure 5 shows that when the loop is open, the antenna does not have the low-band and the high-band starts from about 4.2-GHz.

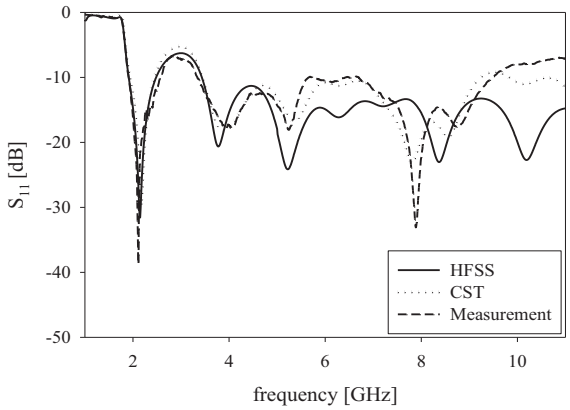

Fig. 3. Measured and simulated S_{11} response of the antenna.

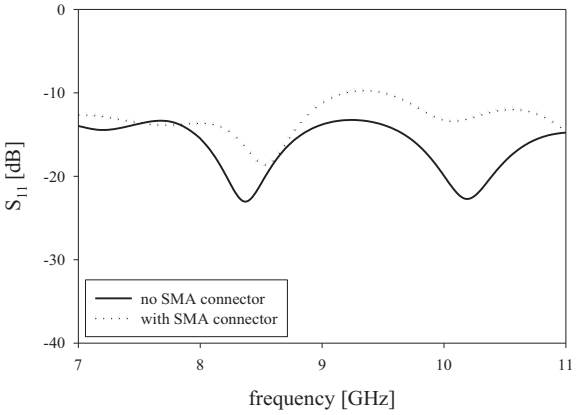

Fig. 4. Effect of the SMA connector on the S_{11} response of the antenna.

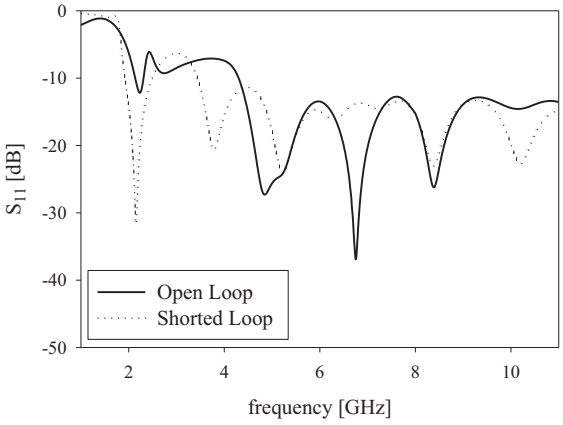

Fig. 5. Effect of the short on the S_{11} response of the antenna.

B. Radiation pattern measurements and simulations

Antenna radiation pattern measurements were performed at TÜBİTAK BİLGEM Antenna Test and Research Center using a wideband double-ridged horn antenna as the probe antenna. The distance between probe and test antennas was about 2.6 meters. The antenna is placed on a positioner that turns only from 0º to ±160º. For this reason, some measurement points were not available. Radiation patterns of the antenna at 2.1, 5.3, 8.1, and 10-GHz are shown in Figs. 6-9, respectively. The coordinate system for the indicated planes are shown in Fig. 1. For the *xy* plane radiation pattern, azimuth angle ϕ varies, whereas the elevation angle θ is set to 90°. For the *xz* plane radiation pattern, θ varies and ϕ=0°.

The probe antenna was in vertical polarization. Vertically polarized patterns have been measured in *xy* and *xz* planes, according to the coordinate system shown in Fig. 1. The peak antenna gains at 2, 5.3, 8.1, and 10-GHz are 2, 4.4, 3.3, and 4-dBi, respectively. The pattern exhibits many lobes at higher frequencies due to complex current distribution on the radiating element. The radiation pattern measurements are in very good agreement with CST and HFSS simulations. Slight discrepancies can be due to RF currents that are re-radiated by the feeding coaxial cable of the antenna and issues related to antenna alignment and positioning.

Antenna realized gain simulations by HFSS and gain measurements are shown in Fig. 10 at 2.1, 5.3, 8.1, and 10-GHz. Realized gain is the power gain of the antenna including mismatch losses. Since the antenna is driven through a microstrip transmission line, effect of this line has also been included in the realized gain. It can be observed from Fig. 10 that measured gain is about 1.0-dB higher than the simulated gain. This difference may be due to calibration issues related to anechoic

antenna chamber. The antenna has a good gain characteristic across the desired frequency range.

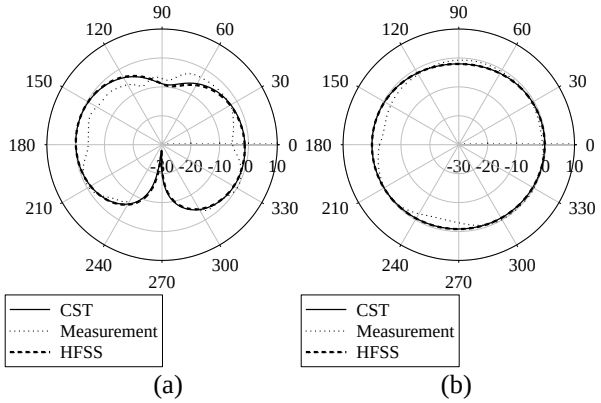

Fig. 6. Radiation pattern at 2.1-GHz in: (a) *xy* and (b) *xz* planes.

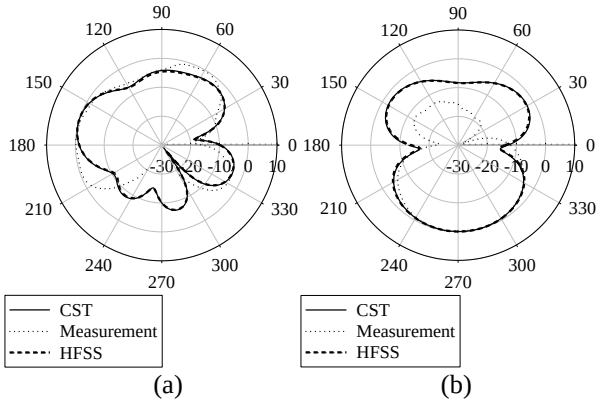

Fig. 7. Radiation pattern at 5.3-GHz in: (a) *xy* and (b) *xz* planes.

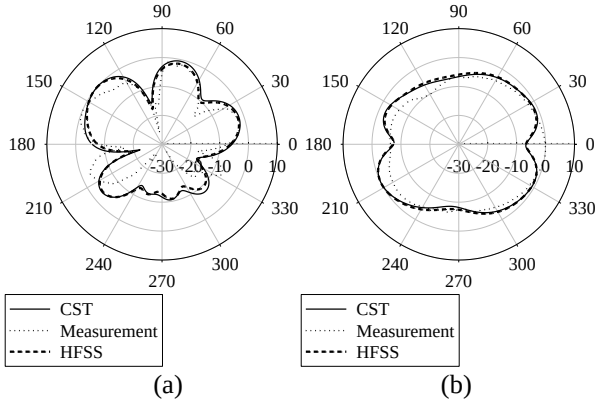

Fig. 8. Radiation pattern at 8.1-GHz in: (a) *xy* and (b) *xz* planes.

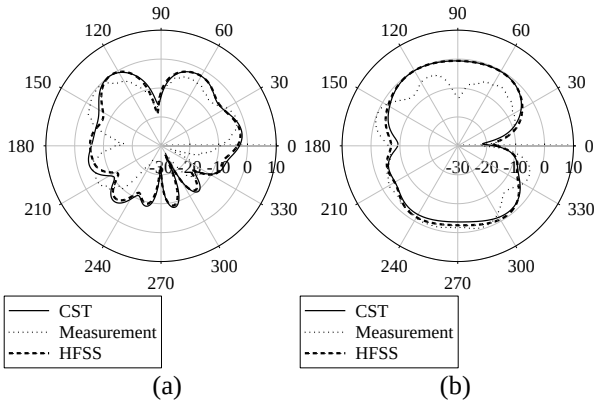

Fig. 9. Radiation pattern at 10-GHz in: (a) *xy* and (b) *xz* planes.

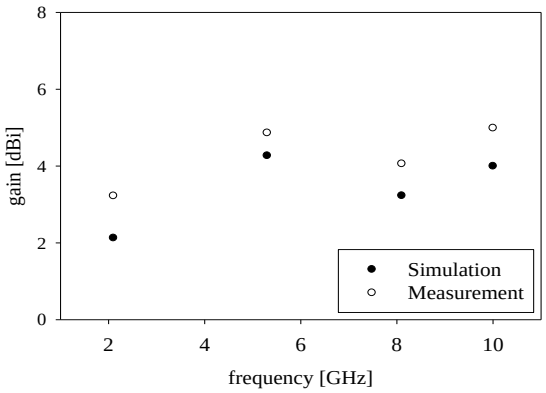

Fig. 10. Measured and simulated antenna gain.

Simulated surface current densities at 2.1, 5.3, 8.1, and 10-GHz are shown in Fig. 11. The maximum scale for each plot is the same. The L-shaped monopole has high current density and appears very active at 2.1-GHz as shown in Fig. 11 (a). At 5.3-GHz the loop is more active as shown in Fig. 11 (b). Figure 11 (c) shows that all elements are active at 8.1-GHz. Since there are three radiating elements, there is always some coupling among them, and the frequency response of the antenna is a result of these complex interactions.

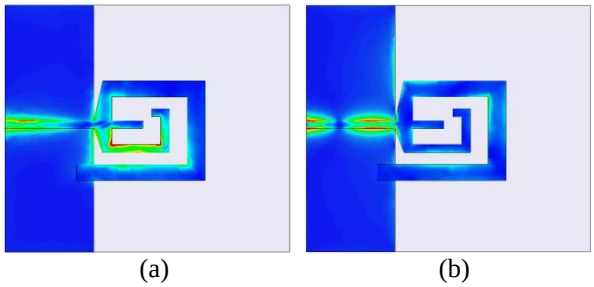

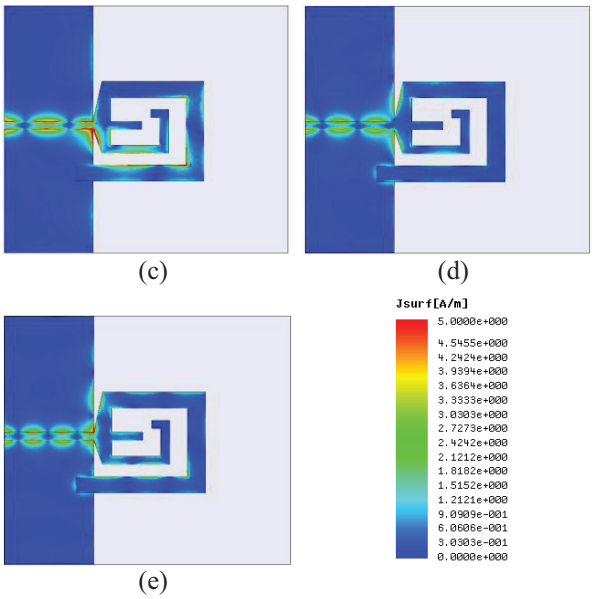

Fig. 11. Simulated surface current densities at: (a) 2.1-GHz, (b) 5.3-GHz, (c) 8.1-GHz, (d) 10-GHz, and (e) 12-GHz. Color scale is from 0 A/m to 5 A/m.

III. CONCLUSION

The presented antenna is compact, wideband, planar, and multiband. The bandwidth spans from about 1.9 to 2.6-GHz, and then from about 3.3 to 11-GHz. Thus, it is suitable for WCDMA, WLAN, UWB, and C band applications. Primary difference between this design and the other UWB antennas is the use of a shorted loop element. UWB response is primarily due to the shorted loop and the coupling between the shorted loop and monopoles, whereas the other UWB antennas use tapered monopoles as their radiating element. The presented antenna exhibits good impedance and gain behavior. Because of its compact size and the microstrip technology, it can be integrated with RF/microwave circuitry on the same board easily.

ACKNOWLEDGMENT

The authors thank to Eren Akkaya and Fatma Zengin at TÜBİTAK BİLGEM Antenna Test and Research Center for their help with radiation pattern and gain measurements.

REFERENCES

[1] K. Y. Yazdandost and R. Kohno, "Ultra wideband L-loop antenna," *IEEE International Conference on Ultra-Wideband*, pp. 201-205, 2005.

[2] M. Kawakatsu and V. Dmitriev, "A compact and simple loop-type planar antenna for broadband applications," *IEEE MTT-S International Microwave and Optoelectronics Conference*, pp. 159-162, 2009.

[3] Y. Shih, B. Wang, Y. Lu, J. Cheng, S. Chen, and P. Hsu, "Capacitively-loaded loop antenna for multi-band mobile handsets," *Proceedings of Int. Workshop on Antenna Technology*, pp. 239-242, 2008.

[4] A. Chen, C. Tang, and Z. Lu, "A loop antenna for WLAN application," *Proceedings of Asia Pacific Microwave Conference*, vol. 2, 2005.

[5] S. Mao and S. Chen, "Frequency- and time-domain characterizations of ultrawideband tapered loop antennas," *IEEE Trans. Antennas and Propag.*, vol. 55, no. 12 , pp. 3698-3701, December 2007.

[6] Y. Lee, C. Wang, and J. Sun, "A new half-loop antenna for UWB spectrum," *Proceedings of Asia Pacific Microwave Conference*, pp. 1987-1989, 2006.

[7] Y. Chi, T. Chiu, and F. Hsiao, "Printed penta-band laptop computer antenna for WWAN operation," *Asia Pacific Microwave Conference*, pp. 1987-1989, 2009.

[8] A. Foudazi, H. R. Hassani, and S. M. A. Nezhad, "Small UWB planar monopole antenna with added GPS/GSM/WLAN bands," *IEEE Transactions on Antennas and Propagation*, vol. 60, no. 6, pp. 2987-2992, June 2012.

[9] Ansoft High Frequency Structure Simulation (HFSS), ver. 11, Ansoft Corporation, Pittsburgh, PA, USA, 2010.

[10] CST Microwave Studio, 3D EM Simulation of High Frequency Components, Darmstadt, Germany, 2011.

Bahadır S. Yıldırım received his M.Sc. and Ph.D. degrees from the University of Colorado at Boulder, USA, and Arizona State University, Tempe, USA, in 1994 and 1998, respectively. He is currently an Associate Professor in the Dept. of Electrical and Electronics Engineering at Muğla Sıtkı Koçman University, Muğla, Turkey. His current research interests include antenna design for mobile equipment, computational electromagnetics, RF/microwave amplifiers, wireless power transmission, and pulsed power electronics.

Erkul Basaran received the B.S. degree in Electrical and Electronics Engineering from the Selcuk University, Turkey, in 2000, the M.S. and the Ph.D. degree in Electronics Engineering from the Gebze Technical University, Turkey, in 2002 and 2008, respectively. Until 2015, he was with the Scientific and Technical

Research Council of Turkey (TUBITAK) as a Senior and a Chief Researcher. He is currently an Assistant Professor in the Department of Electrical and Electronics Engineering at Piri Reis University, Turkey. He is interested in computational electromagnetics and acoustics, radar cross section prediction and measurement, microwave component and antenna design.

Bahattin Türetken has received M.Sc. and Ph.D. degrees from Istanbul Technical University, Istanbul, Turkey in 1998 and 2002, respectively. He has been working as Chief Researcher at TUBITAK-UEKAE (National Research Institute of Electronics and Cryptology) EMC & TEMPEST Test Center in 1998-2009. He managed Electromagnetic and Research Group (EMARG) and the project of Antenna Test and Research Center between 2009 and 2012. He has been the Director of "Millimeter and Terahertz Technologies Research Laboratories (MILTAL)" between 2012-2015. His research topics are radar, antenna design and testing, computational electromagnetic, diffraction & scattering EM Problems, civilian and military EMC/EMI problems, terahertz applications, radiometry, biomedical imaging, implant devices. He is the author and co-author of 1 book chapter and over 100 published papers and proceedings in national and international journals and conferences.

Magnet Modification to Reduce Pulsating Torque for Axial Flux Permanent Magnet Synchronous Machines

Shuanglong Wu, Shuguang Zuo, Xudong Wu, Fu Lin, and Jian Shen

Clean Energy Automotive Engineering Center
Tongji University, Shanghai, 201804, China
zymwgl@foxmail.com, sgzuo@tongji.edu.cn, wuxudong@tongji.edu.cn,
linfu9.11@163.com, shenjian0821@163.com

Abstract ─ To reduce pulsating torque without sacrificing the average torque significantly in axial flux permanent magnet synchronous machines (AFPMSM), this paper presents two optimization techniques which are based on magnet modification: i) combine magnet circumferential displacement with various pole-arc ratios (method one); ii) magnet axial shape design (method two). Firstly, analytical models of air gap magnetic field were derived for the above two methods. Then, according to Maxwell stress tensor method, the analytical expressions of cogging torque and electromagnetic torque were obtained. Average torque, cogging torque and electromagnetic torque ripple were considered simultaneously in the optimization using multi-objective genetic algorithm (MOGA) with the help of the analytical torque models. Finally, 3D finite element models were established to verify the two torque optimization methods. The proposed methods were also compared with skew technique, which is widely used nowadays. Result showed that the proposed optimization techniques can greatly reduce the overall pulsating torque without decreasing the average torque and did not increase the use of permanent magnet.

Index Terms ─ Analytical model, axial flux permanent magnet synchronous machines, magnet displacement, magnet shaping, torque ripple, variable pole-arc.

I. INTRODUCTION

Compare with radial flux permanent magnet synchronous motors, axial flux permanent magnet synchronous machines (AFPMSM) have many unique characteristics such as higher power and torque density, higher efficiency and more suitable structure for installation in tight space, which have made them popular in industry [1]. However, there exists a significant amount of pulsating torque during the operation of AFPMSM, particularly at low speed and light load. Not only does this affect the control precision of the motor, it also aggravates the vibration and noise. Thus, it is necessary to optimize the torque of AFPMSM. Figure 1 depicts the typical structure of an AFPMSM. It is a 3D diagram of the 24 slots, 8 pole pairs machine with concentrated winding.

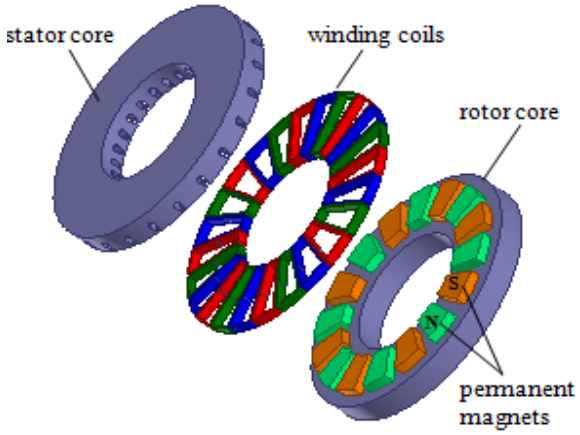

Fig. 1. 3D view of an AFPMSM.

Cogging torque and electromagnetic torque ripple are the two main sources of torque fluctuation in surface mounted AFPM motors. The former is caused by the interaction between the magnet field and stator slotting while the latter is caused by the stator magnetomotive force harmonics and PM field interaction [2]. A large amount of literatures have covered this topic. Skewing the magnets [3-6], employing various pole-arc ratios [4,7], displacing magnets or slots [4,8] and magnet shaping [9] are some of the common techniques used for reducing cogging torque. As for minimization of electromagnetic torque ripple, references [10] and [11] employ Taguchi method and rotor displacement, respectively. In [12], authors investigated the influence of skewing on cogging torque and electromagnetic torque ripple of radial flux machines. However, the optimal skew angle for reducing both the cogging torque and the electromagnetic torque ripple was not given.

Submitted On: September 30, 2015
Accepted On: February 26, 2016

From the above literatures we can see that most of the researchers concentrated on cogging torque alone or electromagnetic torque ripple alone to reduce pulsating torque in AFPMSM and few consider the two simultaneously. On the other hand, because AFPM machines have an inherent 3D electromagnetic structure, when it comes to the finite element method, time-consuming 3D FEA is always required. Therefore, it is important to establish precise analytical model to optimize the torque. References [9] and [11] pointed out that adopting those optimization methods separately such as magnet skew, rotor displacement would decrease the average torque to some extent and thus weaken the motor torque output capacity. So it is necessary to consider the average torque during the optimization and minimize its decline. We can also find that most of the torque optimization methods for AFPMSM up to now are focusing on radial and circumferential direction of the magnet. Few studied the influence of magnet axial profile on the torque. In fact, magnet shaping has already been used to optimize the torque of radial flux PM motors [13-17].

In this paper, two novel techniques for torque optimization are proposed: i) combine magnet circumferential displacement with various pole-arc ratios; ii) magnet axial shape design. Firstly, analytical models of air gap magnetic field were derived for the above two methods. Then, according to Maxwell stress tensor method the analytical expressions of cogging torque and electromagnetic torque were obtained. Average torque, cogging torque and electromagnetic torque ripple were considered simultaneously in the optimization using multi-objective genetic algorithm with the help of the analytical torque models. Finally, 3D finite element models were established to verify the two torque optimization methods. In order to further highlight the superiority of the two methods, comparison of the optimization results between the proposed methods and the skew technique which is widely used nowadays was made. Result showed that the proposed optimization techniques can greatly reduce the overall pulsating torque without decreasing the average torque and did not increase the use of permanent magnet.

II. ANALYTICAL MODEL OF AIR GAP FIELD

Assuming that the rotor and stator iron core have infinite magnetic permeability and magnetic saturation is absent, the air gap magnetic field can be obtained by linear superposition of the PM field and the armature reaction field. Thus, the analytical models of axial and tangential air gap magnetic field for the above two optimization methods can be deduced. Figure 2 shows the machine model for computing the permanent magnet field of the AFPMSM. Variable θ denotes mechanical angle in the circumferential direction along a cylindrical cutting plane of radius R at which the magnetic field is to be computed.

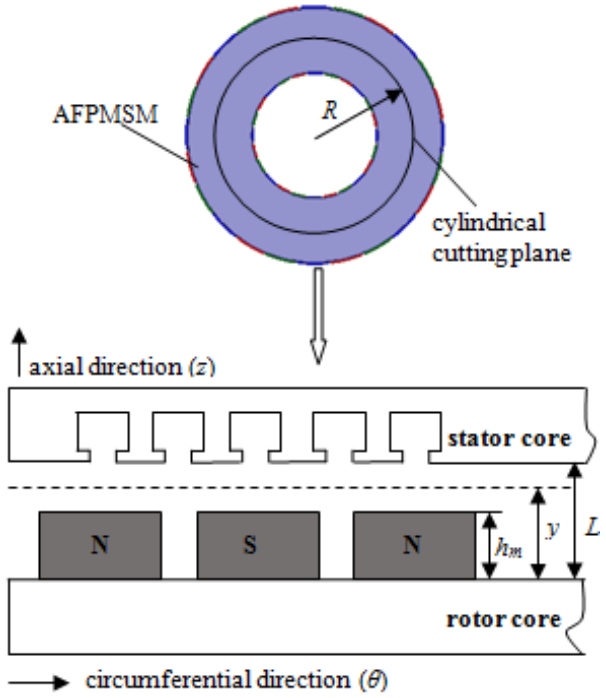

Fig. 2. Model for computation of permanent magnet field of AFPMSM.

A. Permanent magnet field

1) Permanent magnet field of method one

For conventional surface mounted AFPM machine, its magnets have the same shape with each other and are evenly arranged on the rotor surface. However, the first optimization method proposed in this paper changes the pole-arc ratio of each magnet and shifts them from their original centerline a specific angle along the rotor circumference at the same time. So the distribution of permanent magnet field changes as well. The final distribution is shown in Fig. 3. Here, assuming the pole-arc ratio and circumferential shift angle (mechanical degree) of the ith permanent magnet are α_i and d_i ($1 \le i \le 2p$), respectively.

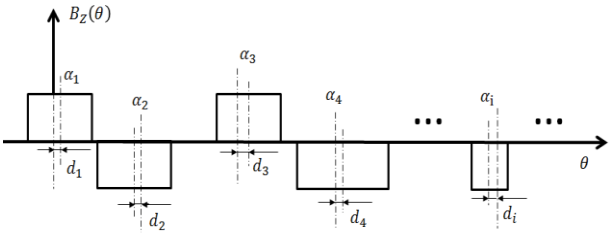

Fig. 3. Distribution of axial flux density produced by PM.

Referring to Fig. 3, the distribution of axial permanent

magnetic field can be described by a Fourier series:

$$B_{zm}(\theta,t)=\frac{a_0}{2}+a_n\cos\left[n\left(\theta-\frac{2\pi f}{p}t\right)\right]+b_n\sin\left[n\left(\theta-\frac{2\pi f}{p}t\right)\right], \quad (1)$$

where

$$\begin{cases} a_0=\dfrac{1}{\pi}\displaystyle\sum_{i=1}^{2p}\int_{-\frac{\alpha_i\pi}{2p}+d_i+\frac{(i-1)\pi}{p}}^{\frac{\alpha_i\pi}{2p}+d_i+\frac{(i-1)\pi}{p}}(-1)^{i-1}B_rK_n d\theta \\ \quad=\dfrac{2}{\pi}\displaystyle\sum_{i=1}^{2p}(-1)^{i-1}B_rK_n\frac{\alpha_i\pi}{2p} \\ a_n=\dfrac{1}{\pi}\displaystyle\sum_{i=1}^{2p}\int_{-\frac{\alpha_i\pi}{2p}+d_i+\frac{(i-1)\pi}{p}}^{\frac{\alpha_i\pi}{2p}+d_i+\frac{(i-1)\pi}{p}}(-1)^{i-1}B_rK_n\cos n\theta d\theta \\ \quad=\displaystyle\sum_{i=1}^{2p}\frac{(-1)^{i-1}B_rK_n}{n\pi}\left\{\begin{aligned}&\sin\left[n\left(\frac{\alpha_i\pi}{2p}+d_i+\frac{(i-1)\pi}{p}\right)\right]\\&-\sin\left[n\left(-\frac{\alpha_i\pi}{2p}+d_i+\frac{(i-1)\pi}{p}\right)\right]\end{aligned}\right\} \\ \quad=\displaystyle\sum_{i=1}^{2p}\frac{2(-1)^{i-1}B_rK_n}{n\pi}\cos\left[\frac{n(i-1)\pi}{p}+nd_i\right]\sin\frac{n\alpha_i\pi}{2p} \\ b_n=\dfrac{1}{\pi}\displaystyle\sum_{i=1}^{2p}\int_{-\frac{\alpha_i\pi}{2p}+d_i+\frac{(i-1)\pi}{p}}^{\frac{\alpha_i\pi}{2p}+d_i+\frac{(i-1)\pi}{p}}(-1)^{i-1}B_rK_n\sin n\theta d\theta \\ \quad\displaystyle\sum_{i=1}^{2p}\frac{(-1)^{i-1}B_rK_n}{n\pi}\left\{\begin{aligned}&-\cos\left[n\left(\frac{\alpha_i\pi}{2p}+d_i+\frac{(i-1)\pi}{p}\right)\right]\\&+\cos\left[n\left(-\frac{\alpha_i\pi}{2p}+d_i+\frac{(i-1)\pi}{p}\right)\right]\end{aligned}\right\} \\ \quad\displaystyle\sum_{i=1}^{2p}\frac{2(-1)^{i-1}B_rK_n}{n\pi}\sin\left[\frac{n(i-1)\pi}{p}+nd_i\right]\sin\frac{n\alpha_i\pi}{2p}, \end{cases} \quad (2)$$

and θ is the mechanical angle, t is the time, n is the order of magnetic field harmonics, f is the current frequency, Br is the remanent flux density, p is the number of pole pairs, K_n is the correction factor which can be found in [18];

$$K_n=\frac{\sinh\left(\frac{n\pi h_m}{\tau_p p}\right)\cosh\left[\frac{n\pi(L-y)}{\tau_p p}\right]}{\Delta}, \quad (3)$$

where

$$\begin{aligned}\Delta=&\mu_r\cosh\left(\frac{n\pi h_m}{\tau_p p}\right)\sinh\left[\frac{n\pi(L-h_m)}{\tau_p p}\right]\\&+\cosh\left(\frac{n\pi(L-h_m)}{\tau_p p}\right)\sinh\left[\frac{n\pi h_m}{\tau_p p}\right],\end{aligned} \quad (4)$$

μ_r is the relative permeability, h_m is the axial thickness of magnets, L is the axial distance between inner surfaces of the rotor and stator, y is the axial distance between rotor inner surface and the axial air gap plane at which field is computed, $\tau_p=\pi R/p$ is the pole pitch in circumferential direction and R is the radius of cutting plane at which field is computed.

Substituting (2) and (3) into (1), the axial component of permanent magnet field in air region of a AFPMSM is:

$$\begin{aligned}B_{zm}(\theta,t)=&\frac{K_nB_r}{\pi}\sum_{i=1}^{2p}\frac{(-1)^{i-1}\alpha_i\pi}{2p}+K_nB_r\\&\times\sum_{n=1}^{\infty}\left\{\begin{aligned}&\sum_{i=1}^{2p}\frac{2}{n\pi}(-1)^{i-1}\cos\left[\frac{n(i-1)\pi}{p}+nd_i\right]\\&\times\sin\frac{n\alpha_i\pi}{2p}\cos\left[n\left(\theta-\frac{2\pi f}{p}t\right)\right]\\&+\sum_{i=1}^{2p}\frac{2}{n\pi}(-1)^{i-1}\sin\left[\frac{n(i-1)\pi}{p}+nd_i\right]\\&\times\sin\frac{n\alpha_i\pi}{2p}\sin\left[n\left(\theta-\frac{2\pi f}{p}t\right)\right]\end{aligned}\right\}.\end{aligned} \quad (5)$$

Similarly, the circumferential component of permanent magnetic field can be obtained as follows:

$$\begin{aligned}B_{\theta m}(\theta,t)=&K_n^*B_r\\&\times\sum_{n=1}^{\infty}\left\{\begin{aligned}&\sum_{i=1}^{2p}\frac{2}{n\pi}(-1)^{i-1}\sin\left[\frac{n(i-1)\pi}{p}+nd_i\right]\\&\times\sin\frac{n\alpha_i\pi}{2p}\cos\left[n\left(\theta-\frac{2\pi f}{p}t\right)\right]\\&-\sum_{i=1}^{2p}\frac{2}{n\pi}(-1)^{i-1}\cos\left[\frac{n(i-1)\pi}{p}+nd_i\right]\\&\times\sin\frac{n\alpha_i\pi}{2p}\sin\left[n\left(\theta-\frac{2\pi f}{p}t\right)\right]\end{aligned}\right\},\end{aligned} \quad (6)$$

where

$$K_n^*=K_n\tanh\left[\frac{n\pi(L-y)}{\tau_p p}\right]. \quad (7)$$

The above analytical expressions of permanent magnetic field contain a total of $4p$ variables α_i and d_i ($1\le i\le 2p$). By choosing different values, we can obtain the magnetic field distribution in the air region under magnets circumferential displacement and employing various pole-arc ratios simultaneously.

2) Permanent magnet field of method two

Divide each piece of the permanent magnets along with the circumferential direction into $N=2k+1$ ($k=0,1,2,3\cdots$) segments with the same arc and each segment can have independent value in thickness as shown in Fig. 4. Theoretically, with the increase of subsection number N, it can approximate any permanent magnet with random axial profile.

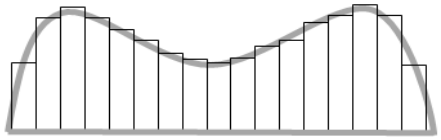

Fig. 4. Segmented permanent magnet.

As for the magnetic field produced by those segmented permanent magnet, we can first derive the field of each segment and then add all of the N sections

to obtain the field of one pole. Finally, by array transformation of the single pole field along with the circumferential direction, the analytical model of the rotor permanent magnetic field is established. The axial and circumferential component of magnetic field of the first segment can be expressed as follows:

$$\begin{cases} B_{zm1}(\theta,t) = B_0 + \sum_{\mu}\left[B_{z_1\mu}\cos(\mu\theta-\mu\omega_r t) + B_{z_2\mu}\sin(\mu\theta-\mu\omega_r t)\right] \\ B_{\theta m1}(\theta,t) = \sum_{\mu}\left[B_{\theta_1\mu}\cos(\mu\theta-\mu\omega_r t) - B_{\theta_2\mu}\sin(\mu\theta-\mu\omega_r t)\right], \end{cases} \tag{8}$$

where θ is the mechanical angle, t is the time, μ is the order of magnetic field harmonics, ω_r is the rotor angular velocity. The coefficients in (8) can be obtained as follows:

$$\begin{cases} B_0 = \dfrac{1}{2\pi}\int_{-\pi}^{\pi} B_{zm1}(\theta)\,d\theta \\ \quad = \dfrac{1}{2\pi}\sum\limits_{i=\frac{N-1}{2}}^{\frac{1-N}{2}}\left[\int_{-\frac{\alpha_p\pi}{2pN}-\frac{\alpha_p\pi i}{pN}}^{\frac{\alpha_p\pi}{2pN}-\frac{\alpha_p\pi i}{pN}} B_r\times\dfrac{h_m(i)}{h_m(i)+\delta(i)\mu_r}\,d\theta\right] \\ \quad = \dfrac{\alpha_p}{pN}\sum\limits_{i=\frac{N-1}{2}}^{\frac{1-N}{2}}\left[B_r\times\dfrac{h_m(i)}{h_m(i)+\delta(i)\mu_r}\right] \\ B_{z_1\mu} = \dfrac{1}{\pi}\int_0^{2\pi} B_{zm1}(\theta)\cos(\mu\theta)\,d\theta \\ \quad = \dfrac{1}{\pi}\sum\limits_{i=\frac{N-1}{2}}^{\frac{1-N}{2}}\left[\int_{-\frac{\alpha_p\pi}{2pN}-\frac{\alpha_p\pi i}{pN}}^{\frac{\alpha_p\pi}{2pN}-\frac{\alpha_p\pi i}{pN}} B_r K_\mu(i)\cos\mu\theta\,d\theta\right] \\ \quad = \sum\limits_{i=\frac{N-1}{2}}^{\frac{1-N}{2}}\dfrac{2}{\mu\pi}B_r K_\mu(i)\cos\dfrac{\alpha_p\mu\pi i}{pN}\sin\dfrac{\alpha_p\mu\pi}{2pN} \\ B_{z_2\mu} = \dfrac{1}{\pi}\int_0^{2\pi} B_{zm1}(\theta)\sin(\mu\theta)\,d\theta \\ \quad = \dfrac{1}{\pi}\sum\limits_{i=\frac{N-1}{2}}^{\frac{1-N}{2}}\left[\int_{-\frac{\alpha_p\pi}{2pN}-\frac{\alpha_p\pi i}{pN}}^{\frac{\alpha_p\pi}{2pN}-\frac{\alpha_p\pi i}{pN}} B_r K_\mu(i)\sin\mu\theta\,d\theta\right] \\ \quad = \sum\limits_{i=\frac{N-1}{2}}^{\frac{1-N}{2}}\dfrac{2}{\mu\pi}B_r K_\mu(i)\sin\dfrac{\alpha_p\mu\pi i}{pN}\sin\dfrac{\alpha_p\mu\pi}{2pN} \\ B_{\theta_1\mu} = B_{z_2\mu}\times\tanh\left[\dfrac{\mu\delta(i)}{2R}\right] \\ B_{\theta_2\mu} = B_{z_1\mu}\times\tanh\left[\dfrac{\mu\delta(i)}{2R}\right], \end{cases} \tag{9}$$

where $h_m(i)$ ($1\le i\le N$) is the thickness of the ith segment, α_p is the pole-arc ratio of one pole, $\delta(i)=h_m+g-h_m(i)$ is the real air gap length of the ith segment, h_m is the initial thickness of the permanent magnet and g is the initial air gap length, $K_\mu(i)$ is the correction factor of the ith segment [18];

$$K_\mu(i) = \frac{\sinh\left[\dfrac{\mu\pi h_m(i)}{\tau_p p}\right]\cosh\left[\dfrac{\mu\pi(L-y)}{\tau_p p}\right]}{\Delta'}, \tag{10}$$

where

$$\begin{aligned}\Delta' = \mu_r\cosh\left[\frac{\mu\pi h_m(i)}{\tau_p p}\right]\sinh\left\{\frac{\mu\pi\left[L-h_m(i)\right]}{\tau_p p}\right\} \\ +\cosh\left\{\frac{\mu\pi\left[L-h_m(i)\right]}{\tau_p p}\right\}\sinh\left[\frac{\mu\pi h_m(i)}{\tau_p p}\right].\end{aligned} \tag{11}$$

Based on the above derivation, the analytical model of the rotor permanent magnetic field can be established eventually by array transformation of the single pole field along with the circumferential direction;

$$\begin{cases} B_{zm}(\theta,t) = \sum\limits_{j=1}^{2p} B_{zmj}(\theta,t) = \sum\limits_{j=1}^{2p}(-1)^{j-1}B_{mz1}\left[\theta-\dfrac{(j-1)\pi}{p},t\right] \\ B_{\theta m}(\theta,t) = \sum\limits_{j=1}^{2p} B_{\theta mj}(\theta,t) = \sum\limits_{j=1}^{2p}(-1)^{j-1}B_{m\theta 1}\left[\theta-\dfrac{(j-1)\pi}{p},t\right], \end{cases} \tag{12}$$

where $B_{zmj}(\theta, t)$ and $B_{\theta mj}(\theta, t)$ are axial and circumferential component of the magnetic field produced by the jst magnet pole, $j(1\le j\le 2p)$ represents the serial number of $2p$ poles.

B. Armature reaction field

The axial flux permanent magnet motors with one rotor and one stator often use the drum winding. While neglecting the current harmonics, the axial and circumferential components of armature reaction field can be obtained as follows [19]:

$$B_{za}(\theta,t) = \frac{4\mu_0 N_c i}{\pi}\sum_{v}\frac{k_{pn}k_{son}}{v\sinh\dfrac{vy_1}{R}}\cosh\frac{vy}{R}\cos\left[v(\theta\pm 2\pi ft)\right], \tag{13}$$

$$B_{\theta a}(\theta,t) = -\frac{4\mu_0 N_c i}{\pi}\sum_{v}\frac{k_{pn}k_{son}}{v\sinh\dfrac{vy_1}{R}}\sinh\frac{vy}{R}\sin\left[v(\theta\pm 2\pi ft)\right], \tag{14}$$

where v is the order of armature reaction field harmonics, μ_0 is the permeability of vacuum, N_{ci} is the ampere-turns of the coil, k_{pn} is the coil pitch factor, k_{son} is the slot opening factor, $y_1=h_m+g$ is the axial distance between the inner surfaces of the rotor and stator.

C. Relative permeance

Slotting will affect the distribution of the flux in the air gap and its effect can be accounted by introducing the relative permeance;

$$\lambda(\theta) = \lambda_0 + \sum_k \lambda_k\cos(kQ_s\theta), \tag{15}$$

where k is the order of the relative permeance harmonics, Q_s is the number of stator teeth, λ_0 is the mean permeance and λ_k is the peak value of the kst harmonic which can be found in [20].

D. Air gap resultant magnetic field

Assuming that the stator and rotor cores are nonsaturated, the air gap resultant magnetic field can be obtained by linear superposition of the PM field and the armature reaction field, while the relative permeance is introduced to account for the effect of slotting;

$$\begin{cases} B_z(\theta,t)=\left[B_{zm}(\theta,t)+B_{za}(\theta,t)\right]\cdot\lambda(\theta) \\ B_\theta(\theta,t)=\left[B_{\theta m}(\theta,t)+B_{\theta a}(\theta,t)\right]\cdot\lambda(\theta). \end{cases} \quad (16)$$

III. ANALYTICAL MODEL OF TORQUE

Torque can be calculated based on double integral of the circumferential component of magnetic force. And the force is obtained by using Maxwell stress tensor method [21];

$$T_{cog}=\int_0^{2\pi}\int_{R_i}^{R_o} f_{\theta 1}drd\theta=\int_0^{2\pi}\int_{R_i}^{R_o}\frac{B_{mz}B_{m\theta}\lambda_a^2}{\mu_0}drd\theta, \quad (17)$$

$$T_{ele}=\int_0^{2\pi}\int_{R_i}^{R_o} f_{\theta 2}drd\theta=\int_0^{2\pi}\int_{R_i}^{R_o}\frac{(B_{mz}+B_{az})\times(B_{m\theta}+B_{a\theta})}{\mu_0}drd\theta, \quad (18)$$

where T_{cog} and T_{ele} represent cogging torque and electromagnetic torque respectively, $f_{\theta 1}$ and $f_{\theta 2}$ are the circumferential component of magnetic force on no-load and load respectively, R_i is inner and R_o is outer radius of the permanent magnet.

IV. TORQUE OPTIMIZATION USING MULTI-OBJECTIVE GENETIC ALGORITHM

As for the assessment of motor torque fluctuation, the torque ripple factor (*TRF*) is often used to describe the electromagnetic torque ripple, while the peak to peak value (T_{cPP}) is used for cogging torque [22];

$$\begin{cases} TRF=\dfrac{T_{ripple}}{T_{average}}=\dfrac{2\sqrt{\sum_i T_i^2}}{T_{average}} \\ T_{cPP}=\max(T_{cog})-\min(T_{cog}), \end{cases} \quad (19)$$

where T_{ripple} is the electromagnetic torque ripple, $T_{average}$ is the average torque, T_i is the ist time harmonic peak value of the electromagnetic torque ripple.

A. Method one

Based on the analytical expressions of (5), (6), (17), (18), and using the multi-objective genetic algorithm, we can obtain the optimal values of shift angle and pole-arc ratio of each magnet on the premise of suppressing the overall pulsating torque greatly without decreasing the average torque.

1) Optimization objectives

According to the assessment criteria in (19), the first optimization goal *Obj1* is set to maximize the average torque and the second goal *Obj2* is set to minimize the summation of the electromagnetic torque ripple and cogging torque;

$$\begin{cases} Obj1=\max(T_{average}) \\ Obj2=\min\left(T_{ripple}+T_{cPP}\right)=\min\left[\sqrt{\sum_i T_i^2}+\dfrac{\max(T_{cog})-\min(T_{cog})}{2}\right], \end{cases} \quad (20)$$

where $T_{average}$ is the average torque, T_{cog} is the cogging torque, T_i is the ist time harmonic peak value of the electromagnetic torque ripple. The original values of *Obj1* and *Obj2* of the virtual prototype studied in this paper before optimization are 57.71 Nm and 7.8 Nm, respectively.

2) Constraints

(a). In order to ensure that any two adjacent permanent magnets do not touch each other after optimization, the shift angle and pole-arc ratio of each magnet should be satisfied:

$$d_{i+1}-d_i<\frac{180}{p}\left(1-\frac{\alpha_{i+1}}{2}-\frac{\alpha_i}{2}\right). \quad (21)$$

(b). Considering the cost, the amount of permanent magnet should remain the same before and after optimization:

$$\sum_{i=1}^{2p}\alpha_i=2p\alpha_p, \quad (22)$$

where α_p is the pole-arc ratio before optimization.

(c). The pole-arc ratio of each magnet after optimization should be satisfied:

$$0<\alpha_i<1. \quad (23)$$

(d). In order to keep the symmetry of the magnetic circuit so as not to produce additional unbalanced magnetic pull and overturning moment after optimization, the shift angle and pole-arc ratio of the two magnets which locate on diametrically opposed position should have the same value. Therefore, for $1<i<p$, we have:

$$\begin{cases} \alpha_i=\alpha_{i+p} \\ d_i=d_{i+p}. \end{cases} \quad (24)$$

3) Optimization variables and parameters of virtual prototype

From the last constraint above we can conclude that although method one contains a total of $4p$ variables α_i and d_i ($1\le i\le 2p$), only half of them are independent. Now we will use this method to optimize the torque of a 16P24S AFPMSM with one stator and one rotor under the rated conditions. The initial parameters of the virtual prototype are listed in Table 1. The average torque before optimization is 57.71 Nm. The amplitude of electromagnetic torque ripple under the rated conditions and cogging torque under no load are 4.71 Nm and 3.13 Nm, respectively.

Table 1: Initial parameters of virtual prototype

Parameter	Value	Parameter	Value
Pole pairs	8	Slot number	24
PM thickness	7.5 mm	Remanence	1.1 T
Air gap length	2 mm	Rotor thickness	15 mm
Outer diameter of PM	89 mm	Inner diameter of PM	55.7 mm
Pole-arc ratio	0.6	Phase number	3
Slot width	8 mm	Coil turns	148
Current frequency	100 Hz	Current amplitude	72.4 A

4) Optimized result

The optimization was accomplished by using the multi-objective genetic algorithm. Here the population size is set to 240 and the creation function is constraint dependent. The selection model is tournament selection and the tournament size is 2. After 352 generations while the function tolerance is 0.0001, a subset of Pareto optimal solutions is obtained as shown in Fig. 5. Then select the optimal value of these variables according to the criteria that average torque remains the same as far as possible before and after optimization (in black circle). The final values of those variables are listed in Table 2. From Fig. 5 we can see that the overall pulsating torque was suppressed greatly while the average torque did not decline.

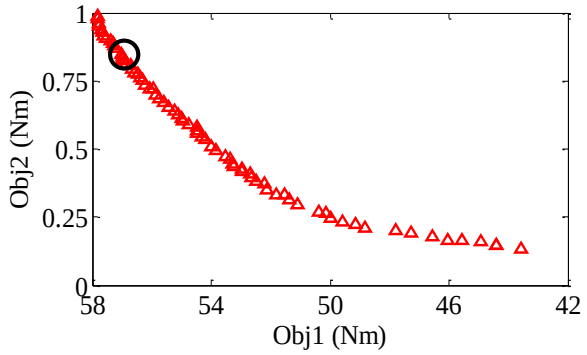

Fig. 5. Pareto optimal solutions set of method one.

Table 2: Variable-value of method one

Variable	Value	Variable	Value
$\alpha_1\ \alpha_9$	0.41	$\delta_1\ \delta_9$	0°
$\alpha_2\ \alpha_{10}$	0.56	$\delta_2\ \delta_{10}$	-1.84°
$\alpha_3\ \alpha_{11}$	0.84	$\delta_3\ \delta_{11}$	-1.89°
$\alpha_4\ \alpha_{12}$	0.43	$\delta_4\ \delta_{12}$	0.69°
$\alpha_5\ \alpha_{13}$	0.77	$\delta_5\ \delta_{13}$	1.41°
$\alpha_6\ \alpha_{14}$	0.63	$\delta_6\ \delta_{14}$	4.30°
$\alpha_7\ \alpha_{15}$	0.42	$\delta_7\ \delta_{15}$	1.63°
$\alpha_8\ \alpha_{16}$	0.76	$\delta_8\ \delta_{16}$	-1.53°

B. Method two

Based on the analytical expressions of (12), (17), (18), and using the multi-objective genetic algorithm, we can obtain the optimal values of each segment permanent magnet thickness on the premise of suppressing the overall pulsating torque greatly without decreasing the average torque.

5) Optimization objectives

For comparison, the optimization objectives used in method two are the same as those in method one, as shown in (20).

6) Constraints

(a). Due to the motor air gap length is generally small and considering the manufacturing and assembly error, keeping the maximum thickness of permanent magnet unchanged before and after optimization:

$$max\left[h_m(i)\right]=h_m, 1\le i\le N. \tag{25}$$

(b). In order to keep the symmetry of the magnetic circuit, each permanent magnet should be symmetrical about its centerline:

$$h_m(i)=h_m(N-i+1). \tag{26}$$

(c). From the first constraint we know that the amount of permanent magnet will be reduced after optimization. So we should increase the pole-arc ratio to compensate for the reduction:

$$\frac{\alpha_p^*}{N}\sum_{i=1}^{N}h_m(i)=\alpha_p h_m, \tag{27}$$

where α_p^* is the pole-arc ratio after optimization.

(d). The pole-arc ratio of each magnet after optimization should be satisfied:

$$0<\alpha_p^*<1. \tag{28}$$

7) Optimization variables and parameters of virtual prototype

The optimization variables of method two are those thickness values of each segment permanent magnet. The optimization object is the same virtual prototype used in method one. The initial parameters of the virtual prototype are listed in Table 1.

8) Optimized result

Theoretically, with the increase of subsection number *N*, it can reflect the continuous variation of permanent magnet outline truly but the optimization iteration time will be longer. In order to determine the optimal value of *N*, we get the subset of Pareto optimal solutions for different *N*, as shown in Fig. 6.

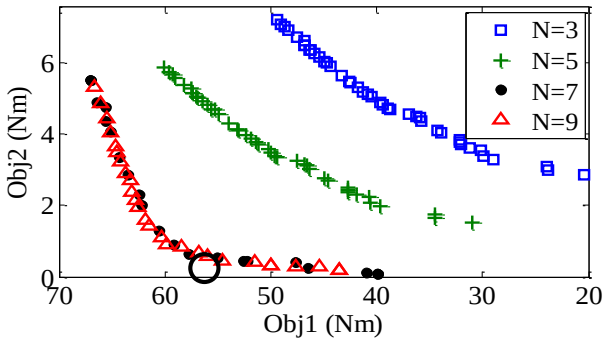

Fig. 6. Pareto optimal solutions set of method two.

We can see that when $N\ge7$, the subset of Pareto optimal solutions overlaps with each other. Continue to

increase the subsection number will only increase the iteration time but not the optimization precision. So we finally chose N=9. During the optimization, the population size is set to 110 and the creation function is constraint dependent. The selection model is tournament selection and the tournament size is 2. It takes 286 generations to get the result as shown in Fig. 6, while the function tolerance is 0.0001. Similarly, select the optimal value of these variables according to the criteria that average torque remains the same as far as possible before and after optimization (in black circle). The final values of those variables are listed in Table 3. The pole-arc ratio after optimization is 0.71.

Table 3: Variable-value of method two

i	$h_m(i)$	i	$h_m(i)$
1	6.50 mm	6	7.10 mm
2	5.13 mm	7	6.00 mm
3	6.00 mm	8	5.13 mm
4	7.10 mm	9	6.50 mm
5	7.50 mm		

Based on the data in Table 3, the permanent magnet axial profile curve after optimization is obtained (as shown in Fig. 7) using polynomial fit technique:

$$h_m(i) = h_m \times \left(p_1 x^4 + p_2 x^3 + p_3 x^2 + p_4 x + p_5 \right), \quad (29)$$

where x=0.5×[N^*/N(2i-1)+1] (1≤i≤N^*), N^*=9 is the subsection number in optimization, N is the subsection number in polynomial fit. p_i=[3.855,-77.1,507.3,-1217,1644]×10^{-3} is the coefficient.

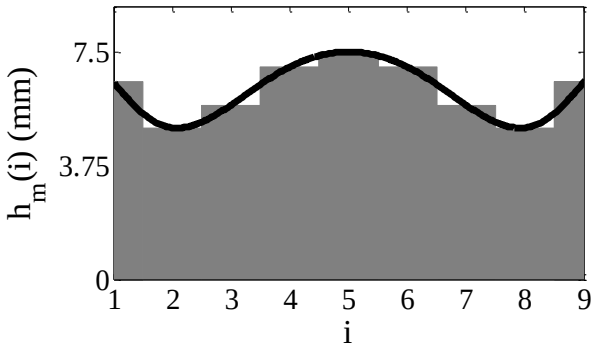

Fig. 7. Permanent magnet axial profile curve.

V. VERIFICATION BY 3D FEM AND RESULTS CONTRAST

According to the two optimization results above, we obtained the corresponding optimized motor models by modifying the initial rotor structure of the virtual prototype as shown in Figs. 8 (a) and (b). On the left side of both Figs. 8 (a) and (b) are the 3D finite element model. The AFPM machine is surrounded by the blue transparent solution region which is generated by the software automatically. On the right side are rotors with optimized permanent magnets.

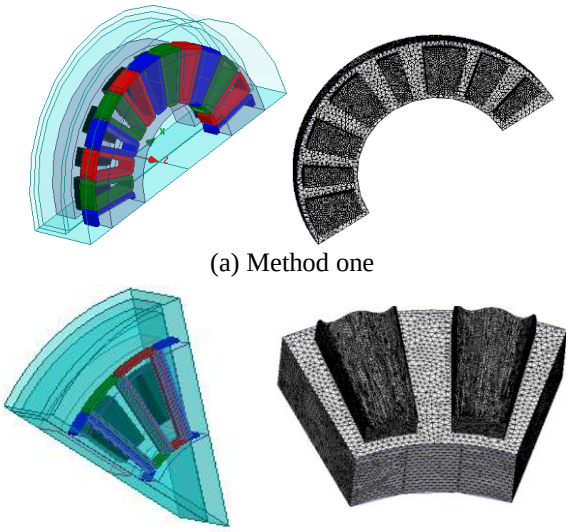

(a) Method one

(b) Method two

Fig. 8. 3D finite element model of the optimized AFPMSM.

A. Verification of the proposed method by 3D FEM

As for method one, the pole-arc ratio of each magnet has been changed but the two magnets which locate on diametrically opposed position have the same pole-arc ratio. By taking advantage of machine symmetry, only one half of the machine is considered as shown in Fig. 8 (a). For method two, since each permanent magnet has the same shape and evenly arranged on the rotor surface, only 1/8 of the machine is needed as shown in Fig. 8 (b).

To verify the accuracy of the analytical models, the electromagnetic torque and cogging torque were computed using both the FEM and analytical method. In addition, the comparison of torque value between optimized models and initial model is also made to verify the validity of the two proposed methods. The results are shown in Fig. 9 and Fig. 10.

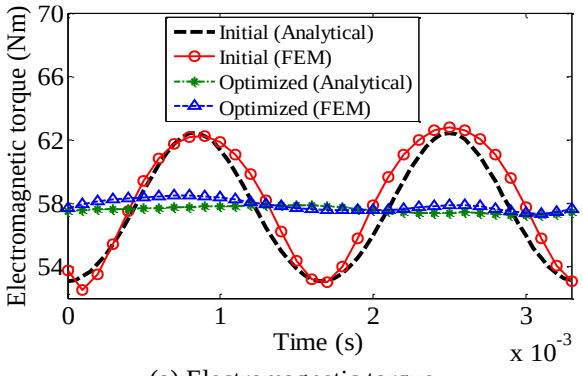

(a) Electromagnetic torque

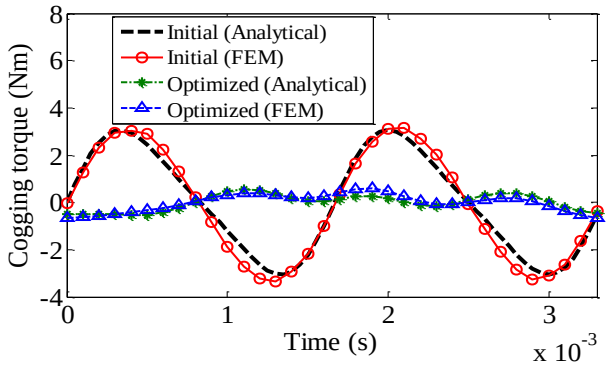

(b) Cogging torque

Fig. 9. Torque contrast before and after optimization of method one.

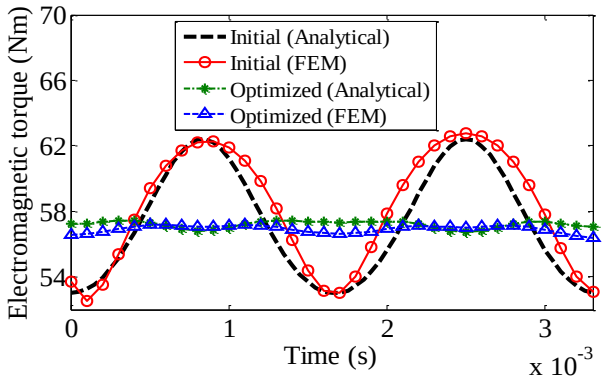

(a) Electromagnetic torque

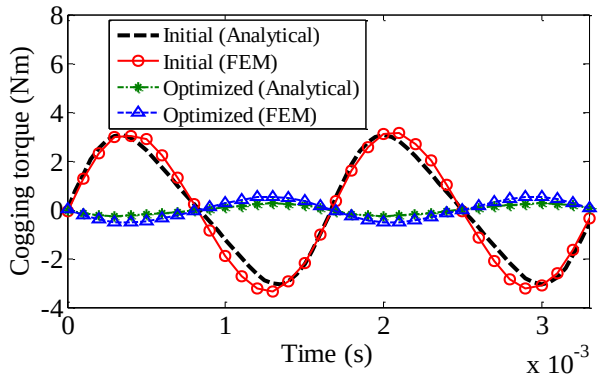

(b) Cogging torque

Fig. 10. Torque contrast before and after optimization of method two.

Good agreement between the analytical result and FEA result confirms the accuracy of the analytical models. On the other hand, we can also see that the overall pulsating torque was suppressed greatly while the average torque almost did not decline after optimization. So the validity of the two proposed methods is verified.

B. Optimization results comparison

In order to further highlight the superiority of the two methods, comparison of the optimization results between the proposed methods and the skew technique is made. After all, skew technique is one of the most effective torque optimization methods which is popular nowadays [2-4].

Similarly, the analytical models of electromagnetic torque and cogging torque for AFPMSM with skew magnets can be derived. Figure 11 shows the variation of the torque relative value waveform of the same virtual prototype as the skew angle is varied. As shown, when the skew angle is 60 electrical degrees, the electromagnetic torque ripple and cogging torque are greatly weakened while the average torque is only a slight decline.

Figure 12 is the 3D finite element model of the same virtual prototype with magnets skewing 60 electrical degrees. The electromagnetic torque and cogging torque were computed using the FEM and compared with those obtained by the two proposed methods as shown in the Fig. 13. It is obvious that not only the skew method is inferior to the two proposed methods in suppressing the pulsating torque, it will also decrease the average torque and thus weaken the motor torque output capacity. For the convenience of comparison, the amplitude of average torque, electromagnetic torque ripple and cogging torque before and after optimization of different methods are listed in the same table (Table 4).

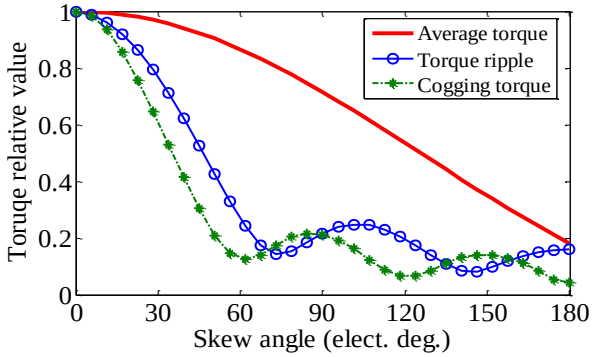

Fig. 11. Torque relative value at different skew angles.

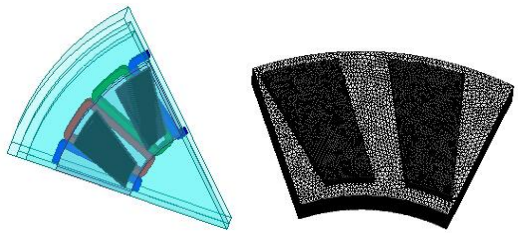

Fig. 12. 3D finite element model of motor after skewing.

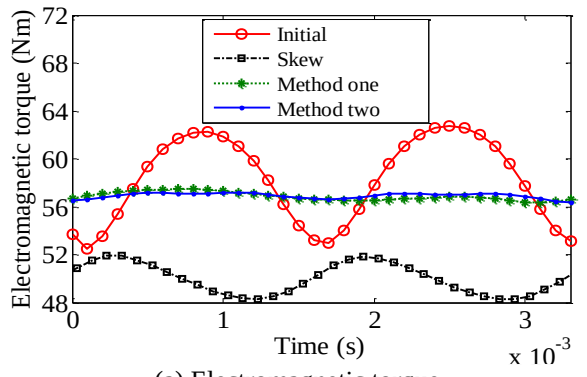

(a) Electromagnetic torque

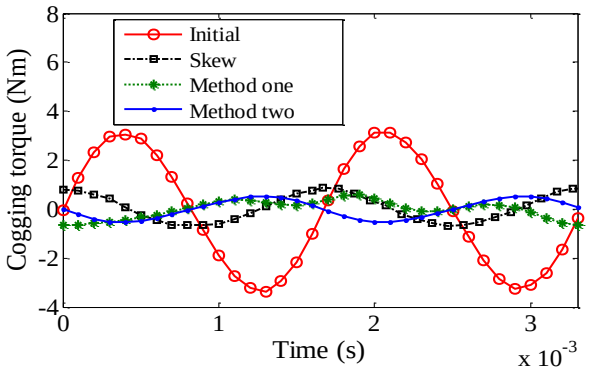

(b) Cogging torque

Fig. 13. Comparison of results by different optimization methods.

Table 4: Results contrast of different optimization methods

	Original	Skew Method	Method One	Method Two
$T_{average}$	57.71 Nm	50.07 Nm	56.80 Nm	57.05 Nm
T_{ripple}	4.71 Nm	1.82 Nm	0.63 Nm	0.58 Nm
T_{cog}	3.13 Nm	0.88 Nm	0.46 Nm	0.43 Nm

From Table 4, we can see that the optimization results of the two proposed methods are almost the same from each other. However, method one will change the spatial distribution of the air gap field and introduce low order magnetic field which may be bad for the vibration and noise. Method two will not change the magnetic field distribution but its magnets have complex structure which will increase the manufacturing cost. So these two methods each has its own advantages and disadvantages. We can make a choice according to the requirement of different application situations.

VI. CONCLUSION

In this paper, two novel techniques for torque optimization in AFPM machines are presented. Their accuracy and validity were verified by 3D FEM. The proposed methods were also compared with skew technique which is popular nowadays. Result showed that the proposed methods can greatly reduce the overall pulsating torque without sacrificing the average torque significantly. Some notable characteristics of the two methods are summarized as follows.

i) By establishing the analytical model of torque, a significant amount of time can be saved during the optimization compared with 3D FEM. This is important in the initial stage of motors design.

ii) Average torque, cogging torque and electromagnetic torque ripple are considered simultaneously in the optimization so it can reduce the overall pulsating torque without decreasing the average torque significantly.

iii) The optimization objectives and constraint conditions can be flexibly adjusted to meet different requests.

As the two proposed methods were only verified by FEM, future work would include manufacturing of prototype and validation of the optimization methods by experimental tests.

ACKNOWLEDGMENT

This work was supported by the National Natural Science Foundation of China (51375343) and the National Major Scientific Instrument Equipment Project of China (2012YQ150256).

REFERENCES

[1] F. G. Capponi, G. D. Donato, and F. Caricchi, "Recent advances in axial-flux permanent-magnet machine technology," *IEEE Trans. Ind. Appl.*, vol. 48, no. 6, pp. 2190-2205, Nov.-Dec. 2012.

[2] M. Aydin and M. Gulec, "Reduction of cogging torque in double-rotor axial-flux permanent-magnet disk motors: A review of cost-effective magnet-skewing techniques with experimental verification," *IEEE Trans. Ind. Electron.*, vol. 61, no. 9, pp. 5025-5034, Sep. 2014.

[3] F. Caricchi, F. G. Capponi, F. Crescimbini, and L. Solero, "Experimental study on reducing cogging torque and no-load power loss in axial-flux permanent-magnet machines with slotted winding," *IEEE Trans. Ind. Appl.*, vol. 40, no. 4, pp. 1066-1075, Jul.-Aug. 2004.

[4] M. Aydin, Z. Q. Zhu, T. A. Lipo, and D. Howe, "Minimization of cogging torque in axial-flux permanent-magnet machines: Design concepts," *IEEE Trans. Magn.*, vol. 43, no. 9, pp. 3614-3622, Sep. 2007.

[5] M. Aydin, "Magnet skew in cogging torque minimization of axial gap permanent magnet motors," in *Proc. 18th Int. Conf. Electr. Mach.*, pp. 1-6, Sep. 2008.

[6] E. Yolacan, E. Ozyurt, and M. Aydin, "Magnet shape optimization of a slotted surface mounted axial gap PM motor for reducing cogging torque," in *Proc. 19th Int. Conf. Electr. Mach.*, pp. 1-6, Sep. 2010.

[7] M. Aydin, R. Qu, and T. A. Lipo, "Cogging torque minimization technique for multiple-rotor, axial-flux, surface-mounted-PM machines: Alternating magnet pole-arcs in facing rotors," in *IEEE Industry Applications Soc. Annu. Meeting*, pp. 555-561, Oct. 2003.

[8] A. B. Letelier, D. A. González, J. A. Tapia, R. Wallace, and M. A. Valenzuela, "Cogging torque reduction in an axial flux PM machine via stator slot displacement and skewing," *IEEE Trans. Ind. Appl.*, vol. 43, no. 3, pp. 685-693, May-Jun. 2007.

[9] D. A. González, J. A. Tapia, and A. B. Letelier, "Design consideration to reduce cogging torque in axial flux permanent-magnet machines," *IEEE Trans. Magn.*, vol. 43, no. 8, pp. 3435-3440, Aug. 2007.

[10] C. Hwang, P. Li, F. C. Chuang, C. Liu, and K. Huang, "Optimization for reduction of torque ripple in an axial flux permanent magnet machine," *IEEE Trans. Magn.*, vol. 45, no. 3, pp. 1760-1763, Mar. 2009.

[11] R. Madhavan and B. G. Fernandes, "A novel technique for minimizing torque ripple in axial flux segmented rotor SRM," in *Proc. IEEE Energy Convers. Congr. Expo.*, pp. 3383-3390, Sep. 2011.

[12] W. Q. Chu and Z. Q. Zhu, "Investigation of torque ripples in permanent magnet synchronous machines with skewing," *IEEE Trans. Magn.*, vol. 49, no. 3, pp. 1211-1220, Mar. 2013.

[13] M. S. Islam, S. Mir, T. Sebastian, and S. Underwood, "Design considerations of sinusoidally excited permanent-magnet machines for low-torque-ripple applications," *IEEE Trans. Ind. Appl.*, vol. 41, no. 4, pp. 955-962, Jul.-Aug. 2005.

[14] R. Islam, I. Husain, A. Fardoun, and K. McLaughlin, "Permanent-magnet synchronous motor magnet designs with skewing for torque ripple and cogging torque reduction," *IEEE Trans. Ind. Appl.*, vol. 45, no. 1, pp. 152-160, Jan.-Feb. 2009.

[15] S. Jang, H. Park, J. Choi, K. Ko, and S. Lee, "Magnet pole shape design of permanent magnet machine for minimization of torque ripple based on electromagnetic field theory," *IEEE Trans. Magn.*, vol. 47, no. 10, pp. 3586-3589, Oct. 2011.

[16] S. Lee, G. Kang, J. Hur, and B. Kim, "Quasi-zero torque pulsation of surface permanent magnet synchronous motor for ship gyro stabilizer by pole slot number and air-gap designs," *IEEE Trans. Magn.*, vol. 50, no. 2, pp. 1033-1036, Feb. 2014.

[17] F. Scuiller, "Magnet shape optimization to reduce pulsating torque for a five-phase permanent-magnet low-speed machine," *IEEE Trans. Magn.*, vol. 50, no. 4, pp. 3431-3439, Apr. 2014.

[18] T. F. Chan, L. L. Lai, and S. Xie, "Field computation for an axial flux permanent-magnet synchronous generator," *IEEE Trans. Energy Convers.*, vol. 24, no. 1, pp. 1-11, Mar. 2009.

[19] Y. J. Zhang, S. L. Ho, H. C. Wong, and G. D. Xie, "Analytical prediction of armature-reaction field in disc-type permanent magnet generators," *IEEE Trans. Energy Convers.*, vol. 14, no. 4, pp. 1385-1390, Dec. 1999.

[20] Z. Q. Zhu and D. Howe, "Instantaneous magnetic field distribution in brushless permanent magnet DC motors, Part III: Effect of stator slotting," *IEEE Trans. Magn.*, vol. 29, no. 1, pp. 143-151, Jan. 1993.

[21] P. Virtič, P. Pišek, M. Hadžiselimović, T. Marčič, and B. Štumberger, "Torque analysis of an axial flux permanent magnet synchronous machine by using analytical magnetic field calculation," *IEEE Trans. Magn.*, vol. 45, no. 3, pp. 1036-1039, Mar. 2009.

[22] M. Aydin, S. Huang, and T. A. Lipo, "Torque quality and comparison of internal and external rotor axial flux surface-magnet disc machines," *IEEE Trans. Ind. Electron.*, vol. 53, no. 3, pp. 822-830, Jun. 2006.

Shuanglong Wu a Ph.D. candidate majoring in Vehicle Engineering at Tongji University, Shanghai, China. He received the Bachelor degree of Vehicle Engineering in 2013 from South China University of Technology,Guangzhou, China. His main research interests are in the control of vibration and noise of motor and generator.

Shuguang Zuo a Professor at Tongji University, Shanghai, China. He received the B.S. degree in Mechanical Design from Hunan Agricultural University, Changsha, China, in 1990, and the M.S. and Ph.D. degrees in Automotive Engineering from Jilin University, Changchun, China, in 1993 and 1996, respectively. From 1996 to 1998, he was a Postdoctoral Researcher with the Aviation and Aerospace Technology Postdoctoral Research Station, Nanjing Aeronautics and Astronautics University, Nanjing, China. He is now a Professor with the College of Automotive Engineering, Tongji University. His research interests include vehicle system dynamics and control, vehicle vibration and noise control, and vibration and noise of electrical machines.

Miniaturization of a Broadband Quadrature Hybrid Coupler Using Π-Model Transformation-Based Artificial Transmission Line

Vahid Iran Nejad, Abbas Ali Lotfi-Neyestanak, and Ali Shahzadi

Department of Electrical Engineering, Yadegar-e-Imam Khomeini (RAH) Shahre Rey Branch
Islamic Azad University, Tehran, 18155-144, Iran
Vahid.irannejad@yahoo.com, aalotfi@ieee.org, shahzadi@iust.ac.ir

Abstract ─ In this paper, a novel compact broadband quadrature hybrid coupler based on planar artificial transmission line is presented. This coupler can be used for WLAN application at 2.4 GHz. The planar artificial transmission line has been implemented using Π-model technique. The size of the proposed coupler is merely 38% of that of a conventional one. The compact coupler performs well wideband response.

Index Terms ─ Broadband quadrature, planar artificial transmission line, Π-model.

I. INTRODUCTION

The quadrature hybrid coupler is one of essential elements in microwave circuits. It has extensively been applied in integrated microwave circuits, e.g., power dividers, and in power combiners of various microwave circuits, e.g., balanced amplifiers, balanced mixers, phase shifters, and butler matrix. However, it occupies a large space due to the use of quarter wavelength transmission lines, especially at low frequencies. Therefore, our motivation by this work is to reduce the size of the broadband branch line coupler.

Recently designing compact passive microwave components using artificial transmission lines have drawn a lot of attention [1-7]. To design microwave circuit components with more size reduction and simple fabrication process, the planar artificial transmission line with a single layer printed circuit board can be a good option and it can create transmission lines with a wide range of characteristic impedances and electrical lengths [2-4].

In this paper, a new artificial transmission line (Π-model transformation-based) is presented and the compact quadrature hybrid coupler has been realized. By utilizing the proposed artificial transmission line, we demonstrate the circuit size of the coupler becomes merely about 38% of the conventional designs.

II. DESIGN AND ANALYSIS OF THE PROPOSED PLANAR ARTIFICIAL TRANSMISSION LINE

We have used the technique given in [2-4], to design an artificial transmission line with a characteristic impedance of 35.35 Ω and an electrical length of 90° on a 32-mil RO4003C substrate with a dielectric constant of 3.55 and a loss tangent of 0.0027. The final size of the line, however, needs to be fine-tuned by a full-wave simulation software, e.g., Ansoft HFSS, to include the parasitic coupling between the elements. The flowchart of design process is shown in Fig. 1.

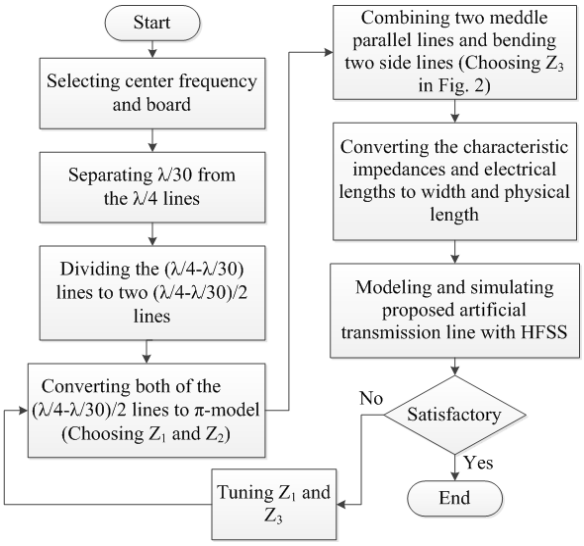

Fig. 1. Flowchart of the design process.

Figure 2 shows a simple equivalent circuit of the quarter wavelength transmission line using Π-model transformation, and as can be seen the length has become shorter.

Each pair of the transmission line is chosen with θ=π/4, amount of impedances and electrical lengths in Fig. 2 can be determined according to [2-4]:

$$Z_1 \sin\theta_1 = Z \sin\theta\,, \tag{1}$$

$$Y_2 \tan\theta_2 = (\cos\theta_1 - \cos\theta)/(Z_1 \sin\theta_1)\,, \tag{2}$$

2.4 GHz is selected as the center frequency of the branch line coupler. We have separated λ/60 lines from the λ/4 lines to determine input and output terminals of

Submitted On: August 21, 2013
Accepted On: February 27, 2016

each line. By choosing Z_1=Z_2=85 Ω, and assuming Z=35.35 Ω and θ=39° ((λ/4-λ/30)/2) in Equation (1), θ_1 will be 16°. Then, after replacing Z_1, Z_2, θ, and θ_1 in Equation (2) θ_2 is found to be 32°.

Now it is time to combine the second black line with the first white line and the bends (Fig. 3) which can be determined as follows:

$$Y_3 \tan\theta_3 = 2Y_2 \tan\theta_2, \quad (3)$$

By choosing Z_3=45 Ω and replacing Z_2 and θ_2 in Equation (3), θ_3=32° is calculated. After simulation and tuning Z_1 and Z_3 are changed to 95 Ω and 50 Ω, respectively.

We can convert the characteristic impedances and electrical lengths to width and physical length according to [8]. All the design parameters can also be adjusted for other frequencies.

Finally, the characteristic impedances and electrical lengths were converted to microstrip transmission lines as shown in Fig. 4: L=18.5 mm, w=3 mm, w_1=1.8 mm, L1=5.5 mm, w_2=3 mm, L_2=10 mm, w_3=0.65 mm and w_4=.5 mm. The simulated characteristic impedances and phase delays of 90°, 35.35 ohm conventional and artificial transmission lines versus frequencies are presented in Fig. 5, which shows a good agreement between them.

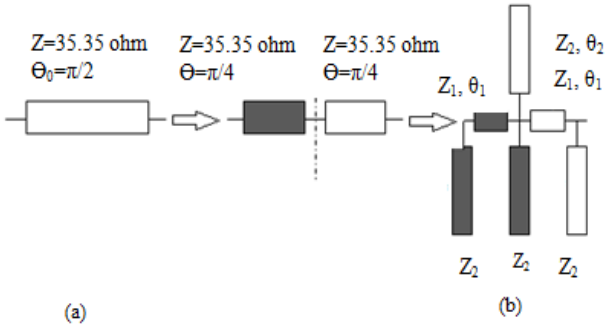

Fig. 2. (a) Conventional quarter wavelength transmission line with Zo = 35.35 Ω, and (b) using two Π-model lines (1st stage).

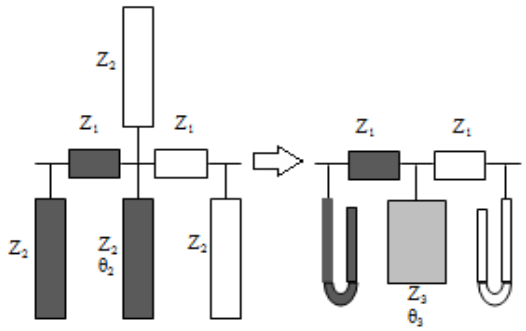

Fig. 3. Combination of the compact Π-model with the bends (2nd and 3rd stages).

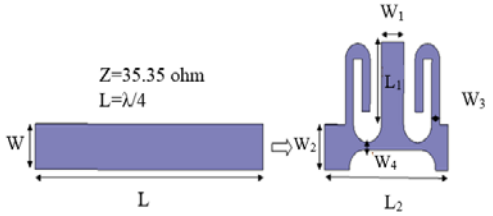

Fig. 4. Layout of the conventional quarter wavelength microstrip transmission line with Z_o=35.35 Ω and the artificial microstrip transmission line.

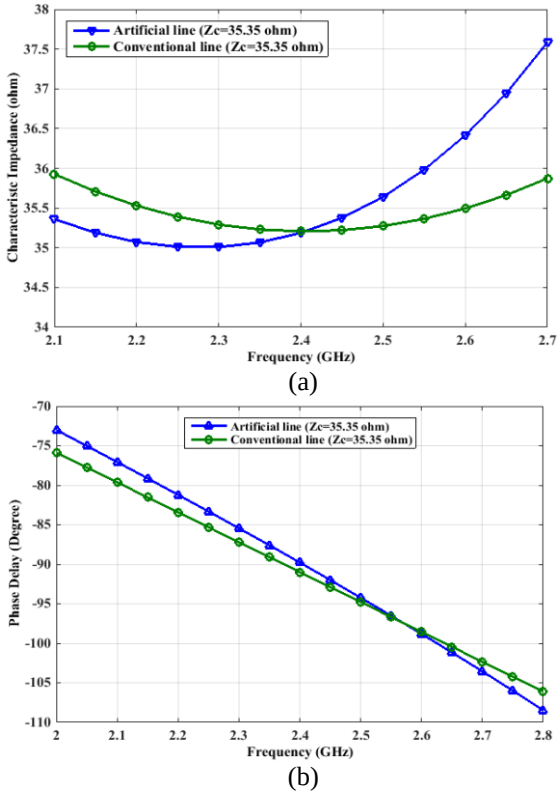

Fig. 5. (a) Simulated characteristic impedances of 90°, 35.35 ohm conventional and artificial transmission lines, and (b) simulated phase delays of the 90°, 35.35 ohm conventional and artificial transmission lines.

III. DESIGNS OF MINIATURIZED BROADBAND QUADRATUREHYBRID

According to [9], characteristic impedances of the broadband branch-line couplers, shown in Fig. 6 are 35.35 Ω and 119 Ω.

In order to miniaturize the size of the branch-line coupler, the artificial transmission lines have been developed to replace with the original quarter wavelength transmission lines.

The circuit layout of the compact quadrature hybrid coupler is shown in Fig. 6. The four artificial transmission lines of the hybrid coupler are initially

designed, and then fine-tuned to include the parasitic coupling between the lines, using Ansoft HFSS [2-3].

The second vertical transmission line has been replaced with a dual transmission line as explained in [4]. The length of all vertical transmission lines is 20 mm. If further size reduction is required it can be achieved by meandering the high impedance vertical lines.

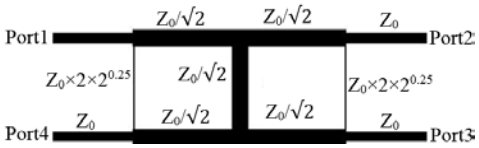

Fig. 6. Structure of the conventional broadband branch line coupler.

A photograph of the proposed compact quadrature hybrid coupler is shown in Fig. 7 (b), and the simulation and measurement results are illustrated in Fig. 8. As can be seen, the measurement results are found to be in good agreement with the simulations.

Figure 8 (b) shows the phase difference between the output ports. The phase difference between outputs is maintained at 90º (+/-2º across the bandwidth).

Finally, a size reduction of about 62% is obtained as can be observed in Fig. 7. In addition, the S-parameters of the compact coupler (Fig. 8) show good balance between the coupled ports, the coupling at the port 2 and 3 are around 3±0.6 dB because port 1 serves as the excitation for the 2-2.8 GHz frequency band. The simulated return loss and isolation are greater than 20 dB.

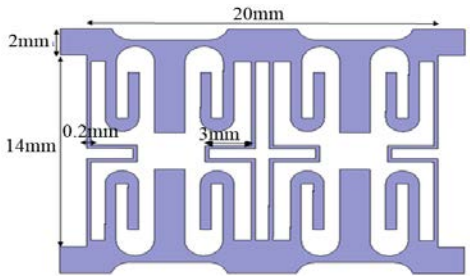

(a)

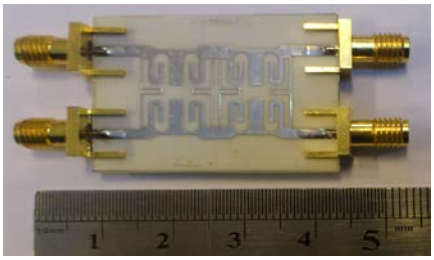

(b)

Fig. 7. (a) Circuit layout of the miniaturized quadrature hybrid coupler, and (b) photograph of the proposed miniaturized quadrature hybrid coupler.

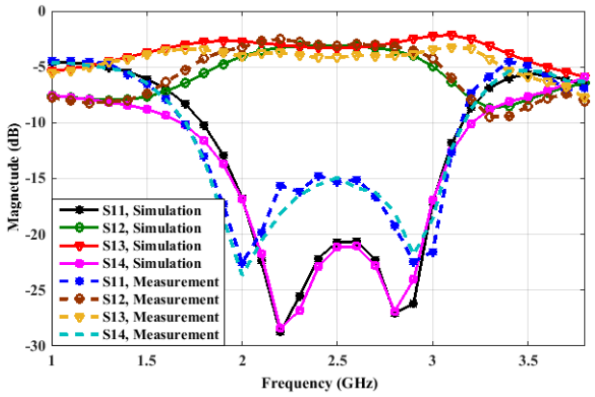

(a)

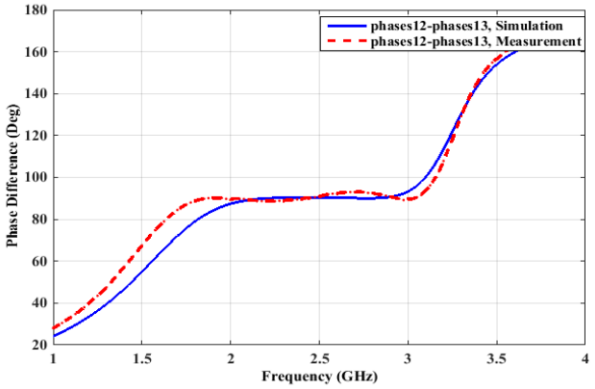

(b)

Fig. 8. Simulated and measured results of the proposed quadrature hybrid coupler: (a) S-parameters and (b) phase difference between S_{12} and S_{13}.

These results confirm that the proposed coupler has a desirable performance, and therefore we have met our goal of achieving a compact and broadband branch line coupler.

The simulated and measured results show good agreement across the entire band of 2-2.8 GHz at center frequency of 2.4 GHz with 800 MHz band width. Table 1 summarizes the performance of the proposed quadrature coupler and previous designs. The superior performance of the proposed design has been confirmed.

Table 1: Comparison of various quadrature hybrid couplers

	Relative Area	Fabrication	Band Width
Conventional	100%	Single Layer	
Chiang [1]	34%	Additional lumped element	Narrow
Chun [3]	45%	Single layer	Wide
Sun [5]	60%	Single layer	Narrow
Eccleston [6]	49%	Single layer	Narrow
Liu [10]	42%	Double layer	Narrow
Iran-Nejad [11]	47%	Single layer	Wide
This Work	38%	Single layer	Wide

IV. COMPARISON OF APPLIED NUMERICAL METHOD SOLUTION (FEM) AND FINITE DIFFERENCE TIME DOMAIN (FDTD)

We have applied HFSS, a finite element method (FEM) solver for electromagnetic structures, for EM computations of the proposed quadrature hybrid. Additionally, we can apply another EM numerical method, such as finite difference time domain (FDTD), to solve the proposed structure and compare them afterwards.

Figure 9 shows a good agreement between S-parameters of both FEM and FDTD, solved by HFSS and CST software's, respectively.

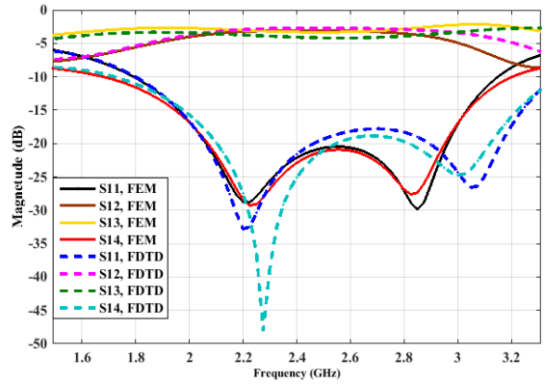

(a)

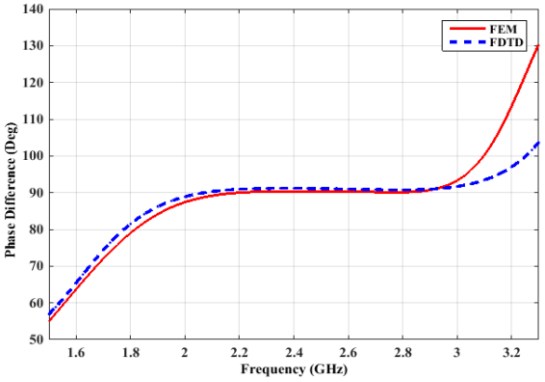

(b)

Fig. 9. FEM vs. FDTD solving for the proposed structure: (a) S-parameters and (b) phase difference

V. CONCLUSION

A new planar artificial transmission line incorporated with Π-model technique has been proposed and demonstrated. This artificial transmission line is capable of synthesizing microstrip lines with a wide variety of characteristic impedances and electrical lengths.

By utilizing the proposed artificial transmission line, a compact broadband hybrid coupler has successfully been designed for WLAN applications. This coupler has low insertion loss, negligible phase imbalance, and significant size reduction of 62%. The proposed artificial transmission line is also expected to find applications in microwave circuits such as butler matrix.

REFERENCES

[1] Y. C. Chiang and C. Y. Chen "Design of a wide band lumped element 3-dB quadrature coupler," *IEEE Trans. Microwave Theory Tech.*, vol. 49, no. 3, pp. 476-479, 2001.

[2] C. W. Wang, T. G. Ma, and C. F. Yang, "A new planar artificial transmission line and its applications to a miniaturized butler matrix," *IEEE Transactions on Microwave Theory and Techniques*, vol. 55, no. 12, pp. 2792-2801, 2007.

[3] Y.-H. Chun and J.-S. Hong, "Compact wide-band branch-Line hybrids," *IEEE Transactions on Microwave Theory and Techniques*, vol. 54, no. 2, pp. 704-709, Feb. 2006.

[4] C. W. Tang, M. G. Chen, and C. H. Tsai, "Miniaturization of microstrip branch-line coupler with dual transmission lines," *IEEE Microwave and Wireless Components Letters*, vol. 18, no. 3, pp. 185-187, 2008.

[5] K. O. Sun, S. J. Ho, C. C. Yen, and D. van der Weide, "A compact branch-line coupler using discontinuous microstrip lines," *IEEE Microwave Wireless Component Lett.*, vol. 15, no. 8, pp. 519-520, 2005.

[6] K. W. Eccleston and S. H. M. Ong, "Compact planar microstrip line branch-line and rat race couplers," *IEEE Trans. Microwave Theory Tech.*, vol. 51, no. 10, pp. 2119-2125, Oct. 2003.

[7] P. Hajizadeh, H. R. Hassani, and S. H. Sedighy, "Planar artificial transmission lines loading for miniaturization of RFID printed quasi-yagi antenna," *IEEE Antennas and Wireless Propagation Letters*, vol. 12, pp. 464-467, 2013.

[8] T. C. Edwards, *Foundations for Microstrip Circuit Design*, 2nd ed., 1991.

[9] D. M. Pozar, *Microwave Engineering*, 3rd ed., John Wiley & Sons, Inc., 2004.

[10] A. S. Liu, H. S. Wu, C. K. C. Tzuang, and R.-B. Wu, "Ka-band 32-GHz planar integrated switched-beam smart antenna," *IEEE MTT-S Int. Microw. Symp. Dig.*, Long Beach, CA, pp. 565-568, June 12-17, 2005.

[11] V. Iran-Nejad, A. A. Lotfi-Neyestanak, and A. Shahzadi "Compact broadband quadrature hybrid coupler using planar artificial transmission line," *Electronics Letters*, vol. 48, no. 25, pp. 1602-1603, Dec. 2012.

Vahid Iran_Nejad was born in Tehran, Iran, in April, 1986. He received the B.Sc. and the M.Sc. degree from the Islamic Azad University, Shahre Rey Branch, Tehran, Iran, in 2009 and 2012, respectively, in Telecommunication Engineering.

His research activities deal with RF/microwave technologies, satellite communications, smart antennas, DF antennas and radio systems, ELF and VLF propagation in the earth-ionosphere duct, wireless communications and numerical methods in electromagnetic.

Abbas Ali Lotfi-Neyestanak (SM'10) was born in Tehran, Iran. He received his B.Sc. degree in Communication Eng. (1993) and M.Sc. degree in Electronic Engineering (1997) and Ph.D. degree in Communication Engineering (2004) from Iran University of Science and Technology (IUST) Tehran, Iran, respectively. From 1997 he was teaching in the Department of Electrical Engineering at the "Islamic Azad University" Shahare Rey branch, Tehran-Iran. Currently, he is collaborating with the Department of Electrical Engineering, University of Waterloo, Ontario, Canada.

His main areas of research interest are Microstrip antenna, Microwave passive and active circuits, Electronic circuits design, EMC & EMI in High voltage, Optimization methods in electromagnetic, Radio wave propagation, Microwave measurement, Numerical methods in electromagnetic problems, RF MEMS and currently bio electromagnetic. Lotfi-Neyestanak is a Senior Member of IEEE and has published two books in Persian and more than 105 papers in international journals and conferences.

A. Shahzadi received the B.Sc., M.Sc. and Ph.D. degrees from the Iran University of Science & Technology (IUST), Tehran, Iran, in 1996, 1999 and 2007, respectively, all in Electrical Engineering.

His research activities deal with wireless and mobile communication systems and networking, cognitive radio and cooperative communications and networking.

Development of a Symmetric Waveguide T-Junction Power Divider with Equal-Phase Characteristic

Guan-Long Huang [1], Shi-Gang Zhou [1,2], and Tan-Huat Chio [1]

[1] Temasek Laboratories
National University of Singapore, Singapore, 117411, Singapore
tslhg@nus.edu.sg

[2] School of Electronics and Information
Northwestern Polytechnical University, Xi-an, 710072, China

Abstract ─ An efficient method is proposed to design a versatile rectangular waveguide T-junction power divider without changing the length of either of the output branches for phase compensation. Instead, the phase balance is controlled by the widths of the output branches, which, in turn, help to achieve the same time-of-arrival of waves propagating to the two output ports. This method does not sacrifice the T-junction's symmetric characteristic physically. Numerical analysis has been utilized to design several T-junction power dividers operating in Ku-Band with different power ratios, and results are compared with the measured ones to verify the design feasibility.

Index Terms ─ Microwave power divider, rectangular waveguide, symmetric T-junction, wideband.

I. INTRODUCTION

In advanced microwave systems, especially in radar and satellite communication systems, high performance power dividers are wanted to achieve particular functions such as low sidelobe radiation patterns on antenna aperture, which is important for avoiding the interference from jamming environments. A proper power distribution feed-network, constructed by multiple power dividers in the rear, is always required to excite the radiation elements with correct amplitudes and phases [1-3]. Waveguide-based power dividers are the preferred candidate due to their unique advantages like robust structure, low loss, high-power handling capability and wide operational bandwidth. Lots of published literatures have focused on the impedance matching design of *H*-plane waveguide T-junction power dividers; and most of them adopted either a central splitter or an inductive post to minimize the reflection [4-9]. Analytical methods have also been reported [10-13], as well as their practical application in constructing array feed-networks [14,15]. Some metamaterial-inspired resonators or dielectric slab insertion have been recently used to design waveguide power dividers [16]. Although low input reflection and required power-split can be obtained in these power dividers, in most of the cases, the only way to achieve phase-balance between two output ports is to modify the length of one output branch compared to the other one's in order to compensate the phase difference. Some typical design examples can be viewed in [7,10]. These designs apparently destroy the symmetry of the T-junction power dividers and result in even larger feed-network in application eventually. Besides, most of their operational bandwidths are limited.

In this paper, an efficient method is proposed to design an equal-phase and unequal-power-division T-junction power divider without changing the length of either of the output branches for phase compensation. Instead, the phase balance is controlled by the widths of the output branches, which, in turn, help to achieve the same time-of-arrival of waves propagating to the two output ports. This method does not sacrifice the T-junction's symmetric characteristic physically.

II. DESIGN METHODOLOGY

The proposed equal-phase and unequal-power-division waveguide T-junction power divider with equal-branch-length is shown in Fig. 1. Here the physical symmetry of the T-junction power divider is illustrated as follows: when the central line of the input port (Port 1) is taken as reference, the physical lengths from this line to the two output ports (Port 2 and Port 3) are equal, i.e., $l_1=l_2+d_1=l_3-d_1$. The waveguide port dimensions (a and b) are the same as those of a standard WR-62 Ku-Band waveguide adapter, which will ease the setup in measurement. Fillets are incorporated to avoid sharp corners in order to take the practical fabrication process (machining method) into consideration. Different power-split ratios can be efficiently obtained by offsetting a

Submitted On: December 8, 2015
Accepted On: February 26, 2016

septum from the center (d_1). Different d_1 corresponds to different output power ratios. To ease the explanation and discussion in this work, the offset value (d_1) is fixed at several values instead of fixing the power ratio. d_1 is set to 1 mm in the models shown in Fig. 1. Impedance matching can be controlled by the dimensions of the septum (h_1 and r_1), and adding a window (p_1) would help to further reduce the input reflections. However, the phase difference between the two output ports is affected significantly while shifting the septum's position to produce the required power ratio. This is mainly due to the unequal propagating distances of electromagnetic (EM) waves from the input port to the two output ports, i.e., $l_2 \neq l_3$. To solve this problem, traditional ways usually extend or shorten one of the output branches in order to compensate the phase difference [5-10]. However, this destroys the physical symmetry of the T-junction power divider.

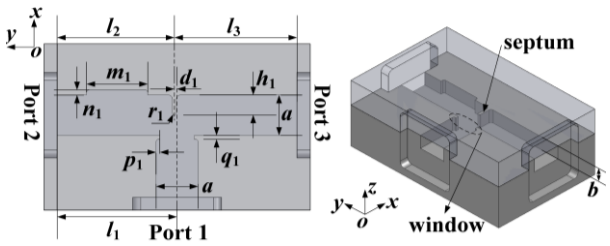

(a) Enlarging the branch width of Port 2

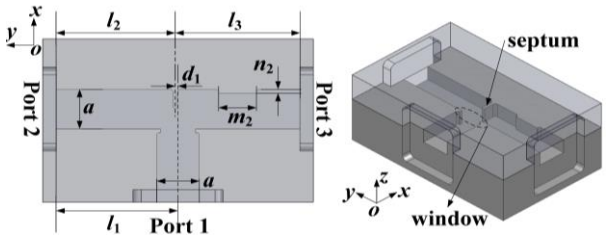

(b) Shrinking the branch width of Port 3

Fig. 1. Symmetric T-junction power divider #1 mm.

Instead of adopting the above-mentioned asymmetric structure, one can consider increasing or slowing down the EM waves inside the T-junction so as to force the propagating waves to arrive at the two output ports simultaneously. The wave velocities can be controlled by tuning the widths of the output branches, i.e., n_1 in Fig. 1 (a) and n_2 in Fig. 1 (b). It can be understood that a waveguide with varying width introduces different propagating velocities and, in effect, produces the required phase compensation so that the physical symmetry of the power divider is retained. More theoretical explanation is as follows.

According to waveguide theory, the guide wavelength (λ_g) can be expressed as:

$$\lambda_g = \lambda_0 / \sqrt{1-(\lambda_0 / \lambda_c)^2}\,, \tag{1}$$

where λ_c is the cut-off wavelength and λ_0 is the wavelength in free-space [17]. The phase velocity inside the waveguide (v_p) is expressed as:

$$v_p = \lambda_g f = v_0 / \sqrt{1-(\lambda_0 / \lambda_c)^2}\,, \tag{2}$$

where v_0 is the phase velocity in free-space and $v_0 = \lambda_0 f$. For the dominant TE_{10} mode, $\lambda_c = 2a$, where a is the width of the waveguide port. Then (2) can be rewritten as;

$$v_p = v_0 / \sqrt{1-(\lambda_0 / 2a)^2}\,. \tag{3}$$

Let the physical distance from input port (Port 1) to the two output ports (Port2, Port 3) be l_2 and l_3, respectively (Fig. 1) where,

$$l_2 = l_1 - d_1,\ l_3 = l_1 + d_1\,. \tag{4}$$

The corresponding wave propagation time from the septum to the two output ports are denoted by τ_2 and τ_3, respectively. The waveguide phase velocities in the two output branches are denoted by v_{p2} and v_{p3} respectively. Therefore, τ_2 and τ_3 can be obtained as follows:

$$\begin{aligned} \tau_2 &= l_2 / v_{p2} = l_2 \sqrt{1-(\lambda_0 / 2a_2)^2} / v_0, \\ \tau_3 &= l_3 / v_{p3} = l_3 \sqrt{1-(\lambda_0 / 2a_3)^2} / v_0, \end{aligned} \tag{5}$$

where a_2 and a_3 indicate the branch widths of the Port 2 and Port 3, respectively. The objective is to achieve unequal power division from Port 1 to Port 2 & Port 3 while maintaining the equal-phase. In other words, the time for the wave propagating from the input port to the two output ports should be equal, namely, $\tau_2 = \tau_3$,

$$l_2 \sqrt{1-(\lambda_0 / 2a_2)^2} / v_0 = l_3 \sqrt{1-(\lambda_0 / 2a_3)^2} / v_0\,. \tag{6}$$

Thus,

$$l_2 / l_3 = \sqrt{1-(\lambda_0 / 2a_3)^2} / \sqrt{1-(\lambda_0 / 2a_2)^2}\,. \tag{7}$$

One should note that, in order to make (7) valid under the condition $l_2 < l_3$ as shown in Fig. 1, a_2 should be larger than a_3. Hence, there are three feasible ways to achieve this requirement: ① enlarging the branch width of Port 2 alone, i.e., $a_2 = a + n_1$ in Fig. 1 (a); ② shrinking the branch width of Port 3 alone, i.e., $a_3 = a - n_2$ in Fig. 1 (b); ③ enlarging and shrinking the branch width of Port 2 and Port 3, respectively. To simplify the analysis, case ① is taken into account below and other cases can be analyzed in the same way. In the case shown in Fig. 1 (a), a_2 is enlarged from a to $(a+n_1)$ in order to reduce the waveguide phase velocity while a_3 is unchanged. The value of n_1 can be obtained by solving (4) and (7):

$$\begin{aligned} n_1 &= \frac{\lambda_0}{2\sqrt{1-(l_3/l_2)^2(1+\lambda_0/2a_3)(1-\lambda_0/2a_3)}} - a \\ &= \frac{\lambda_0}{2\sqrt{1-(\frac{l_1+d_1}{l_1-d_1})^2(1+\frac{\lambda_0}{2a})(1-\frac{\lambda_0}{2a})}} - a \end{aligned}\,. \tag{8}$$

According to (5) and (8), once the branch width of an output port (e.g., a_3) is fixed, the time difference of the wave arriving at the two output ports is determined by the wave propagating velocity via adjusting the other output port's width (a_2). Hence, the unequal-power-

division can be realized in this symmetric structure while maintaining phase-balance from the input to the output ports. Nevertheless, one should note that the above analysis is not rigorous. The main reason of being an approximation is that the formulas, e.g., (8) are frequency dependent. Therefore, there exists no analytical formula which is valid in a frequency band. Higher order modes will occur when enlarging the width of the waveguide to some extent. But (8) can provide a convenient way to get an initial trial value for the parameter n_1 in numerical analysis and save time for the design of an equal-phase performance.

III. RESULTS AND ANALYSIS

Based on the above analysis, the phase-balance in the symmetric T-junction power divider can be realized by adjusting the widths of the output branches. Although enlarging or shrinking the waveguide branch from its narrow wall (changing n_1 or n_2) will cause the magnetic field (*H*-field) in that region to be expanded or squeezed, equivalent to add a shunt reactance in the waveguide circuit [17], the mismatching can be alleviated by adjusting the length of the enlarging or shrinking part (m_1 or m_2). Therefore, further numerical analysis has found that the phase-balance and impedance matching can be improved by optimizing the enlarging parameters (m_1, n_1) or the shrinking parameters (m_2, n_2). Three configurations of the T-junction power divider with septum's offset value d_1 fixed at 1 mm have been designed and fabricated: one without the equal-phase design, two with the equal-phase design (same as shown in Figs. 1 (a) and (b)). The three models are optimized by the commercial EM simulation software HFSS®. Dimensions of the latter two configurations are obtained from the numerical analysis and listed in Table 1. One of the prototypes is shown in Fig. 2 with and without WG-62 waveguide adapters. Figure 3 shows the internal view of the two prototypes before assembly, which are corresponding to those in Fig. 1. All the prototypes are fabricated in aluminum by the milling technique and assembled by screws. It is a standard machining fabrication process and the typical manufacturing accuracy is better than 30 μm, which is much less than a wavelength in Ku-Band and would not affect the power dividers' performance a lot. Some screw holes are opened around the waveguide channels for assembly alignment and tight electrical contact. Each port is connected to a WR-62 waveguide adapter during the measurement. It is worth mentioning that some microwave chokes are incorporated into the prototypes for preventing energy leakage via gaps (if any) after the assembly. All of the prototypes are measured by a two-port Vector Network Analyzer (VNA) while the third port is terminated by a matching load. A measurement setup is shown in Fig. 4.

Experimental results compared with the analytical ones obtained from HFSS® simulation are plotted in Fig. 5 and Fig. 6. It can be seen from Fig. 5 that the measured unequal-power-division level ($|S_{21}/S_{31}|$) remains stably in both designs (Fig. 1 (a) & case ①) and (Fig. 1 (b) & case ②). The reflections of the input port, represented by the voltage standing wave ratios (VSWRs), are less than 1.3 over the major part of a wide bandwidth of 13.0 GHz~17.0 GHz. Figure 6 shows that the phase difference is improved significantly from the original 20° to less than ±6° after adopting the phase-equalization technique. The value of n_1 in the enlarging design is 2 mm, which is close to the estimated initial value (n_1 = 1.6 mm) based on (8) of case ①. Additionally, the phase-balance improvement can also be verified by observing the electric-field (*E*-field) distribution plotted in Figs. 7 (a)~(c). Compared with the T-junction divider without phase-equalization design in Fig. 7 (a), EM waves propagating inside the two output branches almost reach the two output ports simultaneously after applying the equal-phase design, as shown in Fig. 7 (b) and Fig. 7 (c).

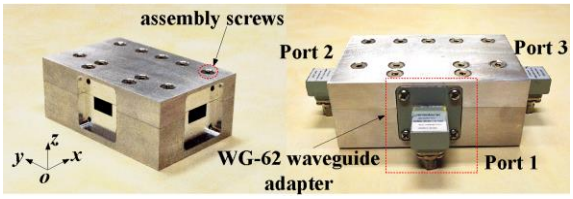

Fig. 2. Prototypes of T-junction power divider.

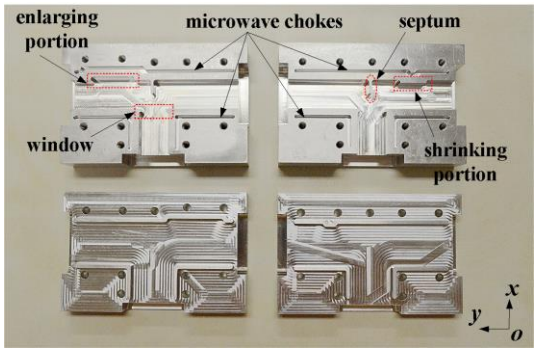

Fig. 3. Parts of the proposed T-junction before assembly.

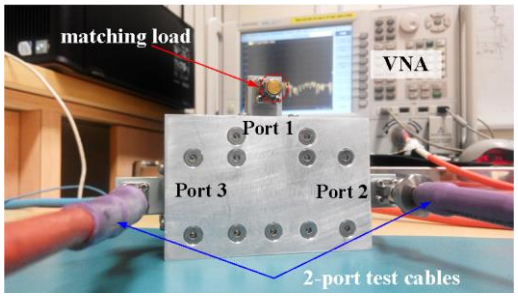

Fig. 4. Power divider measurement setup.

Table 1: Dimensions of T-junction #1 mm (unit: mm)

a	b	l_1	l_2	l_3	d_1	h_1
15.8	7.9	45.0	44.0	46.0	1.0	7.75
r_1	p_1	q_1	m_1	n_1	m_2	n_2
0.75	1.4	1.5	23.0	2.0	14.0	1.6

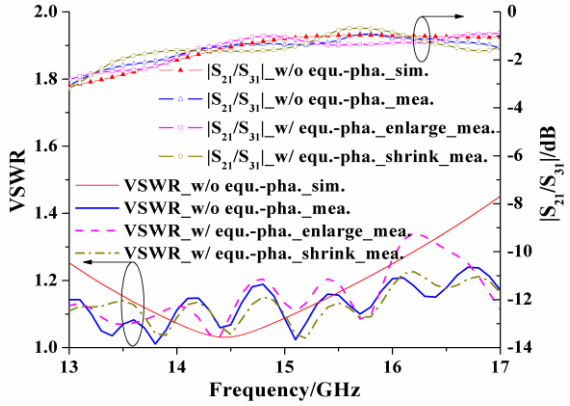

Fig. 5. T-junction amplitude comparison #1 mm.

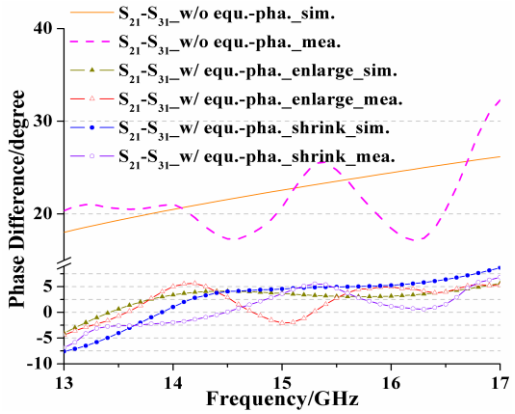

Fig. 6. T-junction phase comparison #1 mm.

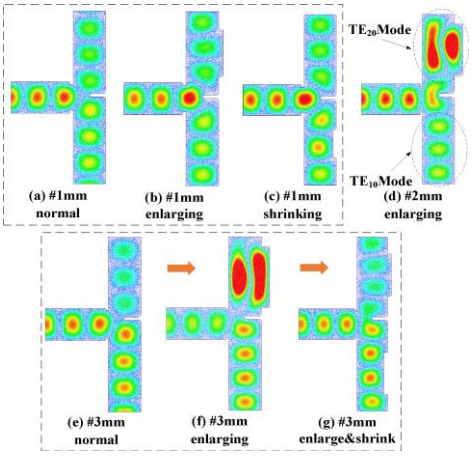

Fig. 7. *E*-field distribution for models of different power-ratios: (a)~(d) at 16.0 GHz, (e)~(g) at 15.8 GHz.

IV. FURTHER INVESTIGATION

The last section verifies the phase-balance of the symmetric T-junction power divider can be greatly improved by using the proposed design method. However, when a larger power ratio is to be realized with a larger septum offset, one cannot monotonically enlarge one branch width to compensate the phase difference without considering the possibility of occurrence of high-order-modes. Figure 8 shows the structure of T-junction power divider with d_3 fixed at 2 mm. Here only the branch width of Port 2 is enlarged to balance the phase difference. Dimensions of the power divider are listed in Table 2. Measured results are compared to the simulated ones before and after enlarging the branch's width, as shown in Fig. 9 and Fig. 10. VSWRs of less than 1.2 and consistent trends of power-division between measurement and simulation, as well as good phase-balance improvement can be achieved in a wide bandwidth. Nevertheless, there is an anomaly at 16.0 GHz for both the amplitude and phase results (highlighted as the shadow areas). Further investigation shows that it is due to a higher-order-mode generated at 16.0 GHz when the waveguide width is enlarged to a certain value. It can also be verified by a close looking at the *E*-field distribution in Fig. 7 (d), where a TE_{20} mode is observed in the enlarging portion.

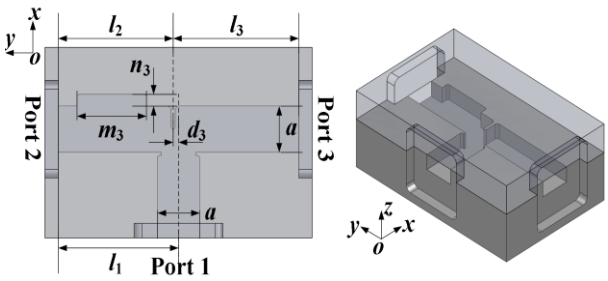

Fig. 8. Symmetric T-junction power divider #2 mm.

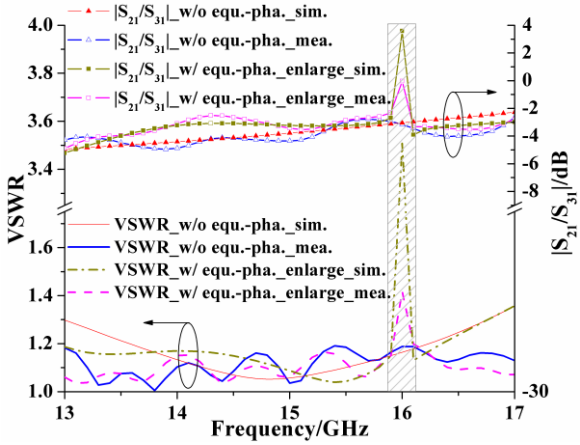

Fig. 9. T-junction amplitude comparison #2 mm.

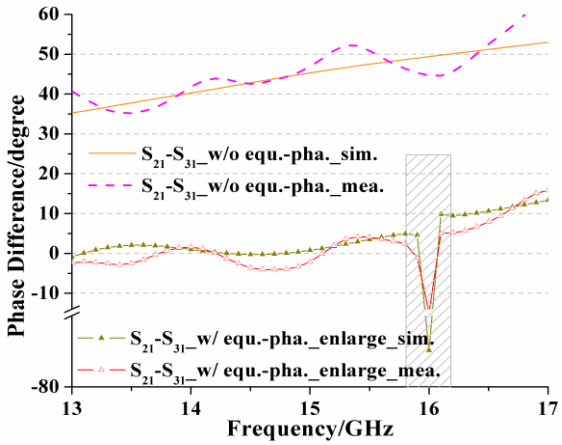

Fig. 10. T-junction phase comparison #2mm.

Table 2: Dimensions of T-junction # 2mm (unit: mm)

a	b	l_1	l_2	l_3	d_3	m_3	n_3
15.8	7.9	45.0	43.0	47.0	2.0	26.0	4.0

(Other parameters are the same as in Fig. 1 and Table 1)

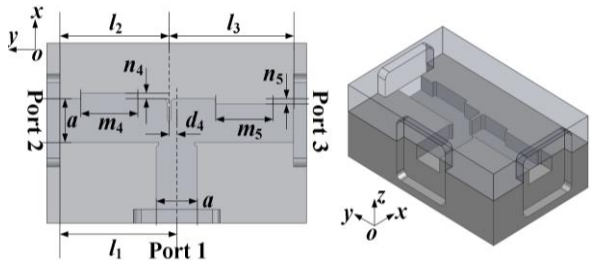

Fig. 11. Symmetric T-junction power divider #3 mm.

Table 3: Dimensions of T-junction #3 mm (unit: mm)

a	b	l_1	l_2	l_3
15.8	7.9	45.0	42.0	48.0
d_4	m_4	n_4	m_5	n_5
3.0	22.0	2.0	22.0	2.0

(Other parameters are the same as in Fig. 1 and Table 3)

Apparently, the occurrence of high-order-modes would limit the operational bandwidth of the power divider. In this work, an effcient approach is devised to solve this problem without monotonically adjusting one branch width alone. When an even larger power ratio is required, e.g., d_4 = V3 mm in Fig. 11, the branch width of Port 2 (n_4) can be enlarged and that of Port 3 (n_5) can be shrunk at the same time in order to avoid high-order-modes. The selection criteria of values is similar to the case ③ of (7). Detailed dimensions of the T-junction power divider are listed in Table 3.

For comparison, results of the T-junction power divider with only one branch width modification (similar to the structure in Fig. 8) are shown in Fig. 12 first. A much wider branch width is required to compensate the larger phase difference caused by the larger power-division. There is obviously a high-order mode occurring at around 15.8 GHz, as shown in the shadow area in Fig. 12. The results of the proposed method of adjusting widths for the two output branches are shown in Fig. 13 and Fig. 14. Compared with Fig. 12, it can be seen that the anomaly at around 15.8 GHz has been removed, which can also be observed in the *E*-field distribution in Figs. 7 (e)~(g). There is a relatively good agreement between measurement and simulation. Phase difference between the two output ports can be improved from around 65º of the original design to less than ±10º of the equal-phase design from 13.0 GHz~15.3 GHz.

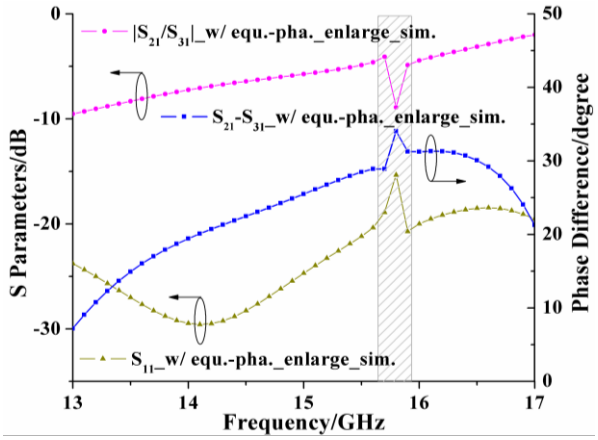

Fig. 12. Results of modifying single branch #3 mm.

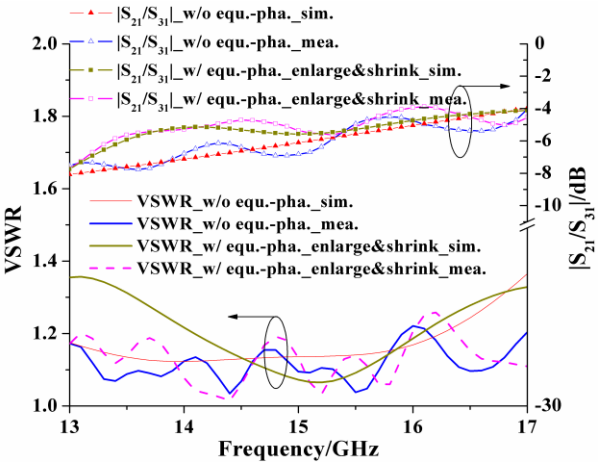

Fig. 13. Amplitudes of modifying two branches #3 mm.

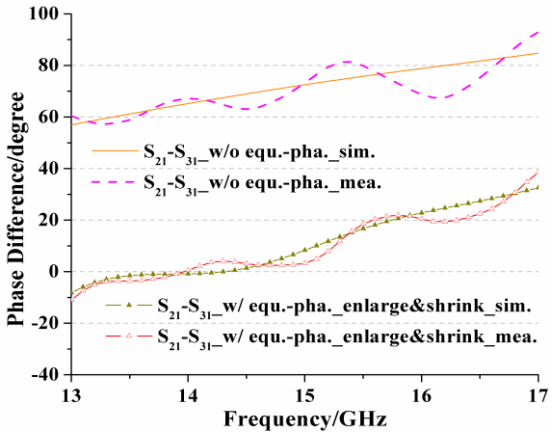

Fig. 14. Phases of modifying two branches #3 mm.

V. CONCLUSION

An efficient method has been proposed for developing a symmetric waveguide T-junction power divider with equal-branch lengths. The phase-balance improvement has been demonstrated via both numerical analysis and practical measurements. High-order-mode phenomenon is also taken into account. Results reveal that the proposed T-junction power divider can achieve good amplitude and phase performance over a wide bandwidth. This device has a potential merit in high-power feed-network designs where equal-phase and unequal-power-division are to be achieved by equal-length feeding lines.

REFERENCES

[1] T. Sehm, A. Lehto, and A. V. Raisanen, "A high-gain 58-GHz box-horn array antenna with suppressed grating lobes," *IEEE Trans. Microw. Theory Techn.*, vol. 47, no. 7, 1125-1130, Jul. 1999.

[2] B. Xiao, J. Hong, and B. Wang, "A novel UWB out-of-phase four-way power divider," *Applied Computational Electromagnetics Society (ACES) Journal*, vol. 26, no. 10, pp. 863-867, Oct. 2011.

[3] V. Demir, D. Elsherbeni, D. Kajfez, and A. Z. Elsherbeni, "Efficient wideband power divider for planar antenna arrays," *Applied Computational Electromagnetics Society (ACES) Journal*, vol. 21, no. 3, pp. 318-324, Nov. 2006.

[4] J. Hirokawa, K. Sakurai, M. Ando, and N. Goto, "An analysis of a waveguide T junction with an inductive post," *IEEE Trans. Microw. Theory Techn.*, vol. 39, no. 3, 563-566, Mar. 1991.

[5] E. Arnold, R. W. Lyon, A. Schlaud, K. Solbach, and J. S. Tanner, "Design of a power divider network for a slotted waveguide array using finite element and finite difference techniques," *8th Int. Conf. Antennas Propaga.*, Edinburgh, UK, vol. 2, pp. 831-833, Mar. 1993.

[6] J. Joubert and S. R Rengarajan, "Design of unequal H-plane waveguide-power dividers for array applications," *IEEE Int. Symp. Antennas Propaga.*, Baltimore, U.S.A., vol. 3, pp. 1636-1639, Jul. 1996.

[7] T. Sehm, A. Lehto, and A. V. Raisanen, "Matching of a rectangular waveguide T junction with unequal power division," *Microw. Opt. Technol. Lett.*, vol. 14, no. 3, pp. 141-143, Feb. 1997.

[8] S. Christopher, V. A. AbidHussain, M. S. Easwarann, and V. N. Dabade, "Design aspects of compact high power multiport unequal power dividers," *IEEE Int. Symp. Phased Array Systems Techn.*, Boston, U.S.A., 63-67, Oct. 1996.

[9] S. Yang and A. E. Fathy, "Synthesis of a compound T-junction for a two-way splitter with arbitrary power ratio," *IEEE MTT-S Int. Microw. Symp.*, Long Beach, U.S.A., 985-988, Jun. 2005.

[10] S. Yang and A. E. Fathy, "Design equations of arbitrary power split ratio waveguide T-junctions using a curve fitting approach," *Int. J. RF Microw. C. E.*, vol. 19, no. 1, 91-98, Jan. 2009.

[11] X.-P. Liang, K. A. Zaki, and A. E. Atia, "A rigorous three plane mode-matching technique for characterizing waveguide T-junctions, and its application in multiplexer design," *IEEE Trans. Microw. Theory Techn.*, vol. 39, no. 12, pp. 2138-2147, Dec. 1991.

[12] T. Sieverding and F. Arndt, "Field theoretic CAD of open or aperture matched T-junction coupled rectangular waveguide structures," *IEEE Trans. Microw. Theory Techn.*, vol. 40, no. 2, pp. 353-362, Feb. 1992.

[13] S.-S. Ha, S.-Y. Lee, H.-W. Ko, D.-H. Park, and B.-C. Ahn, "Design equations for the H-plane power divider with a circular post in a rectangular waveguide," *Journal of the Korea Electromagnetic Engineering Society*, vol. 4, no. 4, pp. 150-155, Dec. 2004.

[14] H. Guan-Long, Z. Shi-Gang, C. Tan-Huat, and Y. Tat-Soon, "Broadband and high gain waveguide-fed slot antenna array in the Ku-band," *IET Microw., Antennas Propag.*, vol. 8, no. 13, pp. 1041-1046, Oct. 2014.

[15] T. Sehm, A. Lehto, and A. V. Raisanen, "A large planar 39-GHz antenna array of waveguide-fed horns," *IEEE Trans. Antennas Propag.*, vol. 46, no. 8, pp. 1189-1193, Aug. 1998.

[16] M. Barbuto, F. Bilotti, and A. Toscano, "Novel waveguide components based on complementary electrically small resonators," *Photonics and Nanostructures – Fundamentals and Applications*, vol. 12, no. 4, pp. 84-290, 2014.

[17] D. M. Pozar, *Microwave Engineering*, 3rd edition, John Wiley & Sons, 2004.

Near-Field Focused Folded Transmitarray Antenna for Medical Applications

Saber H. Zainud-Deen [1*], Walaa M. Hassan [2], and Hend A. Malhat [1]**

[1] Department of Electronics and Communication Engineering
Faculty of Electronic Eng., Menoufia, Egypt
*anssaber@yahoo.com, **er_honida1@yahoo.com

[2] Department of Microwave Engineering
Electronics Research Institute, Giza, 12622, Egypt
walaa81hassan@yahoo.com

Abstract ─ A near-field focused folded transmitarray antenna is proposed at 2.45 GHz for medical applications. The proposed folded transmitarray construction introduces compact design, low profile, and reduced fabrication cost with focused power in both the near-field and far-field regions of the antenna. The transmitarray consists of a feeding horn antenna embedded centrally in the transmitarray structure and a perfect electric conductor plate with the same size as a reflector. The radiation from the feeding horn is reflected by the plate toward the transmitarray. The unit-cell element of the transmitarray is a square dielectric box with four identical circular holes. The transmission coefficient was nearly -3 dB in magnitude and 320 degrees in phase. The radiation characteristics of the unfolded and folded transmitarray are analyzed using the finite integral technique. The normalized power density distribution around a part of the human leg placed in front of the transmitarray is investigated. The proposed antenna is used to heat a specific area on the human leg for treatment.

Index Terms ─ Folded, medical applications, near-field focused, transmitarray.

I. INTRODUCTION

Large aperture antennas are attractive to space applications such as satellite communications, radar systems, and radio astronomy. The most requirements of these applications are the compact structure, high-gain, low production cost and low loss. High gain can be obtained using different antennas, like parabolic reflector, phased array, reflectarray, and transmitarray [1-4]. The disadvantages of the parabolic reflectors are generally being bulky in size, heavy, and large supporting structures. Phased array suffers from network feeding losses and complexity. Reflectarray and transmitarray are easy to fabricate, low profile and have no insertion loss. Reflectarray antenna combines the features of the parabolic reflector and the phased array. It is a planer surface with discrete elements which transform the spherical wave to the plane wave by adding a compensation phase shift. Although the reflectarray has light weight and it is simple to fabricate, it still requires an offset feed to avoid blockage losses. The offset geometry destroys the symmetry of an antenna aperture and increases the angle of incident wave, thus reducing the reflector's gain, decreasing efficiency and complicating the design. In the transmitarray, there is no need for offset feed design. The transmitarray combines the features of lens and phased array antenna. Transmitarray has the same structure of the reflectarray but with opposite beam direction. Transmitarray overcomes the blockage losses in the reflectarray. In open literature, the transmission coefficient magnitude extended from 0 to -4 dB and phase variation of 300 degrees are enough to design the transmitarray [5,6]. Folded transmitarray antennas are compact shape of the transmitarrays. Although transmitarrays employ planar printed structures, they typically require a reasonable depth according to the focal distance of the feed. A reduction of the antenna depth by a factor of about two is achieved using a folded reflectarray as demonstrated in [7-10].

Near-field (NF) focused antennas have been studied over a long time [11-12]. The general purpose of using focused antennas is to concentrate the electromagnetic power in a certain relatively small region of space usually is called the focus (spot). NF-focused antennas have different applications such as microwave remote sensing, local hyperthermia, thermography, and imaging [13-14]. NF-focused microstrip arrays have been designed for gate-access control and management [15]. Radio-frequency identification (RFID) has been introduced as a proper application for NF-focused antennas [16-21]. More recently, NF-focused array microstrip planar antenna for medical applications is investigated in [22]. The NF-focused antennas are needed to concentrate power in a desired spot area to heat a certain tissue without heating adjacent tissues [13, 14]. They depend

Submitted On: June 24, 2015
Accepted On: February 20, 2016

on phase control of the radiation sources on the antenna's aperture in such a way that all their contributions sum in phase at a specific focal point, located in the antenna's near field region. NF-focused antennas can be realized by pyramidal or conical horns, by resorting to a lens in front of the antenna aperture. Alternative solutions are based on either reflector antennas or Fresnel-zone antennas [11]. Another method for NF-focused antenna [13-14] is used of the planar microstrip arrays, with a feeding network, which suffers from complicated beam forming networks, complex feeding circuit and relatively high power loss.

In the present paper, a NF-focused folded transmitarray working on 2.45 GHz for medical application is proposed. The antenna consists of a feeding horn antenna embedded centrally in transmitarray structure and a perfect electric conducting (PEC) plate with the same size of the transmitarray as a reflector. The optimization of the plate position relative to the transmitarray aperture has been investigated. In the proposed antenna, the antenna depth is reduced by a factor of two compared to that required for the un-folded transmitarray. The transmitarray is made from one piece of dielectric material sheet, with a perforated dielectric and completely eliminating all the rest of the dielectric materials. The simplicity of the structure makes it practical in terms of cost, space, and ease to fabricate. Finally, the effect of the NF-focused folded transmitarray on the human leg has been investigated. All the radiation characteristics of the transmitarrays has been analyzed using the CST-microwave studio [25].

II. DESIGN OF THE UNIT-CELL

The configuration of the proposed transmitarray unit-cell element is shown in Fig. 1. It consists of a square dielectric box, with arm length L = 60 mm, thickness h = 60 mm, and dielectric constant ε_r = 12. Each unit-cell element has four identical circular holes. Each hole has radius r. The required transmission coefficient phase and magnitude compensations of each unit-cell element are achieved by varying the hole radius using the waveguide simulator. The perfect electric and magnetic wall boundary conditions are applied to the sides of the surrounding waveguide, and result in image planes on all sides of the unit-cell element to represent an infinite array approximation. A normal incident plane wave was used as the excitation of the unit-cell element inside the waveguide simulator. The variations of the transmission coefficient, phase and magnitude, versus hole radius at 2.45 GHz are shown in Fig. 2. The transmission coefficient phase variation is changed from 0 to 320 degrees, while the transmission coefficient magnitude is varied from 0 to –3.2 dB. The hole radius is changed from 5 to 15 mm. The results are calculated using the CST MWS and compared with that calculated using the HFSS software. Good agreement is achieved.

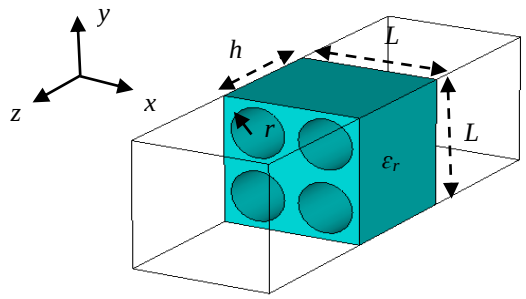

Fig. 1. Transmitarray unit-cell element design at 2.45 GHz.

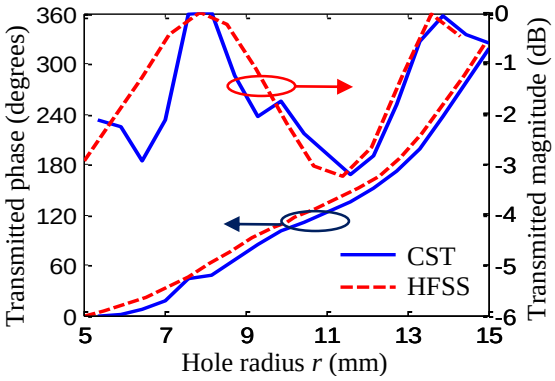

Fig. 2. The variations of the transmission coefficient, phase and magnitude, versus the hole radius at 2.45 GHz.

III. DESIGN OF THE TRANSMITARRAY AND FOLDED TRANSMITARRAY

Figure 3 (a) shows 9 × 9 transmitarray placed in x-y plane with total area of 54 × 54 cm^2. A linearly polarized horn antenna is used to feed transmitarray with dimensions R_i = 10.2 cm, $l_i \times w_i$ = 4.65 × 9.3 cm^2 and thickness t = 0.5 cm. Horn antenna is located at a distance F normal to the transmitarray aperture. The required phase compensation φ_{ij} at each unit-cell element in the transmitarray to collimate a beam in the $(\theta_o, \emptyset_o)$ direction is obtained by:

$$\varphi_{ij}(x_{ij}, y_{ij}) = k_o\left[d_{ij} - x_{ij}\, sin(\theta_o)\, cos(\emptyset_o) - y_{ij}\, sin(\theta_o)\, sin(\emptyset_o)\right], \quad (1)$$

$$where\ \ d_{ij} = \sqrt{(x_{ij} - x_f)^2 + (y_{ij} - y_f)^2 + z_f{}^2}, \quad (2)$$

k_o is the propagation constant, d_{ij} is the distance from the feed point (x_f, y_f, z_f) to the ij^{th} element in the array located at (x_{ij}, y_{ij}). Table 1 lists the required compensation phases and the corresponding holes radii for the transmitarray. A compact folded transmitarray antenna is shown in Fig. 3 (b). It consists of a feeding horn antenna embedded centrally in the transmitarray structure and a PEC plate with the same size of the transmitarray acts as a reflector located at a distance $F/2$ normal to the transmitarray aperture. The radiation from the feeding horn is reflected back by the PEC plate toward the transmitarray. The E-plane and H-plane radiation patterns for unfolded

transmitarray, folded transmitarray and horn antenna at frequency 2.45 GHz are shown in Fig. 4. The unfolded transmitarray introduces maximum gain of 21.4 dBi with first side lobe level (SLL) of -16.4 dB / -17.9 dB in the E-plane /H-plane. The folded transmitarray introduces maximum gain of 21.4 dBi with SLL of -11.6 dB / -12.3 dB in the E-plane/H-plane. The variations of the gain versus frequency are shown in Fig. 5. The same maximum gain of the unfolded transmitarray and folded transmitarray at 2.45 GHz is achieved. The 1-dB gain bandwidth for the unfolded transmitarray is 1.7 GHz compared to 200 MHz for folded transmitarray. The NF-focusing of the transmitarray is achieved by appending an extra phase shift to the elements of the transmitarray to collimate the beam at a focal point R_o as shown in Fig. 6. The extra phase shift of the ijth element can be calculated from [23]:

$$\emptyset_{ijNF} = \frac{2\pi}{\lambda}\left(\sqrt{x_{ij}^2 + y_{ij}^2 + R_o^2} - R_o\right). \quad (3)$$

The total phase for NF-focused folded transmitarray is obtained by adding the phase in Eq. (1) with the corresponding extra phase in Eq. (3). The focal plane is very close to the near edge of the Fresnel region, so it causes that the ratio of active power density to the reactive power density is very large. Table 2 lists the compensation phases and the corresponding holes radii for the first quadrant of the NF-focused transmitarray.

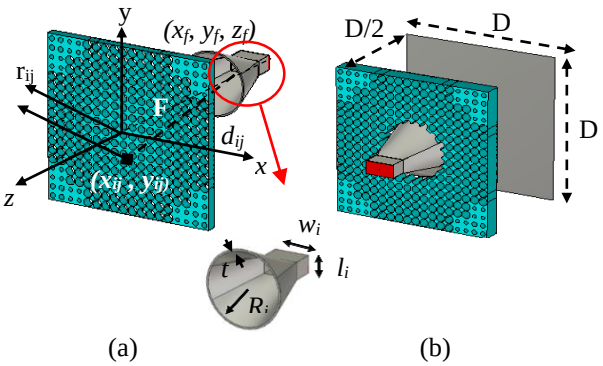

Fig. 3. (a) The 3-D detailed construction of 9 × 9 unfolded transmitarray, and (b) the 3-D detailed construction of 9 × 9 folded transmitarray.

Table 1: The compensation phases and the corresponding holes radii for the first quadrant of the transmitarray

147.6º 12 mm	157.36º 12.33 mm	186.32º 13.05 mm	233.47º 13.81 mm	297.33º 14.7 mm
157.36º 12.33 mm	167.08º 12.62 mm	195.86º 13.22 mm	242.74º 13.94 mm	306.27º 14.8 mm
186.32º 13.05 mm	195.86º 13.22 mm	224.15º 13.68 mm	270.26º 14.32 mm	332.79º 15 mm
233.47º 13.81 mm	242.74º 13.94 mm	270.26º 14.32 mm	315.15º 14.96 mm	16.14º 7 mm
297.33º 14.7 mm	306.27º 14.83 mm	332.79º 15 mm	16.14º 7 mm	75.15º 9 mm

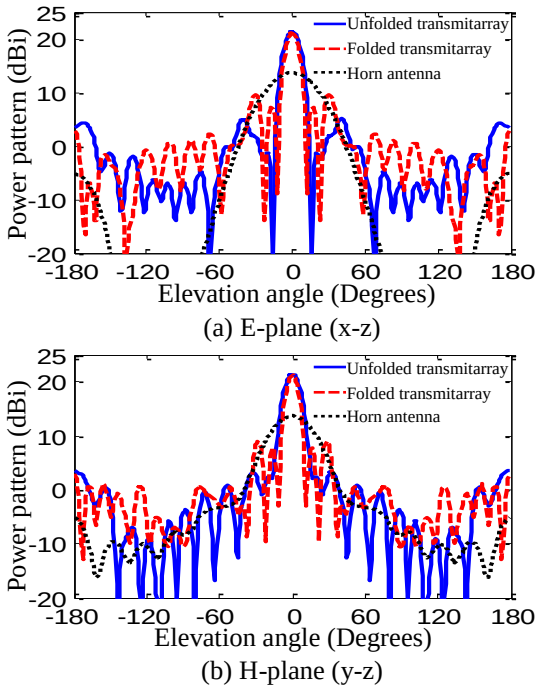

Fig. 4. The E-plane and H-plane radiation patterns variations versus the elevation angle for configuration 9 × 9 unfolded transmitarray, folded transmitarray and the horn antenna for F/D = 1, and f = 2.45 GHz.

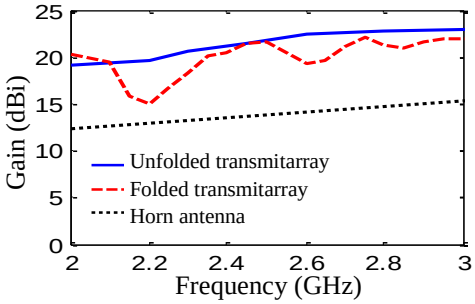

Fig. 5. The variations of the gain versus frequency for 9 × 9 unfolded transmitarray, folded transmitarray and the horn antenna for F/D = 1, and f = 2.45 GHz.

Table 2: The compensation phases and the corresponding holes radii for the first quadrant of the NF-focused transmitarray

147.6º 12 mm	157.36º 12.54 mm	186.32º 13.55 mm	233.47º 14.71 mm	297.33º 8.29 mm
157.36º 12.54 mm	167.08º 12.95 mm	195.86º 13.7 mm	242.74º 14.96 mm	306.27º 8.75 mm
186.32º 13.55 mm	195.86º 13.79 mm	224.15º 14.49 mm	270.25º 6.12 mm	332.79º 10.62 mm
233.47º 14.71 mm	242.74º 14.96 mm	270.26º 6.12 mm	315.18º 9.26 mm	16.14º 13.16 mm
297.33º 8.29 mm	306.27º 8.75 mm	332.79º 10.62 mm	16.14º 13.16 mm	75.15º 14.71 mm

The 3-dB beamwidth in the focal plane is defined as folded transmitarray spot area. The spot area radius W of the near field focused folded transmitarray is given by [24]:

$$W = 0.8868\, R_o.\frac{\lambda_o}{D}, \quad (4)$$

where D is the total transmitarray length. Contour plot of the normalized power density for the non-focused unfolded transmitarray, non-focused folded transmitarray, and NF-focused folded transmitarray on the array aperture in x-y plane at R_o = 72 cm (focal plane) are shown in Fig. 6. The contour lines are closer to each other for the NF-focused folded transmitarray compared to the other two cases. The radius of the 3-dB spot area for the NF-focused folded transmitarray is W = 7.5 cm at the focal plane while it is 12.3 cm for the non-focused unfolded transmitarray and 8 cm for non-focused folded transmiarray. Figure 7 shows the power density in dB versus the axial distance from the antenna aperture. The maximum occurs at a distance about 40 cm from the aperture of the transmitarray.

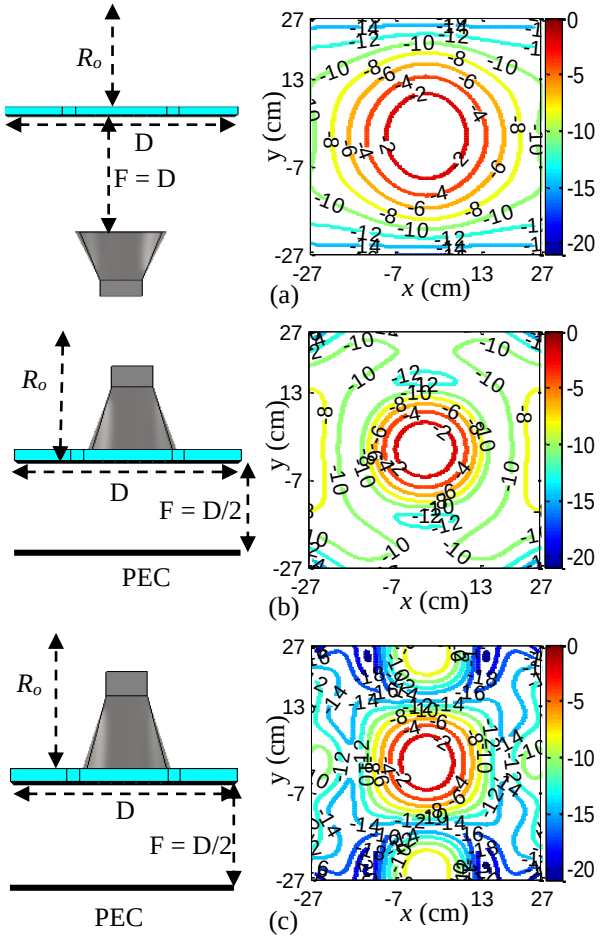

Fig. 6. A contour plot of the normalized power density at distance R_o = 72 cm (focal plane) for: (a) non-focused unfolded transmitarray, (b) non-focused folded transmitarray, and (c) near-field focused folded transmitarray.

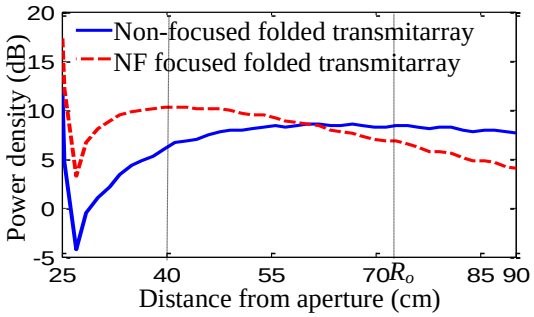

Fig. 7. The power density versus axial distance of the antenna.

IV. APPLICATION

Many people suffer from arthritis, that causes inflammation of the joints and affect anyone from young children to senior. It is typically characterized by joint pain and stiffness that make movement painful and difficult. In addition, arthritis inflammation can result from a variety of conditions and diseases, like gout, lupus and fibromyalgia. There are different arthritis heat treatment as heating pads, paraffin baths, and hot water bottles… etc. Recently, electromagnetic waves are used to treat the arthritis in an easy way. The waves are focused towards the knee to generate a localized heat. Figure 8 shows the anatomy of the part of the leg containing the knee. The electromagnetic properties of the human body at frequency 2.45 GHz are listed in Table 3 [25]. The simulation model is analyzed using the CST microwave studio with resolution 3.6 × 3.6 × 3.6 mm^3, to calculate its electromagnetics properties. The model with dimensions l_w = 52 cm and L_h = 10 cm containing the knee is placed at a distance R_o = 72 cm from the aperture of the antenna as shown in Fig. 9 (a). The contour plots of the normalized power density around the knee model in front of the transmitarray and NF-focused folded transmitarray are shown in Fig. 9 (b). The spot area is very clear in the middle of the model. The body tissues is disturbing the contour plot. The same pervious model is located at distance R_o = 40 cm. The contour plots at a distance of 40 cm show a more focus spot area compared with the previous state as shown in Fig. 10.

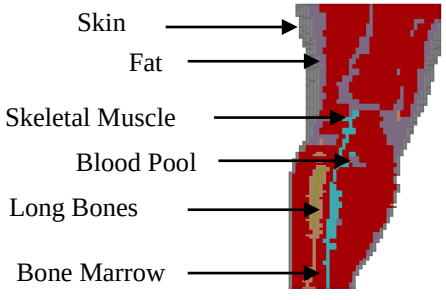

Fig. 8. The anatomy model of the part of the leg tissues [25].

Table 3: Electromagnetic properties of the human body at frequency 2.45 GHz [25]

Tissues	ε_r	σ (S/m)	ρ (Kg/m^3)	σ th (W/K/m)
Skin	40.93	0.89	1100	0.293
Fat	5.34	0.08	1100	0.201
Skeletal muscle	55.19	1.49	1040	0.46
Long bones	12.36	0.15	1850	0.41
Bone marrow	11.19	0.23	1020	0.624
Blood pool	59.19	2.11	1000	0.505

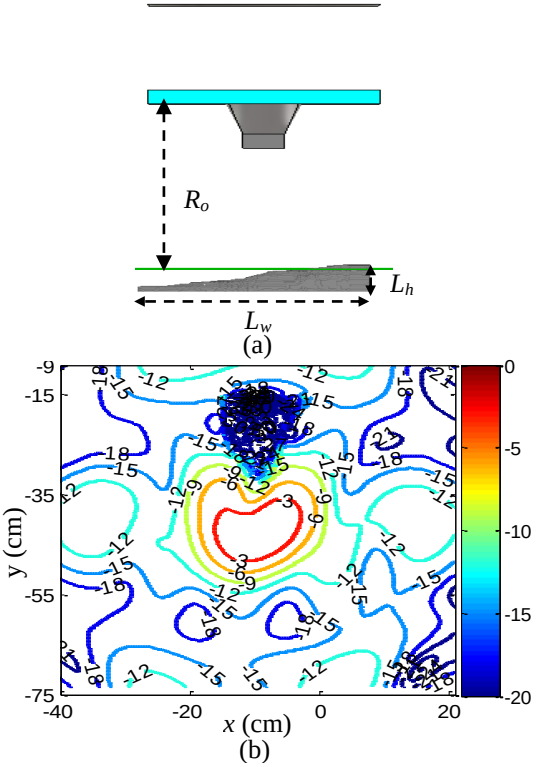

Fig. 9. (a) The construction of the antenna with the anatomy model at R_o = 72 cm, and (b) the contour plot of the normalized power density.

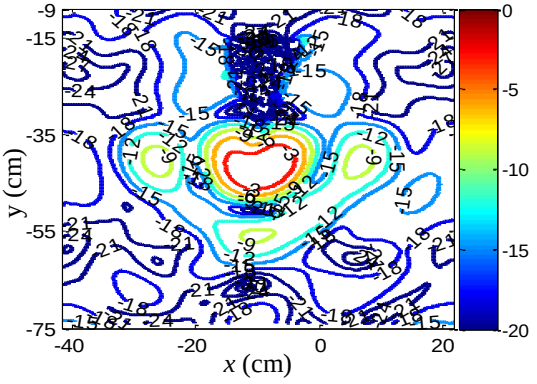

Fig. 10. The contour plot of the normalized power density at R_o = 40 cm.

V. CONCLUSION

A NF-focused folded transmitarray to operate at 2.45 GHz for medical applications has been investigated. The proposed antenna has a compact structure and low profile. The approach depends on focusing the radiated waves in small spot area in the near field region. The unit-cell element of the array consists of a square dielectric box with four identical circular holes. The transmission coefficient phase variation is achieved from 0 to 320 degrees while the transmission coefficient magnitude variation from 0 to –3.2 dB. The radiation characteristics of a 9×9 unfolded, folded, and NF-focused folded transmitarray are investigated. The peak gain is 21.4 dB with 1-dB bandwidth is 200 MHz for folded transmitarray. A model for the part of the human leg is used in front of the transmitarray to show the normalized power density in the near field region around it. The spot area is very clear in the middle of the model. The folded transmitarray size used in this application is 54 × 54 cm^2. Focused spot area is around 7.5 × 7.5 cm^2.

REFERENCES

[1] O. Yurduseven and O. Yurduseven, "Compact parabolic reflector antenna design with cosecant-squared radiation pattern," *Microwaves, Radar and Remote Sensing Symposium*, Kiev, Ukraine, pp. 382-385, 2011.

[2] G. M. Rebeiz, K. J. Koh, T. Yu, D. Kang, C. Y. Kim, Y. Atesal, B. Cetinoneri, S. Y. Kim, and D. Shin, "Highly dense microwave and millimeterwave phased array T/R modules and butler matrices using CMOS and SiGe RFICs," *IEEE International Symposium on, Phased Array Systems and Technology (ARRAY)*, Boston, Massachusetts, USA, pp. 245-249, Oct. 2010.

[3] S. M. Gaber, *Analysis and Design of Reflectarrays/ Transmitarrays Antennas*, Ph.D. Thesis, Faculty of Electronic Engineering, Menoufiya University, Menouf, Egypt, 2013.

[4] S. H. Zainud-Deen, W. M. Hassen, H. A. Malhat, and K. H. Awadalla, "Radiation characteristics enhancement of dielectric resonator antenna using solid/discrete dielectric lens," *Advanced Electromagnetics*, vol. 4, no. 1, pp. 1-8, Feb. 2015.

[5] J. Y. Lau, *Reconfigurable Transmitarray Antennas*, Ph.D. Thesis, University of Toronto, Canada, 2012.

[6] J. Reis, Z. Al-Daher, N. Copner, R. Caldeirinha, and T. Fernandes, "Two-dimensional antenna beam steering using metamaterial transmitarray," *9th European Conference on Antenna and Propagation (EUCAP)*, Lisbon, Portugal, pp. 1-5, Apr. 2015.

[7] D. Pilz and W. Menzel, "Folded reflectarray antenna," *Electron. Lett.*, pp. 832-833, Apr. 1998.

[8] W. Menzel and D. Kessler, "A folded reflectarray antenna for 2D scanning," *IEEE German Microwave*

Conference, Munich, Germany, pp. 1-4, Mar. 2009.

[9] J. A. Zornoza, R. Leberer, J. A. Encinar, and W. Menzel, "Folded multilayer microstrip reflectarray with shaped pattern," *IEEE Trans. Antennas Propag.*, vol. 54, no. 2, pp. 501-518, Feb. 2006.

[10] W. Menzel, D. Pilz, and M. Al-Tikriti, "Millimeter-wave folded reflector antenna with high gain, low loss, and low profile," *IEEE Antennas and Propag. Mag.*, pp. 24-29, June 2002.

[11] S. Karimkashi and A. A. Kishk, "A new Fresnel zone antenna with beam focused in the Fresnel region," *Proceedings of XXIXth General Assembly of the International Union of Radio Science*, Chicago, IL, USA, pp. 7-16, Aug. 2008.

[12] A. Buffi, P. Nepa, and G. Manara, "Design criteria for near-field-focused planar arrays," *IEEE Antennas and Propag. Mag.*, vol. 54, no. 1, pp. 40-50, Feb. 2012.

[13] M. Bogosanovic and A. G. Williamson, "Microstrip antenna array with a beam focused in the near-field zone for application in noncontact microwave industrial inspection," *IEEE Trans. Instrum. Meas.*, vol. 56, no. 6, pp. 2186-2195, Dec. 2007.

[14] K. D. Stephan, J. B. Mead, D. M. Pozar, L. Wang, and J. A. Pearce, "A near field focused microstrip array for a radiometric temperature sensor," *IEEE Trans. Antennas Propag.*, vol. 55, no. 4, pp. 1199-1203, Apr. 2007.

[15] A. Buffi, A. Serra, P. Nepa, G. Manara, and M. Luise, "Near field focused microstrip arrays for gate access control systems," *IEEE Antennas and Propag. Society International Symp., APSURSI'*09, Charleston, SC, USA, pp. 1-4, June 2009.

[16] R. Siragusa, P. Lemaitre-Auger, and S. Tedjini, "Near field focusing circular microstrip antenna array for RFID applications," *IEEE Antennas and Propag. Society International Symp., APSURSI'09*, Charleston, SC, USA, pp. 1-4, June 2009.

[17] R. Siragusa, P. Lemaître-Auger, and S. Tedjini, "Tunable near-field focused circular phase-array antenna for 5.8 GHz RFID applications," *IEEE Antennas and Wireless Propag. Letters*, vol. 10, pp. 33-36, 2011.

[18] B. Shrestha, A. Elsherbeni, and L. Ukkonen, "UHF RFID reader antenna for near-field and far-field operations," *IEEE Antenna and Wireless Propag.*, vol. 10, pp. 1274-1277, 2011.

[19] S. H. Zainud-Deen, H. A. Malhat, and K. H. Awadalla, "8×8 near-field focused circularly polarized cylindrical DRA array for RFID applications," *The Applied Computational Electromagnetics Society ACES*, vol. 27, no. 1, pp. 42-48, 2012.

[20] S. H. Zainud-Deen, S. M. Gaber, H. A. Malhat, and K. H. Awadalla, "Multilayer dielectric resonator antenna transmitarray for near-field and far-field fixed RFID reader," *Progress in Electromagnetics Research C, PIER C*, vol. 27, pp. 129-142, 2012.

[21] A. Buffi, A. A. Serra, P. Nepa, H.-T. Chou, and G. Manara, "A focused planar microstrip array for 2.4 GHz RFID readers," *IEEE Trans. Antennas Propag.*, vol. 58, no. 5, pp. 1536-1544, May 2010.

[22] F. Tofigh, J. Nourinia, M. N. Azarmanesh, and K. M. Khazaei, "Near-field focused array microstrip planar antenna for medical applications," *IEEE Antennas and Wireless Propag. Letters*, vol. 13, pp. 951-954, 2014.

[23] Y. Adanel, M. Wongl, C. Dale', and J. Wiartl, "Near field power density characterization of radio base station antennas using spherical harmonics optimization techniques," *European Conference on Wireless Technology*, Amsterdam, Netherlands, pp. 121-124, Oct. 2004.

[24] R. C. Hansen, "Focal region characteristics of focused array antennas," *IEEE Trans. Antennas Propag.*, vol. 33, no. 12, pp. 1328-1337, Dec. 1985.

[25] User's manual of CST Microwave Studio Suite 2012.

A Compact Dual-Band Patch Antenna Design Based on Single-Ring Split Ring Resonator

Ming-Chun Tang [1,2], Hao Wang [1], Li Guo [1], Xiaoping Zeng [1], Hong Liu [2], and Youbing Pang [2]

[1] College of Communication Engineering
Chongqing University, Chongqing 400044, China
tangmingchun@cqu.edu.cn, wangh_2014@126.com, guoli_31@163.com, zxp@cqu.edu.cn

[2] No. 24 Research Institute
China Electronics Technology Group Corporation, Chongqing 400060, China
liuh1981@126.com, pangyb555@163.com

Abstract **–** A compact dual-band patch antenna based on split ring resonator (SRR) element is demonstrated in this paper. In the design, a single-ring SRR, acting as a near-field resonant parasitic (NFRP) element, is integrated in the same plane of radiating patch. The addition of SRR could create a new operational frequency band much lower than the patch fundamental mode, lower the patch resonance frequency, and improve the patch impedance bandwidth significantly, while maintaining the antenna simplicity and compactness. The experimental results are in agreement with the simulation values, demonstrating that our proposed antenna possesses an excellent dual-band radiation performance characteristic, which includes relatively high radiation efficiencies, low cross-polarization levels, and stable broadside radiation performances.

Index Terms **–** Bandwidth improvement, compact patch antenna, dual-band, near-field resonant parasitic element, split ring resonator.

I. INTRODUCTION

Over the past decades, as the common unit cells in metamaterial designs, the split ring resonators (SRRs) and complementary split ring resonators (CSRRs) have attracted much attention because of their interesting resonance response performance characteristics [1-5]. Integration of SRRs and CSRRs in patch antenna design is one of the popular applications in microwave devices, which are comprehensively under investigation in recent years [6-11]. Up to now, there are many successful attempts reported. For example, the stacked SRRs has been utilized to realize the artificial magnetic substrate of patch antenna, which could improve the impedance bandwidth, as well as maintain high radiation efficiency [6]; a double-SRR element was utilized to place at the upper layer of a traditional patch antenna to explore a new and lower resonance frequency [7]; one or two CSRR units were embedded within the radiation patch to achieve dual-band or circularly polarized (CP) operations [8, 9]; and different kinds of CSRRs were placed horizontally between the radiating patch and the ground plane to achieve antenna miniaturization [10]. We also have considered etching CSRRs on the ground around the patch antenna to lower its operational frequency [11].

While effective, above technologies witnessed a certain drawback, which limited their widespread engineering application, arranging SRR above the radiating patch, periodical SRRs within the substrate, or CSRR below the radiating patch may make the design and fabrication quite complicated [6, 7, 10]; etching CSRR slot in the radiating patch may lead to low overall efficiency [8, 9]; and integrating CSRR on the antenna ground may increase the feedline structure impact on radiation patterns [11].

In this paper, a compact dual-band patch antenna based on SRR element is introduced. In the design, a single-ring SRR is loaded in the near field of radiating patch at the same plane to obtain a new and much lower resonance mode, without degradation of the antenna simplicity and compactness. Moreover, the 3rd resonant mode of SRR is located in the vicinity of the patch fundamental mode, which makes the operational bandwidth from the radiation patch witness 18.7% improvement. The prototype of antenna was fabricated and tested. The experimental results, in good agreement with the simulation ones, demonstrate that it exhibits excellent dual-band radiation performances, which include relatively high radiation efficiencies and stable broadside radiation performance within the dual operational bands.

II. ANTENNA DESIGN

Figure 1 gives the geometrical layout of the proposed antenna. As illustrated, a circular radiating patch with the radius R is etched on the top side of a 0.127 mm-thick

Submitted On: June 29, 2015
Accepted On: February 26, 2016

Rogers Duroid 5880 substrate. The value of patch radius (R) is determined by the patch antenna fundamental resonance frequency center, since it is actually a half-wavelength resonator [12]. In details, the thickness of copper film is 0.017 mm and the substrate has the relative permittivity ε_r = 2.2 and loss tangent tan σ = 0.0009. A single-ring SRR, acting as a near-field resonance parasitic (NFRP) element [13, 14], is constructed to surround the patch in the same plane. The center of the SRR is offset away from the patch (L1) to optimize the capacitive coupling between them. The methodology to determine the SRR size will be illustrated in Section IV in details. And a copper ground with the thickness 0.5 mm is placed right under the substrate. The antenna is fed by a coaxial cable with characteristic impedance 50 Ω. The inner probe and outer metallic part of the coax feedline are, respectively, connected with the patch (via the substrate) and the ground. As is shown in Fig. 1 (b), the gap center of SRR, the feeding point, and the centers of patch and SRR are offset with each other but all along with the *x*-axis.

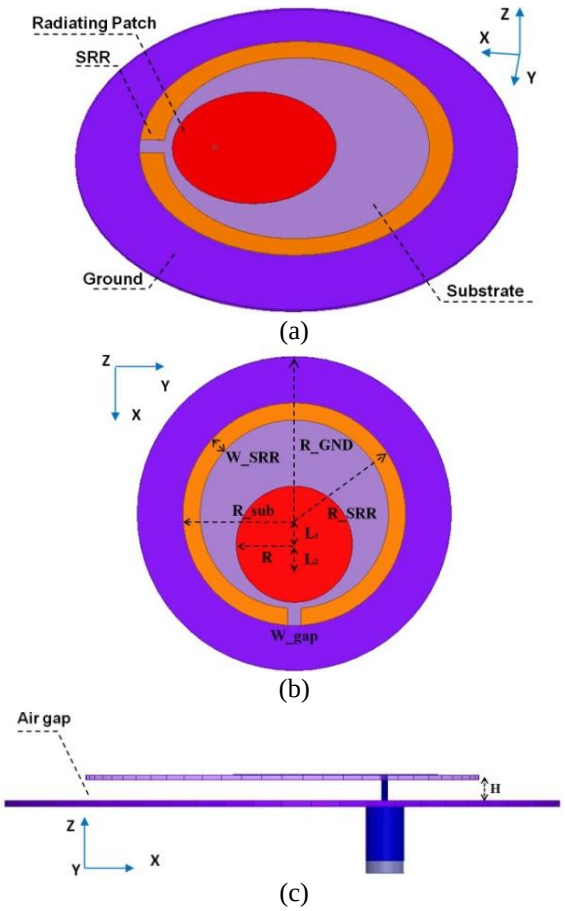

Fig. 1. The configuration of the proposed antenna: (a) 3D view, (b) top view, and (c) side view. Its design parameters are as follows (in millimetre): R_sub = 32.62, R_GND = 46, R_SRR = 32.62, W_gap = 4, W_SRR = 5, R = 16.8, L1 = 8.8, L2 = 7.87, H = 3, and L = 40.

III. ANTENNA PERFORMANCE

The proposed antenna was first simulated with the ANSYS/ANSOFT high frequency structure simulator, HFSS, and then fabricated and tested [15]. The fabricated prototype is shown in Fig. 2. It is noted that, since the substrate is thin and suspended above the ground in the fabricated antenna, several cylindrical rigid foam pillars are placed under the substrate for mechanic supporting in the experimental process.

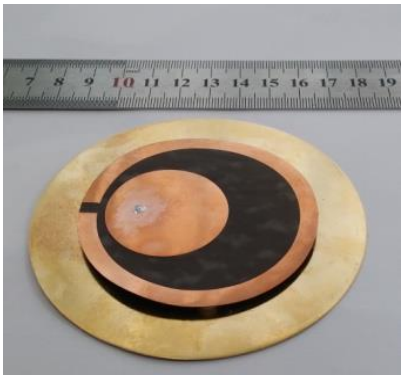

Fig. 2. The fabricated prototype of the proposed antenna.

On one hand, the reflection coefficient of the antenna was measured using Agilent E8361A PNA Vector Network Analyzer (VNA). The measured results together with the corresponding simulation values are plotted in Fig. 3. The experimental (simulation) results indicate that the antenna could provide dual-frequency impedance matching bandwidths with $|S_{11}| < -10$ dB. At lower frequency point 1.602 GHz (1.576 GHz), it has a high impedance matching level with $|S_{11}|_{min}$ = -16.81 dB (-24.16 dB) and a bandwidth 25 MHz (40 MHz), i.e., 1.6% (2.5%) fractional bandwidth. Obviously, the experimental operational frequency center demonstrated 26 MHz blue shift from the simulated one. This acceptable difference (only 1.65%) is quite reasonable, and could be alleviated, if desired, with a careful retuning of the design parameters in Fig. 1. The similar phenomenon was reported in our previous electrically small antenna experimental study [11]. In the higher frequency range, there are two $|S_{11}|$ dips, which are located at 4.5375 GHz (4.550 GHz) and 4.7125 GHz (4.730 GHz), to combine a wide bandwidth 365 MHz (410 MHz), i.e., 8.0% (8.9%) fractional bandwidth. These differences due to the unavoidable errors in the fabrication, installation and measurement process, are deemed to be acceptable. Moreover, in order to emphasize the SRR contributions, the antenna without SRR was simulated as a reference. The simulation results are also shown in Fig. 3 for easy comparison. Note that, all of its constructive parameters are the same as that in Fig. 1. It is observed that, the antenna is also impedance matched to 50 Ω source in the center of 4.600 GHz, with

$|S_{11}|_{min}$ = -21.47 dB. Its -10 dB impedance bandwidth is 347.5 MHz (7.5% fractional bandwidth). By comparison between the simulation results in Fig. 3, it could be easily concluded that, the addition of SRR could create a new much lower operational band, lower the patch resonance frequency center a little, and expand the bandwidth from the patch as high as 18.7% by means of the 3rd resonance mode of SRR, without significant influence on its original impedance match level of the fundamental mode from the patch.

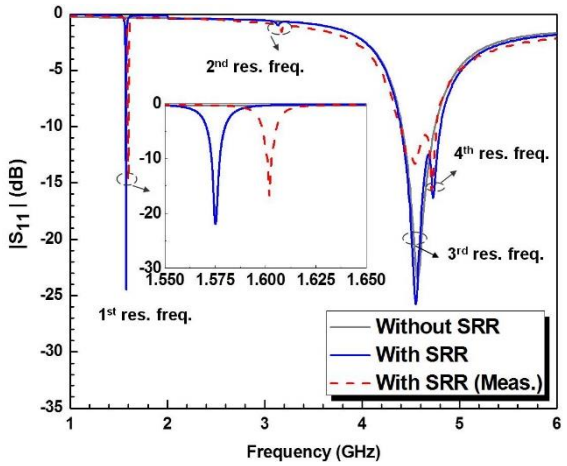

Fig. 3. The simulated and measured reflection coefficients (i.e., $|S_{11}|$ values in dB) for the antennas with and without SRR element.

On the other hand, the far-field radiation patterns of the proposed antenna were measured in an anechoic chamber, which is mainly based on the Agilent EB362C PNA VNA and SATIMO passive measurement system. The measured results together with the corresponding simulation values are shown in Fig. 4. As is shown in Fig. 4 (a), the broadside realized gain is 5.35 dBi in the simulation and 4.59 dBi in the experiment at lower resonance frequency center. And its simulated radiation efficiency is 77.61%. Figures 4 (b) and 4 (c) give the normalized radiation patterns in the upper frequency band. At the two resonance dips of the upper band, the broadside realized gains are 9.91 dBi and 8.58 dBi in the simulation, and 9.48 dBi and 8.17 dBi in the experiment, respectively. Similar to the reported results in Fig. 3, the observed differences between the simulation and experimental results in Fig. 4, while small, arise mainly from the unavoidable errors in the fabrication and measurement process. And its simulated radiation efficiency is higher than 95% over the entire upper band. Moreover, it is easily observed in both simulation and experimental results of Fig. 4, the cross-polarization values in broadside direction are more than 20 dB lower than the co-polarization ones at the three resonance frequency centers, indicating very high linear polarization purity of our proposed antenna. Generally, the broadside radiation performance of antenna is stable.

It should be noted that, lower than -15 dB cross-polarization levels were simultaneously observed in both operational frequency ranges, because of the antenna symmetrical configuration (e.g., ground, patch, and SRR element) along the *x*-axis, resulting in symmetrical current distributions, which will be explained in details in next the section. In addition, because the simulation cross-polarization in the E-plane is lower than −50 dB at each of these frequency points, it was not plotted. In addition, in order to emphasize the design advantages of our proposed antenna clearly, Table 1 is presented for easy comparison between traditional patch antenna and our proposed antenna.

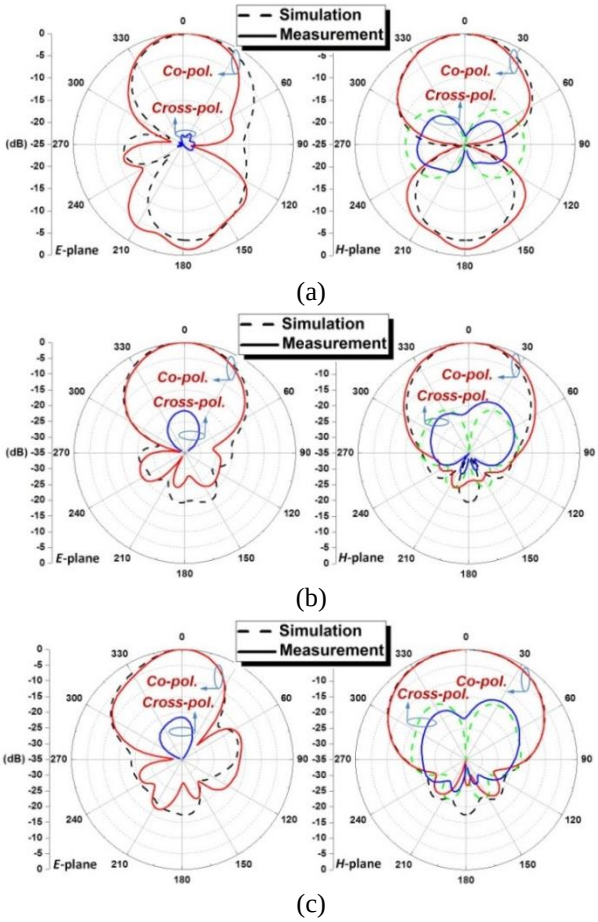

Fig. 4. The simulated and measured normalized radiation patterns at different frequencies in the ZOX plane (*E*-plane) and ZOY plane (*H*-plane): (a) at resonance frequency center of the lower band (1.576 GHz in the simulation and 1.602 GHz in the experiment), (b) at the lower resonance dip of the upper band (4.550 GHz in the simulation and 4.5375 GHz in the experiment), and (c) at the upper resonance dip of the upper band (4.730 GHz in the simulation and 4.7125 GHz in the experiment).

Table 1: Comparisons between traditional patch antenna and our proposed antenna

Category	Traditional Antenna	Proposed Antenna (Sim.)	Proposed Antenna (Exp.)
Lower freq. cent. (GHz)		1.576	1.602
BW in lower freq. range (MHz)		40	25
Gain at lower freq. cent. (dBi)		5.35	4.59
Higher freq. cent. (GHz)	4.600	4.550 & 4.730	4.5375 & 4.7125
BW in higher freq. range (MHz)	347.5	410	365
Gain at higher freq. cent. (dBi)	10.01	9.91 & 8.58	9.48 & 8.17

IV. DISCUSSION

The simulated current distributions on the SRR element and radiating patch at different resonance frequencies are shown in Fig. 5. At the resonance frequency center 1.576 GHz of the lower band, it is observed in Fig. 5 (a) that the majority current is symmetrically concentrated along the SRR surface, which demonstrates that this frequency band is created by SRR electrical resonance [16]. From our calculation, the average electrical length of the current pathway corresponding to 1.576 GHz is l = 92.625 mm = 0.49 λ_{res}, which is very close to half wavelength [16], where,

$$l=(\text{R\_SRR-W\_SRR/2})\times\pi-\text{W\_gap/2}. \quad (1)$$

And then, in Fig. 5 (b), at the 2nd resonance frequency point, i.e., a weak resonance dip around 3.14 GHz in Fig. 3, it is clear that there are two symmetrical anti-phase current pathways along the SRR surface. As is well known, the anti-phase current distribution would lead to a deep null appearance in the radiation pattern in the broadside, which would accordingly degrade the uniformity of the radiation patterns [17]. Thus, the impedance was not optimized to accommodate to 50 Ω source here ($|S_{11}|_{min}$ ~ -1.01 dB). It was worth mentioning that, since its electrical length is twice than the fundamental mode, it could be easily concluded that the SRR resonates in the 2nd harmonic mode at this frequency.

Thirdly, as is shown in Fig. 5 (c), most of the current is polarized on the surface of the radiating patch. Actually, at this frequency point the antenna is operating in TM10 mode. Since a small portion of current is distributed on the SRR, which indicates the SRR has a certain capacitive coupling effect on the patch. Therefore, this resonance frequency center (4.550 GHz) is a little lower than that without SRR (4.600 GHz).

Finally, since the current pathway is three times than that of SRR fundamental mode, it is in theory that the SRR resonates in 3rd harmonic mode, and this phenomenon is confirmed by the current distribution in Fig. 5 (d). Although the antenna at this frequency could exhibit comparable radiation efficiency values to that from the patch resonance in Fig. 5 (c), it is seen that it has a wider beamwidth in H-plane and a little lower broadside realized gain value shown in Fig. 4. The reason is that, at above two different frequency points the antenna operation mechanisms are quite different.

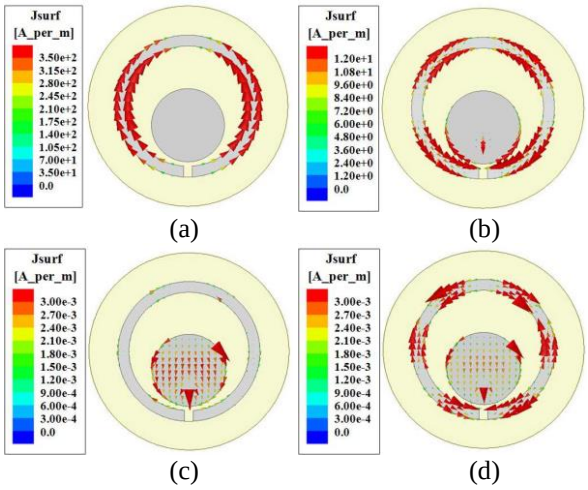

Fig. 5. Simulated current distributions on the radiating patch and SRR element at different resonance frequencies: (a) at resonance frequency center of the lower band (1.576 GHz), (b) at the resonance frequency of 3.14 GHz, (c) at the lower resonance dip of the upper band (4.550 GHz), and (d) at the upper resonance dip of the upper band (4.730 GHz).

In order to comprehensively study our proposed antenna design, two important constructive parameters impact on the antenna impedance performance characteristics is parametrically investigated. Note that, only one parameter is changed and the others remain the same. First, by increasing the SRR gap size (W_gap), it is seen that the first and third modes of SRR shift higher by steps while the fundamental mode of radiating patch almost remains unchanged on the whole, as is shown in Fig. 6 (a). We noted that the resonance frequency of SRR is determined by the formula $f = c/[2l\times(\varepsilon_{eff})^{1/2}]$, where l is average electrical length of the current pathway and is determined by the Equation (1), and $\varepsilon_{eff} \sim (\varepsilon_r+1)/2$ indicates the equivalent relative permittivity. Therefore, when the gap size (W_gap) increases, the total length l decreases, and f goes higher accordingly. Second, the feedline point position effect on the antenna performance is discussed. By changing the position (L2) the SRR fundamental resonance mode is not impacted on the whole, but the 3rd resonance mode of SRR and fundamental resonance mode of the patch are both

affected significantly. Thus, in our optimization process, the impedance matching and impedance bandwidth in the higher frequency band could be improved by only changing the feed position without influence on its performance characteristics in the lower band.

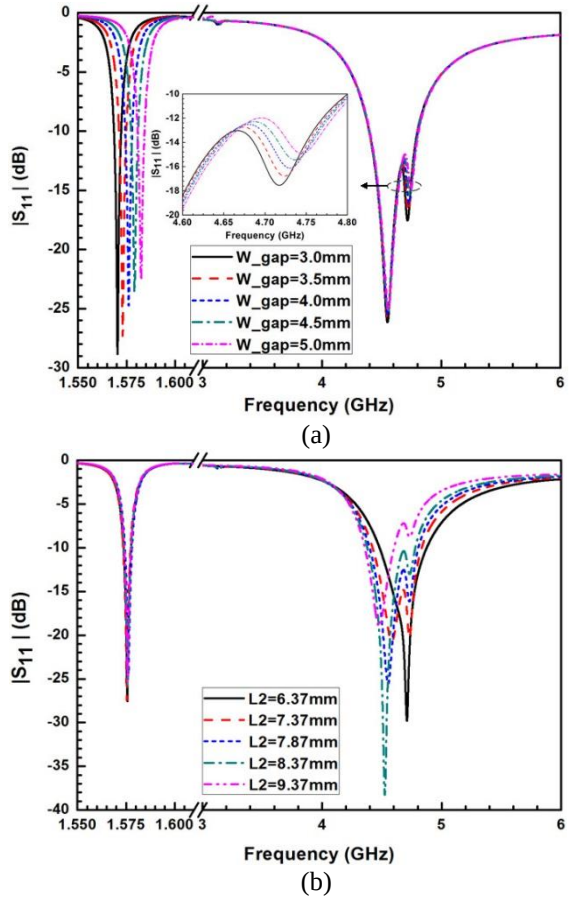

Fig. 6. Impact of two constructive parameters on the antenna impedance matching: (a) the SRR gap size (W_gap), and (b) the feedline point position (L2).

V. CONCLUSION

We proposed a compact, SRR-based, dual-band, NFRP patch antenna. Benefitting from the electrical resonance from SRR element in the near field of radiating patch, a new operational frequency band much lower than the patch fundamental mode is produced, and the fundamental resonance frequency bandwidth of the patch is improved. The addition of SRR has not degraded the antenna simplicity and compactness on the whole. The experimental results, in a good agreement with the simulations, showed that the proposed antenna has high radiation efficiency and stable broadside radiation performances in the two operational bands. Benefiting from its excellent performance characteristic, the proposed compact antenna would be a good candidate in many engineering applications, such as GPS (due to its high polarization purity) [18, 19] and implantable devices (due to its dual-band operation with large dual-frequency interval) [20].

ACKNOWLEDGMENT

This work was supported in part by the National Natural Science Foundation of China contract numbers 61471072 and 91438104, in part by the Focus Project of Chongqing for application and development contract number cstc2013yykfB40009, and in part by the Fundamental Research Funds for the Central Universities contract number 106112015CDJZR165510.

REFERENCES

[1] J. D. Baena, J. Bonache, F. Martin, R. M. Sillero, F. Falcone, T. Lopetegi, M. A. G. Laso, J. Garcia-Garcia, I. Gil, M. F. Portillo, and M. Sorolla, "Equivalent-circuit models for split-ring resonators and complementary split-ring resonators coupled to planar transmission lines," *IEEE Trans. Microw. Theory Tech.*, vol. 53, pp. 1451-1461, 2005.

[2] J. C. Liu, W. Shao, and B. Wang, "A dual-band metamaterial design using double SRR structures," *Appl. Comp. Electro. Society (ACES) Journal*, vol. 26, pp. 459-463, June 2011.

[3] N. Engheta and R. W. Ziolkowski, *Electromagnetic Metamaterials: Physics and Engineering Explorations*, New York, Wiley-IEEE Press, 2006.

[4] D. Jiang, Y. Xu, and R. Xu, "A microstrip printed band-notched UWB antenna using modified CSRR structure," *Appl. Comp. Electro. Society (ACES) Journal*, vol. 28, pp. 521-527, June 2013.

[5] Q. Xiang, Q. Feng, and X. Huang, "Tunable bandstop filter based on split ring resonators loaded Coplanar waveguide," *Appl. Comp. Electro. Society (ACES) Journal*, vol. 28, pp. 591-596, July 2013.

[6] M. Kärkkäinen and P. Ikonen, "Patch antenna with stacked split-ring resonators as an artificial magneto-dielectric substrate," *Microw. Opt. Tech. Lett.*, vol. 46, pp. 554-556, 2005.

[7] O. Quevedo-Teruel, M. N. M. Kehn, and E. Rajo-Iglesias, "Dual-band patch antennas based on short-circuited split ring resonators," *IEEE Trans. Antennas Propag.*, vol. 59, pp. 2758-2765, 2011.

[8] H. Zhang, Y. Q. Li, X. Chen, Y. Q. Fu, and N. C. Yuan, "Design of circular/dual-frequency linear polarization antennas based on the anisotropic complementary split ring resonator," *IEEE Trans. Antennas Propag.*, vol. 57, pp. 3352-3355, 2009.

[9] Y. Dong, H. Toyao, and T. Itoh, "Design and characterization of miniaturized patch antennas loaded with complementary split-ring resonators," *IEEE Trans. Antennas Propag.*, vol. 60, pp. 772-785, 2012.

[10] R. O. Ouedraogo, E. J. Rothwell, A. R. Diaz, K. Fuchi, and A. Temme, "Miniaturization of patch

antennas using a metamaterial-inspired technique," *IEEE Trans. Antennas Propag.*, vol. 60, pp. 2175-2182, 2012.

[11] M.-C. Tang and R. W. Ziolkowski, "A study of low-profile, broadside radiation, efficient, electrically small antennas based on complementary split ring resonators," *IEEE Trans. Antennas Propag.*, vol. 61, pp. 4419-4430, 2013.

[12] I. J. Bhal and P. Bhartia, *Microstrip Antenna*, Dedham, MA: Artech House, 1980.

[13] R. W. Ziolkowski, P. Jin, and C.-C. Lin, "Metamaterial-inspired engineering of antennas," *Proc. IEEE*, vol. 99, pp. 1720-1731, 2011.

[14] M.-C. Tang, R. W. Ziolkowski, S. Xiao, and M. Li, "A high-directivity, wideband, efficient, electrically small antenna system," *IEEE Trans. Antennas Propag.*, vol. 62, pp. 6541-6547, 2014.

[15] ANSYS/ANSOFT High Frequency Structure Simulation (HFSS), ver. 13.0, ANSYS Corp. [Online]. Available at www.ansoft.com.

[16] M.-C. Tang, S. Xiao, D. Wang, J. Xiong, K. Chen, and B. Wang, "Negative index of reflection in planar metamaterial composed of single split-ring resonators," *Appl. Comp. Electro. Society (ACES) Journal*, vol. 26, pp. 250-258, Mar. 2011.

[17] C. A. Balanis, *Antenna Theory: Analysis and Design*, 3rd edition, New York, Wiley Interscience, 2005.

[18] N. Amani and A. Jafargholi, "Internal uniplanar antenna for LTE/WWAN/GPS/GLONASS applications in tablet/laptop computers," *IEEE Antennas Wireless Propag. Lett.*, vol. 14, pp. 1654-1657, 2015.

[19] R. Zhang, H.-H. Kim, and H. Kim, "Triple-band ground radiation antenna for GPS, WiFi 2.4 and 5 GHz band applications," *Electron. Lett.*, vol. 51, no. 25, pp. 2082-2084, Dec. 2015.

[20] C. Liu, Y.-X. Guo, and S. Xiao, "Compact dual-band antenna for implantable devices," *IEEE Antennas Wireless Propag. Lett.*, vol. 11, pp. 1508-1511, 2012.

Microstrip Fed Multiband Hybrid Fractal Antenna for Wireless Applications

Yadwinder Kumar [1] and Surinder Singh [2]

[1] Department of Electronics and Communication Engineering
YCOE (Punjabi University Regional Campus), Talwandi Sabo, Bathinda, Punjab 151302, India
ykece@pbi.ac.in

[2] Department of Electronics and Communication Engineering
SLIET (Deemed University), Longowal, Sangrur, Punjab 148106, India
surinder_singh@rediffmail.com

Abstract ─ A hybrid fractal multiband antenna is designed by integrating Koch curve and meander antenna. Scripting method (*.vbs) is adopted to obtain the hybrid fractal structure using IFS and MATLAB. Final structure is obtained by perturbing the reference fractal shape. Proposed antenna exhibits multiband characteristics capable of operating in four different wireless frequency bands including very popular Bluetooth (2.4 GHz), WiMAX (3.4-3.7 GHz), WLAN 802.11 a/b/g (5.3-6.1 GHz) and Aeronautical radionavigation (8.68-9.05GHz). The antenna has a planar structure, compact size of 39 mm × 32 mm × 1.58 mm and is suitable for wireless applications. Prototype of the proposed structure is developed on easily available and low cost FR4 substrate. The antenna has acceptable values of return loss, VSWR and gain. Measured characteristics are in good agreement with the simulated one.

Index Terms ─ FR4, hybrid fractal, IFS multiband.

I. INTRODUCTION

Progress in the modern wireless communications systems has generated the demand for compact, multiband, wideband and cost effective antennas. Fractal antennas have the capability to fulfill these requirements due to their self-similarity, space filling properties and ability of miniaturization [1]. Fractal geometries were 1st proposed by Mandelbrot in 1953 [2] which were later widely adopted in various engineering fields. Due to self-similarity, fractal structures are generated by repeated recursive process which further increases the effective electrical path length and generates a wide surface area in a limited space. This helps in achieving multiband behavior and also reduction in size and volume [3]. Even in USB (Universal Serial Bus) applications the remedy to space limitation makes the fractal geometries an interesting case of study. By perturbing the reference geometrical parameters one can tune the antenna to the desired frequency bands [4-5]. So antenna geometries and their dimensions are deciding factors to determine their operating frequencies [6]. Wireless standards like bluetooth, Wireless Local Area Network (WLAN) and Worldwide Interoperability for Microwave Access (WiMAX) are becoming more popular for wireless applications and data sharing, hence, there is huge demand for antennas with moderate gain, compact size, light weight and single-fed feed lines [7].

The proposed antenna has an advantage of compact size and simple structure which makes it better choice for wireless applications. Hybrid fractal geometries are generated by combining of two different fractal antennas or a fractal and a non-fractal antenna to form a hybrid antenna, this combination can be at generator level or at final stage of compete antenna structure [8-11].

The combination process to design the proposed hybrid antenna structure is shown in Fig. 1. Koch like microstrip structure with indention angle θ = 60° and meander like microstrip structure [12] with indention angle θ = 90° are combined to form the desired generator structure. Both Koch and meander are widely used antenna elements in wireless communication standards like ISM, GSM, UMTS, WIFI, WLAN, Bluetooth etc. Number of segments in the proposed hybrid structure (Fig. 1 (c)) is 7, whereas in case of Koch it is 4 and 5 in case of meander. This helps to achieve more miniaturization and increased effective electric length as compared to individual Koch curve or meander like structures.

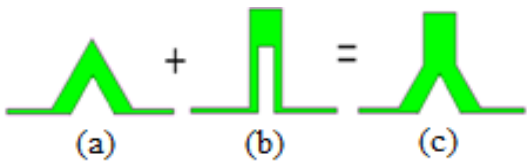

Fig. 1. (a) Koch curve, (b) meander antenna, and (c) hybrid fractal structure used as generator (n=1).

Submitted On: June 5, 2015
Accepted On: February 24, 2016

II. IFS - ITERATED FUNCTION SYSYTEM

IFS is a versatile mathematical representation to describe a fractal structure. It is used to define a generator structure by creating a series of self-affine transformation *w* [13] which can be formulated as:

$$W\begin{pmatrix}x\\y\end{pmatrix} = \begin{pmatrix}a & b\\c & d\end{pmatrix}\begin{pmatrix}x\\y\end{pmatrix} + \begin{pmatrix}e\\f\end{pmatrix}, \quad (1)$$

where *a*, *b*, *c*, *d*, *e* and *f* are real numbers. The *a*, *b*, *c* and *d* control the rotation and scaling, while *e* and *f* control linear shift or translation. Assuming w_1 w_2 … w_n as series of linear affine transformations and let *A* be the initial geometry. By applying set of transform on *A*, it can be expressed as follows:

$$W(A) = \cup_{n=1}^{N} W\ n(A). \quad (2)$$

Here, *W* is called Hutchinson operator which is used to obtain the final geometry. The transformations to obtain 7 segments of the proposed generator geometry are as follows:

$$W_1\begin{pmatrix}x\\y\end{pmatrix} = \begin{pmatrix}1/5 & 0\\0 & 1/5\end{pmatrix}\begin{pmatrix}x\\y\end{pmatrix} + \begin{pmatrix}0\\0\end{pmatrix}, \quad (3)$$

$$W_2\begin{pmatrix}x\\y\end{pmatrix} = \begin{pmatrix}1/5 & -1/4\\1/4 & 1/5\end{pmatrix}\begin{pmatrix}x\\y\end{pmatrix} + \begin{pmatrix}1/5\\0\end{pmatrix}, \quad (4)$$

$$W_3\begin{pmatrix}x\\y\end{pmatrix} = \begin{pmatrix}0 & -1/4\\1/4 & 0\end{pmatrix}\begin{pmatrix}x\\y\end{pmatrix} + \begin{pmatrix}2/5\\1/4\end{pmatrix}, \quad (5)$$

$$W_4\begin{pmatrix}x\\y\end{pmatrix} = \begin{pmatrix}1/5 & 0\\0 & 1/5\end{pmatrix}\begin{pmatrix}x\\y\end{pmatrix} + \begin{pmatrix}2/5\\1/2\end{pmatrix}, \quad (6)$$

$$W_5\begin{pmatrix}x\\y\end{pmatrix} = \begin{pmatrix}0 & 1/4\\-1/4 & 0\end{pmatrix}\begin{pmatrix}x\\y\end{pmatrix} + \begin{pmatrix}3/5\\1/2\end{pmatrix}, \quad (7)$$

$$W_6\begin{pmatrix}x\\y\end{pmatrix} = \begin{pmatrix}1/5 & 1/4\\-1/4 & 1/5\end{pmatrix}\begin{pmatrix}x\\y\end{pmatrix} + \begin{pmatrix}3/5\\1/4\end{pmatrix}, \quad (8)$$

$$W_7\begin{pmatrix}x\\y\end{pmatrix} = \begin{pmatrix}1/5 & 0\\0 & 1/5\end{pmatrix}\begin{pmatrix}x\\y\end{pmatrix} + \begin{pmatrix}4/5\\0\end{pmatrix}, \quad (9)$$

where, W_1 *to* W_7 are set of linear affine transformations. The generator is then obtained by union of all above transformations:

$$W(A)=W_1(A)\cup W_2(A)\cup W_3(A)\cup W_4(A)\cup W_5(A) \cup W_6(A)\cup W_7(A). \quad (10)$$

The process can be repeated if higher iterations are needed. As there are 7 segments in the generator structure located in 5 vertical divisions so fractal similarity dimensions can be calculated [14] using the equation:

$$D = \frac{\log(n)}{\log(r)} = \frac{\log 7}{\log 5} = 1.20906. \quad (11)$$

The proposed design is based on the 2nd iteration of the new generator to form a hybrid fractal structure antenna as shown in Fig. 2.

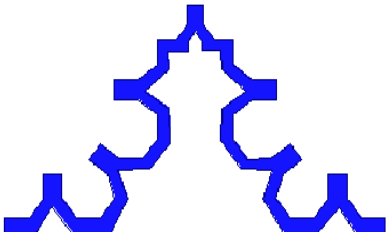

Fig. 2. Proposed hybrid fractal geometry for 2nd iteration.

The total length *l* of the structure is given by the function:

$$l = h\left(\frac{N}{r}\right)^n, \quad (12)$$

here, *N* represents the number of segments the geometry has, *r* the number that each segment is divided on each iteration and *h* the height of the curve and *n* is the number of iterations resulting in $l = h\left(\frac{7}{5}\right)^2$. The effective electrical path length is increased by each iteration, hence, for 1st iteration the length increases by a factor of 1.4.

III. ANTENNA DESIGN AND STRUCTURE

A. Methodology

Fractal structures are complex in nature and contains large number of corners, bends and edges so it is difficult to draw fractal shapes manually in HFSS. For easy understanding of the entire procedure used in designing the proposed hybrid fractal antenna structure, the procedure is shown in Fig. 3.

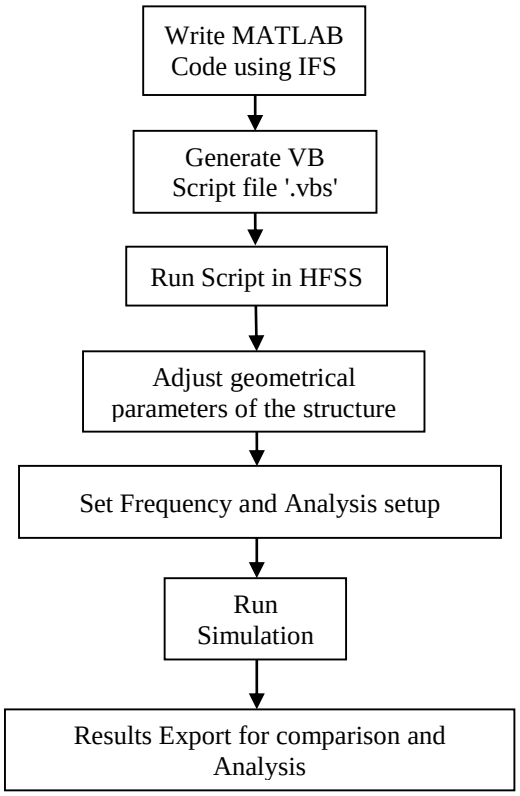

Fig. 3. Flow chart showing the various steps followed in designing and simulation of the proposed antenna.

It shows various steps starting from writing a MATLAB [15] code using IFS and generating a *.vbs script [16-17] file to draw the structure in HFSS simulator. This geometry is further used as a reference

structure for completing the final proposed antenna structure. Step 4 can be repeated to obtain desired results.

The initial design shown in Fig. 2 is used to make the final structure by combining the similar structure on a rectangular substrate.

B. Structural schematic

A Novel hybrid fractal structure is presented in this article. The purpose of designing this hybrid fractal antenna is to obtain multi-band characteristics for wireless applications. The antenna is fed through a edge connected SMA coaxial connector using microstrip feed line feed. Figure 4 shows the detailed structure of the proposed geometry along with the coordinates. In order to reduce the stray fringing fields and to improve the radiation efficiency, proposed antenna has been designed by following basic rules L1/h>>1 (L1 is length of patch), W1/h>>1 (W1 is width of microstrip feed and h is thickness of substrate), $\mathcal{E}_r$ >>1 and 1 < $\mathcal{E}_{reff}$ < $\mathcal{E}_r$ [18].

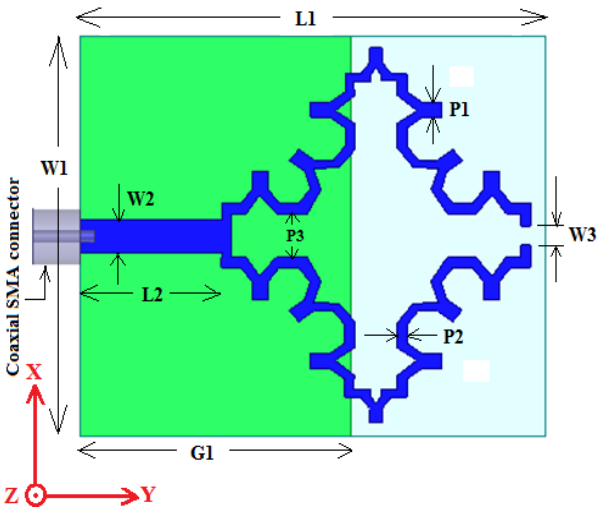

Fig. 4. Structural details of complete antenna schematic.

The antenna is designed on easily available and cost effective FR4 substrate, which is sandwiched between copper layers of radiating antenna structure and defected ground structure. It has dielectric constant $\mathcal{E}_r$ = 4.4 and dielectric loss tangent 0.02 and mass density 1900 Kg/m^3, thickness of the substrate (h) = 1.58 mm. Length L1 and width W1 of the substrate is 39 mm and 32 mm, respectively.

G1 represents the length of ground conductor layer, L2 & W2 represents length and width of microstrip feed line, whereas W3 shows the minimum gap between the two hybrid fractal arm ends. P1 shows the width of crown head and P2 shows the width of connecting arm, whereas P3 represents the maximum gap between the two hybrid fractal arms. Table 1 shows the detailed dimensional distribution of the proposed antenna geometry.

Table 1: Dimensions of the proposed hybrid fractal structure

Parameters	Dimensions (mm)
L1	39
L2	11.8
W1	32
W2	2.6
W3	1.498
P1	1.152
P2	0.85
P3	3.45
G1	22.7

All the simulations are carried out using Ansoft HFSS simulator. Proposed antenna is fed through a 2.6 mm wide and 11.8 mm long microstrip line feed. Values of effective dielectric constant and impedance is calculated using (13) and (14) [18]:

$$\mathcal{E}_{reff} = \frac{\mathcal{E}_r+1}{2} + \frac{\mathcal{E}_r-1}{2}\left[1/\sqrt{1+12h/w}\right], \quad (13)$$

$$Z_0 = \frac{120\pi}{\sqrt{\mathcal{E}reff}\left[\frac{w}{h}+1.393+0.667ln\left(\frac{w}{h}+1.444\right)\right]}. \quad (14)$$

Calculated values of $\mathcal{E}_{reff}$ and Z_0 form Equation (13) and (14) are 4 and 50 Ω for the proposed geometry.

To achieve the desired multiband characteristics while maintaining the compact size of the antenna, several design parameters of the antenna are optimized which includes varying the width of the antenna radiator (P1 and P2) structure, varying the thickness of substrate (h) and varying the length of ground plane (G1). Variation of all these parameters have a significant effect on the S_{11} characteristics and correspondingly on bandwidth and gain also. Geometrical values given in Table 1 are optimized values selected after taking a large number of trials of simulations and analysis of results. After comparison of various variations in ground length 'G1' optimized value 22.7 mm is observed and selected.

The proposed antenna has a radiating structure containing many bends, corners and edges which not only increases the total electric length of the antenna, it also causes the change in the current path which leads to more radiation and more number of resonant frequencies [19].

IV. RESULTS AND DISCUSSION

The prototype of the optimized structure is developed on easily available FR4 substrate. Figure 5 shows the complete prototype structure (top as well as bottom view) with soldered coaxial edge mounted (with clipped mounts on top) coaxial SMA connector.

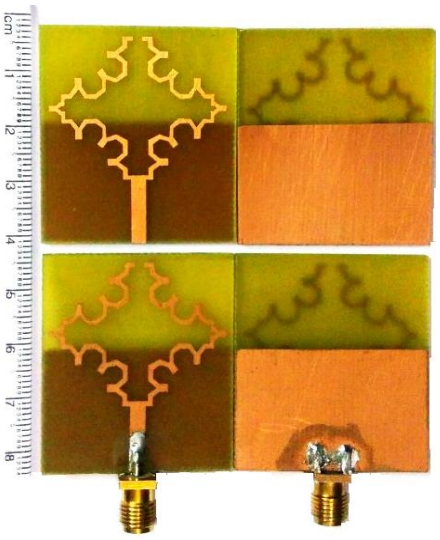

Fig. 5. Top and bottom view of fabricated hybrid fractal antenna structure.

Figure 6 shows the comparison of simulated return loss for different available and widely used substrate materials. It shows that best results are obtained by using the FR4 substrates as we get resonance in useful frequencies like 2.4 GHz, 3.4 GHz, 5.57 GHz and 8.82 GHz, whereas other substrates may show good results but they do not resonate in useful frequencies range.

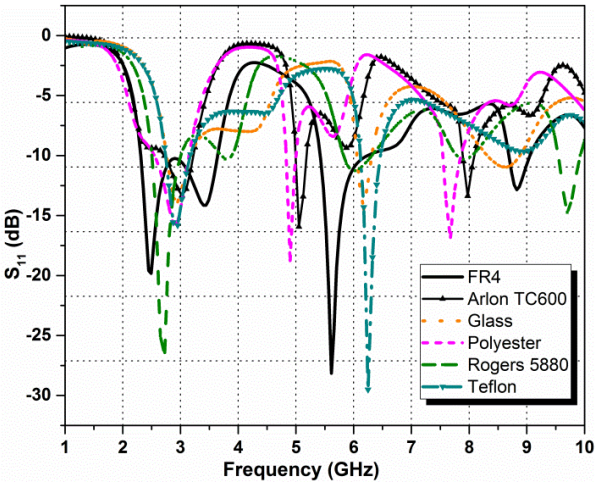

Fig. 6. Comparison of return loss for different substrates materials.

For 1st iteration, two resonating frequency bands are obtained having resonating frequencies at 3.7 GHz and 5.9 GHz having return loss values of 13 dB and 14.8 dB respectively. For 2nd iteration, four resonating bands are obtained .Table 2 shows the distribution of the obtained frequency bands along with their lower, upper and center frequency values. It also shows the associated values of S_{11} in decibels and bandwidth. The proposed antenna follows the constraint values of VSWR $\leq$ 2. All resonating frequencies have values of VSWR ranging from 1.08_{min} to 1.59_{max}. It suggests that the number of resonating bands increases with the level of iteration however the number of iterations for practical feasibility is limited to 2nd iteration only as further increase can lead to more complex structure and hence, diminishes the possibility to fabricate the structure with required precision.

Table 2: Distribution of frequency bands showing associated bandwidth and VSWR for N=2

Freq. Band No.	F_L (GHz)	F_C (GHz)	F_H (GHz)	S_{11} dB	B.W. (MHz)	VSWR
1.	2.3	2.4	2.89	-19	590	1.23
2.	2.89	3.4	3.6	-16.9	710	1.48
3.	5.35	5.57	6.1	-25.3	750	1.08
4.	8.68	8.82	9.05	-12.8	361	1.59

Figure 7 shows the 2D far-field radiation pattern with elevation planes for φ=0° (taken for reference purpose only), 90° and 180° for centre frequencies 'F_c' for each frequency band.

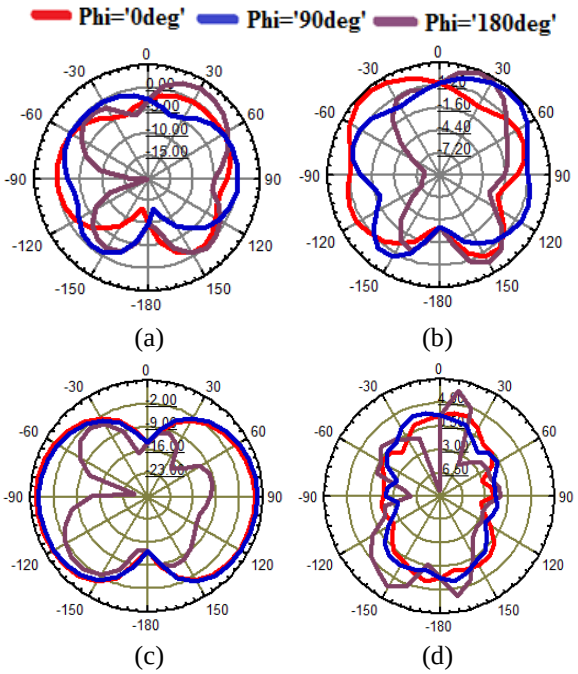

Fig. 7. Simulated E-plane (x-z) 2-D radiation pattern of proposed antenna at frequencies: (a) F_c = 2.4 GHz, (b) F_c = 3.4 GHz, (c) F_c = 5.57 GHz, and (d) Fc = 8.8 GHz.

It is seen that the fractal antenna provides almost stable patterns nearly in the form of figure-eight in the E-plane (x-z plane). The radiation pattern (as in Fig. 7 (d)) is distorted at higher frequencies as compared to lower

ones. This is due to change in the nature of current due to edge reflection resulting from standing waves from lower frequencies to a travelling wave at higher frequencies [20]. Total simulated gain of the proposed antenna is 7 dB_{max} and 3-D radiation pattern obtained at 9 GHz is almost omnidirectional as shown in Fig. 8.

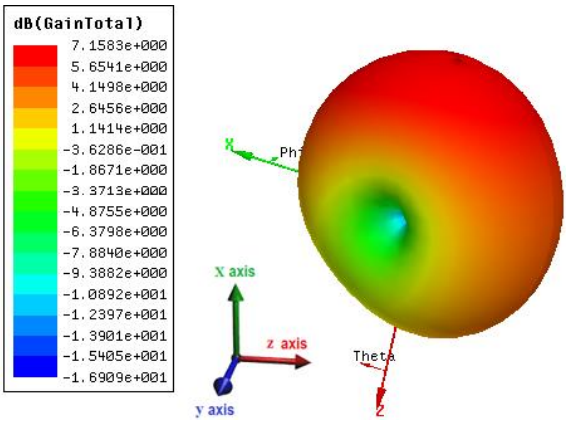

Fig. 8. Simulated 3-D radiation pattern of proposed antenna and gain total in decibels.

The prototype of the proposed structure of hybrid fractal multiband antenna is tested on Agilent's vector network analyzer (VNA). Figure 9 shows the comparison of simulated and tested return loss graphs.

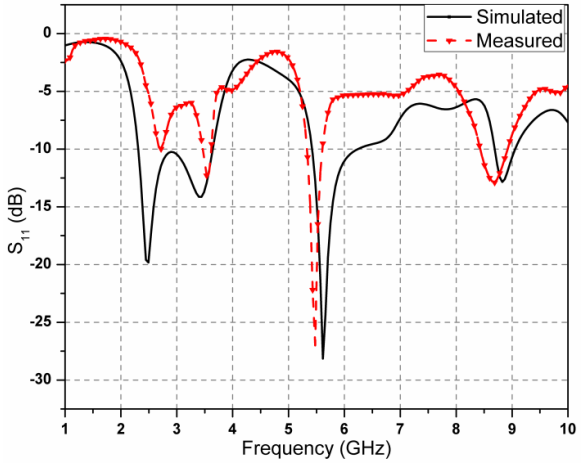

Fig. 9. Simulated versus measured return loss results of proposed antenna at different frequencies for N=2.

Both the simulated and tested return loss graphs are in good agreement with each other; however, the variation in the tested results is due to some factors in the measuring environment which includes fabrication tolerance, solder bumps, losses due to SMA connectors, losses in connecting cable etc., which are not considered in the simulation environment.

A comparison for the compactness, gain and number of frequency bands of the proposed antenna with previous work on similar fractal antennas and hybrid fractal antennas is shown in Table 3.

Table 3: Comparison of proposed antenna with other similar fractal antennas

Author	Frequency Bands	Gain dBi (max)	Size (mm^2)
S. K. Behera [3]	2	6	25 × 66
R. Azaro [5]	3	5	40 × 40
A. Jamil [6]	2	3.87	38 × 10
S. K. Sharma [8]	4	4	100 × 50
Y. Kumar [11]	7	4	28 × 15
R. A. Kumar [20]	3	4.7	30 × 25
This work	4	7	39 × 32

V. CONCLUSION

The hybrid fractal antenna exhibiting multiband behavior is analyzed and investigated. The amalgamation of Koch-Meander geometry generates a novel design which not only provides desired multiband behavior it also provides miniaturization due to increase in effective length of the antenna. Number of segments in generator structure increases to 7, whereas individual Koch curve has only 4 segments. Optimized antenna parameters are selected after taking large number of trials by varying different parameters of the antenna structure. Proposed hybrid fractal antenna resonates at four frequencies including important wireless standards like Bluetooth (2.4 GHz), WiMAX (3.4-3.7 GHz), WLAN 802.11 a/b (5.3-6.1 GHz) and Aeronautical radionavigation (8.68-9.05 GHz). Proposed antenna has acceptable values of return loss (S_{11}), VSWR (1.08_{min} to 1.59_{max}), gain (7 dB_{max}) and bandwidth (361 MHz, 750 MHz and 1300 MHz). Proposed antenna fulfills all the requirements to be used in handheld devices due to its compactness and light weight. The measured results are in good agreement with the simulated results.

REFERENCES

[1] S. H. Lee, "Multiband antenna for wireless USB dongle applications," *IEEE Antennas Wireless Propagation Letter*, vol. 10, pp. 25-28, 2011.

[2] B. B. Mandelbort, "The fractal geometry of nature," *American Journal of Physics*, vol. 51, no. 3, pp. 286, 1983.

[3] Y. K. Choukiker and S. K. Behera, "Design of wideband fractal antenna with combination of fractal geometries," *IEEE Conference Publication: ICICS*, pp. 1-3, 2011.

[4] C. Puente, J. Romeu, R. Bartoleme, and R. Pous, "Perturbation of the Sierpinski antenna to allocate operating bands," *Electronics Letters*, vol. 32, no. 24, pp. 2186-2188, 1996.

[5] R. Azaro, F. De Natale, M. Donelli, E. Zeni, and A. Massa, "Synthesis of a prefractal dual-band monopolar antenna for GPS applications," *IEEE Antennas Wireless Propagation Letter*, vol. 5, pp. 361-364, 2006.

[6] A. Jamil, M. Z. Yusoff, N. Yahya, and M. A. Zakariya, "A compact multiband hybrid meander-Koch fractal antenna for WLAN USB dongle," *IEEE Antennas Wireless Propagation Letters*, pp. 290-293, 2011.

[7] S. H. Lee, "Multiband antenna for wireless USB dongle applications," *IEEE Antennas Wireless Propagation Letter*, vol. 10, pp. 25-28, 2011.

[8] Y. K. Choukiker, S. K. Sharma, and S. K. Behera, "Hybrid fractal shape planar monopole antenna covering multiband wireless communication with MIMO implementation for handheld mobile devices," *IEEE Transactions on Antennas and Propagation*, vol. 62, no. 3, pp. 1483-1488, 2014.

[9] R. Azaro, L. Debiasi, E. Zeni, M. Benedetti, P. Rocca, and A. Massa, "A hybrid prefractal three-band antenna for multistandard mobile wireless applications," *IEEE Antennas Wireless Propagation Letter*, vol. 8, pp. 905-908, 2009.

[10] A. Azari, A. Ismail, A. Sali, and F. Hashim, "A new super wideband fractal monopole-dielectric resonator antenna," *IEEE Antennas Wireless Propagation. Letters*, vol. 12, pp. 1014-1016, 2013.

[11] Y. Kumar and S. Singh, *A Compact Multiband Hybrid Fractal Antenna for Multistandard Mobile Wireless Applications*, Wireless Personal Communications-Springer, vol. 84, no. 1, pp. 55-67, Apr. 2015.

[12] C-W. P. Huang, A. Z. Elsherbeni, and C. E. Smith, "Analysis and design of tapered meander line antennas for mobile communications," *ACES Journal*, vol. 15, no. 3, pp. 159-166, Nov. 2000.

[13] D. H Werner and S. Ganguly, "An overview of fractal antenna engineering research," *IEEE Antennas Propagation Magazine*, vol. 45, pp. 38-57, 2003.

[14] K. J. Vinoy, J. K. Abhraham, and V. K. Varadan, "On the relationship between fractal dimension and the performance of multi-resonant dipole antennas using Koch curves," *IEEE Transactions on Antenna and Propagation*, vol. 51, pp. 2296-2303, 2003.

[15] Available at http://www.mathworks.in/products/symbolic.

[16] Ansoft High Frequency Structure Simulation (HFSS), ver. 13, Ansoft Corporation, Pittsburg, PA, 2008.

[17] S. Tripathi, A. Mohan, and S. Yadav, "Ultra-wideband antenna using Minkowski-like fractal geometry," *Microwave and Optical Technology Letters*, vol. 56, no. 10, pp. 2273-2279, Oct. 2014.

[18] C. A. Balanis, *Antenna Theory: Analysis and Design*, Wiley, pp. 817-820, 2005.

[19] M. R. Haji-Hashemi, H. M. M. Sadeghi, and V. M. Moghtadai, "Space-filling patch antennas with CPW feed," *Progress in Electromagnetic Research Symposium 2006*, pp. 69-73, Mar. 2006.

[20] R. A. Kumar, Y. K. Choukiker, and S. K. Behera, "Design of hybrid fractal antenna for UWB applications," *IEEE ICCEET (International Conference on Computing, Electronics and Electrical Technologies)*, pp. 691-693, 2012.

Yadwinder Kumar born in Jalandhar District (Punjab), India on March, 1979. He has done B.Tech. in ECE from G.N.D.E.C, Ludhiana in 2001, M.Tech. in Microelectronics from Panjab University, Chandigarh in 2005 and pursuing his research work from SLIET, Longowal. Presently he is working as Sr. Assistant Professor in YCOE, Talwandi Sabo (a regional campus of Punjabi University, Patiala), Department of Electronics & Communication Engineering. Kumar is actively working in the field of Microstrip Fractal Antennas and Microelectronics and is a Lifetime Member of IMS (Indian Microelectronics Society).

Surinder Singh born in Hoshiarpur (Punjab), India, on December 27, 1975. He received B.Tech. degree from Dr. B. R. Ambedkar Regional Engineering College, Jalandhar in 1997, M.Tech. degree from GNDEC, Ludhiana in 2003 and Ph.D. degree from T.I.E.T University, Patiala, India. His area of interests are optical amplifiers, sensors and antenna for broadband communication system & networks. Presently he is working as Professor (ECE) at SLIET, Longowal, Sangrur, Punjab. He has over 93 research papers out of which 40 are in international journals and 53 are in international and national conferences. Singh is a Member of Indian Society for Technical Education, Institution of Engineers (India). He has also received the award for Best Work in Telecommunication from PAS, Punjab.